The Dissertation Committee for Leander Michael Cinninger Certifies that this is the approved version of the following dissertation:

Design of Luminescent Dinuclear Platinum(II) Complexes and Iridium(III) Catalytic Hydrogen Gas Generation

Committee:

Richard A. Jones, Supervisor

Michael Rose

Emily Que

Steve Swinnea

Jason D. Slinker

Design of Luminescent Dinuclear Platinum(II) Complexes and Iridium(III) Catalytic Hydrogen Gas Generation

by

Leander Michael Cinninger, B.S.

Dissertation

Presented to the Faculty of the Graduate School of

The University of Texas at Austin

in Partial Fulfillment

of the Requirements

for the Degree of

Doctor of Philosophy

The University of Texas at Austin

May, 2017

Dedication

To my family and friends,

Thank you for your endless support during this challenging journey of mine and for never giving up on me. You are what made this possible.

Acknowledgements

I would like to thank my advisor, Prof. Richard Jones, for all of his help, guidance, and support during my time at UT Austin. The mentorship he has provided me has been crucial in both my research and professional development, and my success in graduate school would not be possible without it. I would also like to thank the members of my committee: Dr. Emily Que, Dr. Michael Rose, Dr. Jason Slinker, and Dr. Steve Swinnea for always being there to lend a helping hand and for all of their guidance with my research. I would like to specifically thank Dr. Jason Slinker for his contribution of fabricating and testing light emitting electrochemical cell devices made with one of the dinuclear Pt(II) complexes which I synthesized. I would also like to thank Dr. Vincent Lynch for his help in development of my skills as a crystallographer, and for his patients with me when I always had a million different questions to ask.

Thank you to my co-workers Dr. Kory Mueller, Dr. Sarah Moench, Dan Strohecker, Claudina Cammack, Tyler Davis, Yawei Liang, Weiran Wang, Jason Michael, Ryan Cuifo, and Josh Pender for their friendship, discussion, and suggestions as well as making the day-to-day work truly enjoyable. I would also like to thank my friends Dr. Nolan Waggoner, Mikey Waggoner, Matt Beaudry, Landon Eads, and Tyler Hughes for their friendship and support. My success in graduate school would not be possible without them.

Design of Luminescent Dinuclear Platinum(II) Complexes and Iridium(III) Catalytic Hydrogen Gas Generation

Leander Michael Cinninger, Ph.D.

The University of Texas at Austin, 2017

Supervisor: Richard A. Jones

The use of hydrogen gas as an alternative to a petroleum fuel source has become a primary focus in research in the last decade to decrease global greenhouse gas emissions. However, further improvements in the safe storage of hydrogen gas must be developed before it can become a viable alternative fuel source. One possibility is the use of the non-flammable solid, ammonia-borane, as a form of molecular hydrogen storage. Ammonia-borane can be readily dehydrogenated using transition metal catalysts to generate hydrogen gas. One such dehydrogenation catalyst is the iridium pincer complex, (1,3-OP*t*-$Bu_2)_2C_6H_3$)$Ir(H)_2$, which has been shown to readily react with substituted ammonia-borane to generate hydrogen gas by Heinekey and coworkers. Our focus is to functionalize the iridium catalyst, (1,3-OP*t*-$Bu_2)_2C_6H_3$)$Ir(H)_2$, with capped 3,4-ethylenedioxythiophene groups to determine if functionalization of the ligand with electropolymerizable groups will alter the catalytic activity.

The transportation sector along with the production of electricity for lighting applications is estimated to generate 18% of the global greenhouse gas emissions. Thus, efficiency gains in the lighting sector along with alternative fuel sources for transportation would significantly cut the global greenhouse gas emissions. One potential way to more effectively use electricity for lighting applications is the development of more efficient

solid-state lighting. One promising new form of solid-state lighting that is currently being developed are light-emitting electrochemical cells (LEECs). Herein is reported the synthesis, characterization, and study of the photophysical properties of a series of novel pyrazolate bridged dinuclear Pt(II) complexes. The incorporation of the 3,5-diphenylpyrazole bridged dinuclear Pt(II) complex into a light-emitting electrochemical cell is also discussed.

In developing novel ligands and metal complexes, understanding the solid-state properties of these materials is of fundamental importance. One way in which this may be accomplished is through the use of x-ray crystallography. Single crystals of several novel organic ligands and metal complexes have been grown and their single crystal structures have been determined and fully analyzed for key crystallographic features.

Table of Contents

List of Tables

List of Figures

List of Schemes

Chapter 1: Latest Advancements in Hydrogen Storage and Solid-State Lighting

INTRODUCTION: GREENHOUSE GASES AND HYDROGEN PRODUCTION

Greenhouse gases are gases in the atmosphere that absorb and emit infrared radiation and are responsible for the greenhouse effect by keeping heat and energy trapped within the planet's atmosphere. Water vapor, methane, nitrous oxide, ozone, and carbon dioxide are the primary greenhouse gases in Earth's atmosphere. Due to these gases, the current average temperature on Earth's surface is 15 ºC, but without these gases, the average temperature would drop to roughly -18 ºC.[1,2]

The main gas involved with increasing surface temperatures on Earth is carbon dioxide. Since the start of the industrial revolution in 1750, human activities such as burning of coal, oil, and natural gas have caused a 40% increase in the atmospheric concentration of carbon dioxide from 280 ppm in 1750 to 400 ppm in 2015.[3,4] Other forms of anthropogenic carbon dioxide emissions include deforestation, soil erosion, and animal agriculture.[4] Increasing carbon dioxide levels are particularly concerning due to the very long lifetime of carbon dioxides in the atmosphere (30-95 years) compared to methane (12 years).[5,6] With increasing greenhouse gas emissions, more and more radiation from the sun is trapped within Earth's atmosphere, leading to global warming and climate change. It is estimated that the global surface temperature is likely to rise a further 0.3 to 1.7 ºC for the lowest emission estimates to 2.6 to 4.8 ºC for the highest emission estimates.[7] This global warming could lead to numerous impacts on Earth, including sea level rise, changes in climate extremes, and melting of the Artic sea ice. Development of carbon neutral alternative fuels for the transportation sector can greatly help cut the amount of greenhouse gas emissions. One such attractive alternative fuel is hydrogen gas.

Hydrogen is the most abundant element on Earth, but the majority of it is chemically bound as water. Overall, less than 1% of the total hydrogen on Earth is available as molecular hydrogen gas (H_2). Hydrogen gas is an attractive alternative to petroleum fuels due to the chemical energy per mass of hydrogen (142 MJ kg^{-1}) being over three times higher than that of liquid hydrocarbons (47 MJ kg^{-1}). When burnt in the presence of pure oxygen, the only by-product is water. However, when burnt in the presence of air, lean mixtures must be used to avoid the formation of nitrous oxides.

Sources of Hydrogen Gas

Currently, the four main sources of hydrogen production are natural gas (48%), oil (30%), coal (18%), and electrolysis (4%).[8] The production of hydrogen from natural gas is primarily done though steam reforming which involves the heating of the gas in the presence of steam and a nickel catalyst, producing one equivalent of carbon monoxide and three equivalents of hydrogen. The carbon monoxide can then be further mixed with steam and passed over iron oxide to produce another equivalent of hydrogen and one equivalent of carbon dioxide in a water-gas shift reaction. While this method produces four equivalents of hydrogen gas, the production of carbon dioxide is not ideal and it requires high temperatures (700-1100 ºC for steam reforming and ~360 ºC for the water-gas shift reaction). Depending on the quality of the feed stock used, 9 to 12 tons of CO_2 are produced for every ton of hydrogen.[9]

The production of hydrogen from oil is achieved via partial oxidation. Similar to the process of producing hydrogen from natural gas, the partial oxidation of oil uses the water-gas shift reaction. In the partial oxidation of oil, the fuel-air mixture is carefully controlled to give only partially combustion. The heat of the combustion produces the energy required to drive the water-gas shift reaction forward. This process results in an H_2

rich gas, which the hydrogen can be separated from the other components of the resulting gas for further use.[8]

The production of hydrogen from coal uses the process of coal gasification. Coal gasification is primarily used for the production of electricity, but the hydrogen gas produced as a by-product is separated from the other gases formed. This process is similar to steam reforming except the available hydrocarbon is coal instead of natural gas and the amount of oxygen or air that is used is carefully controlled so that the process is gasification instead of combustion.[10]

Water electrolysis is the electrochemical decomposition of water to form molecular hydrogen and molecular oxygen. The most ideal method for the generation of hydrogen gas via water electrolysis is the use of solar energy for water splitting. In this method, photovoltaic cells are used to harvest the energy from the light generated by the sun. This electricity is then used in water electrolysis to generate hydrogen gas and molecular oxygen. Unfortunately, the thermodynamics of water electrolysis are not favorable at standard temperature and pressures, requiring -1.23 V in an ideal system. However, most systems are not at ideal conditions, so water electrolysis requires large overpotentials to overcome various activation barriers. This is further hindered by the limited self-ionization of water.[11]

ADVANCEMENTS IN HYDROGEN STORAGE FOR THE TRANSPORTATION SECTOR

Metal-Organic Frameworks for Hydrogen Storage

One of the key issues facing the use of hydrogen gas is the safe storage on-board a vehicle. A modern, commercially available car which is designed for mobility with a range of roughly 250 miles requires 24 kg (8.8 gallons) of gasoline. To cover that same range,

roughly 8 kg of hydrogen would be required in a combustion engine, and half that would be required in an electric car with a fuel cell.[12]

Hydrogen gas is light-weight, highly combustible, and liquifies at very low temperature (b.p. = -252.89 ºC). For these reasons, advancements in hydrogen storage must be achieved before the use of hydrogen gas as an alternative fuel can become commercially viable. One of the promising current areas of research in the area of hydrogen storage is the use of metal-organic frameworks. Metal-organic frameworks (MOFs), as the name implies, are compounds made up of metal ions that are coordinated to organic ligands to make one-, two-, or three-dimensional structures. These structures can be very porous, which if stable upon evacuation of these pores, can then be used for the storage of gases such as hydrogen. Two ways in which hydrogen interacts with MOFs are chemisorption and physisorption. Chemisorption occurs when hydrogen interacts though stronger chemical associations with the MOF and generally involves the formation of new bonds. Physisorption occurs when hydrogen binds to the surfaces of MOFs through weak dispersive interactions and is dependent on the available surface area. MOFs are attractive for the use of hydrogen storage materials due to their large surfaces areas, which can take advantage of higher physisorption of hydrogen, as well as their low densities. However, in the temperature range of hydrogen storage for automotive applications, dispersive interactions cannot facilitate substantial hydrogen storage.[13] Therefore, current research in the area of MOFs for hydrogen storage is focused on strategies designed to increase the storage capacity of these materials.

The use of "close-packing" alignment in MOFs for hydrogen storage has been studied by Zhou and co-workers. The strategy that they employed was to increase the number of open metal sites within each H_2-hosting void and to align the open metal sites to enhance MOF-H_2 interactions.[14] The alignment of the open metal sites was key as to

allow for direct interaction with the guest H_2 molecules. The Cu-mdip (mdip = 5,5'-methylene-di-isophthalate) MOFs in which they studied were PCN-12 and PCN-12', which are polymorphs of each other. In PCN-12, all of the open metal sites are aligned and, in PCN-12', the open metal sites are out of alignment. The polymorphism arises from the ability of the mdip ligand to have either C_s or C_{2v} symmetry. PCN-12 shows a surface area of 2425 $m^2 g^{-1}$ while PCN-12' shows a surface area of 1962 $m^2 g^{-1}$. PCN-12 has a hydrogen uptake of 3.05 wt % at 77 K and 1 atm, while PCN-12' has a decreased hydrogen uptake of 2.40 wt % under the same conditions.[14] These results demonstrate the ability of the alignment of open metal sites to increase the hydrogen storage ability of MOFs.

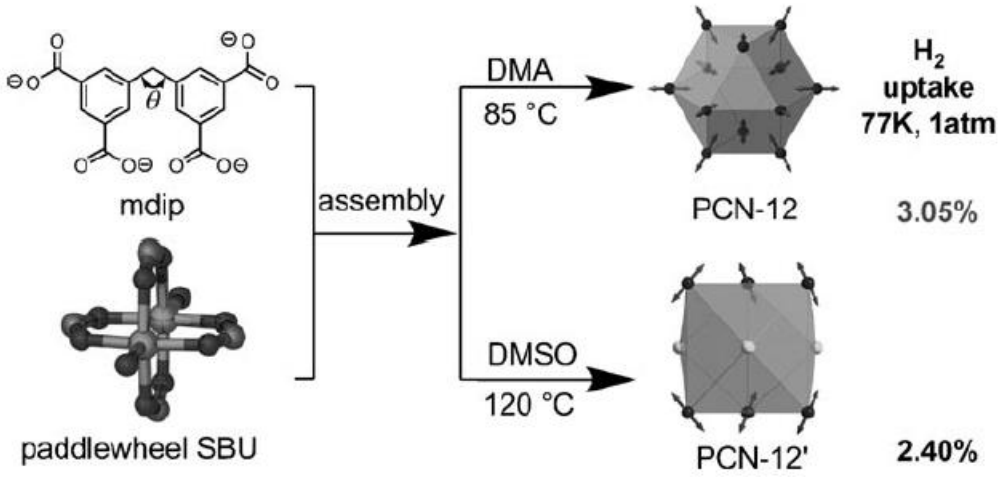

Figure 1. The synthesis, open metal site alignment, and hydrogen uptake of PCN-12 and PCN-12'.[14]

Long and co-workers have studied two different MOFs using tetrakis(4-tetrazolylphenyl)methane (H_4ttpm) as the organic linker which exhibit rare 4,6- and 4,8-connected topologies identical to garnet and fluorite.[15] Solventothermal reactions between H_4ttpm and $Mn(NO_3)_2 \cdot 4H_2O$ or $CuCl_2 \cdot 2.5H_2O$ in mixtures of DMF and methanol yielded MOFs $Mn_6(ttpm)_3 \cdot 5DMF \cdot 3H_2O$ or $Cu[(Cu_4Cl)(ttpm)_2]_2 \cdot CuCl_2 \cdot 5DMF \cdot 11H_2O$,

respectively. The combination of the 4-connected node of $ttpm^{4-}$ with the 6-connected node of the Mn^{2+} ion bound to 6 tetrazolate rings of $ttpm^{4-}$ gives rise to MOF $Mn_6(ttpm)_3 \cdot 5DMF \cdot 3H_2O$, which displays a 4,6-connected framework with garnet topology. The combination of the 4-connected node of $ttpm^{4-}$ with the 8-connected node of the $\{Cu_4Cl\}^{7+}$ unit in which each Cu^{2+} ion is bridged by two tetrazolate rings gives rise to the MOF $Cu[(Cu_4Cl)(ttpm)_2]_2 \cdot CuCl_2 \cdot 5DMF \cdot 11H_2O$, which displays a 4,8-connected framework with fluorite topology.

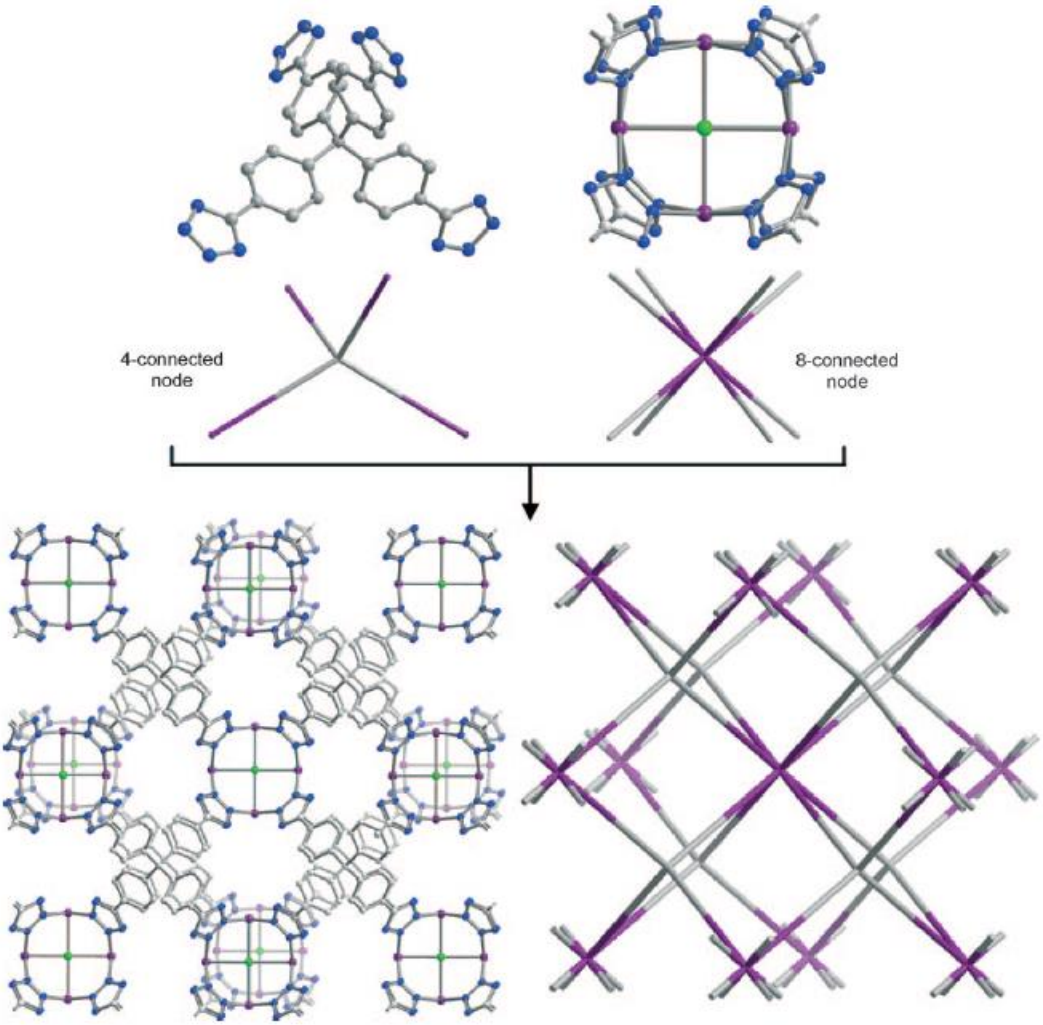

Figure 2. Portions of the crystal structure of $Cu[(Cu_4Cl)(ttpm)_2]_2 \cdot CuCl_2 \cdot 5DMF \cdot 11H_2O$: the four- and eight-connected nodes, depicted in gray and purple and represented by $ttpm^{4-}$ and $\{Cu_4Cl(tetrazole)_8$ units, respectively, combine to form a three-dimensional structure with the fluorite topology. Purple, green, blue, and grey spheres represent Cu, Cl, N, and C atoms respectively. Solvent molecules and hydrogen atoms were omitted for clarity.[15]

Unlike $Mn_6(ttpm)_3 \cdot 5DMF \cdot 3H_2O$, $Cu[(Cu_4Cl)(ttpm)_2]_2 \cdot CuCl_2 \cdot 5DMF \cdot 11H_2O$ remains intact both during methanol exchange and evacuation at 65 °C under reduced pressures. Soxhlet extraction of $CuCl_2$ using hot methanol caused a anionic-to-neutral

transformation of $Cu[(Cu_4Cl)(ttpm)_2]_2 \cdot CuCl_2 \cdot 5DMF \cdot 11H_2O$. After five days of $CuCl_2$ extraction from $Cu[(Cu_4Cl)(ttpm)_2]_2 \cdot CuCl_2 \cdot 5DMF \cdot 11H_2O$ and subsequent evacuation at 65 ^oC under reduced pressures yielded the new high surface area (2745 $m^2\ g^{-1}$) MOF, $Cu_4(ttpm)_2 \cdot 0.7CuCl_2$, which displayed Cu_4 squares void of chloride anions. Due to the lack of the chloride anions, which generated open metal coordination sites, $Cu_4(ttpm)_2 \cdot 0.7CuCl_2$ displayed a high H_2 uptake of 2.8 wt % at 77 K and 1.18 atm.[15] This research shows that anionic-to-neutral transformations within MOFs can potentially be used to generate MOFs with high H_2 uptake.

One strategy employed by Suh and co-workers was the use of a redox-active MOF which had been fabricated with palladium nanoparticles.[16] The MOF which they studied, $[Zn_3(ntb)_2]_n$ (SNU-3) where ntb = 4,4',4"-nitrilotrisbenzoate, was chosen due to the redox-activity of the ntb ligand. SNU-3 was shown to adsorb 1.03 wt % of hydrogen at 77 K and 1 atm. Incorporation of the Pd nanoparticles (3.0 ± 0.4 nm, 3 wt %) was achieved in 30 minutes via the autoredox reaction of the ntb ligands and the Pd(II) ions in an acetonitrile solution of $Pd(NO_3)_2 \cdot 2H_2O$ to yield PdNPs@$[SNU\text{-}3]^{0.54+}(NO_3^-)_{0.54}$. The surface area of PdNPs@$[SNU\text{-}3]^{0.54+}(NO_3^-)_{0.54}$ is 242 $m^2\ g^{-1}$, which is a decrease from the surface area of SNU-3 (559 $m^2\ g^{-1}$). This is not surprising due to the inclusion of the PdNPs and the NO_3^- counter anions. Despite the decrease in surface area, hydrogen absorption was increased to 1.48 wt % at 77 K and 1 atm, which increased the effective enhancement factor of hydrogen absorption by 350%, when considering the reduced surface area and increased host weight. At 298 K and 95 bar, the excess hydrogen capacity is increased to 0.30 wt % for PdNPs@$[SNU\text{-}3]^{0.54+}(NO_3^-)_{0.54}$, in comparison to SNU-3 which has a hydrogen capacity of 0.13 wt % under the same conditions. While the hydrogen capacity of PdNPs@$[SNU\text{-}3]^{0.54+}(NO_3^-)_{0.54}$ is enhanced in comparison to SNU-3, it is still lower than the very best MOFs for hydrogen capacity, which are in the regime of 2.8-3.0 wt % hydrogen capacity

at 77 K and 1 atm and an excess hydrogen capacity at 298 K of 0.3-0.6 wt %.[14,15,17–20] However, the hydrogen uptake of PdNPs@$[SNU\text{-}3]^{0.54+}(NO_3^-)_{0.54}$ is remarkable considering the surface area (242 $m^2\ g^{-1}$) in comparison to others with much larger surface areas (2000-5500 $m^2\ g^{-1}$), demonstrating the ability of Pd nanoparticles to increase hydrogen storage in MOFs.[16]

Liquid Organic Hydrogen Carriers

Liquid organic hydrogen carriers (LOHCs) are an attractive form of hydrogen storage due to their high density of available hydrogen and the ability to be readily dehydrogenated/hydrogenated for use and reuse. LOHC systems enable hydrogen storage without binding or releasing other substances from or to the atmosphere. LOHCs consist of two different phases in the scheme as alternative fuel sources. The first is hydrogen-rich LOHCs, which are ideally high-boiling carrier molecules which can be compressed and stored in liquid form. Pure H_2 is obtained after dehydrogenation of the LOHCs. The hydrogen-rich LOHC compounds can be stored for extended periods of time without energy loss and transported over long distances using established energy transport logistics for liquid fuels, which builds on the existing public confidence in dealing with liquid energy carriers. The second is hydrogen-lean LOHCs, which are the dehydrogenation byproducts after use as a hydrogen storage materials.[21]

One class of compounds which could be used as hydrogen-rich/hydrogen-lean storage molecules are aromatic hydrocarbons. Some of the aromatic hydrocarbon systems which have been studied are toluene/methylcyclohexane, naphthalene/tetralin/decalin, benzyltoluene/perhydrobenzyltoluene, and dibenzyltoluene/perhydrobenzyltoluene (Scheme 1). The toluene/methylcyclohexane system has a hydrogen storage capacity of 6.1 mass % hydrogen. However, the toluene/methylcyclohexane system has a high

thermodynamic barrier for dehydrogenation, which requires harsh conditions of at least 320 °C at 1 bar H_2.[22] Yolcular and co-workers studied the dehydrogenation of methylcyclohexane using a nickel catalyst supported on Al_2O_3.[23] The amount of nickel loaded onto the Al_2O_3 support was varied at 5, 10, 15, and 20 wt % nickel and the reactions were carried out in a fixed-bed catalytic reactor between 380 °C and 440 °C. However, under such harsh conditions, the formation of side products via dealkylation or coking was typically observed, which lead to poor conversion of methylcyclohexane to toluene.[23]

Scheme 1. Potential aromatic hydrocarbon LOHC systems: a) toluene/methylcyclohexane, b) naphthalene/tetralin/decalin, c) benzyltoluene/perhydrobenzyltoluene, d) dibenzyltoluene/perhydrobenzyltoluene.

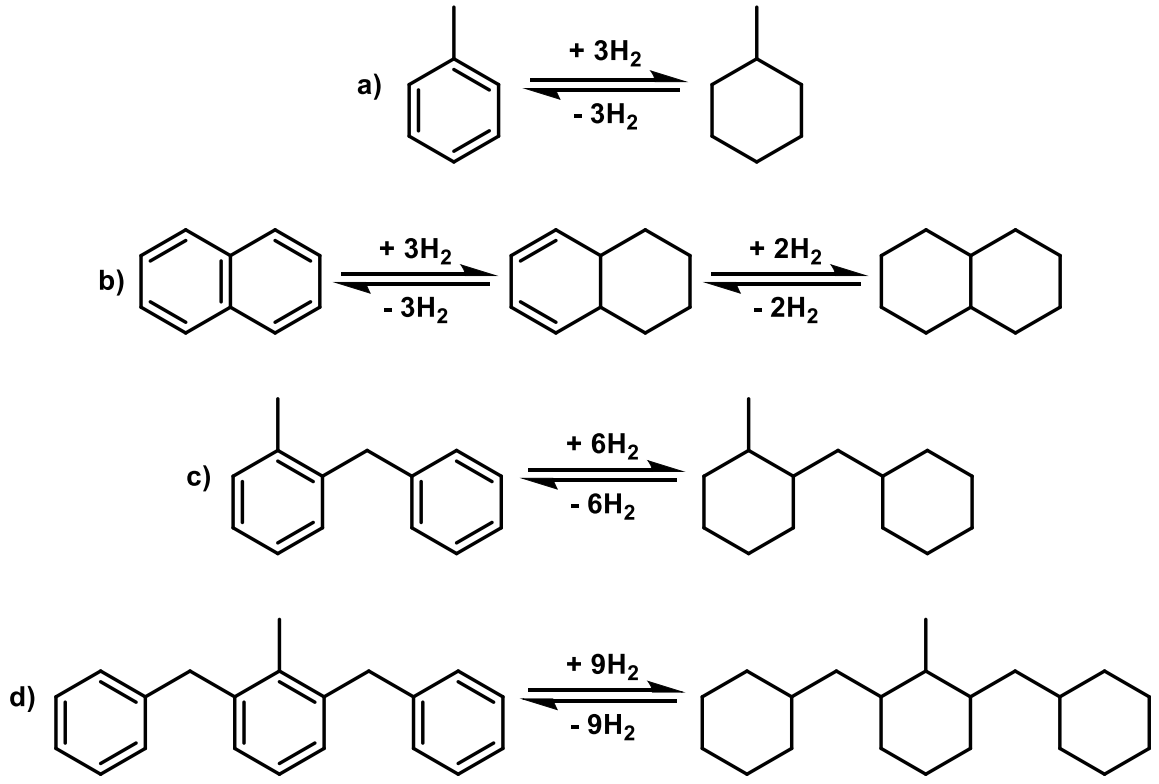

The naphthalene/tetralin/decalin, benzyltoluene/perhydrobenzyltoluene, and dibenzyltoluene/perhydrobenzyltoluene systems have a hydrogen storage capacity of 6.2 mass % hydrogen. The use of benzyltoluene and dibenzyltoluene is particularly attractive due to excellent thermal robustness, low flammability, and very favorable toxicological profiles. Furthermore, benzyltoluene and dibenzyltoluene are already in large-scale use as heat transfer oils which adds the benefit of well-established quality standards for production.[21] The use of the LOHC dibenzyltoluene/perhydrobenzyltoluene system has been studied by Wasserscheid and co-workers.[24] In their work, they studied the use of a ruthenium catalyst supported on aluminum oxide for hydrogenation of dibenzyltoluene to perhydrobenzyltoluene and then subsequent dehydrogenation of perhydrobenzyltoluene to dibenzyltoluene using a Pt catalyst supported on aluminum oxide (Scheme 2).

Scheme 2. Hydrogenation/dehydrogenation of dibenzyltoluene/perhydrobenzyltoluene for the use as a LOHC system.[21]

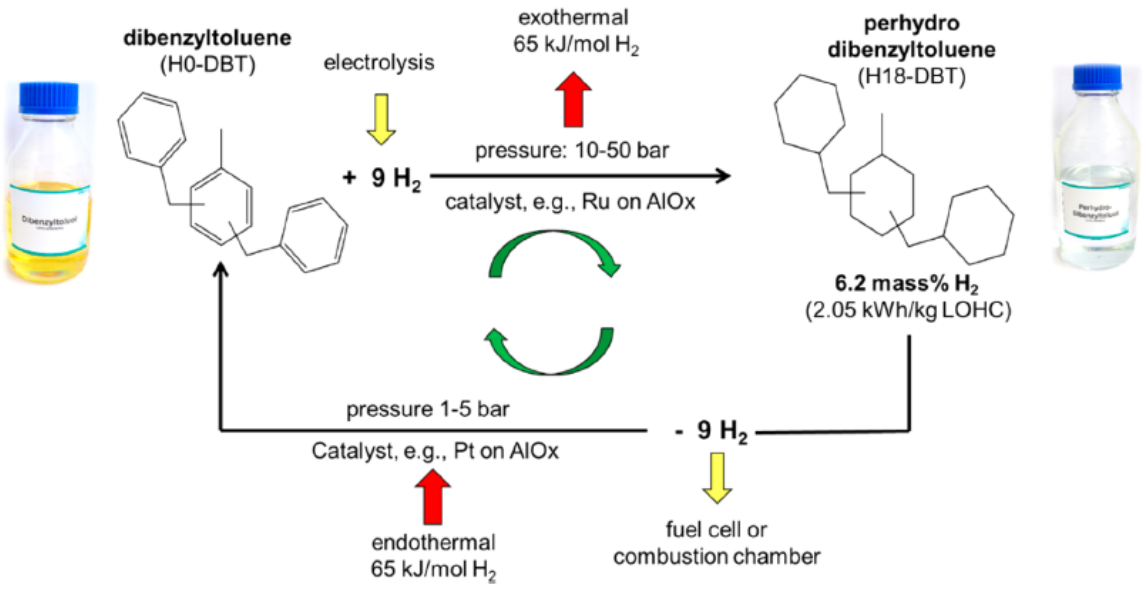

Due to the high thermodynamic barriers of aromatic hydrocarbons as LOHCs, research has been focused on the development of N-heteroaromatics as LOHC systems, which have lower thermodynamic barriers for dehydrogenation. A few of the LOHC systems which have been studied are N-ethylcarbazole/dodecahydro-N-ethylcarbazole, indole/indoline, and quinoline/1,2,3,4-tetrahydroquinoline. However, the LOHC system of N-ethylcarbazole/dodecahydro-N-ethylcarbazole (hydrogen capacity = 5.8 mass %) has a melting point of 68 ºC.[21] The use of different N-alkyl substituted carbazoles was studied by Stark and co-workers, in which they were able to lower the melting point to 24 ºC.[25] However, at temperatures below the decomposition of the heteroaromatic ring structure, the *N*-ethyl group of N-ethylcarbazole and dodecahydro-N-ethylcarbazole have a tendency to cleave off.[21] Jessop and co-workers have studied the dehydrogenation of indoline to indole using Pd supported on silica as a catalyst, which showed an 81% dehydrogenation of indoline within one hour at 100 ºC .[26] Fujita and co-workers studied the dehydrogenation of 1,2,3,4-tetrahydroquinoline using homogeneous Cp* iridium complexes, which were able to reach 100% conversion of 1,2,3,4-tetrahydroquinoline to quinoline within 20 hours at 138 ºC.[27]

Scheme 3. Potential N-heteroaromatics LOHC systems: a) N-ethylcarbazole/dodecahydro-N-ethylcarbazole, b) indole/indoline, c) quinoline/1,2,3,4-tetrahydroquinoline.

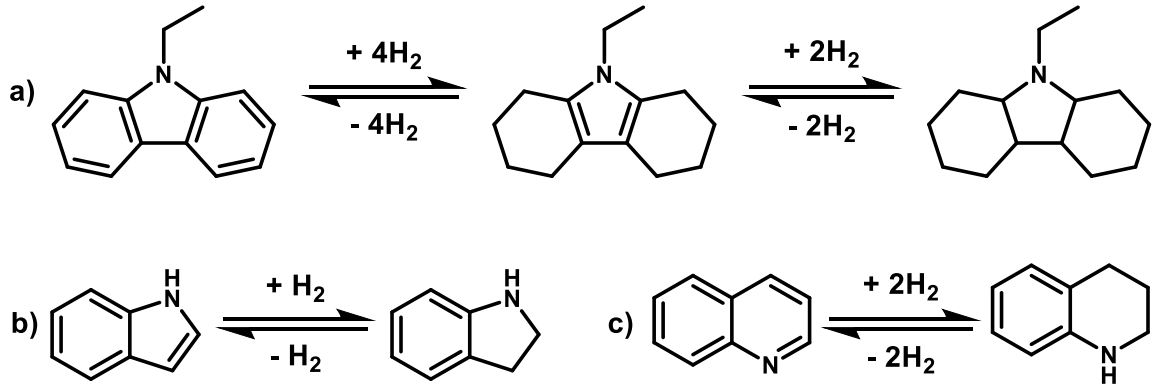

ADVANCES IN SOLID-STATE LIGHTING

As of 2010, the transportation sector along with the production of electricity for lighting applications was estimated to generate 19% of the global greenhouse gas emissions.[28,29] With an increasing global demand for electricity for myriad applications, including electricity for lighting applications, renewable, carbon neutral methods of generating electricity must be developed. The use of wind power, hydropower, solar energy, and geothermal energy to generate electricity can greatly cut the amount of greenhouse gases emitted. While developing renewable, carbon neutral methods for the production of electricity is desirable, more efficient uses of electricity can also cut global greenhouse gas emissions. One such area is the development of alternative lighting applications. Incandescent lightbulbs are a highly inefficient source of light and only convert on average 2.2 % of the energy used into visible light.[30] The rest of the energy is lost via non-radiative pathways such as heat generation. Compact fluorescent lighting (CFL) is also widely used as a light source. CFLs are much more energy efficient than incandescent lightbulbs. In comparison, the CFL counterpart to a 60 watt incandescent

lightbulb uses 77 % less energy and has a lifespan over eight times greater.[31] However, advancements in solid-state lighting are proving to be even more efficient due to lower energy consumption and longer lifetimes.

Light-Emitting Diodes

Light-emitting diodes (LEDs) have emerged as commercial options in lighting applications such as lightbulbs, televisions, automotive headlamps, and traffic signals. LEDs have many advantages over incandescent bulbs and CFLs, such as lower energy consumption (10 watts vs 14 watts for CFLs and 60 watts for incandescent bulbs), longer lifetimes (50,000 hours vs 10,000 hours for CFLs and 1,200 hours for incandescent bulbs), improved physical robustness, faster turn-on times, and smaller size.[31]

LEDs are a two-lead semiconductor light source made of a p-n junction diode, which emits light in the form of electroluminescence when an electrical current is applied. Most LEDs are comprised of III-V compound semiconductor systems based on gallium, arsenide, indium, aluminum, zinc, and selenide which have been doped with impurities such as phosphorous and nitrogen.[32] Light emission occurs when the valence band is filled with a large number of electrons, while the conduction band is practically empty due to lying at a higher energy level. Electrical conductivity is attributed to the transport of electrons in the conduction band and can be changed by filling the conduction band with electrons donated by appropriate impurity atoms.[33] The doping of these materials allows for tuning of the semiconductor direct bandgap, which then can emit light in the near-IR, visible, or near-UV range. In direct-band gap semiconductors, this transition of electrons is radiative and results in the emission of photons via electron-hole recombinations.[33]

LEDs are constructed by growing an n-type material on a p-type base. The n-type material is doped with donor atoms and the p-type material is doped with acceptor atoms.

Donor atoms are elements that have one or more valence electron than the host, where acceptor atoms have one less valence electron than the host.[33] These materials, which must be fabricated using high purity components, are typically made using techniques such as chemical vapor deposition, plasma-enhanced molecular beam epitaxy, and metal-organic vapor deposition.[32,33]

Table 1. Typical LED characteristics.[34]

Semiconductor Material	Wavelength (nm)	Color
GaAs	850-940	Infra-red
GaAsP	630-660	Red
GaAsP	605-620	Amber
GaASP:N	585-595	Yellow
AlGaP	550-570	Green
SiC	430-505	Blue
GaInN	450	White

Organic Light-Emitting Diodes

Organic light-emitting diodes (OLEDs) have attracted a considerable amount of interest due to their promising applications in flat-panel displays for technologies such as television, computer, and cell phone displays. OLEDs offer many advantages for lighting applications due to their self-emitting properties, high luminous efficiencies, full-color capabilities, low power consumption, and low bulk density.[35] OLEDs also offer the ability for flexible displays. Like LEDs, OLEDs emit light via electroluminescence. However, as the name implies, OLEDs use organic materials rather than inorganic materials such as

GaAs and GaInN. Electroluminescence in organic materials was first observed from single crystals of anthracene in the 1960s.[36] In 1987, research performed by Tang and co-workers demonstrated efficient, low-voltage OLEDs from p-n heterostucture devices using thin films of vapour-deposited organic materials.[37]

OLEDs, in the most-simple form, are constructed on a substrate with the organic material sandwiched between an anode and a cathode. The organic materials are typically pi-conjugated molecules, however, organic polymers may also be used (PLEDs).[35,38,39] The anode is a transparent material such as indium tin oxide (ITO) and the cathode is typically reflective and made of metal. When a voltage is applied to the electrodes, holes from the anode and electrons from the cathode are injected into the organic material. The charges move within the organic material typically via hopping processes and then recombine to form excitons and photons are generated.[35] The wavelength of the photon released is a function of the energy difference between the HOMO and LUMO of the electroluminescent molecules. To further increase the efficiencies, OLEDs are typically fabricated with additional electron/hole injection and transport layers.[40] Hole injection can be further enhanced via oxygen plasma treatment of the ITO[41,42] while electron injection can be enhanced using low work function metals such as calcium and magnesium.[35] However, calcium and magnesium are problematic due to their high sensitivity to moisture, so rigorous encapsulation must be used to inhibit interaction of these materials with ambient conditions.[40] More stable materials have been developed, such as magnesium/silver alloys, thin LiF layers capped with a thicker Al layer, as well as CsF, MgO, Al_2O_3, and NaCl.[35]

The main requirements for OLED materials are high luminescence quantum yields in the solid-state, good carrier mobility, good film-forming properties, good thermal and oxidative stability, and good color purity.[35] The first generation of OLEDs typically used

fluorescent molecules (Figure 3), which emit via the recombination of singlet exitons. However, singlet emission only allows for 25% quantum efficiencies due to forbidden emission from triplet excited states.

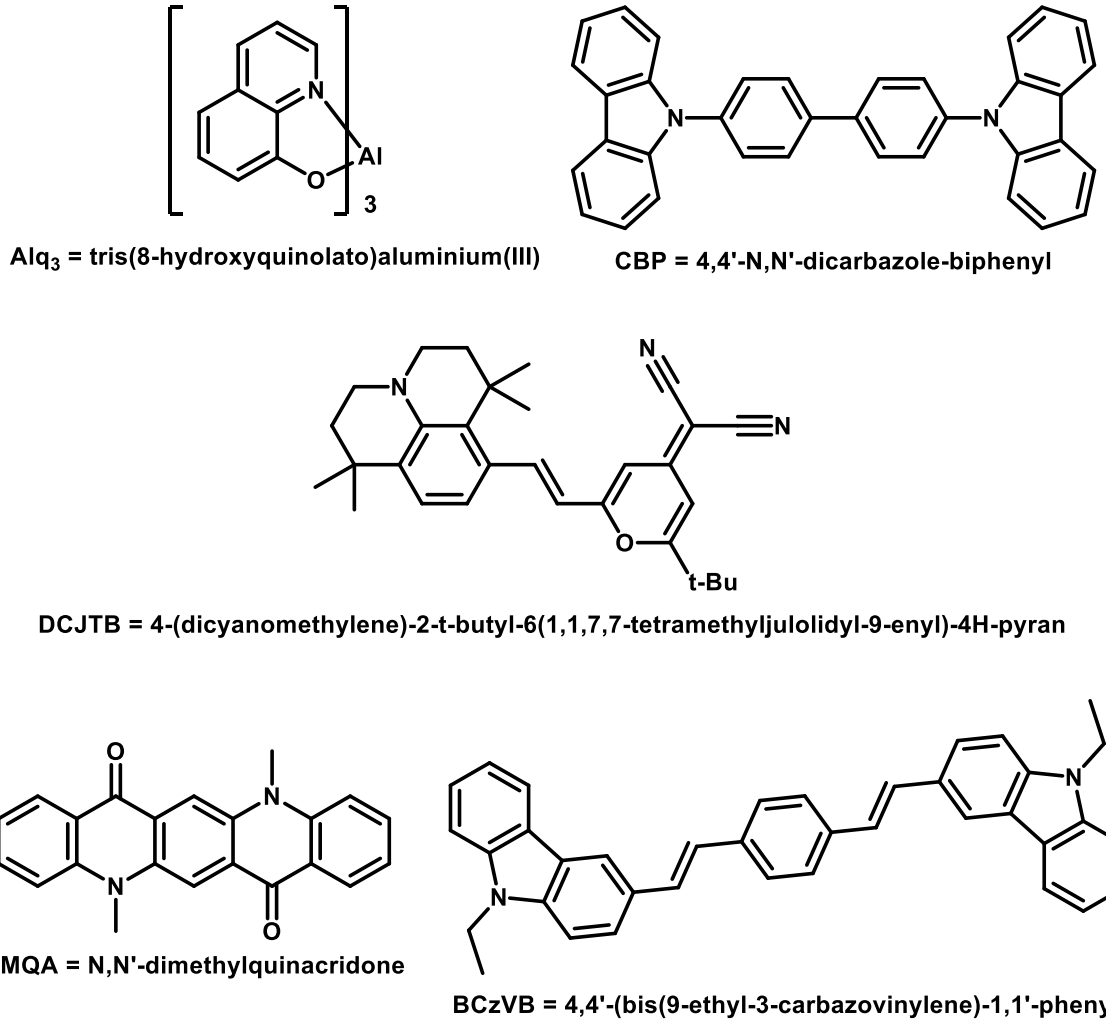

Figure 3. Examples of fluorescent molecules used in OLEDs.

To overcome this, new materials have been developed which allow for emission via triplet excited states, theoretically allowing 100% quantum efficiencies through phosphorescent emission. These materials employ heavy atoms such as iridium and

platinum, which, due to the heavy-metal effect, use spin-orbit coupling and inter-system crossing to allow radiative triplet emission. Baldo and co-workers were the first to report the use of green phosphorescent dyes to increase device efficiencies.[43] Highly efficient green and red emitters have been since developed which demonstrated internal quantum efficiencies approaching 100%.[43–45]

Chapter 2: Functionalization of an Ir(III) Catalyst with Ethyl Capped 3,4-ethylenedioxythiophene Groups for Catalytic Hydrogen Gas Generation

INTRODUCTION

The Use of Ammonia-Borane as a Hydrogen Storage Material

Ammonia-borane, NH_3BH_3, (AB) and related amine-borane complexes have been studied for their potential use as hydrogen storage materials. AB is an attractive hydrogen storage media due to the high weight percent of available hydrogen (19.6%) as well as being a light-weight, non-flammable, non-explosive solid at room temperature. AB can be synthesized in various ways, but the most common are salt metathesis of ammonium salts with borohydride salts or direct reaction of ammonia with B_2H_6 or $BH_3 \cdot THF$.[46] However, these methods of generating AB are expensive. Currently, according to the Sigma-Aldrich catalog, the price of 10 g of 90% technical grade AB is $158 while the price of 10 g of 97% technical grade AB is $325. Therefore, more efficient and cost effective methods of large-scale production of AB must be realized before its use in practical applications such as hydrogen storage are feasible. An alternative synthetic route for the production of AB has been studied by Gargare and co-workers which reveals a promising method for large-scale production.[46] They synthesized high purity AB (98%) from sodium borohydride and ammonium formate in dioxane in high yields of 95%.[47]

The dehydrogenation of AB can be achieved simply via the thermolysis of AB and subsequent $[NH_2BH_2]_n$ and $[NHBH]_n$ dehydrogenation products, liberating a total of three equivalents of H_2. However, the thermolysis of AB requires high temperatures of 70-200 ^oC and long induction periods for the release of H_2, making this method of dehydrogenation unfeasible for practical applications.[46] Research has been done in improving the induction

time of H_2 release via thermolysis by using either ionic liquids[48], organic solvents[49], or high-surface area templates such as mesoporous silica.[50]

Dehydrogenation of Ammonia-Borane Mediated by Transition-Metal Catalysts

Another approach for H_2 generation from AB is the use of transition-metal catalysts. There are two general methods for the dehydrogenation of AB using transition-metal complexes. The first of which is hydrolysis of AB in aqueous solutions. Many different transition metal complexes have been shown to be active in the hydrolysis of AB, most of which consist of cobalt, iron, copper, molybdenum, vanadium, rhodium, and iridium.[51–53] The use of cobalt, nickel, iron, copper, gold, ruthenium, rhodium, palladium, and platinum nanoparticles for the hydrolysis of AB has also been studied by various groups.[47,54–56] However, hydrolysis of AB generates various borate products which are thermodynamically difficult to rereduce as well as ammonia, which is a known poison for proton exchange membrane fuel cells.[57]

The second method is the nonhydrolytic dehydrogenation of AB. Typical homogeneous transition-metal catalysts which are used in this method are complexes of iron[58–60], molybdenum,[61] iridium,[62,63] rhodium,[64–68] nickel,[69] palladium,[70,71] and ruthenium.[57,72–76] Of these catalysts, very few are capable of releasing two or more equivalents of H_2, and the ones that are capable of releasing more than two equivalents of H_2 require long reaction times.[57,60,61,69] Fagnou and co-workers have studied the use of ruthenium-based known alcohol redox process catalysts as ammonia-borane dehydrogenation catalysts (Figure 4).[72] Catalysts **F1** and **F2** proved to be particularly active toward AB dehydrogenation, generating one equivalent of H_2 within five minutes with as little as 0.03 mol % catalyst loading at room temperature in THF.

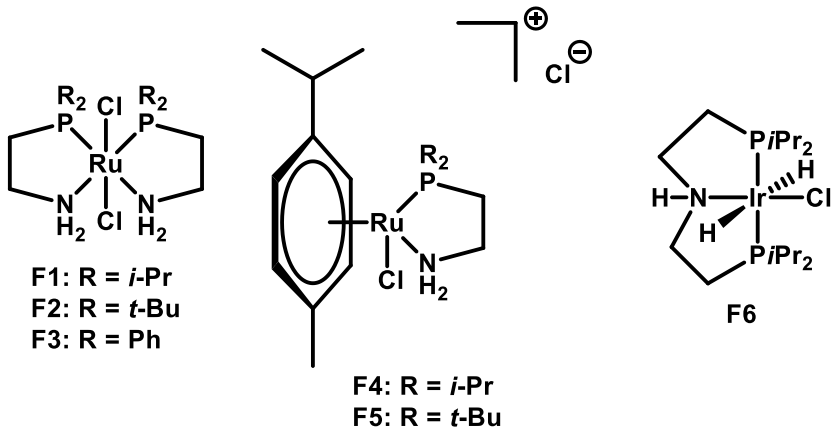

Figure 4. Ammonia-borane dehydrogenation catalysts studied by Fagnou and co-workers.

Heinekey and co-workers have studied the catalytic AB dehydrogenation using an Ir(III) PCP catalyst.[62,63] The catalyst, (POCOP)IrH_2 (where POCOP = [η^3-1,3-(OP(*t*-Bu)$_2$)$_2$$C_6H_3$], was first studied by Brookhart for the transfer dehydrogenation of alkanes.[77,78] The theory proposed by Heinekey is that the Ir(III) PCP catalyst could effectively dehydrogenate AB due to ammonia-borane being isoelectronic with the ethane. Indeed, they were able to show that (POCOP)IrH_2 was highly active toward AB dehydrogenation, where using 0.5 mol % catalyst loading of (POCOP)IrH_2 generated one equivalent of H_2 within 14 minutes at room temperature in THF. Decreasing the catalyst loading to 0.25 mol % extended the reaction time of H_2 generation to over 30 minutes while increasing the catalyst loading to 1.0 mol % decreased the reaction time of H_2 generation to roughly 4 minutes. Only one equivalent of H_2 was generated for the reactions using 0.25 mol % and 1.0 mol % of (POCOP)IrH_2 as well. In all cases, a solid precipitate was formed which was identified as the known cyclic pentamer, [H_2NBH_2]$_5$. However, after complete consumption of the AB, gas generation was immediately renewed upon addition of more AB.[62] The (POCOP)IrH_2 catalyst is of particular interest due to the ability change the

electron donating ability of the phosphine "arms" of the ligand via the use of different substituted phosphines as well as the ability to easily functionalize the benzene core.

EXPERIMENTAL

Instrumentation

All ^{1}H, ^{13}C, ^{19}F, and ^{31}P NMR spectra were recorded on either a Varian Unity 300 spectrometer (300 MHz), Varian Mercury 400 spectrometer (400 MHz), Varian DirectDrive 400 spectrometer (400 MHz), or Agilent MR 400 spectrometer (400 MHz). All ^{1}H and ^{13}C NMR signals were referenced to residual solvent peaks and reported in ppm; all coupling constants are reported in Hz. Infrared spectra were recorded on a Nicolet iS50 FT-IR spectrophotometer. Low-resolution and high-resolution mass spectrometry was performed on an Agilent Technologies 6530 Accurate Mass QTofLC/MS spectrometer. Melting points were recorded on an OptiMelt Automated Melting Point System made by Stanford Research Systems. Elemental analysis was performed by Midwest MicroLab Inc. (Indianapolis, IN).

Crystal Structure Determination

Crystallographic data for complex **8** is given in Table S1. Single crystals of **8** were grown via slow evaporation of a CH_2Cl_2/Et_2O solution of **8**. Crystals were covered in a Paratone/chloroform mixture and mounted on a nylon thread loop. Data was collected at 100 K on an Agilent Technologies SuperNova Dual Source diffractometer equipped with a AtlasS2 CCD detector using a μ-focus Cu Kα radiation source (λ = 1.5418 Å) and an Oxford 700 Cryostream system. Data collection, unit cell refinement, and data reduction were performed using the Agilent Technologies CrysAlisPro software. The structure of **8** was solved by direct methods using the SIR2014 program and refined by full-matrix least-squares on F2 with anisotropic displacement parameters for all non-H atoms using

SHELXL-2014. The structural analyses were performed using the PLATON98 and WinGX programs. The hydrogen atoms were placed in fixed, calculated positions with isotropic displacement parameters set to 1.2 x Ueq with respect to the attached atom. Crystallographic images were created using the Cambridge Crystallographic Data Centre's Mercury program and rendered using POV-ray. All bond angles, torsion angles, and intermolecular interactions were calculated using the Cambridge Crystallographic Data Centre's Mercury software. The intermolecular interactions are calculated by the Mercury software by looking for atoms within close contact of each other based on their Van der Waal's radii plus 0.15 Å.

Electrochemistry

All electrochemical experiments were performed under nitrogen in a glovebox using a GPES system from Eco. Chemie B. V. and an Autolab Potentiostat. The electrolyte used was 0.1 M tetrabutylammonium hexafluorophosphate, $[(n\text{-}Bu)_4N][PF_6]$ ($TBAPF_6$) in either dry CH_3CN, CH_2Cl_2, or THF. The electrolyte was purified via three recrystallizations from hot ethanol before drying under dynamic vacuum for three days at 100 ^oC. Electrochemical experiments on **7** and **8** were carried out in a 20 mL electrochemical cell using a glassy carbon button working electrode (1.6 mm diameter), a $Ag/AgNO_3$ (0.01 M $AgNO_3$ and 0.1 M $TBAPF_6$ in dry CH_3CN) non-aqueous reference electrode, and a Pt wire coil counter electrode. All potentials were reported relative to ferrocene/ferrocenium, which was used as an external standard to calibrate the reference electrode. Ferrocene was purified by sublimation at 95 ^oC. A step potential of 10 mV and a scan rate of 100 mV s-1 were used unless otherwise noted.

Synthesis

All air and moisture-sensitive reactions were performed using standard Schlenk, high vacuum, and glovebox techniques using a nitrogen atmosphere unless otherwise noted. All dry solvents were dried using an Innovative Technology, Pure Solv solvent purifier with a double purifying column and sitting over 3 Å molecular sieves for 48 hours. The ammonia-borane complex (Sigma Aldrich) was purified via vacuum sublimation at 75 ^{o}C/ 140 militorr and all other chemicals were used as received. The following compounds were prepared by literature procedures: 4,6-diiodobenzene-1,3-diol (**1**), 1,5-diacetoxy-2,4-diiodobenzene (**2**), and 2-n-hexyl-3,4-ethylenedioxythiophene (**3a**).

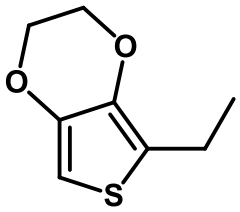

3

Preparation of 3

In a Schlenk flask equipped, 3,4-ethylenedioxythiophene (5 mL, 46.81 mmol) was dissolved in THF (250 mL). The solution was cooled to -78 ^{o}C then *n*-BuLi (32 mL of a 1.6 M hexane solution, 51.49 mmol) was added drop-wise. Upon complete addition of the *n*-BuLi solution, the reaction was stirred for one hour. Iodoethane (5.64 mL, 70.21 mmol) was then added drop-wise to the solution. The solution was stirred for 16 hours, warming to room temperature. The THF was removed under vacuum giving an orange oil. The oil was dissolved in Et_2O (50 mL), washed with aqueous NH_4Cl (2 x 20 mL of 3.58 M solution) followed by a final wash with cold DI water (20 mL). The organic layer was dried over anhydrous magnesium sulfate and filtered. The solvent was removed under vacuum,

resulting in an orange oil. The oil was purified via column chromatography on silica gel using 10% ethyl acetate in hexane. The product (**3**) was collected as a pale-yellow oil (1.76 g, 10.34 mmol, 22%). ^{1}H NMR (300 MHz, Chloroform-*d*) δ 6.12 (s, 1H), 4.18 (d, *J* = 0.9 Hz, 4H), 2.69 (q, *J* = 7.5 Hz, 2H), 1.25 (t, *J* = 7.5 Hz, 3H). ^{13}C {^{1}H} NMR (100.52 mHz, CD_2Cl_2) 141.51, 137.04, 119.78, 94.84, 64.64, 64.49, 19.34, 14.78.

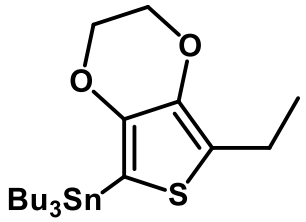

4

Preparation of 4

In a 3-neck flask, **3** (1.76 g, 10.34 mmol) was dissolved in THF (100 mL). The solution was cooled to -78 ^{o}C then *n*-BuLi (7.11 mL of a 1.6 M hexane solution, 40.54 mmol) was added drop-wise. Upon complete addition of the *n*-BuLi solution, the reaction was stirred for one hour at -78 ^{o}C. Tributyltinchloride (3.9 mL, 14.47 mmol) was added to the flask drop-wise. The resulting pale yellow solution was stirred for 16 hours, warming to room temperature. The THF was removed under vacuum, resulting in a pale yellow, oily residue. The residue was dissolved in Et_2O (20 mL) then washed with water (2 x 10 mL). The organic layer was dried over anhydrous magnesium sulfate and filtered. The Et_2O was removed under vacuum, producing a pale-yellow oil (5.73 g). The oil was used in future reactions without further purification.

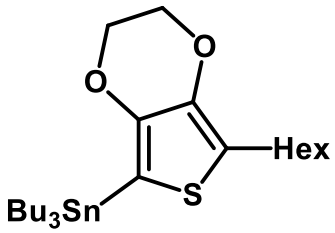

4a

Preparation of 4a

In a dry 3-neck flask, 2-*n*-hexyl-3,4-(ethylenedioxy)thiophene (8.74 g, 38.62 mmol) was dissolved in dry THF (500 mL). The solution was cooled to -78 ^{o}C then *n*-BuLi (38.25 mL of a 1.6 M solution in hexanes, 40.54 mmol) was added drop-wise using an addition funnel. Upon complete addition of the *n*-BuLi solution, the reaction was stirred for one hour at -78^{o}C. Tributyltinchloride (15.29 mL, 54.05 mmol) was added to the flask drop-wise using an addition funnel. The resulting orange solution was stirred overnight, warming to room temperature. The THF was removed by rotary evaporation, resulting in an orange, oily residue. The residue was dissolved in diethylether (50 mL) then washed twice with water (2 x 20 mL). The organic layer was dried with anhydrous magnesium sulfate, and then filtered. The solvent was removed by rotary evaporation, producing 29.88 g of a dark orange oil. The oil was used in future reactions without further purification.

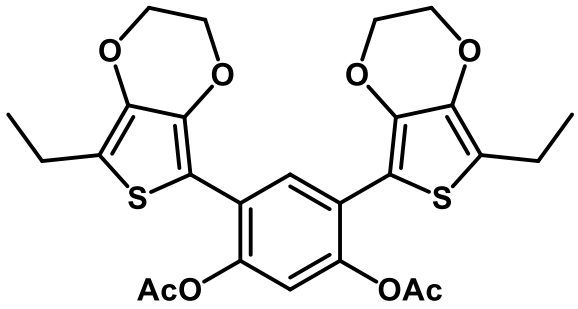

5

Preparation of 5

To a Schlenk flask, 1,5-diacetoxy-2,4-diiodobenzene (1 g, 2.24 mmol), **4** (3.16 g, 8.97 mmol), CsF (1.36 g, 8.97 mmol), CuI (42.7 mg, 0.22 mmol), tris(dibenzylideneacetone)dipalladium(0) (102.7 mg, 0.11 mmol), and [(*t*-Bu)$_3$PH][BF$_4$] (71.6 mg , 0.24 mmol). Reagents were dissolved in *n*-methylpyrolidone (NMP, 20 mL) then heated to 85 ^{o}C for 4 days. The reaction mixture was diluted with CH_2Cl_2 (30 mL) then washed with aqueous NaCl (3 x 20 mL of 3.07 M solution) followed by a final wash with cold DI water (20 mL). The organic layer was dried over anhydrous magnesium sulfate then filtered. The solvent was removed under vacuum to yield a dark brown liquid. Residual NMP was removed by column chromatography on silica gel using Et_2O/hexanes (1:1 v/v) as an elutant, which could be monitored by following the yellow band on the column. The crude product was recovered from the column by flushing with ethyl acetate then the solvent was removed under vacuum resulting in a brown oil. The crude product was purified by column chromatography on silica gel using CH_2Cl_2 as the elutant. Partial deprotection occurred during the column chromatography, and separation of the two different products was difficult. Therefore, the two products were collected together and used in the following reaction crude.

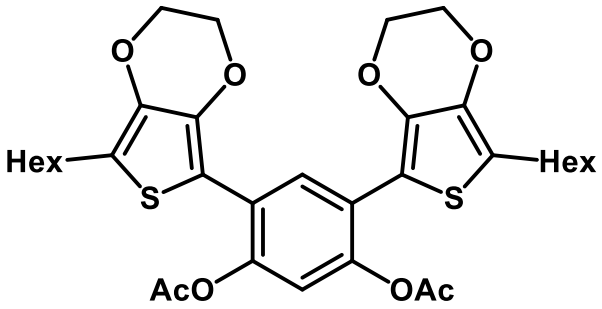

5a

Preparation of 5a

To a dry Schlenk flask, 1,5-diacetoxy-2,4-diiodobenzene (2.00 g, 4.48 mmol), **4a** (9.25 g, 17.94 mmol), tris(dibenzylideneacetone)dipalladium(0) (205.40 mg, 0.22 mmol), and [(*t*-Bu)$_3$PH][BF_4] (138.00 mg, 0.47 mmol) were added. Reactants were dissolved in dry *n*-methylpyrolidone (NMP, 25 mL). The solution was heated to 85 ^oC and stirred for three days. The NMP was removed by column chromatography on silica gel using diethylether/ hexanes (1:1 v/v) as the elutant. Upon removal of the NMP, the column was flushed with ethyl acetate. The ethyl acetate solution was concentrated to ~20 mL then washed with water (2 x 20 mL). The organic layer was dried with anhydrous magnesium sulfate, and then filtered. Removal of the solvent resulted in a brownish yellow oil. The oil was purified by column chromatography on silica gel using CH_2Cl_2 as the elutant to afford **5a** (2.01 g, 3.13 mmol, 70%) as a brown solid. m.p. 112 ^oC (decomp.). ^1H NMR (399.77 MHz, $CDCl_3$): δ 8.07 (s, 1H), 6.98 (s, 1H), 4.19 (s, 8H), 2.65 (t, *J*=7.6, 4H), 2.29 (s, 6H), 1.62 (p, *J*=7.6, 4H), 1.35 (m, 12H), 0.90 (t, *J*=6.8, 6H). ^{13}C NMR (100.52 MHz, $CDCl_3$) δ 168.97, 145.31, 138.54, 137.13, 131.58, 123.43, 118.47, 118.03, 106.92, 64.77, 64.23, 31.50, 30.29, 28.86, 25.74, 22.55, 21.34, 14.04. FTIR (cm^{-1}): 2924, 2853 (s, alkyl C-H); 1752 (s, C=O). HRMS (ESI) m/z calculated for $C_{34}H_{42}O_8S_2$ 665.8126 $[M+Na]^+$, found 665.2208.

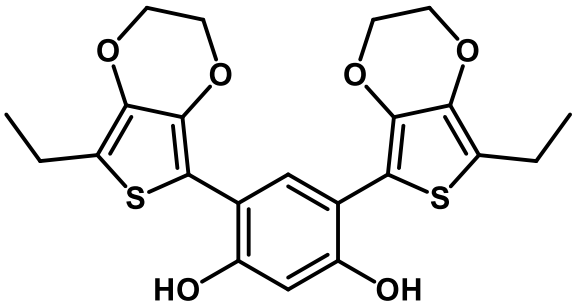

6

Preparation of 6

In a Schlenk flask, **5** (100 mg, 0.19 mmol) was dissolved in THF (3 mL). The solution was cooled to 0 °C then lithium aluminum hydride ($LiAlH_4$, 43 mg, 1.13 mmol) was added to the solution slowly. The reaction was stirred for 16 hours, warming to room temperature. Unreacted $LiAlH_4$ was quenched with ethyl acetate (2 mL) slowly then the solvent was removed *in vacuo*. The resulting residue was dissolved in deoxygenated chloroform (7 mL) then washed with Rochelle's salt (2 x 5 mL of a 1.17 M aqueous, deoxygenated solution) followed by washes with cold, deoxygenated DI water (2 x 5 mL). Each wash was removed by cannula filtering off the top aqueous layer from the chloroform. Solvent was removed *in vacuo* then the resulting residue was dissolved in CH_2Cl_2 (10 mL). The CH_2Cl_2 solution was cannula filtered into a new Schlenk flask. The CH_2Cl_2 was removed *in vacuo* resulting in a tan solid (72.80 mg, 0.16 mmol, 87%). The product glows purple upon excitation with a long-wave UV lamp (λ_{max} = 365 nm). ^{1}H NMR (400 MHz, Methylene Chloride-d_2) δ 7.22 (s, 1H), 6.94 (s, 2H), 6.56 (s, 1H), 4.38 – 4.32 (m, 4H), 4.27 – 4.22 (m, 4H), 2.70 (q, J = 7.5 Hz, 4H), 1.24 (t, J = 7.5 Hz, 6H).

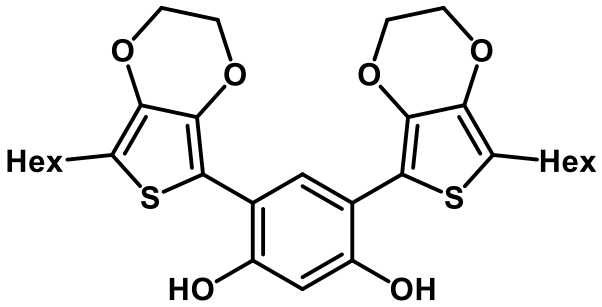

6a

Preparation of 6a

In a dry Schlenk flask, **5a** (500 mg, 0.78 mmol) was dissolved in dry THF (15 mL). The solution was cooled to 0 ºC then $LiAlH_4$ (147.61 mg, 3.89 mmol) was added to the flask. Upon addition, the solution bubbled and then turned a slight greenish, grey color. The solution was stirred overnight, warming to room temperature. Remaining $LiAlH_4$ was quenched using deoxygenated ethyl acetate (1 mL). Solvent was removed *in vacuo* then the remaining residue was dissolved in deoxygenated CH_2Cl_2 (10 mL) then washed with Rochelle's salt (2 x 5 mL of a 1.17 M aqueous, deoxygenated solution) followed by washes with cold, deoxygenated DI water (2 x 5 mL). Each wash was removed by cannula filtering off the top aqueous layer from the CH_2Cl_2. The CH_2Cl_2 solution was cannula filtered into a new Schlenk flask. The CH_2Cl_2 was removed *in vacuo* resulting in **3** (350 mg, 0.63 mmol, 81%) as a brown solid. ^{1}H NMR (399.77 MHz, CD_2Cl_2): δ 7.22 (s, 1H), 6.95 (s, 2H), 6.56 (s, 1H), 4.30 (dm, *J*=44.0, 8H), 2.66 (t, *J*=7.6, 4H), 1.62 (p, *J*=8.0, 4H), 1.33 (m, 12H), 0.90 (t, *J*=7.0, 6H). ^{13}C NMR (100.52 MHz, CD_2Cl_2) δ 154.60, 137.58, 135.37, 130.34, 118.97, 113.82, 110.19, 106.59, 66.19, 64.64, 31.91, 30.80, 29.17, 26.09, 22.97, 14.22. FTIR (cm^{-1}): 3293 (br, O-H); 2924, 2854 (s, alkyl C-H).

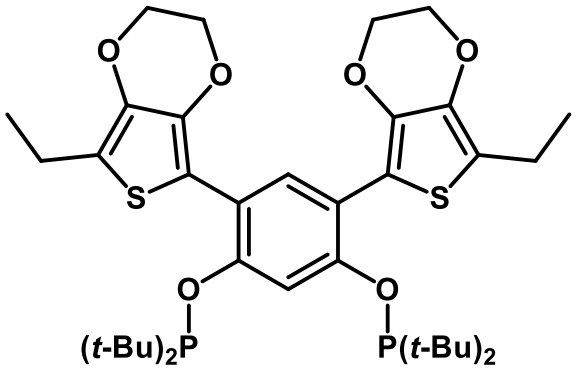

7

Preparation of 7

In a Schlenk flask equipped a condenser, **6** (108.5 mg, 0.24 mmol) was dissolved in THF (20 mL). To the solution, NaH (20.41 mg of 60% NaH suspended in paraffin oil, 0.51 mmol) was added to the solution slowly. The reaction was heated to 75 ºC for one hour then cooled to room temperature. To the reaction, di-*tert*-butylchlorophosphine (10.09 mL of a 48.5 μM THF solution) was added slowly. The solution was heated to 75 ºC for 2 days. The solvent was removed *in vacuo* to yield a tan solid. The solid was dissolved in toluene (10 mL) and insoluble impurities were removed by filtration through a neutral alumina plug. The toluene was removed *in vacuo*. The product was purified by recrystallization from CH_2Cl_2 (3 mL) by slowly adding pentane until the formation of a precipitate was noticed. The impurities were removed by filtration through celite, then the CH_2Cl_2 was removed *in vacuo* to yield a tan solid (123.9 mg, 0.17 mmol, 69%). The product glows purple upon excitation with a long-wave UV lamp (λ_{max} = 365 nm). ^{1}H NMR (300 MHz, Methylene Chloride-d_2) δ 7.76 (t, J = 5.4 Hz, 1H), 7.68 (s, 1H), 4.18 (s, 8H), 2.70 (q, J = 7.5 Hz, 3H), 1.32 – 1.06 (m, 42H). ^{31}P NMR (121 MHz, Methylene Chloride-d_2) δ 158.20.

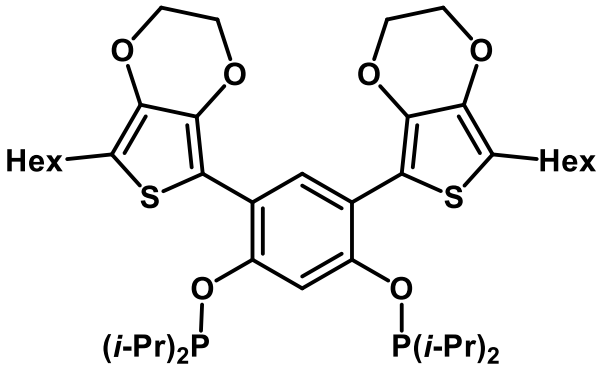

7a

Preparation of 7a

In a dry Schlenk flask, **6a** (100 mg, 0.18 mmol) and NaH (15 mg of 60% NaH suspended in paraffin oil, 0.38 mmol) were dissolved in dry THF (2 mL). The solution was heated to 90 ºC and stirred for one hour. The solution cooled to room temperature then di-*iso*-propylchlorophosphine (57.35 mg, 0.38 mmol) dissolved in dry THF (1 mL) was added to the reaction drop-wise. The solution was heated to 90 ºC and stirred for 24 hours. The solvent was removed *in vacuo*, resulting in an orange oil with a white precipitate. The residue was extracted with dry hexanes (5 mL) then purified on a neutral alumina plug using dry hexanes as the elutant. The solvent was removed *in vacuo* resulting in **4** (132.30 mg, 0.17 mmol, 93 %) as an orange oil. ^{1}H NMR (399.77 MHz, CD_2Cl_2): δ 8.09 (s, 1H), 7.58 (t, *J*=4.8, 1H), 4.20 (m, 8H), 2.68 (t, *J*=7.6, 4H), 2.04 (sepd, *J*=7.2, *J*=3.2, 4H), 1.64 (quin, *J*=7.2, 4H), 1.34 (m, 12H), 1.14 (m, 24H), 0.92 (t, *J*=4.8, 6H). ^{13}C NMR (100.52 MHz, CD_2Cl_2) δ 155.22 138.06, 137.44, 131.24, 116.86, 116.35, 108.96, 106.71, 65.86, 64.86, 32.09, 30.93, 29.17, 28.47 (d, *J*=18.2), 25.98, 23.11, 17.92 (d, *J*=19.7) 17.42 (d, *J*=9.1), 14.34. ^{31}P NMR (161.83 MHz, CD_2Cl_2) δ 150.69. FTIR (cm^{-1}): 2923, 2854 (s, alkyl C-H). HRMS (CI) m/z calculated for $C_{42}H_{64}O_6P_2S_2$ 790.3624 $[M]^+$, found 790.3610.

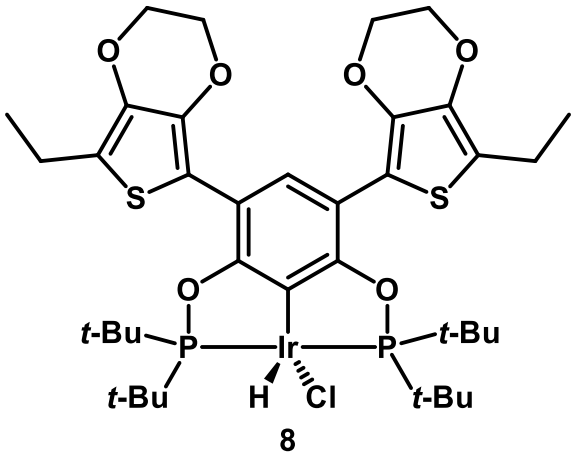

8

Preparation of 8

In a Schlenk flask equipped with a reflux condensor, **7** (123.9 mg, 0.17 mmol) and bis(1,5-cyclooctadiene)diiridium(I) dichloride (46.6 mg, 0.08 mmol) were dissolved in toluene (2 mL). The reaction was heated to 150 ^{o}C for 24 hours. The toluene was removed *in vacuo* to yield an orange/brown solid. The product was purified by recrystallization from CH_2Cl_2 (3 mL) by slowly adding pentane until the formation of a precipitate was noticed. The impurities were removed by filtration through celite, then the toluene was removed under vacuum. The product was collected as a dark red solid (75 mg, 0.08 mmol, 46%). Melting point, 226-275 ^{o}C (decomposition). Elemental analysis calcd for $C_{38}H_{56}ClIrO_6P_2S_2$ (962.59): C, 47.42; H, 5.86. Found: C, 48.03; H, 5.75. ^{1}H NMR (300 MHz, CD_2Cl_2) δ 8.08 (s, 1H), 4.23 (d, *J* = 1.5 Hz, 8H), 2.70 (q, *J* = 7.5 Hz, 4H), 1.40 (t, *J* = 7.6 Hz, 36H), 1.25 (t, *J* = 7.5 Hz, 6H), -41.32 (t, *J* = 13.0 Hz, 1H). ^{13}C NMR (101 MHz, CD_2Cl_2) δ 161.30, 137.87, 137.22, 126.07, 117.62, 111.58, 109.73, 65.18, 64.80, 43.47 (t, *J* = 11.3 Hz), 40.02 (t, *J* = 12.5 Hz), 27.81 (dt, *J* = 28.1, 3.1 Hz), 19.54, 15.03. HRMS (ESI) m/z calculated for $C_{38}H_{56}IrO_6P_2S_2$ 927.26 $[M\text{-}Cl]^+$, found 927.26.

RESULTS AND DISCUSSION

Initial Pathways to Model Ir(III) Ammonia-Borane Dehydrogenation Catalyst

Initial attempts in producing a model Ir(III) ammonia-borane dehydrogenation catalyst involved "capping" of the 3,4-ethylenedioxythiophene (EDOT) moieties with hexyl groups. Hexyl groups were chosen to increase the solubility of the intermediates during the synthetic process as well as to inhibit unintentional polymerization of the intermediates through the EDOT groups. The synthetic route to produce the hexyl-capped Ir(III) complex, **8a**, is shown in Schemes 4-6. The route to **8a** began with the synthesis of the two Stille coupling partners, diacetoxydiiodobenzene (**2**) and tributyl(7-hexyl-2,3-dihydrothieno[3,4-b][1,4]dioxin-5-yl)stannane (**4a**). The synthesis of **4a** was performed via the stanyllation of **3a** using tributyltin chloride (Scheme 4) to produce **4a** as a dark orange oil, which was used without further purification in the following Stille coupling reaction with **2**.

Scheme 4. Stanyllation of **3a** to produce the Stille coupling partner **4a**.

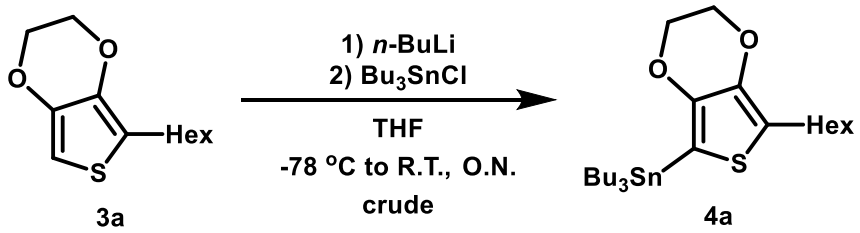

Compound **4a** was coupled to **2** (Stille) to render the desired protected precursor **5a**. The deprotection of **5a** was achieved by removal of the acyl groups using lithium aluminum hydride to generate the di-hydroxyl intermediate **6a**. Compound **6a** was unstable in the presence of light and oxygen, which is likely due to the *meta*-phenylene linkages

promoting oxidation and dearomatization of the benzene core to the quinone form.[79] Compound **6a** was then reacted with NaH and di-*iso*-propylchlorophosphine to produce the ligand **7a** as a light orange oil (Scheme 5). The formation of **7a** was confirmed by $^{31}P\{^{1}H\}$ NMR (singlet resonance at δ 151 ppm).

Scheme 5. Synthetic route to ligand **7a**.

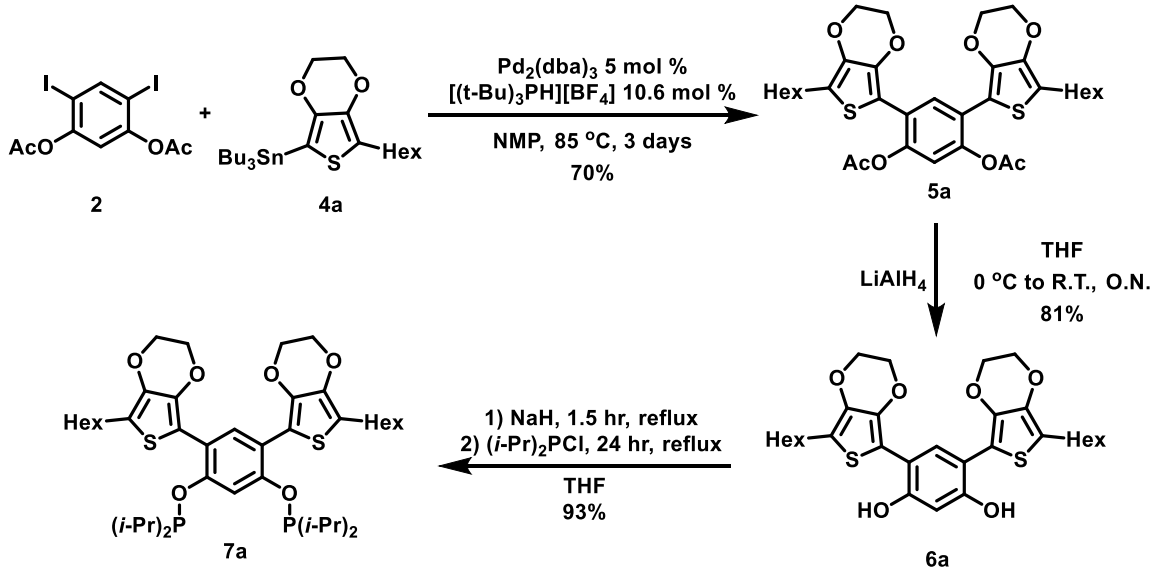

Metallation was attempted by heating **7a** in the presence of bis(1,5-cyclooctadiene)diiridium(I) dichloride in deoxygenated toluene at 150 °C in a pressure vessel for 24 hours (Scheme 6). However, attempts at purification of the metallated product, **8a**, were unsuccessful. Thus, different recrystallization conditions, ranging from recrystallization from CH_2Cl_2 using hexane to recrystallization from EtOH using water afforded no pure sample of **8a**. The likely cause of this is due to the high solubility of **8a** due to the presence of the hexyl groups, making it nearly impossible to isolate **8a** from impurities with similar solubility properties. However, formation of **8a** was detected via

^{1}H NMR and ^{31}P{^{1}H} NMR. The ^{1}H NMR showed a metal hydride resonance at -25 ppm as a triplet and the ^{31}P{^{1}H} NMR showed a doublet at 159 ppm. Mass spectrometry also confirmed the formation of **8a** via detection of the charge species of **8a**, [**8a**-Cl]$^{+}$, with m/z equal to 983.

Scheme 6. Attempted metallation of **7a** with $[Ir(cod)Cl]_2$ to produce **8a**.

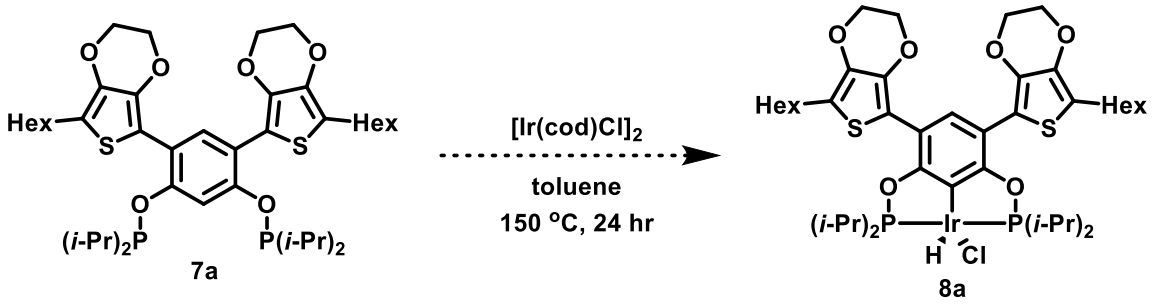

Model Ir(III) Complex with Ethyl-Capped EDOTs

As described above, isolation of **8a** proved to be problematic because of the high solubility of the complex. Instead, a new target was designed by "capping" the EDOTs with ethyl groups instead of hexyl groups. It was hypothesized that using ethyl groups instead of hexyl groups would still hinder the random polymerization of the intermediates during the synthesis of the Ir(III) catalyst while making all the intermediates and the desired metallated product, **8**, less soluble.

The synthesis of the ethyl EDOT functionalized pincer ligand **7** required producing two Stille coupling partners, diacetoxydiiodobenzene (**2**) and tributyl(7-ethyl-2,3-dihydrothieno[3,4-b][1,4]dioxin-5-yl)stannane (**4**). Diacetoxydiiodobenze was synthesized according to known literature procedures.[80,81] The synthesis of **4** began by first functionalizing 3,4-ethylenedioxythiophene at the 2-position with an ethyl group using

iodoethane (Scheme 7). This reaction yielded **3** as a slight yellow oil, but in a low yield of 22 % due to the production of the 2,5-ethyl-3,4-ethylenedioxythiophene byproduct as well as unreacted 3,4-ethylenedioxythiophene. Stanylation of **3** was achieved using tributyltin chloride to produce **4** as a pale-yellow oil (Scheme 7), which was used in the following Stille coupling reaction without further purification.

Scheme 7. Synthetic route to the Stille coupling partner **4**.

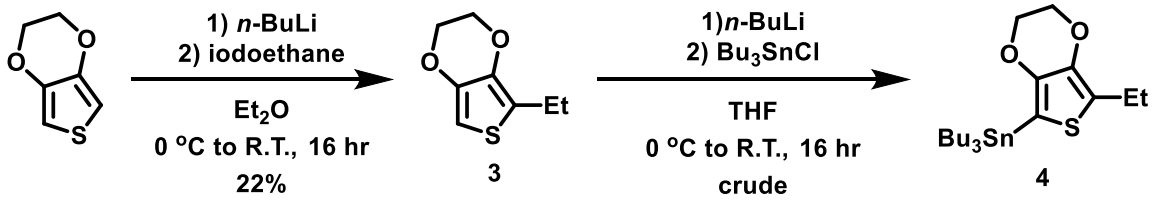

Compound **4** was Stille coupled with **2** to render the desired protected precursor **5** followed by subsequent deprotection of **5** by removal of the acyl groups using lithium aluminum hydride to generate **6** (Scheme 8). Compound **6** was unstable in the presence of light and oxygen, which is due to the *meta*-phenylene linkages promoting oxidation and dearomatization of the benzene core to the quinone form.[79] Compound **6** was then reacted with NaH and di-*tert*-butylchlorophosphine to produce the ligand **7** as a slight brown solid (Scheme 8). The formation of **7** was confirmed by $^{31}P\{^{1}H\}$ NMR as a singlet resonance at δ 158 ppm which is similar to the $^{31}P\{^{1}H\}$ NMR singlet resonance of 2,6-bis(di-*tert*-butylphosphinito)-phenyl at δ 153 ppm.

Scheme 8. Stille coupling of **4** to **2** followed by subsequent synthetic steps to ligand **7**.

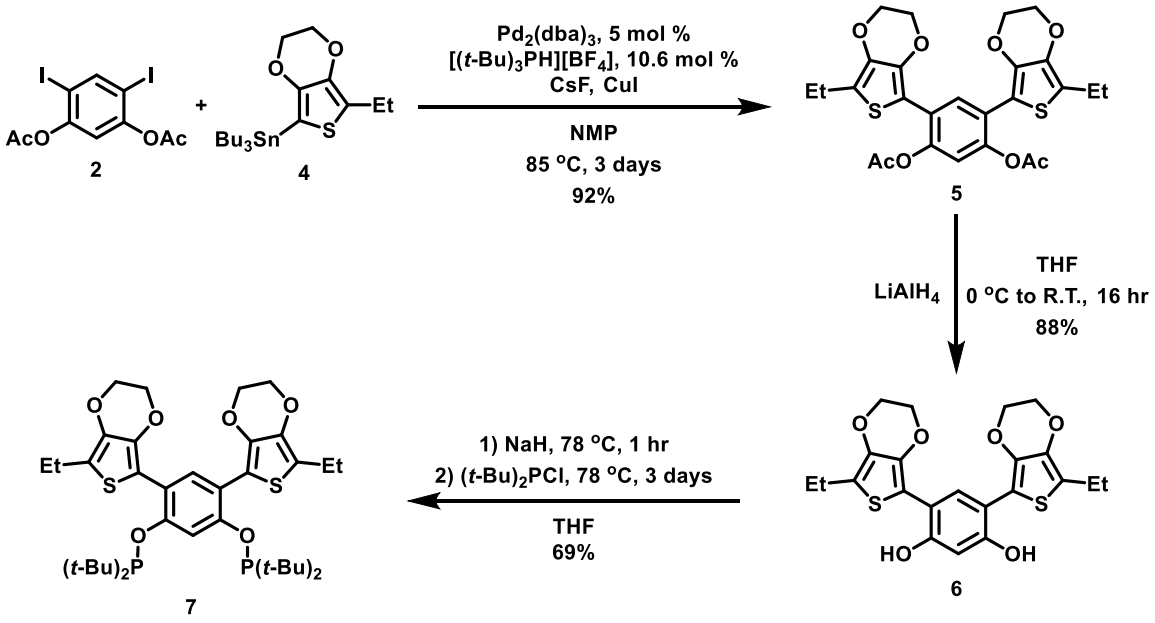

Metallation of the ligand was achieved by heating **7** with bis(1,5-cyclooctadiene)diiridium(I) dichloride in toluene at 150 °C for 24 hours to afford the iridium(III) complex **8**. The formation of **8** was confirmed by ^{1}H and $^{31}P\{^{1}H\}$ NMR. The ^{1}H NMR displays a metal-hydride triplet resonance at δ -41 ppm and the $^{31}P\{^{1}H\}$ NMR singlet resonance at δ 158 ppm shifted to δ 180 ppm and is shown as a doublet.

Scheme 9. Metallation of **7** using $[Ir(cod)Cl]_2$ to produce complex **8**.

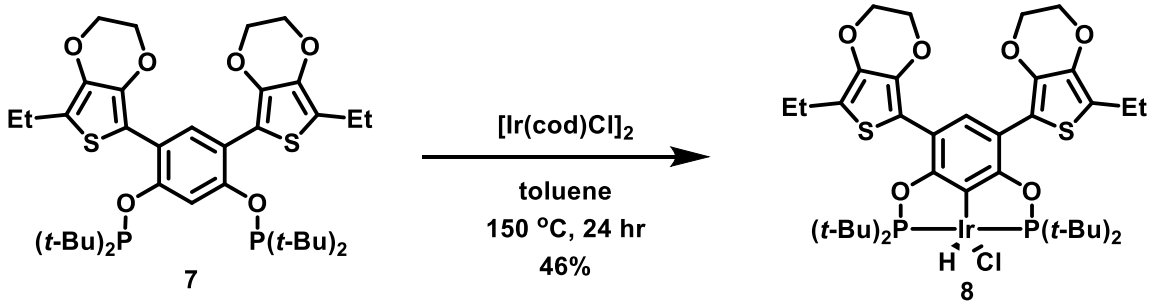

Slow evaporation of a solution of **8** dissolved in a CH_2Cl_2/Et_2O mixture gave block-like single crystals suitable for X-ray diffraction; the single crystal structure of **8** is shown below in Figure 5. The structure of **8** shows that the Ir metal center is bound in square planar geometry by ligand **7** and the chloride. The metal hydride was not found in the structure due to the resolution of the data being 0.84 Å. This is not surprising due to the large electron density difference between Ir and a hydride.. Nonetheless, the presence of a metal hydride was detected by ^{1}H NMR, as described above. The ethyl-capped 3,4-ethylenedioxythiophene groups show a torsion angle of 24 degrees away from the plane of the benzene core of the pincer ligand **7**, which is due to solid-state short C-H contacts between the hydrogens on the 3,4-ethylenedioxythiophene groups on one complex and the carbons on the benzene core, 3,4-ethylenedioxythiophene groups, and *t*-Bu groups on an adjacent complex in the crystal structure.

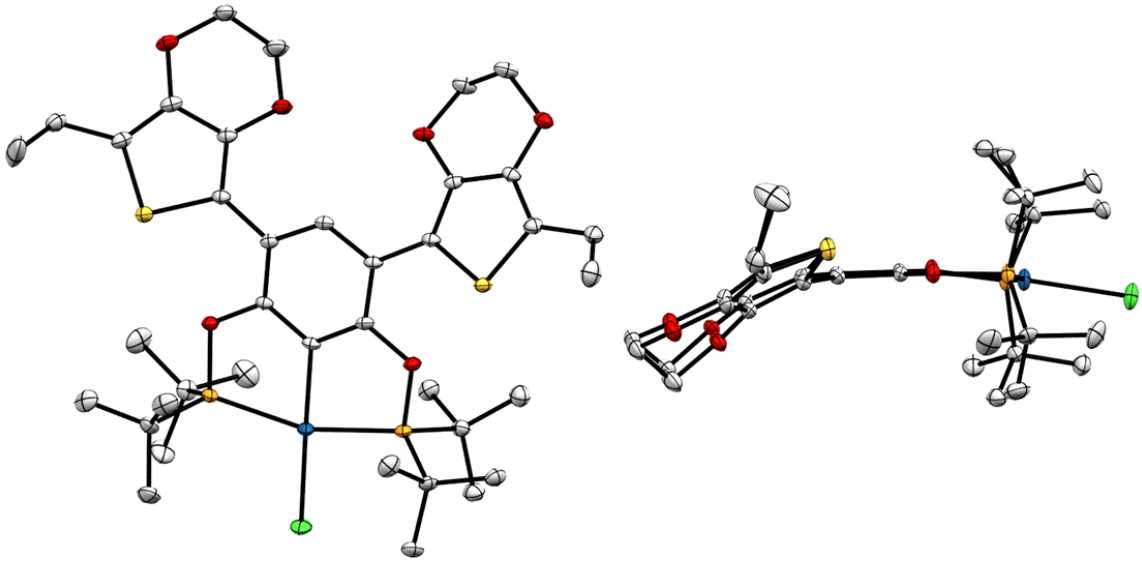

Figure 5. Single crystal structure of **8** (50% thermal ellipsoid probability) as viewed from a) the top down and b) the side to show the square planar geometry and torsion of the 3,4-ethylenedioxythiophene groups away from the plane of the benzene core.

Electrochemistry of 7 and 8

The electrochemistry of **7** was studied using cyclic voltammetry and the electrochemistry of **8** was studied using both cyclic voltammetry and differential pulsed voltammetry. The cyclic voltammogram of **7** (Figure 6) in CH_2Cl_2 shows three irreversible oxidative events centered at 0.34 V, 0.76 V, and 1.11 V vs Fc/Fc^+. We postulate that in the cyclic voltammogram of **7**, the peak at 0.34 V is due to oxidation of one of the EDOT groups which is then followed by the oxidation of the other EDOT group at 0.76 V. This is supported by the relatively equal size of the oxidative waves, which suggest a one-electron oxidation of one EDOT group at 0.34 V and a one-electron oxidation of the other EDOT group at 0.76 V. The oxidative peak at 1.11 V appears to be a two-electron oxidative event, due to the overall size of the peak being twice the size of either the 0.34 V peak or the 0.76 V peak. This 2-electron process is likely due to oxidation of one of the phosphines from P(III) to P(V). This is further supported by the disappearance of the oxidative peak at 1.11 V in the cyclic voltammogram of **8** in which phosphorous oxidation is inhibited by coordination to iridium.

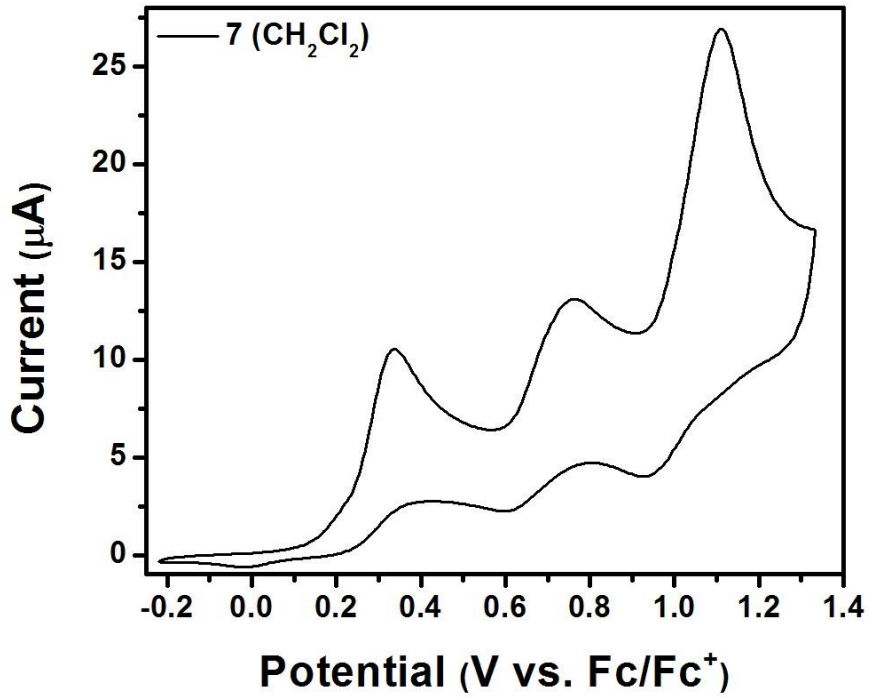

Figure 6. Cyclic voltammogram of **7** in CH_2Cl_2.

The cyclic voltammogram of **8** in CH_2Cl_2 shows two irreversible oxidative events centered at 0.33 V and 0.77 V vs Fc/Fc^+ (Figure 7). At first analysis of the cyclic voltammogram of **8**, we assigned the two oxidative events to a one-electron oxidation of one of the EDOT groups followed by a one-electron oxidation of the other EDOT group. This assignment is supported by the relatively similar size of the oxidative waves. However, the differential pulsed voltammogram of **8** does not support this theory. The differential pulsed voltammogram of **8** shows two oxidative peaks at 0.33 V and 0.77 V, with the peak at 0.33 V about twice the size of the peak at 0.77 V, which suggests that the peak at 0.33 V is a two-electron event and the peak at 0.77 V is a one-electron event. An explanation of the observed oxidative events in the differential pulsed voltammogram could be that the peak at 0.33 V is oxidation of the EDOT groups, with each group having

a one-electron oxidation. The peak at 0.77 V could then be a one-electron oxidation of the Ir metal center from Ir(III) to Ir(IV). However, this assignment is not fully supported by the cyclic voltammogram of **8**, even though determination of how many electrons involved per event via cyclic voltammetry is flawed. Further electrochemical studies would need to be performed to be able to fully assign the oxidative events observed in **7** and **8**, such as differential pulsed voltammetry of **7**.

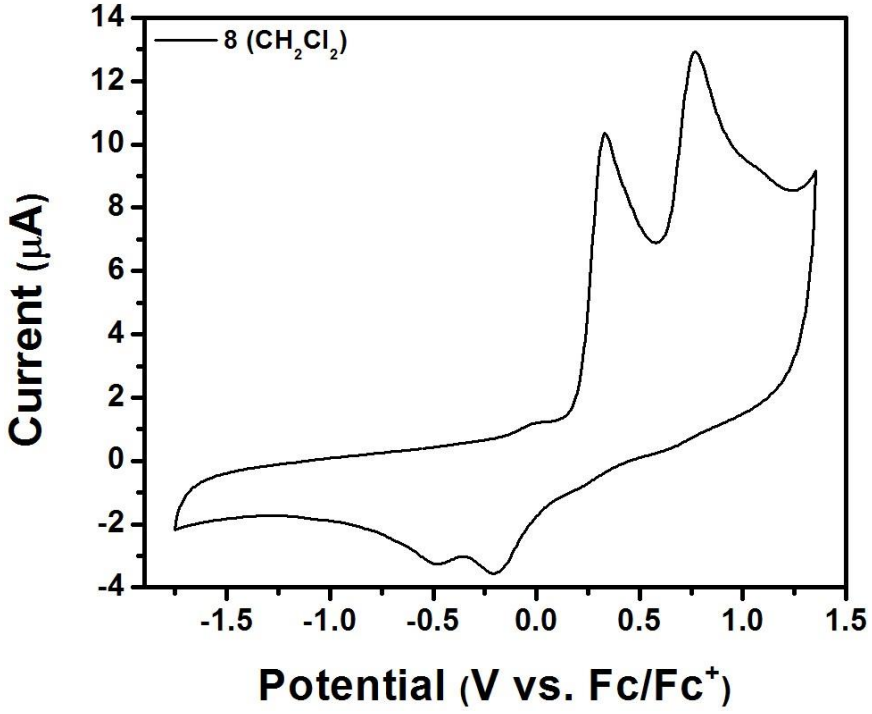

Figure 7. Cyclic voltammogram of **8** in CH_2Cl_2.

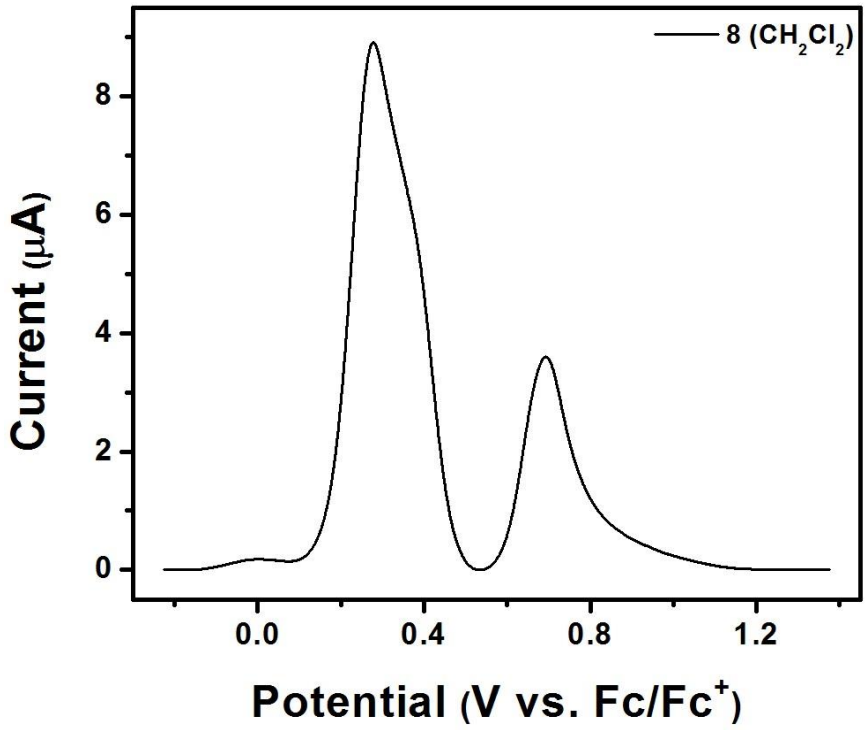

Figure 8. Differential pulsed voltammogram of **8** in CH_2Cl_2.

Catalytic Ammonia-Borane Dehydrogenation

We next investigated the ability of **8** to perform catalytic AB dehydrogenation. Experiments were conducted where activation of the catalyst was achieved by stirring **8** with 1.1 equivalents of NaO(*t*-Bu) in H_2 saturated THF under an argon atmosphere for 30 minutes at room temperature to generate **9** *in situ* (Scheme 10).

Scheme 10. Activation of **8** with NaO(*t*-Bu) and H_2 to generate **9** *in situ*.

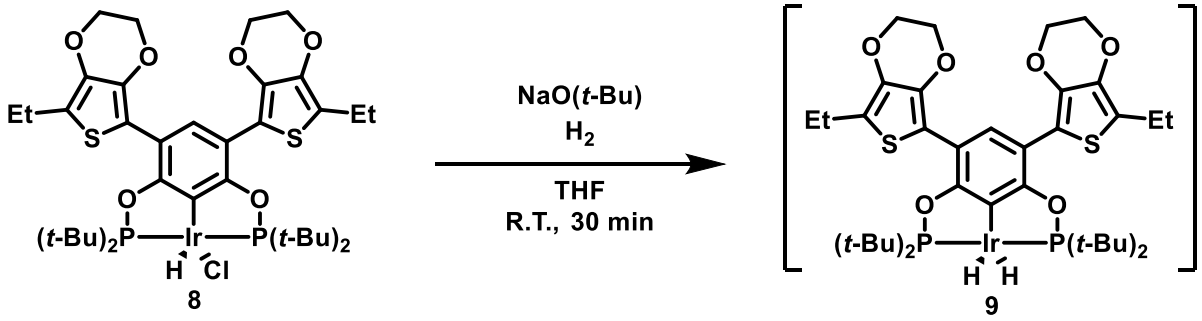

The catalytic dehydrogenation of ammonia-borane (AB) using 1.00 mole %, 0.50 mole %, and 0.25 mole % catalyst loading of **9** (generated *in situ*) in a 0.5 M solution of AB in THF was studied (Figure 10-12). The amount of THF and the concentration of the **9** THF solution was varied so that a constant volume of 0.8 mL of the stock solution of **9** could be added to the AB solution so that the total volume in the reaction was always 3 mL. With 1.00 mole % of **9**, release of 1 equivalent of H_2 was observed within 4 minutes. With 0.50 mole % of **9**, release of 1 equivalent of H_2 was observed within 15 minutes. In both cases, a precipitate was formed during the catalysis. The precipitate was identified as the cyclic oligomer, $(NH_2BH_2)_5$ via infrared spectroscopy. These results match well with the results observed by Heineky and co-workers, where generation of 1 equivalent of H_2 using 1.00 mole % catalyst loading and 0.50 mole % catalyst loading in a 0.5 M solution of AB in THF was observed within 4 minutes and 14 minutes, respectively.[62]

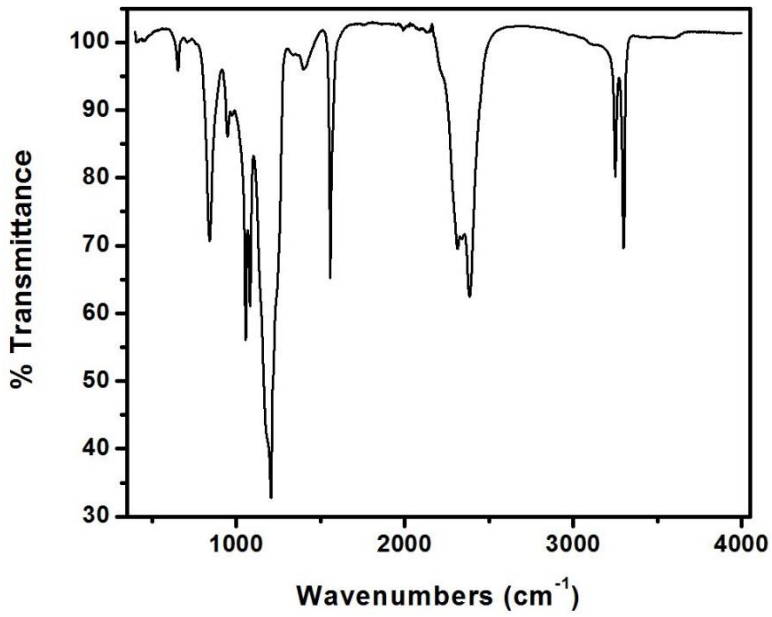

Figure 9. Infrared spectrum of precipitate, $(NH_2BH_2)_5$, generated following reactions of **9** with AB, which matches reported literature spectrum.[82]

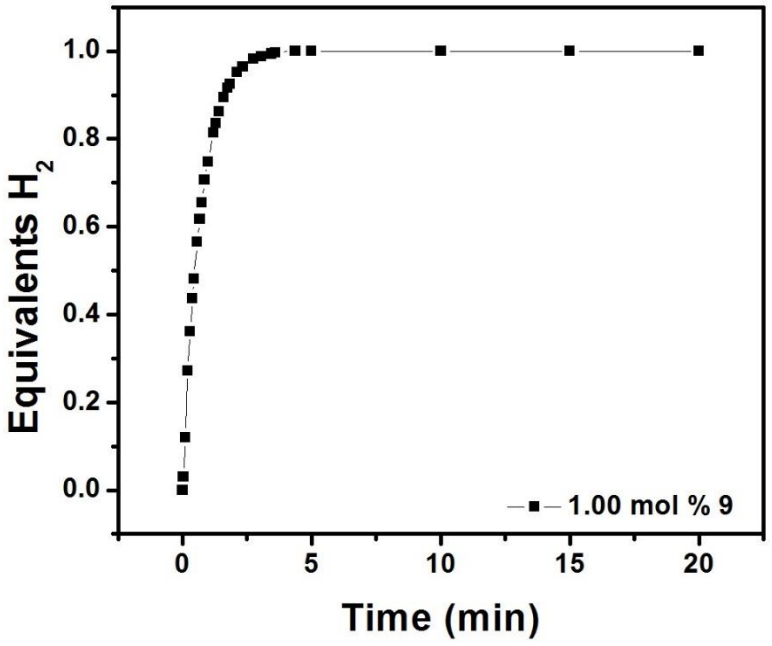

Figure 10. Ammonia-borane dehydrogenation using 1.00 mole % of **9**.

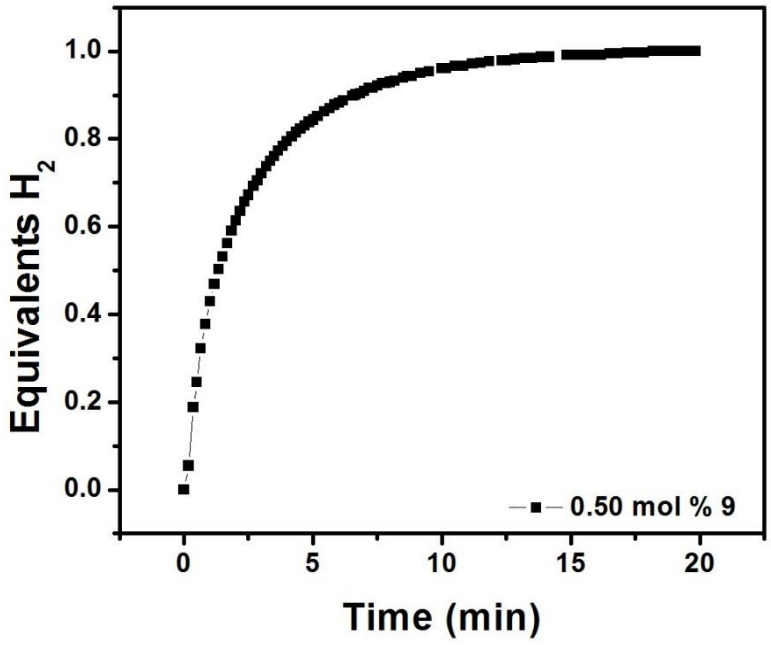

Figure 11. Ammonia-borane dehydrogenation using 0.50 mole % of **9**.

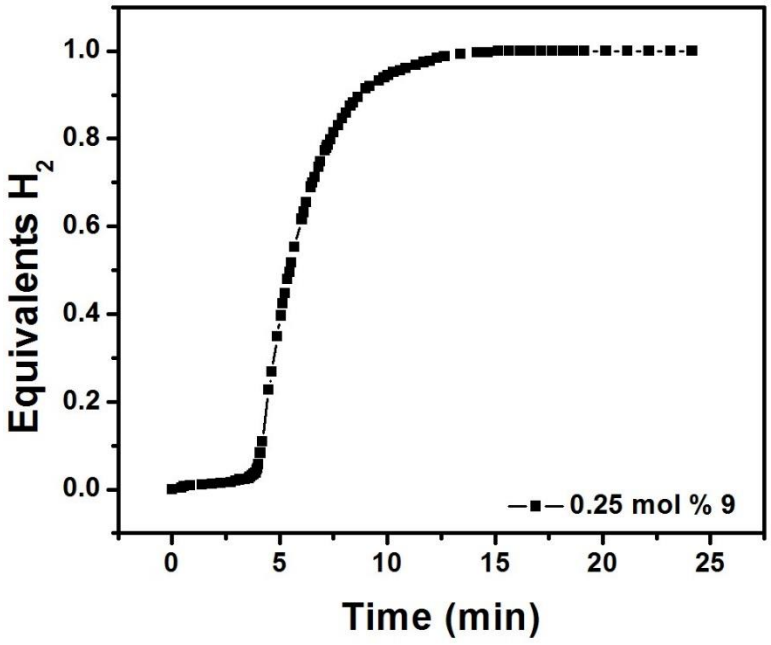

Figure 12. Ammonia-borane dehydrogenation using 0.25 mole % of **9**.

However, with a 0.25 mole % catalyst loading of **9**, there was an observed induction period of the catalyst where very little gas generation was observed that lasted about 4 minutes. After the induction period, rapid generation of H_2 was observed with 1 equivalent of H_2 being released within 15 minutes. These results are not consistent with what was observed by Heineky *et al*., where they observed generation of 1 equivalent of H_2 in 30 minutes.[62] One possible explanation is that not all of the catalyst was fully activated upon addition to the AB solution, potentially due to the THF used in the activation step of **8** not having enough H_2 dissolved in it. The induction period could be due to some portion of **8** being activated, which would release H_2 when added to the AB solution. The released H_2 could have then been used by the unactivated portion of the catalyst to become activated. NMR studies done by Heineky *et al.* could also shed some light on this phenomenon, where upon addition of AB to a solution of (POCOP)IrH_2 (where POCOP = [η^3-1,3-(OP(*t*-Bu)$_2$)$_2$$C_6H_3$], the signals of (POCOP)IrH_2 immediately disappeared and the tetrahydride species, (POCOP)IrH_4 was observed.[62] The complex (POCOP)IrH_2 was originally studied by Brookhart *et al.*, but they were unable to isolate the tetrahydride species (POCOP)IrH_4 due to the complex losing H_2 when not stored over an atmosphere of H_2, even in the solid-state .[83] Since **8** was not activated under an atmosphere of H_2 and lower concentrations of the catalyst were used in the dehydrogenation of AB for the 0.25 mole % catalyst loading studies, it is possible that only a small portion of the activated catalyst was the active tetrahydride species, and it took 4 minutes for enough H_2 to be generated to fully activate all of the catalyst. However, this still does not explain why, when using 0.25 mole % of **9** in the dehydrogenation of AB, that 1 equivalent of H_2 was released within 15 minutes, even with the 4-minute induction period. Further NMR studies would need to be performed to shed light onto the possibility that, in the case of **9**, another form of active catalyst is generated *in situ* at lower concentrations than is more catalytically active than **9**.

CONCLUSIONS AND FUTURE DIRECTIONS

PCP-type ligands are attractive motifs for homogeneous catalysis due to the easily modifiable structure and strong sigma-donation of the cyclometallating carbon of the aryl core. The sterics and electronic properties of the catalyst are also easily tuned via incorporation of different phosphine groups. The targeted PCP-type ligand, **7**, was successfully synthesized with ethyl-capped 3,4-ethylenedioxythiophene groups and successfully metallated to generate the targeted Ir(III) complex, **8**. Activation of complex **8** was achieved to form complex **9** which was successfully used in the catalytic dehydrogenation of ammonia-borane, demonstrating that functionalization of the known ammonia-borane dehydrogenation catalyst first studied by Heinekey *et al.* at the 4 and 6-positions would not hinder the catalytic activity. Future directions would include the synthesis of the un-capped version of **8**, followed by incorporation of the catalyst into a conducting metallopolymer. Finally, the catalytic activity toward ammonia-borane dehydrogenation of the resulting conducting metallopolymer should be studied before and after electrochemical oxidation of the metallopolymer backbone.

Chapter 3: Photophysical Properties of Substituted Pyrazolate Bridged Dinuclear Pt(II) Complexes

Light emitting electrochemical cell device fabrication and testing was performed by Dr. Jason Slinker at The University of Texas at Dallas.

INTRODUCTION

Platinum Luminescence

Platinum is typically found in the 2+ oxidation state with a d^8 electronic configuration and a square planar geometry. The stable square planar geometry pushes the un-occupied d_{x2-y2}^* molecular orbital to high energies while allowing for stabilization of the occupied d_{z2}, d_{xy}, d_{xz}, and d_{yz} molecular orbitals. The square planar geometry is responsible for many of the key features which are characteristic for platinum(II) absorption, luminescence, and other excited state properties.[84]

The d_{x2-y2} orbital is strongly antibonding in nature. Therefore, if population of this orbital occurs through photoexcitation, the molecule will undergo a significant distortion and the platinum-ligand bond lengths will increase. Upon relaxation, the energy lost is typically via a non-radiative pathway. This is one of the reasons platinum complexes with simple inorganic ligands (NH_3, Cl, etc.) are either weakly luminescent or not luminescent in solution. In the solid-state or at low temperatures, this distortion upon photoexcitation is inhibited to some extent, and emission can then be observed in some cases.[84]

The use of conjugated aromatic ligands around the platinum(II) center allows for ligand-centered (^{3}LC) and metal-to-ligand charge transfer (^{3}MLCT) emission pathways. The ^{3}LC transition is typically a π-π^* or n- π^* transition which is localized on the ligand, as the name suggests. The ^{3}MLCT transition is excitation of a metal d-electron to a π^* orbital on the conjugated ligand. In many platinum(II) complexes which have conjugated aromatic ligands, either the ^{3}LC or the ^{3}MLCT states, or both, may lie at lower energies than the d-

d states which allows for ^{3}LC or ^{3}MLCT emission rather than non-radiative decay from excitation to the d_{x2-y2}^* orbital.[84] The use of cyclometallating ligands, due to their strong σ-donating ability, also allows for platinum luminescence in solution through either ^{3}LC or ^{3}MLCT transitions. This is caused by the cyclometallating ligand raising the energy of the deactivating d-d excited states, inhibiting non-radiative decay through the excitation of the d_{x2-y2}^* orbital.[84]

Luminescent Dinuclear Pt(II) Complexes

Another key feature of platinum(II) luminescence is the ability to have Pt-Pt interactions in both the ground state (intermolecular stacking or dimerization) and the excited state (excimer formation). This property is facilitated by platinum(II) complexes with sterically undemanding ligands adopting the flat square planar geometry. Ground state stacking of platinum(II) complexes typically occurs through the open d_{z2} orbitals, where a separation of 3-3.5 Å is appropriate for the formation of weakly bonding and antibonding dσ and dσ* molecular orbitals. One of the implications of such interactions is that the highest occupied metal-based molecular orbital is raised in energy compared to that of the isolated molecules, so that lowest-energy optical transitions are shifted to lower energies. This can lead to a switch in the nature of the lowest-energy excited state (e.g. π-π* in the monomer to dσ*- π* in the presence of such interactions).[84]

Due to the close proximity of the metal centers to each other, as stated above, the metal-metal contacts create the possibility of a lower-energy photoluminescence that is red-shifted from the ^{3}MLCT. This type of transition is considered a metal-metal-to-ligand charge transfer (^{3}MMLCT or dσ*-π*). Due to the interesting photophysical properties which arise from this form of interaction of separate platinum(II) complexes, much

research has been devoted to the area of synthetically forcing two platinum(II) centers within close contact of each other.[85–91]

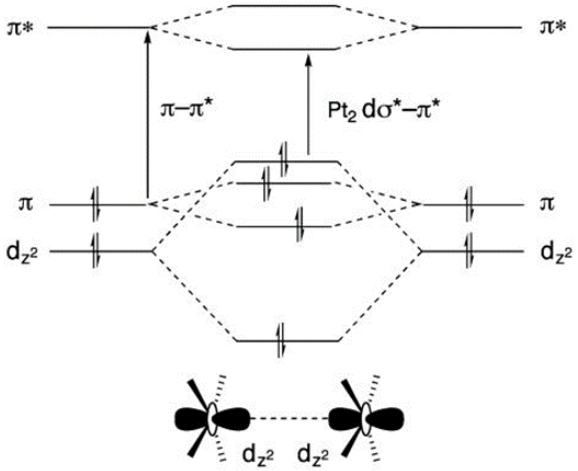

Figure 13. Simplified frontier molecular orbital diagram showing the effect of face-to-face interactions and intermolecular d_{z2} orbital overlap. In this example, such interaction leads to a change in the nature of the lowest-energy excited state from π-π^* (^{3}LC) transitions to $d\sigma^*$-π^* (^{3}MMLCT) transitions.[84]

Che and co-workers have studied the ^{3}MMLCT of 6-phenyl-2,2'-bipyridine dinuclear platinum(II) complexes. In their studies, they used bis(diphenylphosphino)-methane, -propane, and -pentane as well as pyrazolate as the bridging ligand. The Pt-Pt bond lengths of the complexes ranged from 3.6 Å for the pyrazolate bridged dinuclear complex to 3.3 Å for the bis(diphenylphosphino)methane bridged complex. All of the dinuclear complexes were luminescent in solution at room temperature. Of the complexes studied, only the bis(diphenylphosphino)methane bridged complex displayed a ^{3}MMLCT transition. This is attributed to the bis(diphenylphosphino)methane ligand forcing the platinum(II) centers within close contact of each other, changing the emission from ^{3}MLCT in the case of the bis(diphenylphosphino)propane, bis(diphenylphosphino)pentane, and

pyrazolate bridged complexes (which do not display close Pt-Pt interactions) to a ^{3}MMLCT transition.[86,87]

Castellano and co-workers have also studied the ^{3}MMLCT transition of platinum(II) complexes. In their report, they studied the photophysical properties of an array of 3,5-susbstituted pyrazolate bridged platinum(II) complexes (Figure 14) to examine the effects of changing the cyclometallating ligand while imposing various degrees of steric bulk provided by the 3,5-substituted pyrazolates. The Pt-Pt distances were not studied via X-ray crystallography. All of the complexes studied were luminescent both at room temperature and 77 K. Complexes **c1a-c1d** all displayed an emission transition at ~563 nm which showed some vibronic structure. Upon cooling to 77 K, the vibronic progression sharpened slightly but no shift in emission was observed. Based on these observations, the observed emission profile was attributed to a ^{3}LC transition located on the 2-(2'-thienyl)pyridine ligand. Furthermore, the variation of the bridging pyrazolate ligand had no effect on the emission of **c1a-c1d**.[90]

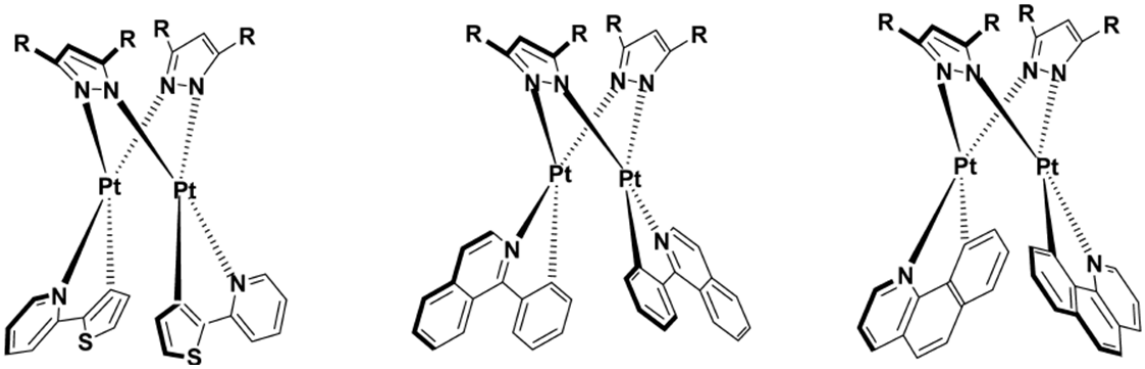

c1a: R = H
c1b: R = Me
c1c: R = *i*-Pr
c1d: R = Ph

c2a: R = Me
c2b: R = *i*-Pr
c2c: R = Ph

c3a: R = H
c3b: R = Me
c3c: R = *i*-Pr
c3d: R = Ph

Figure 14. Pryazolate bridged dinuclear platinum(II) complexes studied by Castellano and co-workers.[90]

Complexes **c2a** and **c2b** both displayed a similar emission profile at room temperature with a transition at ~607 nm which displayed vibronic side bands which are less defined than in **c1a-c1d**. However, the emission of **c2c** was quite different, displaying a structureless transition at 713 nm. Upon cooling to 77 K, the emission profile of complexes **c2a** and **c2b** remained relatively the same. However, the emission profile of **c2c** displayed a hypsochromic shift to 596 nm as well as the same structured appearance as that of **c2a** and **c2b**. These observations lead to the assignment of the observed transition in **c2a** and **c2b** as a ^{3}LC transition while the observed transition of **c2c** is assigned as ^{3}MMLCT. Furthermore, this series of complexes does show that the bridging pyrazolate ligand can play an important role in the photophysical properties.[90]

Complexes **c3b-c3d** all display a similar structureless emission profile to that of **c2c** while **c3a** displays a higher energy shoulder. Upon cooling to 77 K, similar to **c2c**, the emission profile of **c3a-c3c** becomes structured and displays a hypsochromic shift. However, complex **c3d** remains quite broad and structureless at 77 K. These observations lead to the assignment of the room temperature transition of **c3b-c3d** as a ^{3}MMLCT while the emission profile of **c3a** was assigned to be a mix of a ^{3}LC transition and a ^{3}MLCT transition which are in thermal equilibrium of each other. Furthermore, as the steric bulk imposed by the bridging pyrazolate ligand increased across the series, there was an observed bathochromic shift in the emission profile from 596 nm for **c3b** to 631 nm for **c3d**. This observation is likely due to an increase in the Pt-Pt interaction associated with an increase in the steric bulk imposed by the bridging pyrazolate ligand.

Light-Emitting Electrochemical Cells

Light-emitting electrochemical cells (LEECs) are a new form of solid-state lighting which has received considerable attention in recent years.[40,92–106] LEECs offer many

advantages over other forms of solid-state lighting due to their potential for low-cost fabrication via solution-based technologies such as spin-coating, printing, or slot-die coating, the ability to use air-stable electrodes, and the ability to use thick active layers which can make the devices more fault tolerant.[40] Unlike OLEDs, which have multiple layers to facilitate more efficient electron and hole injection/transportation, LEECs have the ability to be single-layer devices (Figure 15).

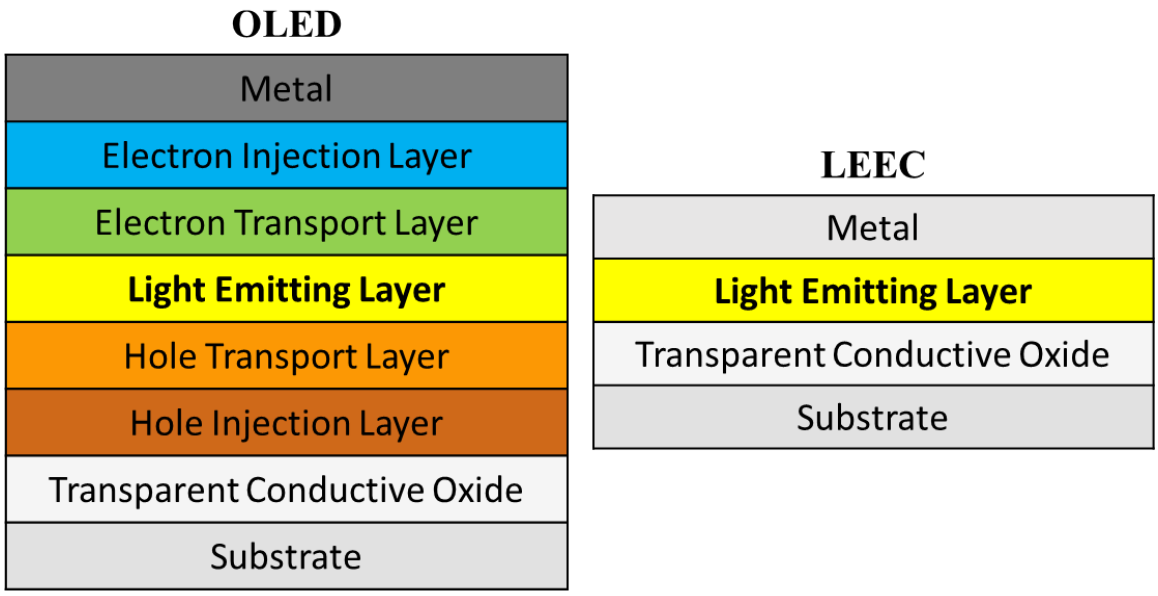

Figure 15. The different layers of an OLED vs the different layers of an LEEC.[40]

The active layer in an LEEC is typically comprised of a polymeric material (pLEEC) or ionic transition-metal complexes (iTMC-LEEC). iTMC-LEECs typically used ruthenium[100,103] or iridium[94,96,99,101,106] based ionic complexes. However, ionic copper complexes have also been used in the active-layer of an iTMC-LEEC.[93] In pLEECs, the ionic and electronic conductivity is decoupled but for iTMC-LEECs, the ionic complex is

responsible for both events.[40] For pLEECs, it is essential that ions are added to the light-emitting layer to facilitate electrical conductivity, while this is not necessarily the case for iTMC-LEECs. However, the type of counter-ion used to balance the charge of iTMC-LEECs has a large effect on device performance. An example of this is iTMC-LEECs which have small counter-ions. These devices have faster turn-on times when compared to similar devices which employ larger counter-ions.[40,107] The use of lithium-salt additives in LEECs has also been studied, which helps with device performance in allowing for faster turn-on times and longer stability when operated at constant voltage.[98,99,101]

EXPERIMENTAL

Instrumentation

All ^{1}H, ^{13}C, ^{19}F, and ^{31}P NMR spectra were recorded on either a Varian Unity 300 spectrometer (300 MHz), Varian Mercury 400 spectrometer (400 MHz), Varian DirectDrive 400 spectrometer (400 MHz), or Agilent MR 400 spectrometer (400 MHz). All ^{1}H and ^{13}C NMR signals were referenced to residual solvent peaks and reported in ppm; all coupling constants are reported in Hz. Infrared spectra were recorded on a Nicolet iS50 FT-IR spectrophotometer. Low-resolution and high-resolution mass spectrometry was performed on an Agilent Technologies 6530 Accurate Mass QTofLC/MS spectrometer. Melting points were recorded on an OptiMelt Automated Melting Point System made by Stanford Research Systems. Elemental analysis was performed by Midwest MicroLab Inc. (Indianapolis, IN).

Crystal Structure Determination

Crystallographic data for complexes **11a-11f** are given in Tables S2-S6. Single crystals of **11a**, **11b**, **11d** and **11f** were grown via layer diffusion of hexane into a CH_2Cl_2 solution of **11a**, **11b**, and **11f**, separately. Single crystals of **11c** were grown via layer

diffusion of benzene into a N,N-dimethylformamide solution of **11c**. Single crystals of **11e** were grown via layer diffusion of pentane into a CH_2Cl_2 solution of **11e**. Crystals were covered in a Paratone/chloroform mixture and mounted on a nylon thread loop. Data was collected for **11a** and **11b** at 100 K on an Agilent Technologies SuperNova Dual Source diffractometer equipped with a AtlasS2 CCD detector using a μ-focus Cu Kα radiation source (λ = 1.5418 Å) and an Oxford 700 Cryostream system. Data collection, unit cell refinement, and data reduction of **11a** and **11b** were performed using the Agilent Technologies CrysAlisPro software. Data was collected for **11c-11f** at 100 K on a Rigaku AFC-12 diffractometer equipped with a Saturn 724+ CCD detector using a μ-focus Mo Kα radiation source (λ = 0.7107 Å) and a Rigaku XStream low-temperature system. Data collection, unit cell refinement, and data reduction of **11c-11f** were performed using Rigaku's CrystalClear software. The structures of **11a-11f** were solved by direct methods using the SIR2014 program and refined by full-matrix least-squares on F2 with anisotropic displacement parameters for all non-H atoms using SHELXL-2014. The structural analyses were performed using the PLATON98 and WinGX programs. The hydrogen atoms were placed in fixed, calculated positions with isotropic displacement parameters set to 1.2 x Ueq with respect to the attached atom. Crystallographic images were created using the Cambridge Crystallographic Data Centre's Mercury program and rendered using POV-ray. All bond angles, torsion angles, and intermolecular interactions were calculated using the Cambridge Crystallographic Data Centre's Mercury software. The intermolecular interactions are calculated by the Mercury software by looking for atoms within close contact of each other based on their Van der Waal's radii plus 0.15 Å.

Electrochemistry

All electrochemical experiments were performed under nitrogen in a glovebox using a GPES system from Eco. Chemie B. V. and an Autolab Potentiostat. The electrolyte used was 0.1 M tetrabutylammonium hexafluorophosphate, [(*n*-Bu)$_4$N][PF$_6$] (TBAPF$_6$) in either dry MeCN, dry CH_2Cl_2, or dry dimethylformamide. The electrolyte was purified via three recrystallizations from hot ethanol before drying under dynamic vacuum for three days at 100 ^{o}C. Electrochemical experiments of **11a-11f** were carried out in a 20 mL electrochemical cell using a platinum button working electrode (1.6 mm diameter), a Ag/AgNO$_3$ (0.01 M AgNO$_3$ and 0.1 M TBAPF$_6$ in dry MeCN) non-aqueous reference electrode, and a Pt wire coil counter electrode. All potentials were reported relative to ferrocene/ferrocenium, which was used as an external standard to calibrate the reference electrode. Ferrocene was purified by sublimation at 95 ^{o}C. A step potential of 10 mV and a scan rate of 100 mV s^{-1} were used unless otherwise noted. The band gap was determined from the difference between the onset of oxidation (HOMO) and the onset of reduction (LUMO).

Optical Spectroscopy

Solvents used for emission, excitation, and lifetime studies were degassed (freeze-pump-thaw) under a N_2 atmosphere. Absorption spectra were recorded on a Varian Cary 6000i UV-VIS-NIR spectrophotometer. Luminescence measurements were recorded using FeliX32 software with a BryteBox interface on a Photon Technology International (PTI) QuantaMaster 4 spectrophotometer equipped with a 6-inch diameter K Sphere-B integrating sphere. Steady-state luminescence spectra were measured by exciting the sample with a xenon short arc lamp (USHIO, UXL-75XE) connected to a PTI lamp power supply (LPS-250B) and recording the emission with a PTI detection system (model 814) using a photomultiplier tube (Hamamatsu, R928P). Time-resolved luminescence

spectroscopy was used to measure the excited-state lifetimes by exciting the sample with a xenon flash lamp (Hamamatsu, L4633), connected to a PTI XenoFlash power supply, and recording the decay using a photomultiplier tube (Hamamatsu, R562).

All solution measurements were recorded with the samples in Starna quartz fluorimeter cells (pathlength of 1 cm). For solution spectra, each complex was dissolved in the desired solvent and diluted until the UV-Vis absorbance was below 0.1. For solid spectra, the solid was ground into a powder and loaded into either the main box (PTI, K-149) or the sphere powder holder (PTI, K-205). Frozen spectra were taken using a fluorimeter dewar (Wilmad Glass Co., Inc.) with a Suprasil quartz sample tube, which fits into the cuvette dewar (PTI, K-158) in the spectrophotometer. Samples were made by slowly freezing a solution of each complex dissolved in 2-methyltetrahydrofuran (2-MeTHF) in an EPR tube with liquid nitrogen in the fluorimeter dewar. Optical filters from Edmund Industrial Optics were used where specified.

All quantum yield measurements were recorded using the integrating sphere. For solution quantum yields, the concentration of the solution was maximized to the point before concentration quenching of the emission occurred. Quantum yields were calculated by dividing the area under the emission peak of the complex by the difference between the area under the excitation peak of the sample from that of a blank solution ($A_{em\ sample}$ /($A_{ex\ blank} - A_{ex\ sample}$), where A = area under peak).[108] The reported quantum yields are an average of three trials.

LEEC Device Fabrication and Testing

The overall LEEC device composition was as follows: ITO/PEDOT:PSS/Active Layer/LiF/Al. Active layers of **11b** were tested with and without the 0.3% $LiPF_6$ salt additive. $LiPF_6$ was purchased from Sigma Aldrich in the highest available purity and used

as received. Prepatterned ITO-coated glass substrates were purchased from Thin Film Devices, Anaheim, CA. These substrates were cleaned in a non-ionic detergent and water bath, followed by UV ozone treatment. Aqueous PEDOT:PSS solutions (1.3 – 1.7%, Clevios AI 4083) were filtered through a 0.45 μm GHP filter and then spin coated (~20 nm thick) onto the ITO-coated glass substrates. The substrates were subsequently transferred into a dry nitrogen glovebox for further processing and characterization. Separate solutions of **11b** and $LiPF_6$ were prepared (24 mg/mL in MeCN) inside the glovebox. For the devices with the 0.3% $LiPF_6$ additives, the $LiPF_6$ salt and iTMC solutions were subsequently mixed at a volume ratio of 3 to 997, respectively. The final solutions were then heated on a hotplate at 85 °C while stirring for 10 minutes and allowed to cool down to room temperature before being passed through a 0.1 μm nylon filter. The iTMC films, with and without $LiPF_6$, were spin cast at 900 rpm and thermally annealed at 120 °C for 1 hour. The active layers were generally ~100 nm thick. Then the samples were transferred to a vacuum chamber, where 10 Å of LiF and 800 Å of Al were deposited through a shadow mask that defined 12 devices per substrate, each with a 3 mm^2 active area.

Electroluminescence LEEC Device Testing

The electrical and radiant flux characteristics were obtained with a custom LEEC multiplexer testing station capable of measuring 16 device slides simultaneously. In brief, this instrument served as a current or voltage source and measuring unit and captured radiant flux with a calibrated Hamamatsu photodiode (S2387-1010R) for each device. The device slides were driven at a constant current of 1.5 mA (10 V compliance). These results were verified against measurements obtained with a 760D electrochemical analyzer from CH Instruments (Austin, TX) and a calibrated Labsphere integrating sphere, equipped with a thermoelectric cooled silicon photodetector and Keithley 6485 Picoammeter.

Electroluminescence spectra were measured from thin film single layer devices with an Ocean Optics Jazz fiber spectrometer.

Synthesis

All air and moisture-sensitive reactions were performed using standard Schlenk and high vacuum techniques. All solvents were dried using an Innovative Technology, Pure Solv solvent purifier with a double purifying column and sitting over 3 Å molecular sieves for 48 hours. All chemicals were used as received without further purification. The following molecules were synthesized from literature procedures: 3,5-di-tert-butyl-1H-pyrazole ,[109] 1,3-di(2-pyridyl)benzene (**9**)[110] and platinum 1,3-di(2-pyridyl)benzene chloride (**10**).[111]

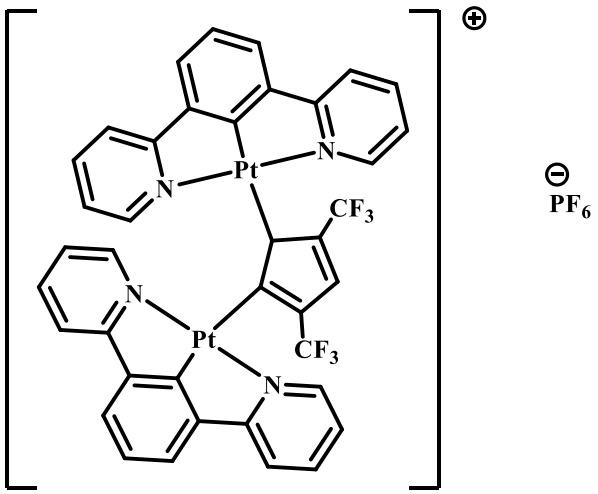

Preparation of 11a

In a Schlenk flask, **10** (200 mg, 0.43 mmol) was dissolved in CH_2Cl_2 (10 mL) then $AgPF_6$ (110 mg, 0.43 mmol) was added to the flask. The solution immediately changed from yellow to red but was stirred at room temperature for an hour. After the hour, the solution was a very faint yellow and a black solid had precipitated. The CH_2Cl_2 was

evaporated under a gentle stream of N_2. In a separate Schlenk flask, 3,5-bis(trifluoromethyl)pyrazole (44 mg, 0.22 mmol) was dissolved in THF (10 mL). To this solution, NaH (11 mg of 60% NaH suspended in paraffin oil, 0.26 mmol) was added slowly, then the solution was stirred at room temperature for 16 hours. Upon removal of the CH_2Cl_2 from the reaction of $AgPF_6$ with **10**, there remained a black solid and a slight amount of orange/yellow powder. Acetonitrile (10 mL) was added to the black solid, which instantly turned red. After stirring for one hour, the MeCN solution was orange and a white solid had precipitated, which was removed by filtration through celite. The MeCN was removed *in vacuo* at 40 ºC, resulting in an orange/yellow solid. THF (20 mL) was added to the orange/yellow solid, creating a suspension. The solution containing the deprotonated 3,5-bis(trifluoromethyl)pyrazole was slowly added to the suspension via a cannula transfer. The reaction was allowed to stir for 16 hours, changing to an orange solution with a small amount of solid present. The THF was removed *in vacuo*, resulting in an orange solid and a dark brown solid. CH_2Cl_2 was added to the solids, creating an orange solution with an insoluble solid. The insoluble solid was removed by filtration, leaving behind a dark red precipitate. The CH_2Cl_2 was evaporated under a gentle stream of N_2, resulting in an orange solid. Any further impurities were precipitated by recrystallization from CH_2Cl_2 (10 mL) by slowly adding hexanes until the formation of a precipitate was noticed. The precipitate was removed via filtration. The CH_2Cl_2 was removed under vacuum, resulting in a bright orange solid (137 mg, 0.11 mmol, 26%). The solid glows orange upon excitation with a long-wave UV lamp. m.p. 136-305 ºC (slow decomp.), FTIR (solid): 1611 (w, aromatic C=C) cm^{-1}. ^1H NMR (400 MHz, CD_2Cl_2): δ 7.77 (td, *J = 7.8*, *J = 1.6*, 4H), 7.67 (d (unresolved Pt satellites), *J=5.3*, 4H), 7.60 (s, 1H), 7.42 (d (unresolved additional splitting), *J=8.0*, 4H), 7.20 – 7.07 (m, 6H), 6.85 (ddd, *J = 7.4*, *J = 5.7*, *J = 1.5*, 4H). HRMS (ESI) m/z calculated for $C_{37}H_{23}F_6N_6Pt_2$ 1055.12 $[M]^+$, found 1055.1. Elemental analysis

calcd for $C_{37}H_{23}F_{12}N_6PPt_2$ (1200.76): C, 37.01; H, 1.93; N, 7.00. Found: C, 37.42; H, 1.93; N, 6.77.

General Synthetic Procedure for 11b-11f

In a Schlenk flask, the desired di-substituted pyrazole (1.9 equivalents) and NaH (1.4 equivalents of 60% NaH suspended in paraffin oil) were dissolved in THF (20 mL). The solution was stirred for one hour at room temperature then **10** (200 mg, 0.43 mmol) was added to the flask. The reaction was heated to 76 ^oC and stirred for 20 hours. The reaction was cooled to room temperature then potassium hexafluorophosphate (4 equivalents) was added to the flask. The reaction was stirred for an additional hour. The THF was removed under vacuum, then the resulting brown solid was washed with cold DI water (10 mL) then collected by filtration. From here, **11b** and **11d-11f** were purified by washing the brown solid with Et_2O (3 x 5 mL) over filter paper then dissolving the solid in CH_2Cl_2 (5 mL). The desired product was purified via recrystallization from CH_2Cl_2 (5 mL) by adding either hexanes or Et_2O until the formation of a brown precipitate was noticed. The brown precipitate was removed via filtration, resulting in the desired product. Complex **11c** was purified after filtration from the cold DI water wash by dissolving any impurities in excess CH_2Cl_2 then excess methanol. The solid was then washed with excess Et_2O, leaving behind pure product on the filter paper as a bright yellow solid.

[((N^C^N)Pt)$_2$(μ-(Ph)$_2$Pz)][PF$_6$] (**11b**). Isolated as a bright orange solid (215 mg, 0.18 mmol, 41 %). Solid glows bright orange when exited with a long-wave UV lamp. (m.p. 250-302 ^oC (slow decomp.), FTIR (solid): 1608 cm^{-1} (m, aromatic C=C) cm^{-1}. ^1H NMR (300.14 MHz, CD_2Cl_2): δ 8.57 (d (unresolved additional splitting), *J*=7.5, 4H), 7.85 (d (unresolved additional splitting), *J*=7.5, 4H), 7.71 (t (unresolved additional splitting), *J*=7.5, 4H), 7.63 (s, 1H), 7.44-7.22 (m, 10H), 7.20-7.06 (m, 6H), 6.68 (t (unresolved

additional splitting), *J*=7.75, 4H). ^{13}C {^{1}H} NMR (100.53 mHz, CD_2Cl_2) δ 167.40, 162.23, 153.21, 151.41, 141.42, 139.90, 132.92, 129.23, 128.34, 126.54, 124.48, 124.23, 123.49, 120.26, 103.79. HRMS (ESI) m/z calculated for $C_{47}H_{33}N_6Pt_2$ 1071.99 $[M]^+$, found 1071.21. Elemental analysis calcd for $C_{47}H_{33}F_6N_6PPt_2$ (1216.96): C, 46.39; H, 2.73; N, 6.91. Found: C, 46.41; H, 2.64; N, 6.86.

[((N^C^N)Pt)$_2$(μ-(H)$_2$Pz)][PF$_6$] (**11c**). Isolated as a yellow solid (171 mg, 0.16 mmol, 37%). Solid glows faint yellow when excited with a long-wave UV lamp. ^{1}H NMR (400 MHz, DMSO-d_6): δ 8.29 (d, J = 2.0, 2H), 8.06 (d (unresolved Pt satellites), J = 5.7, 4H), 7.89 (td, J = 7.8, J = 1.6, 4H), 7.87 (d (additional unresolved splitting), J = 8.0, 4H), 7.53 (d, J = 7.7, 4H), 7.18 – 7.04 (m, 6H), 6.95 (t, J = 2.1, 1H). ^{13}C{^{1}H} NMR: Product was too insoluble in deuterated solvents to acquire a spectrum. HRMS (ESI, complex fragments into $C_{16}H_{11}N_2Pt$) m/z calculated for $C_{16}H_{11}N_2Pt$ 426.06 $[M]^+$, found 426.1. Elemental analysis calcd for $C_{35}H_{25}H_6N_6PPt_2$ (1064.76): C, 39.48; H, 2.37; N, 7.89. Found: C, 39.45; H, 2.32; N, 7.69.

[((N^C^N)Pt)$_2$(μ-(Me)$_2$Pz)][PF$_6$] (**11d**). Isolated as a bright orange solid (232 mg, 0.21 mmol, 58%). Solid glows orange when excited with a long-wave UV lamp. ^{1}H NMR (300 MHz, Methylene Chloride-d_2) δ 7.89 (d (unresolved Pt satellites), J = 5.6, 4H), 7.78 (t (unresolved additional splitting), J = 7.8, 4H), 7.45 (d (unresolved additional splitting), J = 8.0, 4H), 7.22 (d, J = 7.4, 4H), 7.07 (dd, J = 8.3, J = 7.0, 4H), 6.84 (ddd, J = 7.0, J = 5.5, J = 1.4, 4H), 6.51 (s, 1H), 2.56 (s, 6H). ^{13}C NMR (100 mHz, CD_2Cl_2) δ 168.10, 163.81, 151.76, 149.45, 142.03, 140.23, 124.60, 124.31, 123.59, 120.34, 106.27, 14.30. HRMS (ESI) m/z calculated for $C_{37}H_{29}H_6Pt_2$ 947.17 $[M]^+$, found 947.2. Elemental analysis calcd for $C_{37}H_{29}F_6N_6PPt_2$ (1092.81): C, 40.67; H, 2.67; N 7.69.

[((N^C^N)Pt)$_2$(μ-(iPr)$_2$Pz)][PF$_6$] (**11e**). Isolated as a dark red solid (119 mg, 0.10 mmol, 24%). m.p. 206-243 ^{o}C (slow decomp.). ^{1}H NMR (400 MHz, Methylene Chloride-

d_2) δ 7.93 – 7.70 (m, 8H), 7.47 (d (unresolved additional splitting), J = 8.1, 4H), 7.23 (d, J = 7.5, 4H), 7.10 (dd, J = 8.2, J = 7.1, 2H), 6.86 (ddd, J = 7.3, J = 5.6, J = 1.4, 4H), 6.55 (s, 1H), 3.40 (p, J = 6.9, 2H), 1.45 (d, J = 6.8, 12H). HRMS (ESI) m/z calculated for $C_{41}H_{37}N_6Pt_2$ 1003.24 $[M]^+$, found 1003.2. Elemental analysis calcd for $C_{41}H_{37}F_6N_6PPt_2$ (1148.92): C, 42.86; H, 3.25; N, 7.31. Found: C, 43.01; H, 3.37; N, 7.23.

[((N^C^N)Pt)$_2$(μ-(tBu)$_2$Pz)][PF$_6$] (**11f**). Isolated as a yellow solid (136 mg, 0.12 mmol, 26 %). Solid glows yellow/orange when excited with a long-wave UV lamp. m.p. 178-300 ºC (slow decomp), FTIR (solid): 2948.42 (w, C-H), 1606 (m, aromatic C=C) cm^{-1}. ^{1}H NMR (400 MHz, Methylene Chloride-d_2) δ 7.80 (td, J = 7.8, J = 1.6, 4H), 7.58 (d (unresolved Pt satellites), J = 5.8, 4H), 7.39 (d, J = 8.0, 4H), 7.13 (d, J = 7.6, 4H), 7.02 (dd, J = 8.3, J = 7.0, 2H), 6.79 (ddd, J = 7.3, J = 5.8, J = 1.5, 4H), 6.64 (s, 1H), 1.58 (s, 18H). ^{13}C NMR (100 mHz, CD_2Cl_2) δ 167.89, 162.64, 162.52, 151.66, 141.65, 140.07, 124.43, 124.08, 123.35, 120.21, 102.34, 32.96, 31.87. HRMS (ESI) m/z calculated for 1031.27 $[M]^+$, found 1031.3. Elemental analysis calcd for $C_{43}H_{41}F_6N_6PPt_2$ (1176.98): C, 43.88; H, 3.51; N, 7.14. Found: C, 45.04; H, 3.50; N, 6.84.

RESULTS AND DISCUSSION

Synthesis of Pyrazolate Bridged Dinuclear Pt(II) Complexes

Synthesis of the cyclometallating ligand, 1,3-di(2-pyridinal)benzene (**9**), was accomplished by a known literature Negishi coupling reaction of 2-bromopyridine and 1,3-dibromobenzene in a 79% yield as a yellow oil.[110] Reaction of the 1,3-di(2-pyridinal)benzene ligand with potassium tetrachloroplatinate in deoxygenated acetic acid afforded the metallated precursor platinum 1,3-di(2-pyridinal)benzene chloride (**10**) in a 75% yield as a yellow solid, which displayed Pt satellites in the ^{1}H NMR signal located at 9.26 ppm.[111] The 3,5-bis(trifluoromethyl)-1H-pyrazolate bridged platinum(II) dimer was

synthesized by first reacting **10** with silver hexafluorophosphate to remove the chloride ligand. In a separate flask, 3,5-bis(trifluoromethyl)-1H-pyrazole was deprotonated using NaH, which was then added to the solution containing **10** and silver hexafluorophosphate to yield the desired 3,5-bis(trifluoromethyl)-1H-pyrazolate bridged complex (**11a**), as shown in Scheme 11. The complex **11a** was isolated as a bright orange solid which glowed orange when excited using a long-wave UV lamp (365 nm).

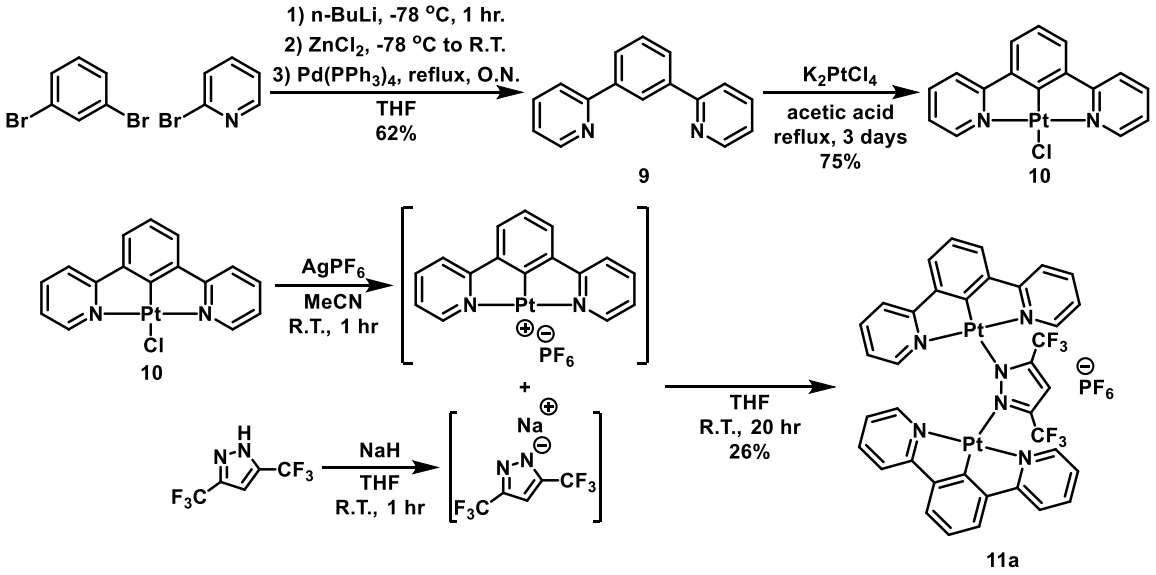

Scheme 11. Synthetic scheme of **9**, **10**, and **11a**.

The targeted 3,5-diphenyl-1H-pyrazolate, 3,5-dimethyl-1H-pyrazolate, 3,5-di-iso-propyl-1H-pyrazolate, 3,5-di-tert-butyl-1H-pyrazolate, and unsubstituted pyrazolate bridged platinum(II) dimers were all synthesized from **10** in a similar fashion, but without the use of silver hexafluorophosphate. As shown in Scheme 12, the desired pyrazolate was synthesized by deprotonation in THF using NaH. To this solution, platinum 1,3-di(2-pyridinal)benzene chloride was added. After refluxing the solution for twenty hours, the

targeted pyrazolate-bridged platinum(II) dimer was obtained as a positively charged cation with a chloride counter anion. Due to the ability of the chloride counter ion to act as a binding ligand and potentially degrading the desired product, potassium hexafluorophosphate was added before work-up of the reaction to replace the chloride anion with a non-binding hexafluorophosphate anion. The 3,5-diphenyl-1H-pyrazolate bridged complex (**11b**) was isolated as a bright orange solid which glowed bright orange when excited using a long-wave UV lamp. The pyrazolate bridged complex (**11c**) was isolated as a yellow solid which glowed a faint yellow when excited using a long-wave UV lamp (λ_{max} = 365 nm). The 3,5-dimethyl-1H-pyrazolate bridged complex (**11d**) was isolated as a bright orange solid which glowed bright orange when excited using a long-wave UV lamp. The 3,5-di-iso-propyl-1H-pyrazolate bridged complex (**11e**) was isolated as a dark orange solid which glowed orange when excited using a long-wave UV lamp. The 3,5-di-tert-butyl-1H-pyrazolate bridged complex (**11f**) was isolated as a yellow solid which glowed orange-red when excited using a long-wave UV lamp.

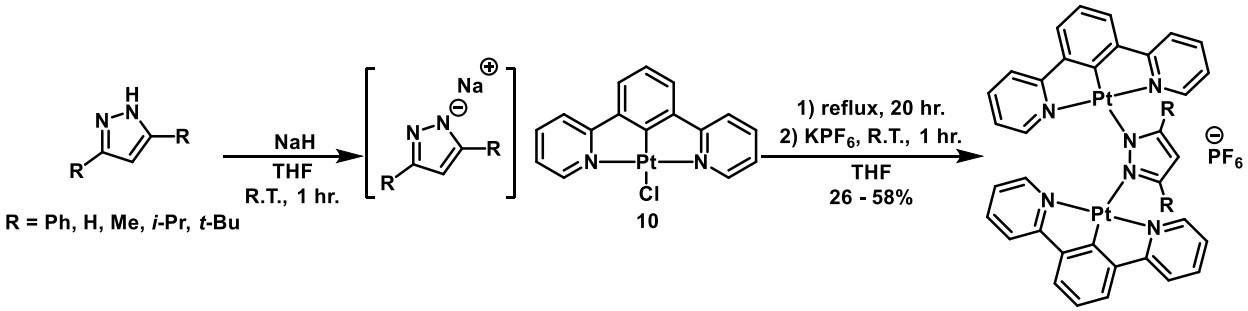

Scheme 12. General synthetic scheme of **11b** (R = Ph), **11c** (R = H), **11d** (R = Me), **11e** (R = *i*-Pr), and **11f** (R = *t*-Bu).

The single crystal X-ray diffraction determined structures of **11a-11f** are shown below in Figure 16. Crystals of **11a** were obtained by layering hexanes on top of a CH_2Cl_2 solution of **11a**. Crystals of **11b** were obtained via layering hexanes on top of a CH_2Cl_2 solution of **11b**. Crystals of **11c** were obtained via layering benzene on top of a N,N-dimethylformamide solution of **11c**. Crystals of **11d** were obtained via the slow evaporation of a CH_2Cl_2/ hexanes solution of **11d**. Crystals of **11e** were obtained via the layering of pentane on top of a CH_2Cl_2 solution of **11e**. Crystals of **11f** were obtained via the layering of hexanes on top of a CH_2Cl_2 solution of **11f**. The structure of each complex show two square-planar platinum(II) moieties bridged by the μ-3,5-substituted pyrazolate ligand. The structures of **11a**, **11b**, **11d**, and **11f** show very close Pt-Pt interactions with a Pt-Pt distance ranging from 3.01 Å in **11a** to 3.08 Å in **11d**. These close interactions are due to the steric bulk in the 3 and 5 positions of the bridging pyrazolate ligands.

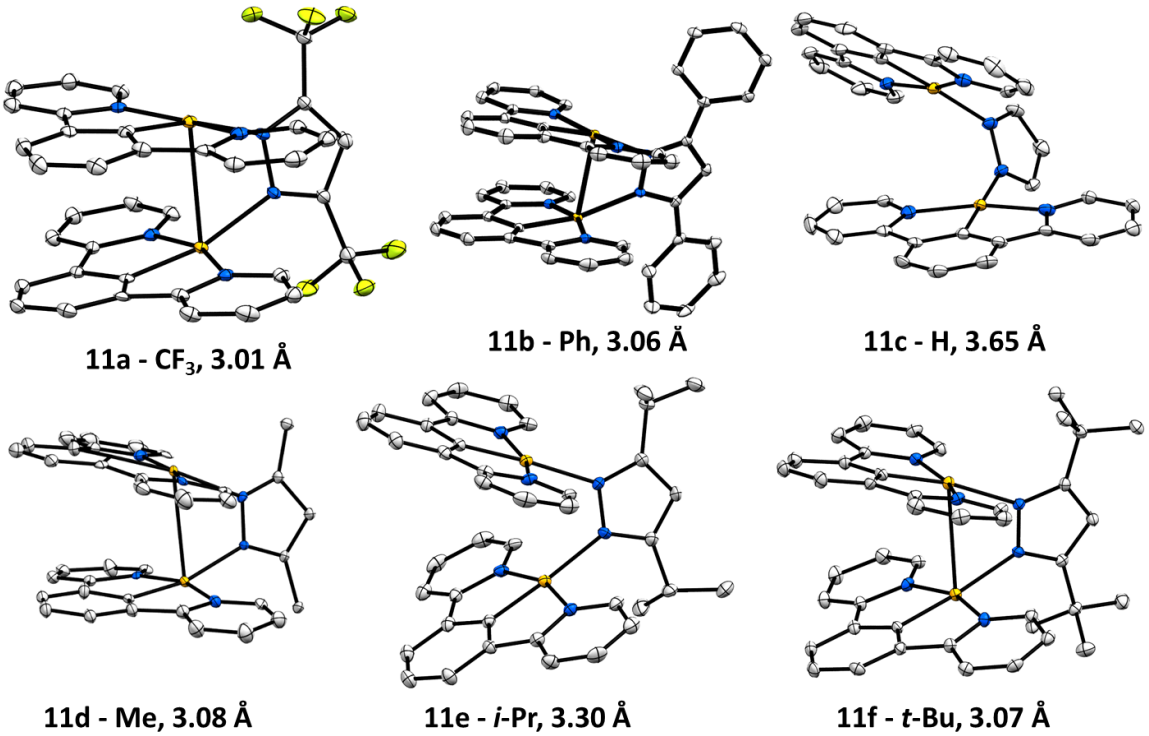

Figure 16. Single crystals structures and Pt-Pt distances for **11a-11f**.

Interestingly, **11d** has a closer Pt-Pt interaction than that of **11e**, which has a Pt-Pt distance of 3.30 Å. The most likely cause is due to how each complex packs together in their respective crystal structures. The packing of **11d**, Figure 17, shows the platinum complexes stacked together in columns due to π-π interactions ranging from 3.53 Å to 3.48 Å between the 1,3-di(2-pyridinal)benzene ligands of separate **11d** molecules. There are also close contacts between each column of molecules either in a "head-to-head" fashion or a "tail-to-tail" fashion. In the "head-to-head" fashion, the carbon atoms farthest from the platinum center on the 1,3-di(2-pyridinal)benzene ligands of one column interact with the hydrogen atoms on the carbon atoms farthest from the platinum centers on the 1,3-di(2-pyridinal)benzene ligands in the other column. These interactions range from 2.90 Å to

3.05 Å. In the “tail-to-tail” fashion, the hydrogen atoms on the methyl groups interact with the carbon atom at the 4 position on the pyrazolate ligand, ranging from 2.82 Å to 3.00 Å.

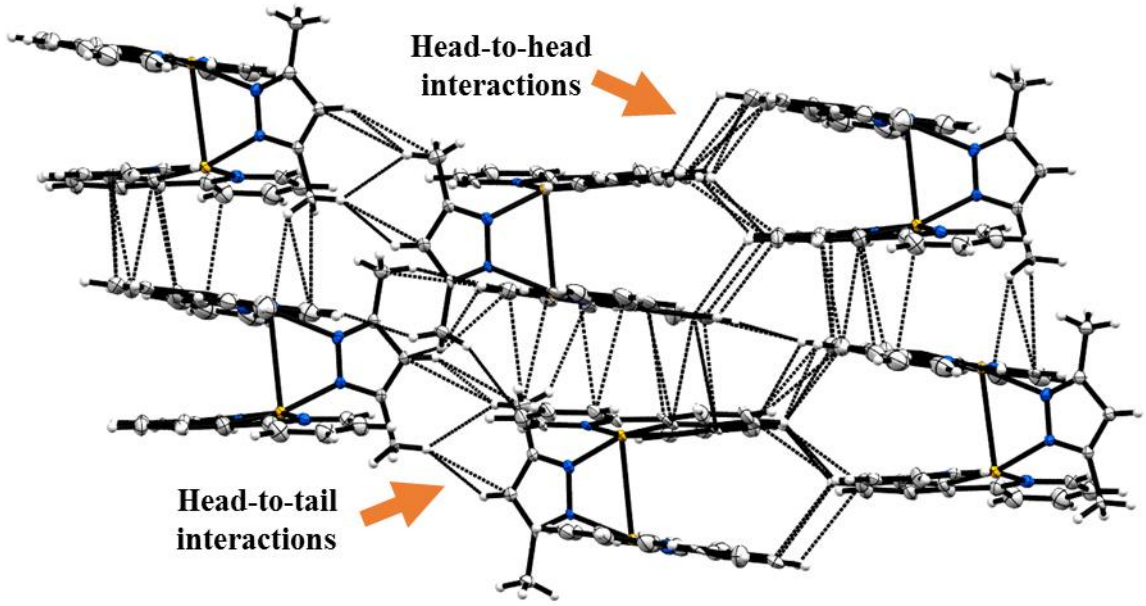

Figure 17. Crystal packing of **11d**, showing the contacts in both the “head-to-head” fashion and the “tail-to-tail” fashion.

The packing of **11e**, Figure 18, shows the platinum complexes packed together in rows, where each complex is rotated by approximately 90 degrees relative to its neighbor. There are close contacts between the hydrogen atoms of the iso-propyl moieties and the carbon atoms of the 1,3-di(2-pyridinal)benzene ligands, ranging from 3.79 Å to 3.88 Å. These interactions are likely the cause of a larger than expected Pt-Pt distance. Notably, there is no Pt-Pt interaction between the platinum centers of **11c** due to the lack of steric bulk in the 3 and 5 positions of the bridging pyrazolate ligand.

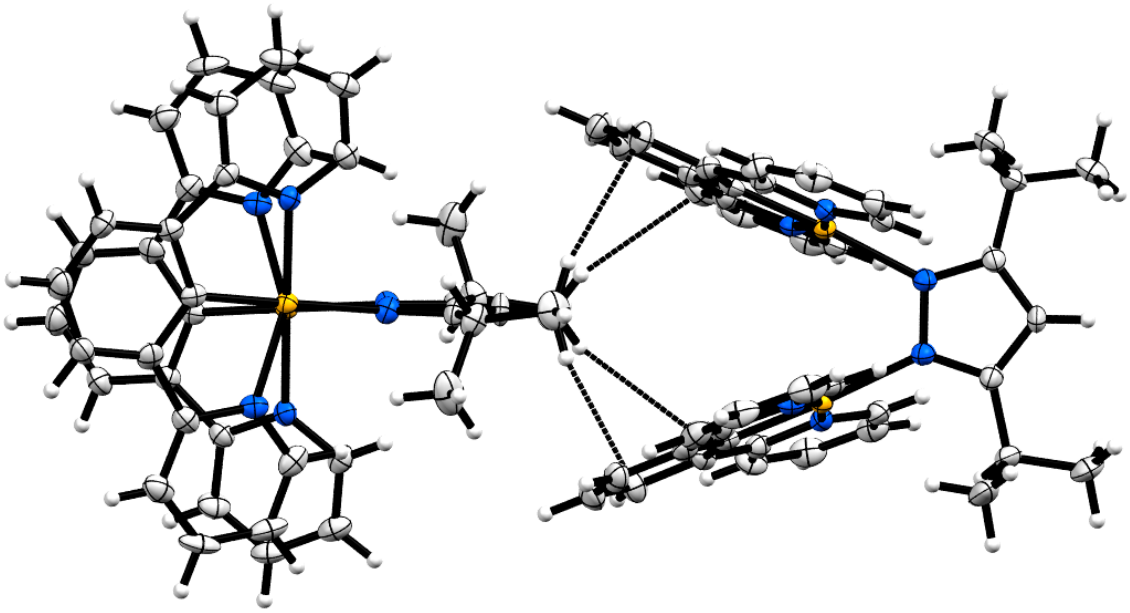

Figure 18. Crystal packing of **11e**, showing the contacts between the hydrogen atoms on the iso-propyl moieties and the carbon atoms of the 1,3-di(2-pyridinal)benzene.

Electrochemistry of 11a-11f

Cyclic voltammetry was used to evaluate the redox potentials of **11a-11f**, the values of which are reported relative to a ferrocene/ferrocenium external reference. The cyclic voltammograms for **11a-11f** as shown below in Figures 19-24. Complex **11a** shows an irreversible oxidative event at $E_{p,a}$ = 0.61 V.

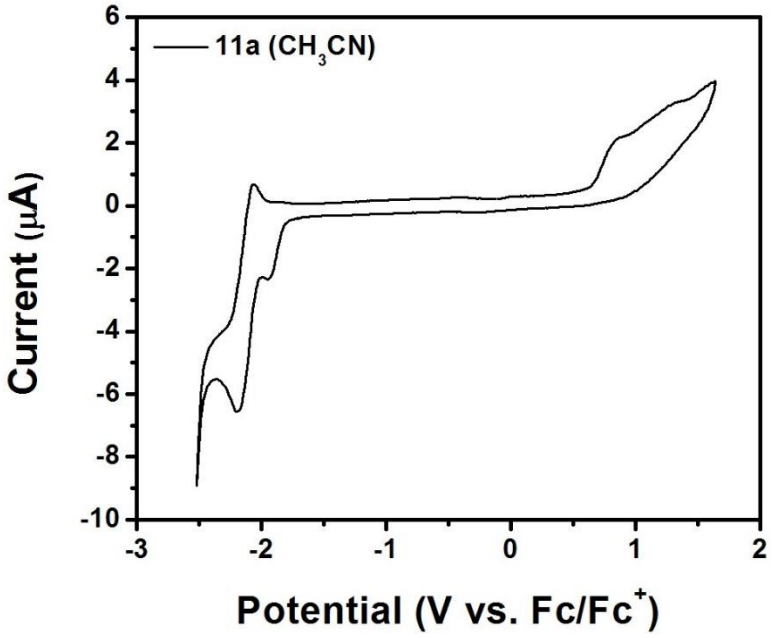

Figure 19. Cyclic voltammogram of **11a** in CH_3CN.

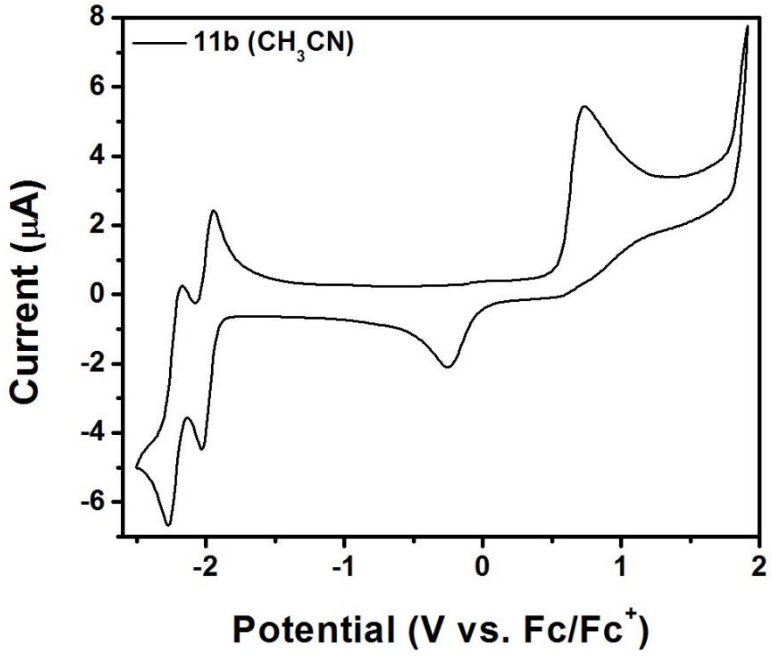

Figure 20. Cyclic voltammogram of **11b** in CH_3CN.

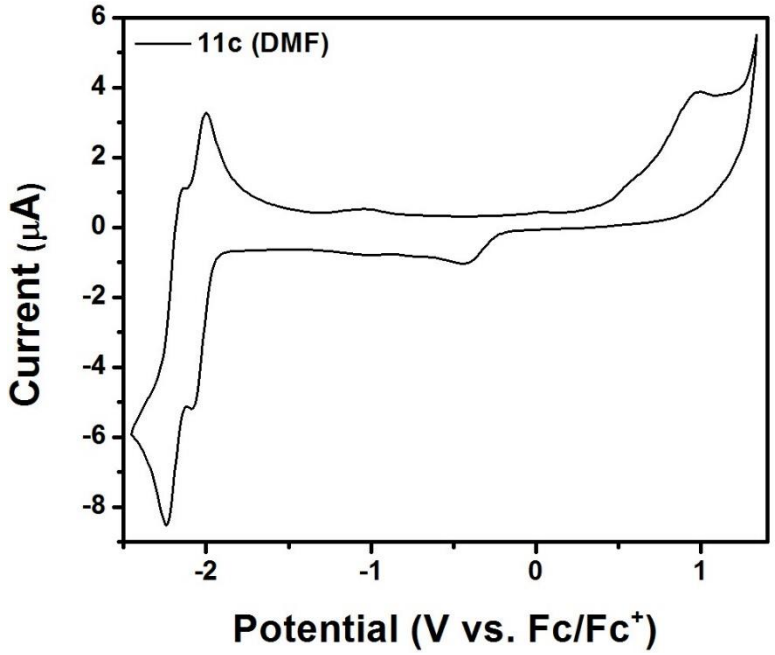

Figure 21. Cyclic voltammogram of **11c** in N,N-dimethylformamide.

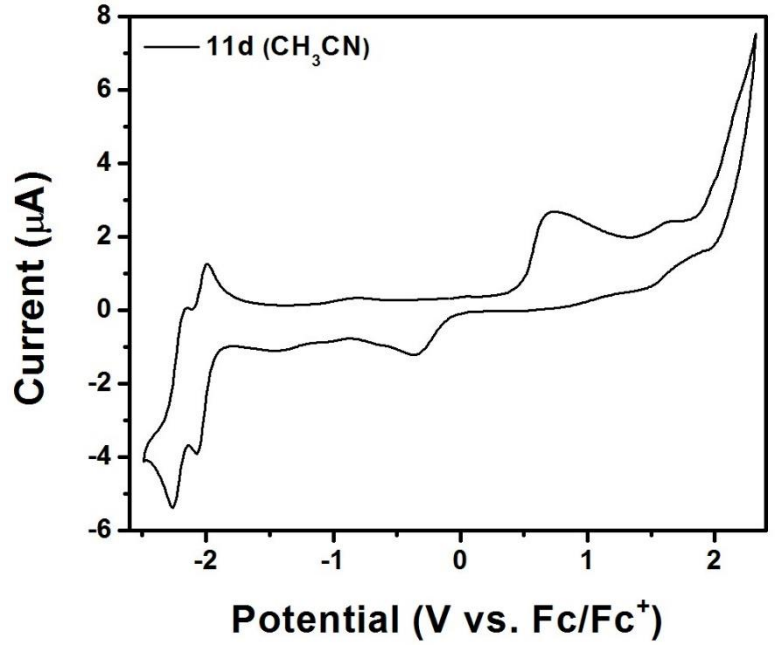

Figure 22. Cyclic voltammogram of **11d** in CH_3CN.

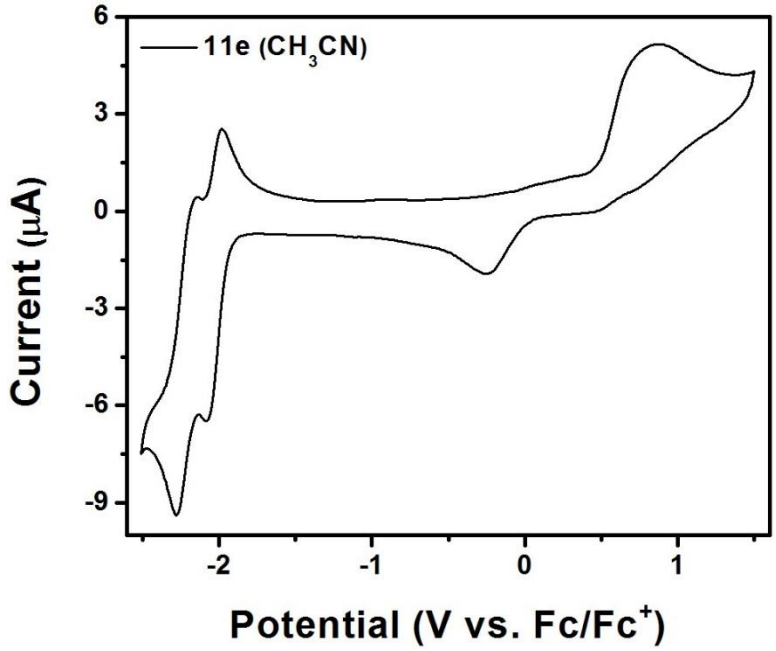

Figure 23. Cyclic voltammogram of **11e** in CH_3CN.

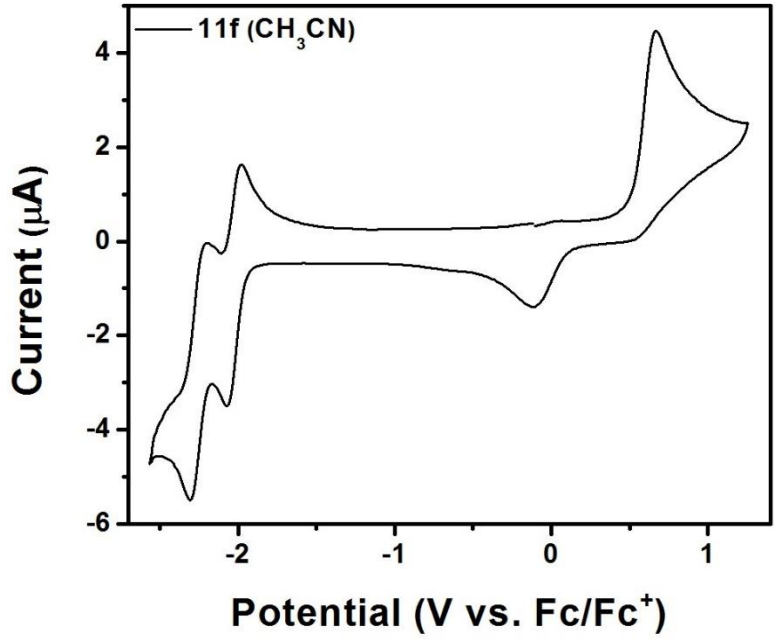

Figure 24. Cyclic voltammogram of **11f** in CH_3CN.

Complexes **11b-11f** show an irreversible oxidative event ranging from $E_{p,a}$ = 0.48 V to $E_{p,a}$ = 0.53 V which is coupled to a reductive event ranging from $E_{p,c}$ = 0.16 V to $E_{p,c}$ = -0.19 V. It was determined that these events are coupled to each other by first scanning toward negative potentials before scanning toward positive potentials. In each case, there was no reductive event until the oxidative event occurred upon scanning toward positive potentials, Figures 25-29. It is believed that the oxidation of each complex occurs at the platinum center, while reduction occurs mainly on the 1,3-di(2-pyridinal)benzene ligand, which is consistent with reports on related platinum(II) complexes.[112] The large gap between the coupled oxidative and reductive events is likely due to a structural conformation change of each complex upon oxidation.

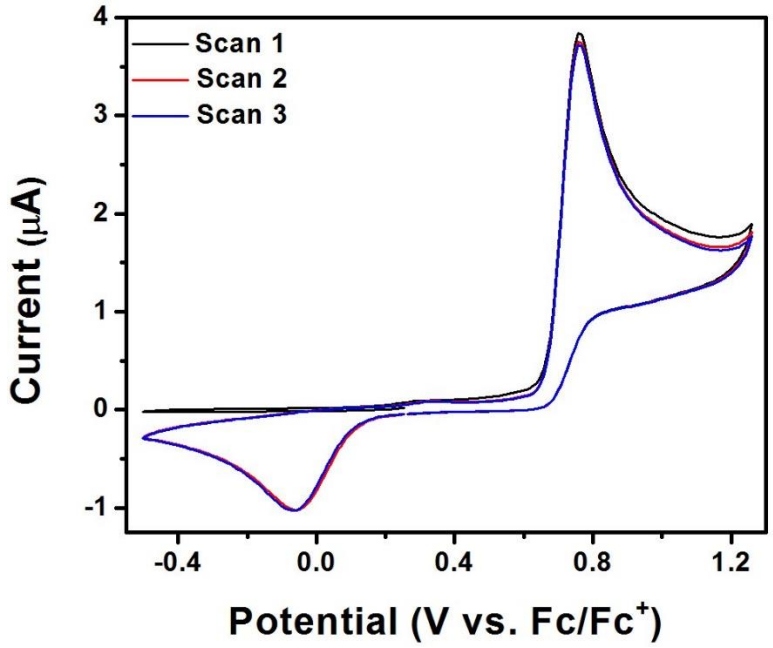

Figure 25. Cyclic voltammogram of **11b** in CH_2Cl_2.

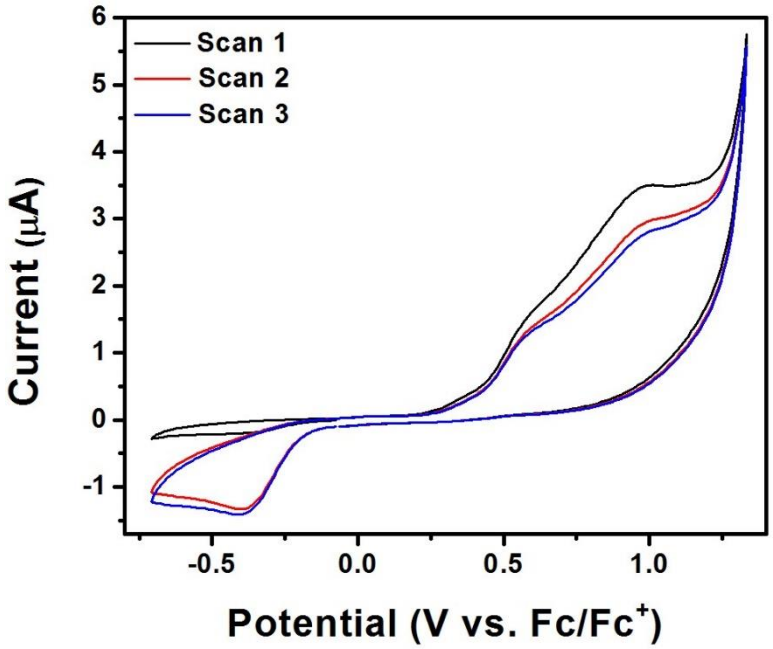

Figure 26. Cyclic voltammogram of **11c** in N,N-dimethylformamide.

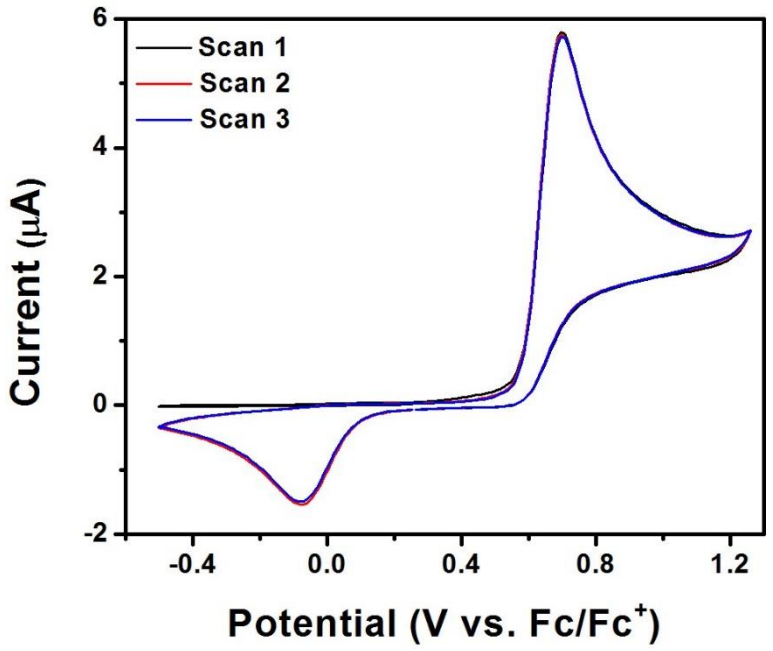

Figure 27. Cyclic voltammogram of **11d** in CH_2Cl_2.

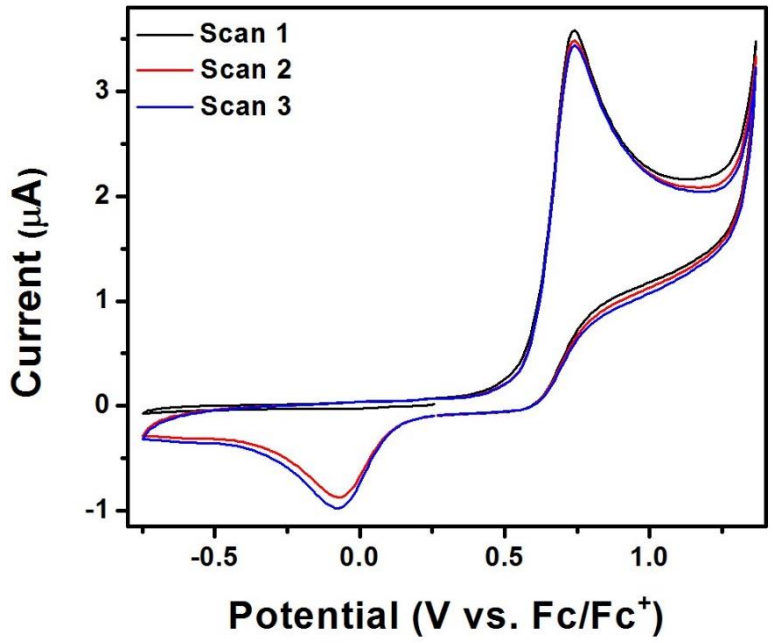

Figure 28. Cyclic voltammogram of **11e** in CH_2Cl_2.

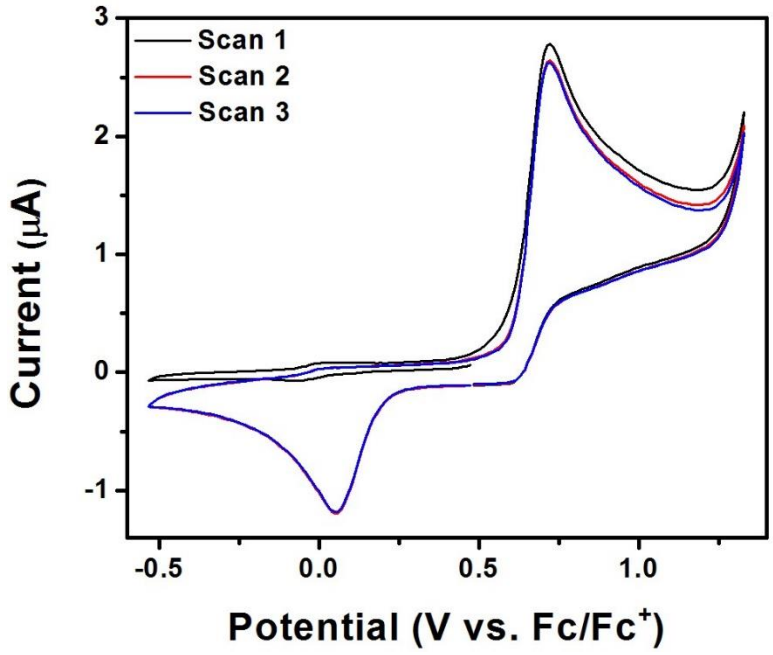

Figure 29. Cyclic voltammogram of **11f** in CH_2Cl_2.

The electrochemical HOMO/LUMO band gaps were determined for each complex by measuring the difference between the onset of oxidation on the platinum center and the onset of reduction on the 1,3-di(2-pyridinal)benzene ligand, the values of which are shown in Table 2.

Table 2. Electrochemically determined HOMO/LUMO band gaps for **11a-11f**.

Complex	**11a**	**11b**	**11c**	**11d**	**11e**	**11f**
Electrochemical Band Gap (eV)	2.48	2.46	2.36	2.44	2.43	2.48

Photophysical Properties of 11a-11f

Absorption Spectroscopy

The photophysical properties of **11a-11f** were studied under a variety of conditions. The UV-Vis spectra of **11a-11f** showed several transitions between 275 nm and 550 nm, which are shown below in Figures 30-35. Each complex has a similar spectrum which displays broad peaks between 235-535 nm, the molar absorptivity of which can be found in Table 3. The bands below 300 nm are due to π-π^* transitions located on the 1,3-di(2-pyridinal)benzene ligands. The bands between 350 nm and 425 nm are attributed to ^{1}MMLCT transitions and the bands between 440 nm and 540 nm are due to the ^{3}MMLCT transitions. This is due to the steric bulk from the substitution on the 3 and 5 positions of the bridging pyrazolate ligand, which produces significant Pt-Pt σ interactions, except in the case of **11c**. These results are consistent with a similar systems reported by Che *et al.*,[86] and Castellano *et al.*[90]

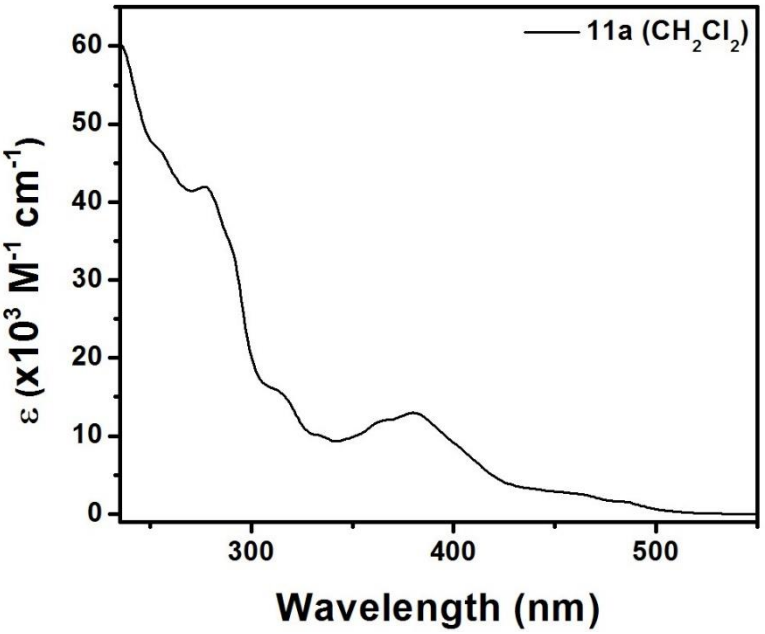

Figure 30. UV-Vis spectrum of **11a** in CH_2Cl_2.

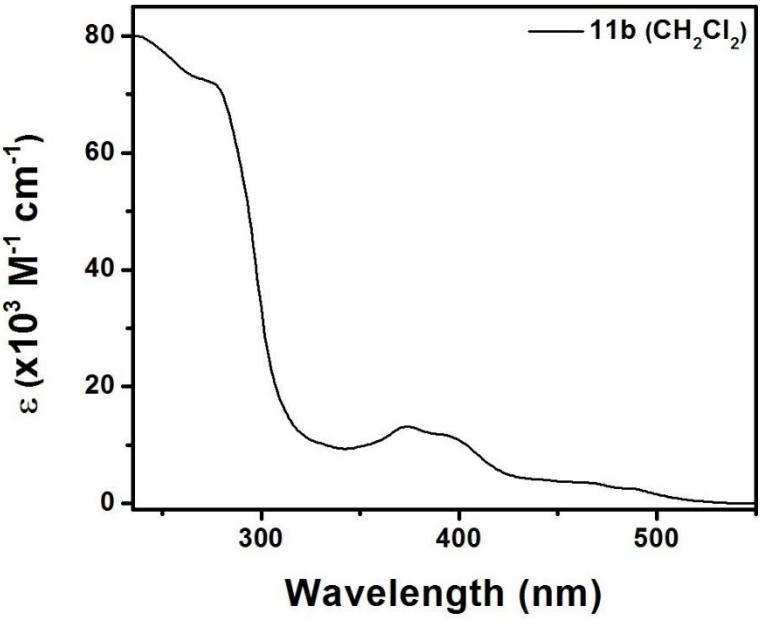

Figure 31. UV-Vis spectrum of **11b** in CH_2Cl_2.

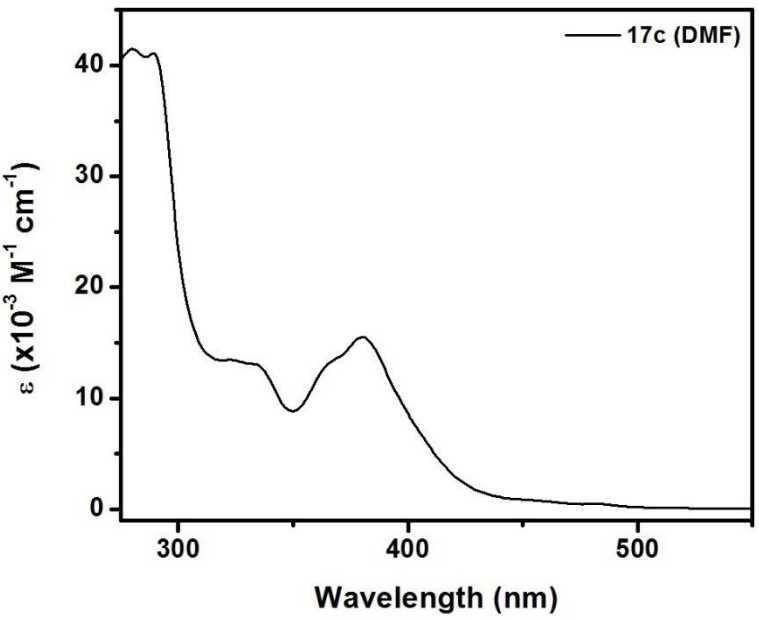

Figure 32. UV-Vis spectrum of **11c** in N,N-dimethylformamide.

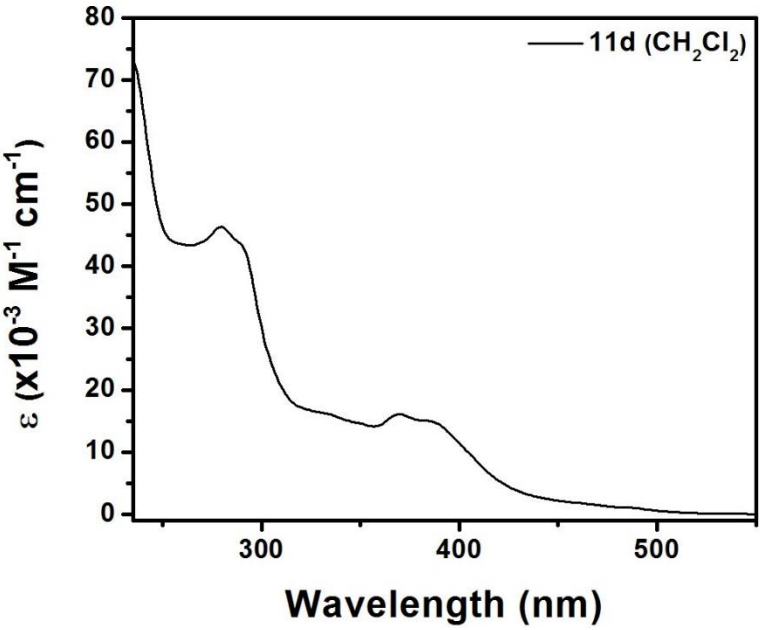

Figure 33. UV-Vis spectrum of **11d** in CH_2Cl_2.

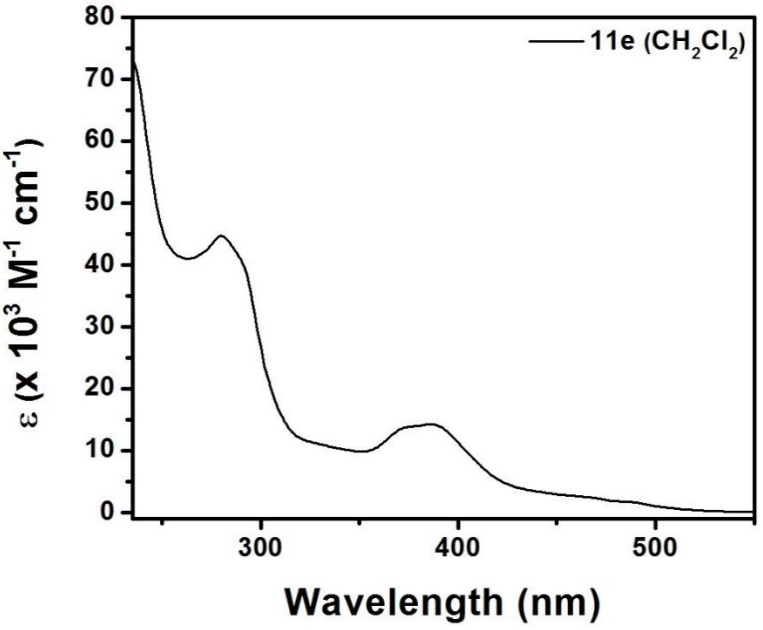

Figure 34. UV-Vis spectrum of **11e** in CH_2Cl_2.

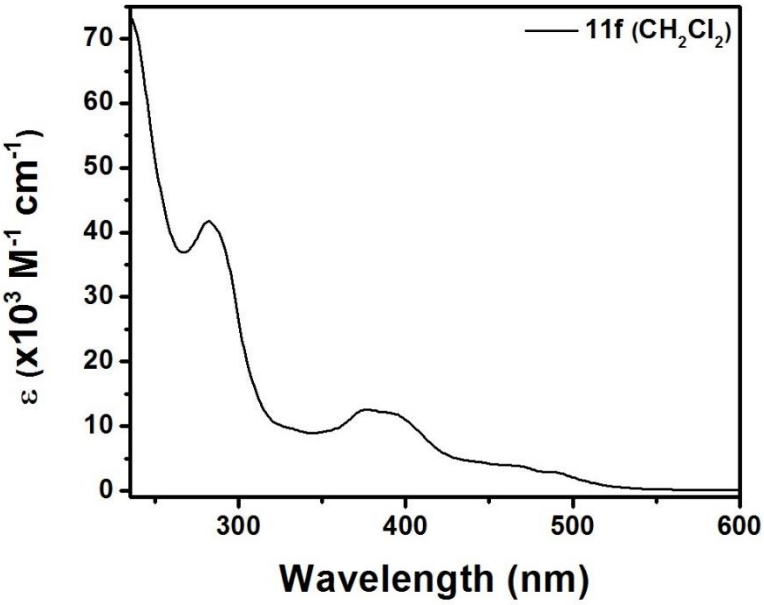

Figure 35. UV-Vis spectrum of **11f** in CH_2Cl_2.

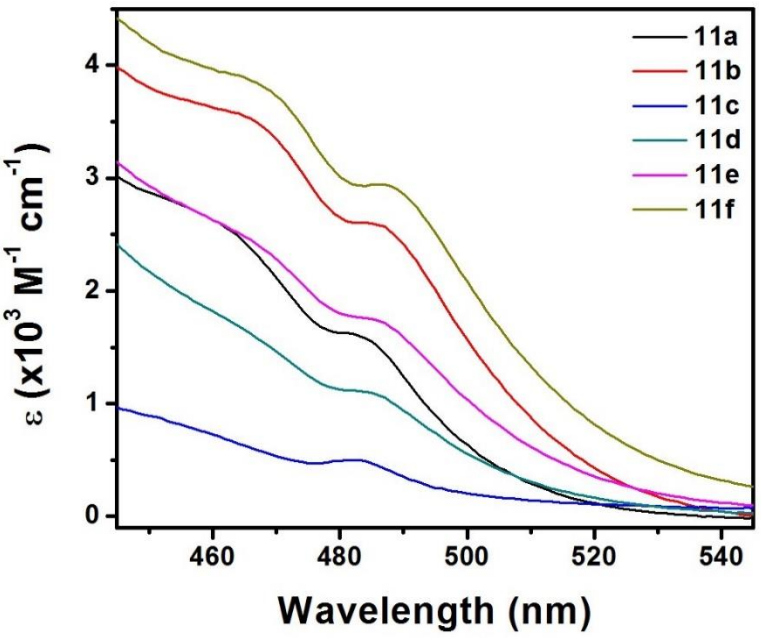

Figure 36. Zoom in of ^{3}MMLCT transition in UV-Vis spectra of **11a-11f**.

Room Temperature Solution Fluorimetry

The excitation and emission spectra of **11a-11f** at room temperature are shown in Figures 37-42. When excited at 380 nm, each complex shows a transition at 490 nm which has a luminescent lifetime (τ) in the microsecond regime (Table 3). Due to the microsecond τ and the clear vibronic progression of these peaks, this transition was assigned as the triplet ligand-centered (^{3}LC) transition from the 1,3-di(2-pyridinal)benzene ligands, which matches previously reported data on the chloride containing precursor **16**.[112] In the cases of **11a**, **11b**, and **11d-11f**, there is a second transition which is broad and structureless in nature between 652 nm and 690 nm with a microsecond τ (Table 3). These transitions have been assigned as the ^{3}MMLCT transition, which is common in other reports of dinuclear platinum(II) complexes with close Pt-Pt interactions.[86,90,91] There is a noticeable bathochromic shift in the ^{3}MMLCT of **11a**, **11b**, and **11d-11f** (Figure 43). The shift is due to the increasing electron donating ability of the bridging pyrazolate ligand, where **11a** is

the most blue-shifted (λ_{max} = 652 nm) and **11f** is the most red-shifted (λ_{max} = 690). This may suggest that the excited state photophysics is dominated more by electronics, rather than sterics. The lack of a ^{3}MMLCT in the case of **11c** is likely due to the lack of steric bulk on the bridging pyrazolate ligand which forces the two platinum centers into close contact with each other. Therefore, **11c** behaves more like two independent mononuclear complexes. This also suggests that, while electronics may dominate in the case of the ^{3}MMLCT for complexes **11a**, **11b**, and **11d-11f**, steric bulk still plays an important role in the emission profile of these complexes. Each complex is highly luminescent in solution, with the exception of **11c** (Φ_{soln} = 14.6%), with absolute quantum yields ranging from 51.3% in the case of **11f** to 86.2% for **11b** (Table 3).

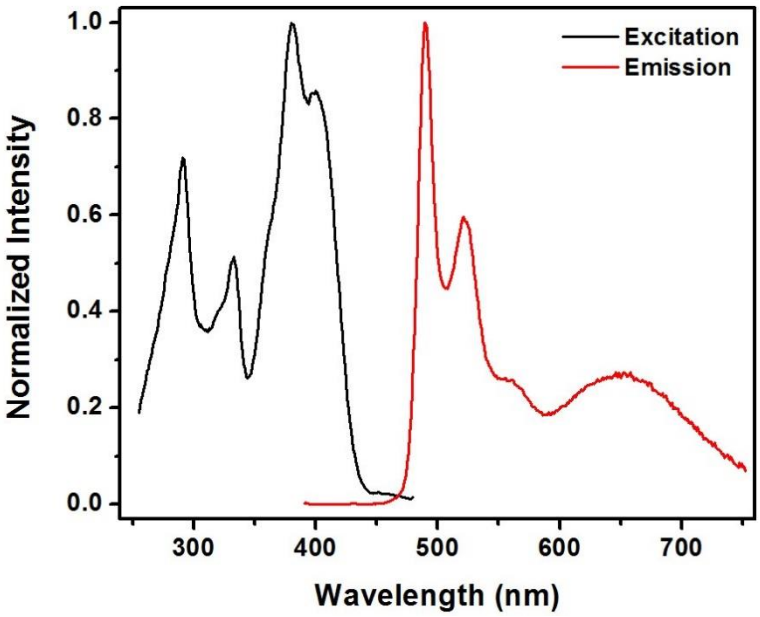

Figure 37. Room temperature excitation and emission profile of **11a** in CH_2Cl_2.

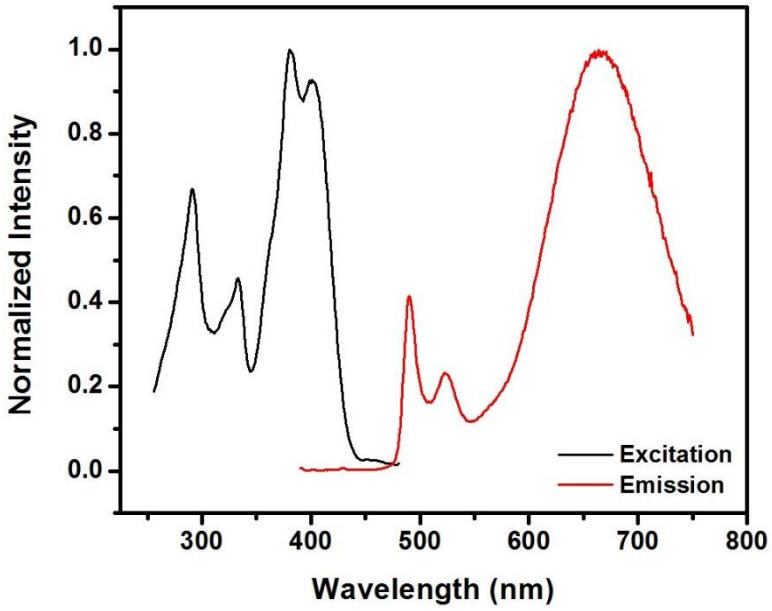

Figure 38. Room temperature excitation and emission profile of **11b** in CH_2Cl_2.

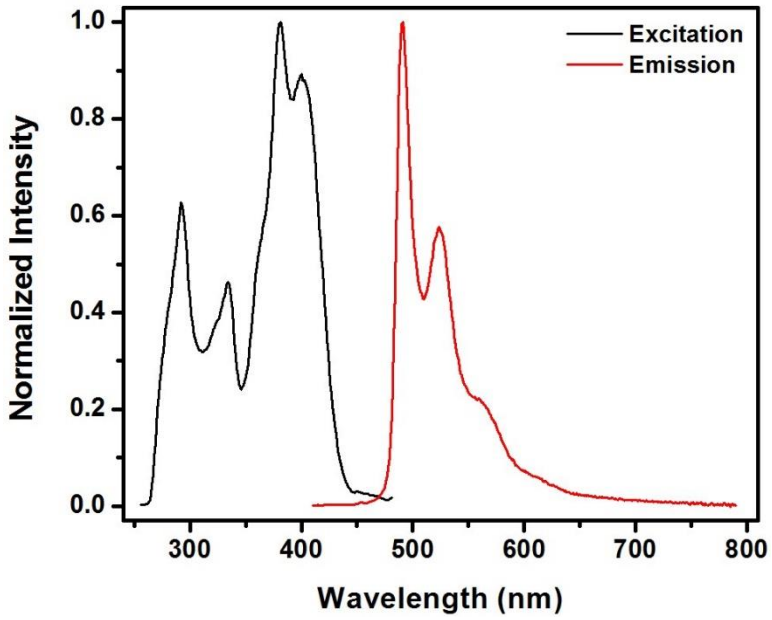

Figure 39. Room temperature excitation and emission profile of **11c** in N,N-dimethylformamide.

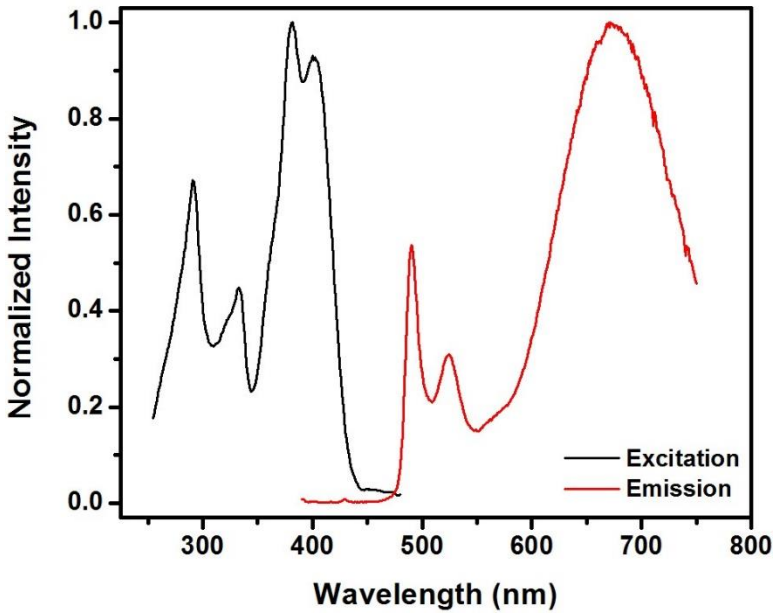

Figure 40. Room temperature excitation and emission profile of **11d** in CH_2Cl_2.

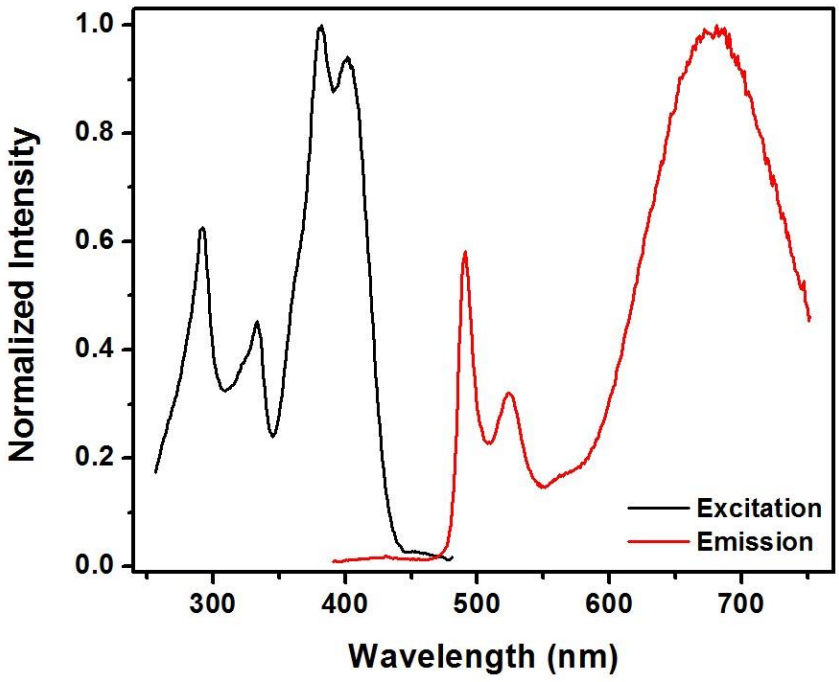

Figure 41. Room temperature excitation and emission profile of **11e** in CH_2Cl_2.

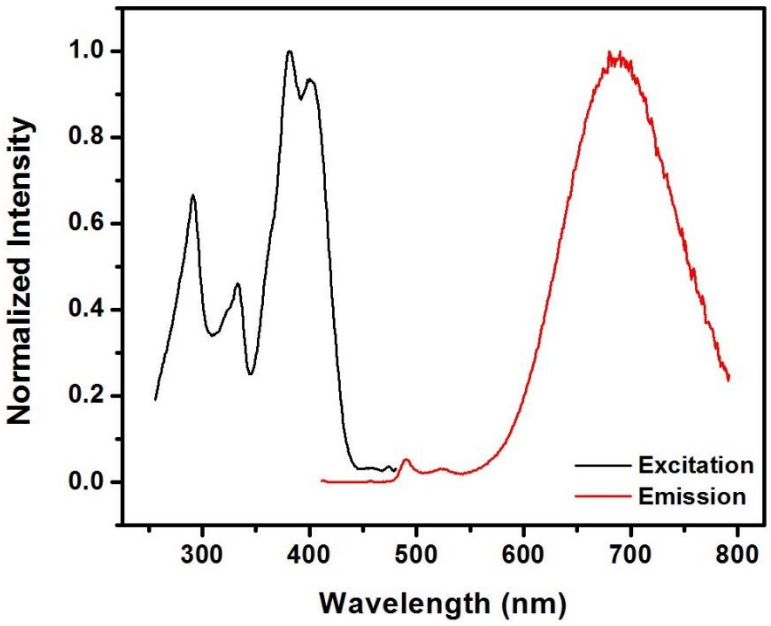

Figure 42. Room temperature excitation and emission profile of **11f** in CH_2Cl_2.

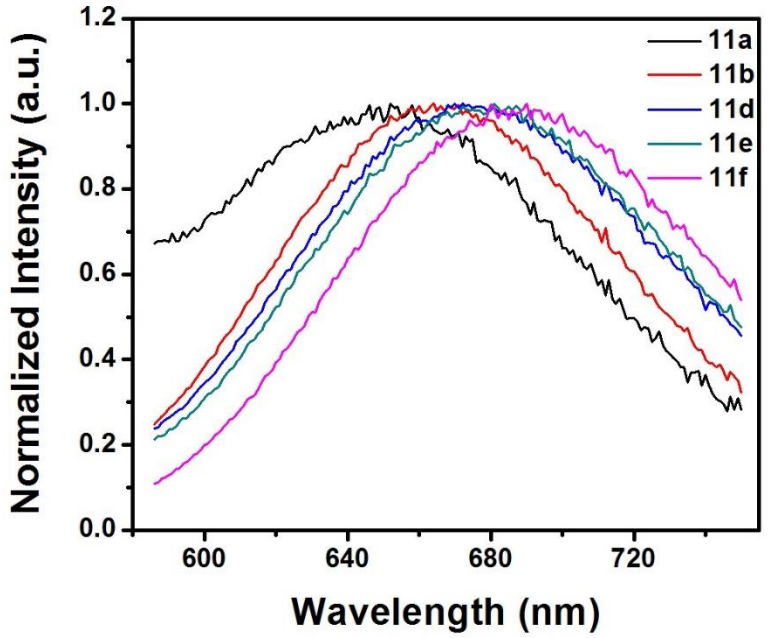

Figure 43. Room temperature ^{3}MMLCT emission in CH_2Cl_2 of **11a**, **11b**, and **11d-11f**.

Table 3. Room temperature solution photophysical data for **11a-11f**.

Complex	λ_{abs}/nm (ε, M^{-1} cm^{-1})	λ_{em} (nm)	τ_{lc}, τ_{MMLCT} (μs)[c]	Φ (%)[d]
11a	254 (46907), 277 (41978), 316 (15264), 366 (12017), 380 (12980), 462 (2567), 485 (1553)	490, 652	7.87, 2.80	84.6
11b	239 (79919), 277 (71722), 374 (13140), 395 (11567), 467 (3491), 487 (2568)	490, 664	6.92, 4.64	86.2
11c[b]	280 (41490), 289 (41083), 329 (13202), 366 (13250), 380 (15522)	490	7.33, N/A	14.6
11d	237 (71287), 280 (48322), 290 (43416), 370 (16086), 388 (14780), 466 (1622), 486 (1076)	490, 674	4.68, 6.00	57.6
11e	237 (71501), 281 (44638), 291 (40273), 373 (13701), 388 (14169), 464 (2517), 489 (1642)	490, 681	7.06, 5.65	59.2
11f	238 (71708), 282 (41731), 376 (12591), 395 (1176), 469 (3774), 490 (2862)	490, 690	6.13, 2.74	51.3

[a]Room-temperature measurements were performed in CH_2Cl_2 unless otherwise noted. [b]Room-temperature measurements and absolute quantum yields determinations were performed in N,N-dimethylformamide due to lack of solubility in most solvents. [c]Intensity decays, ± 1.3 μs. [d]Absolute quantum yields, ± 8%.

77 K 2-MeTHF Glass Fluorimetry

The excitation and emission profile of **11a**, **11b**, and **11d-11f** in 2-MeTHF glass at 77 K is shown below in Figures 44-48. The emission profile of **11c** in 2-MeTHF glass at 77 K was not obtained due to the complex's lack of solubility in 2-MeTHF. The

photophysical properties of **11a**, **11b**, and **11d-11f** are presented in Table 4. Each complex emits green in color when dissolved in 2-MeTHF at 77 K, but rapidly turns orange upon warming. This observation is supported by the emission spectrum of **11a**, **11b**, and **11d-11f** in 2-MeTHF glass, where the ^{3}MMLCT is either nonexistent or drastically less dominant in intensity in comparison to the ^{3}LC transition. Complexes **11b** and **11f** still display a ^{3}MMLCT, each of which is drastically decreased in intensity and blue shifted by 53 nm and 134 nm, respectively. Other reported dinuclear platinum(II) complexes also show a hypsochromic shift of the ^{3}MMLCT transition at 77 K.[86] As the solution begins to warm to room temperature, the ^{3}MMLCT transition begins to become more and more dominant, causing the color shift of emission from green to red. The decrease in the intensity of the ^{3}MMLCT is most likely due to each complex being "physically locked" in the 2-MeTHF glass, where a photoinduced molecular structure change involving a shortening of the Pt-Pt distance in the excited state is inhibited. Therefore, when comparing relative intensities of the ^{3}MMLCT at 77 k in 2-MeTHF glass, the steric bulk on the bridging pyrazolate ligand seems to play a role. This characteristic has also been observed in other pyrazolate bridged platinum(II) binuclear complexes.[91] This is further supported when comparing the emission spectra of **11a**, **11b**, and **11d-11f** in 2-MeTHF at 77 K. When normalizing the intensity of emission to the dominating ^{3}LC transition for each complex, the relative intensity of the ^{3}MMLCT transition for each complex can be compared (Figure 49). Complex **11f** has the most intense ^{3}MMLCT transition, followed by **11b**. For complexes **11a**, **11d**, and **11e**, where the ^{3}MMLCT is very minimal in intensity, **11a** displays the most intense ^{3}MMLCT follows closely by **11e** then **11d**. This data suggests that the steric bulk imparted by substitution on the 3 and 5 positions of the bridging pyrazolate ligand is the dominating factor on the emission profile of these complexes when frozen in the steady state at 77 K in 2-MeTHF, where the steric bulk of the *t*-Bu groups on

11f and the phenyl groups on **11b** still cause close Pt-Pt interactions and the appearance of a ^{3}MMLCT.

Table 4. Solution 77 K photophysical data for **11a**, **11b**, and **11d-11f**.

Complex	$\lambda_{excitation}$ (nm)	λ_{max} (nm)	$\tau \pm 0.5$ (μs)
11a	379	480	N/A
11b	380	487	6.98
11d	385	484	8.54
11e	382	485	8.84
11f	384	485	6.82

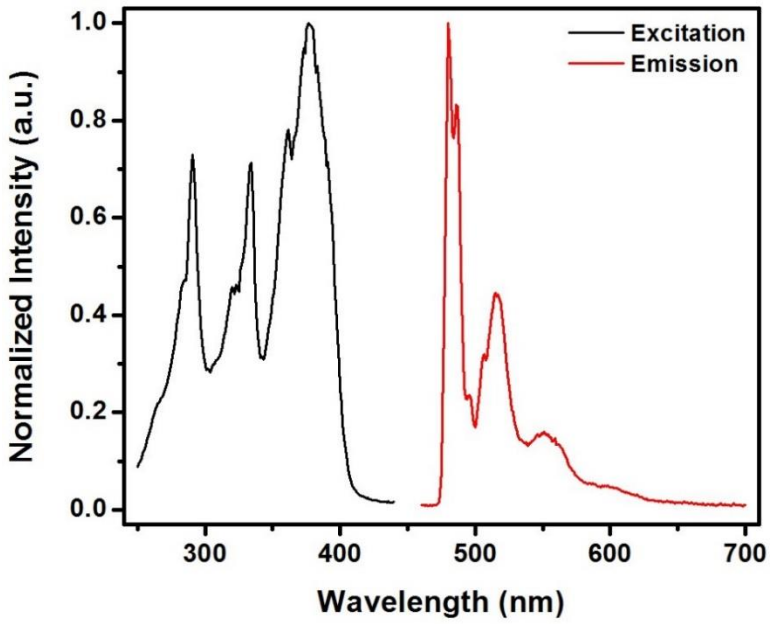

Figure 44. Excitation and emission (excitation at 379 nm) profile of **11a** at 77 K in 2-MeTHF glass.

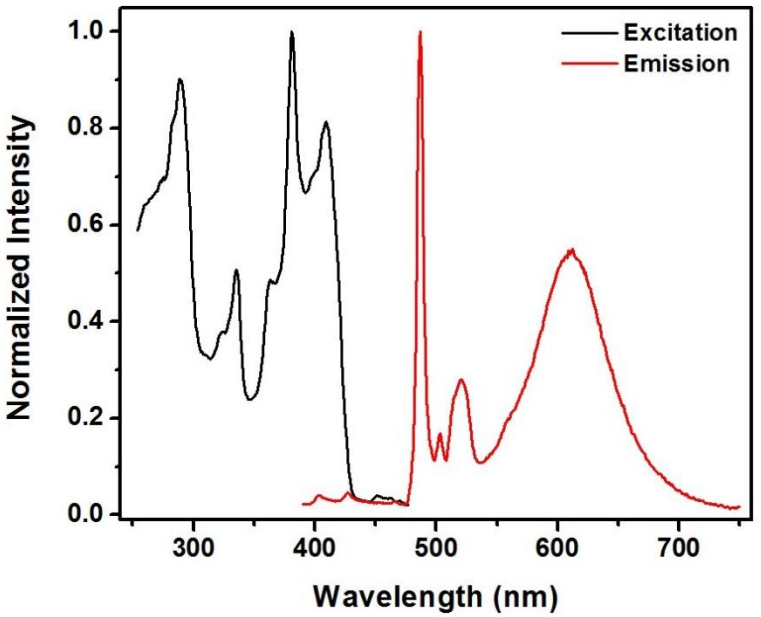

Figure 45. Excitation and emission (excitation at 380 nm) profile of **11b** at 77 K in 2-MeTHF glass.

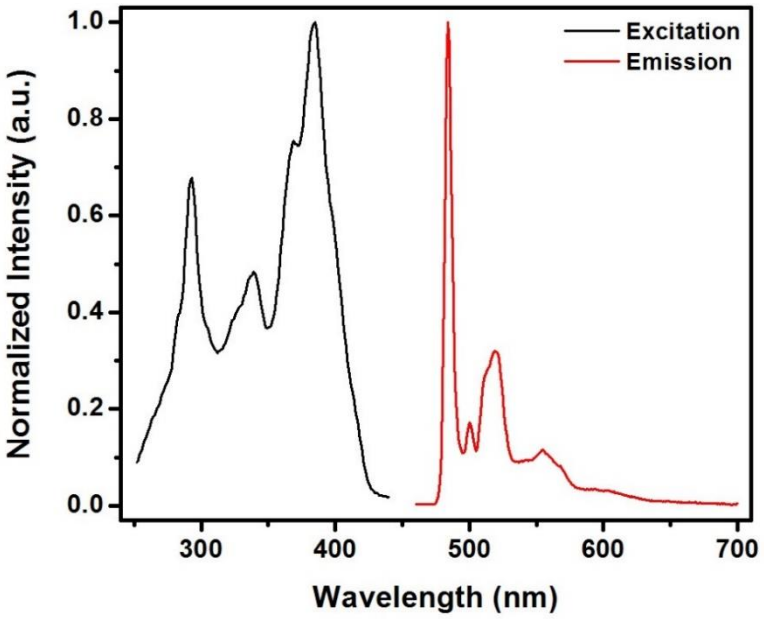

Figure 46. Excitation and emission (excitation at 385 nm) profile of **11d** at 77 K in 2-MeTHF glass.

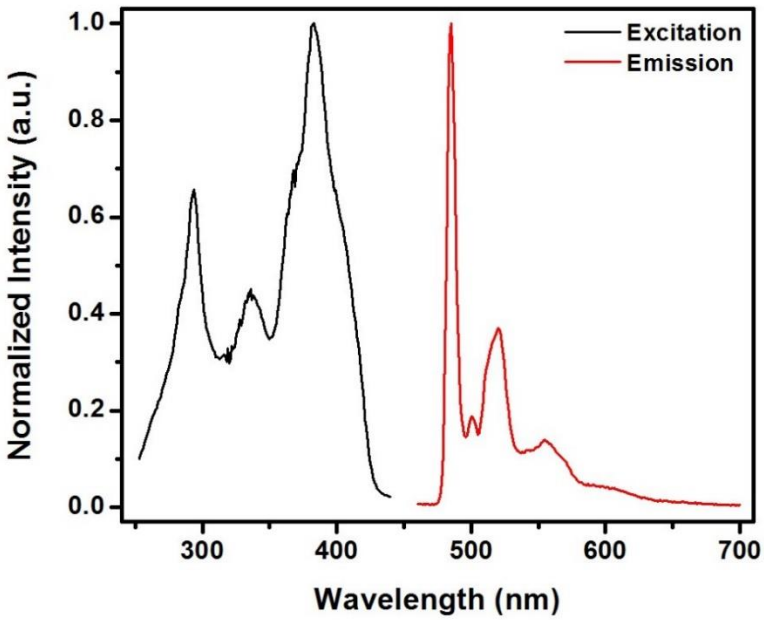

Figure 47. Excitation and emission (excitation at 382 nm) profile of **11e** at 77 K in 2-MeTHF glass.

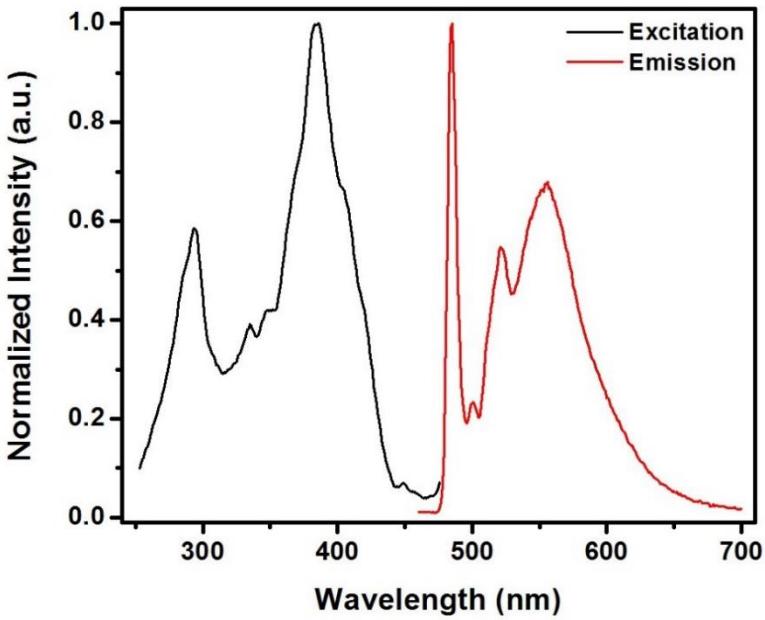

Figure 48. Excitation and emission (excitation at 384 nm) profile of **11f** at 77 K in 2-MeTHF glass.

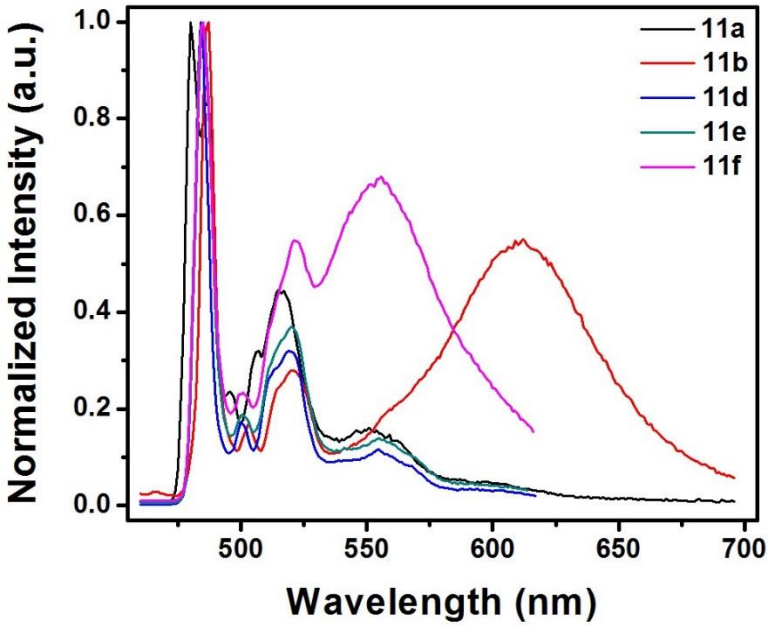

Figure 49. Overlay of the emission profile of **11a**, **11b**, and **11d-11f** at 77 K in 2-MeTHF.

Room Temperature Solid-State Fluorimetry

The emission profile of **11a-11f** was studied in the solid-state at room temperature; the spectra of which can been seen in Figures 50-55 and the photophysical data for **11a-11f** is shown in Table 5. In all cases, the ^{3}LC transition has been completely quenched, showing only a broad ^{3}MMLCT transition. All complexes show a hypsochromic shift of the ^{3}MMLCT transition from room temperature solution emission to room temperature solid emission, except for **11a** and **11c**. The ^{3}MMLCT emission of **11a** is essentially the same, only showing a bathochomic shift of 1 nm. It is believed that the solid-state emission of **11c** is due to aggregation effects based on the broad, abnormal character of the emission profile. This is further supported by an uncharacteristically long intensity decay of τ = 27.9 μs, when compared to the intensity decays of the other complexes. Complexes **11b**, and **11d-11f** display a hypsochromic shift of the ^{3}MMLCT by 29 nm, 19 nm, 13 nm, and 30 nm, respectively. Other related dinuclear platinum(II) complexes also display a

hypsochromic shift in the room temperature solid-state emission from the room temperature solution emission.[86] The cause is likely due to the complexes being "physically locked" in the solid-state, inhibiting a photoinduced molecular structure change involving a shortening of the Pt-Pt distance, destabilizing the excited state.

Table 5. Solid-state photophysical data for **11a-11f**.

Complex	$\lambda_{excitation}$ (nm)	$\lambda_{emission}$ (nm)	τ (μs)[a]	Φ (%)[c]
11a	469	653	4.6	22.9
11b	469	635	3.3	38.6
11c	425	630	27.9[b]	6.4
11d	469	655	4.7	27.8
11e	470	668	2.8	13.0
11f	474	660	3.3	13.3

[a]Intensity decays, ± 1.6 μs. [b]Intensity decay, ± 2.5 μs. [c]Absolute quantum yield, ± 4.3 %.

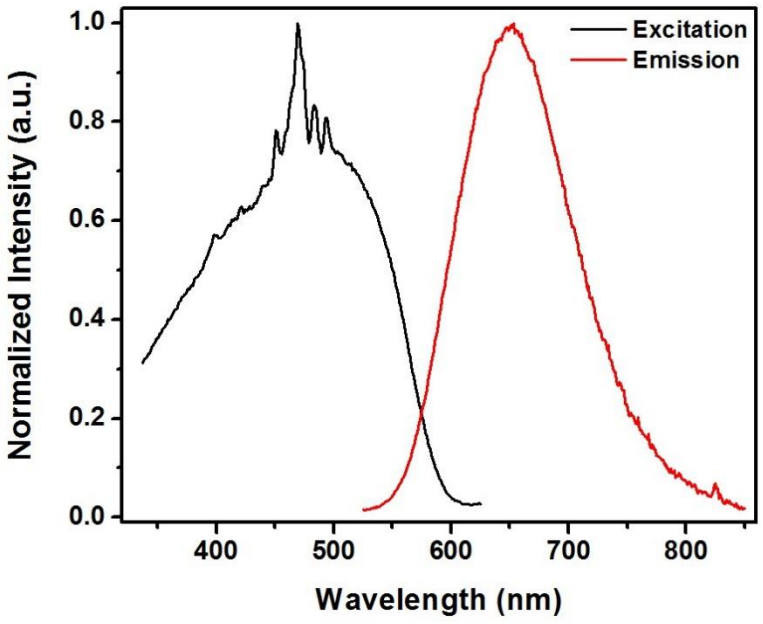

Figure 50. Solid-state excitation and emission profile of **11a** at room temperature.

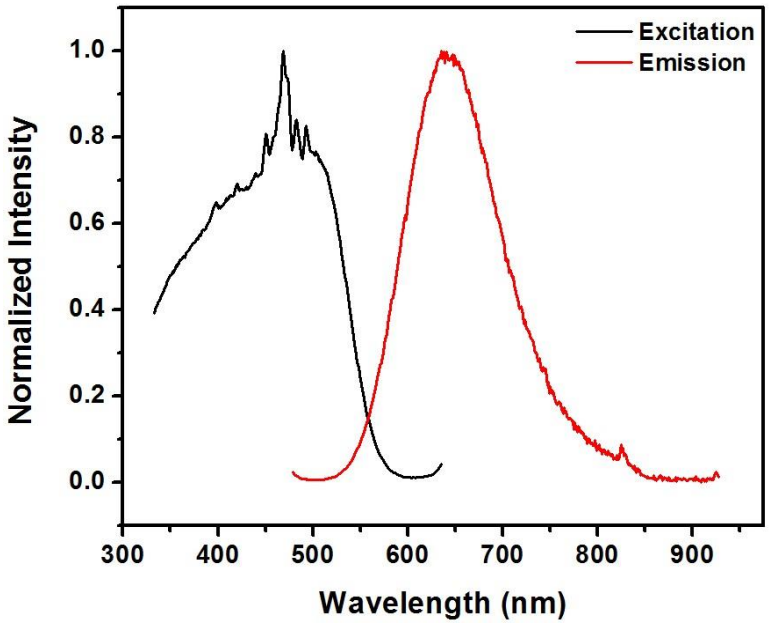

Figure 51. Solid-state excitation and emission profile of **11b** at room temperature.

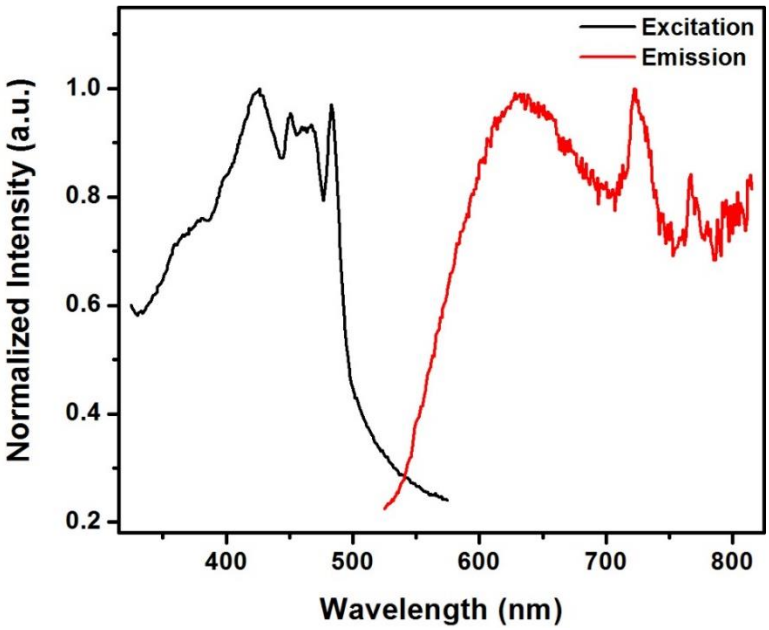

Figure 52. Solid-state excitation and emission profile of **11c** at room temperature.

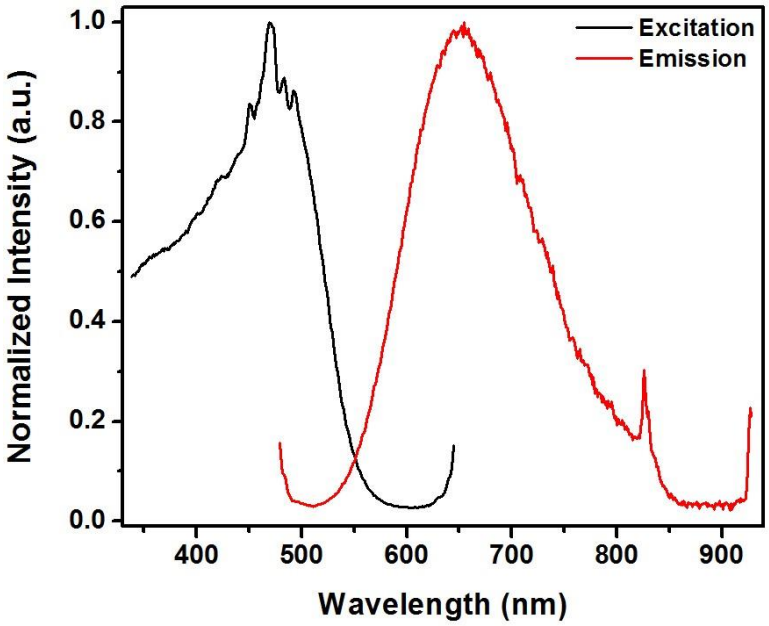

Figure 53. Solid-state excitation and emission profile of **11d** at room temperature.

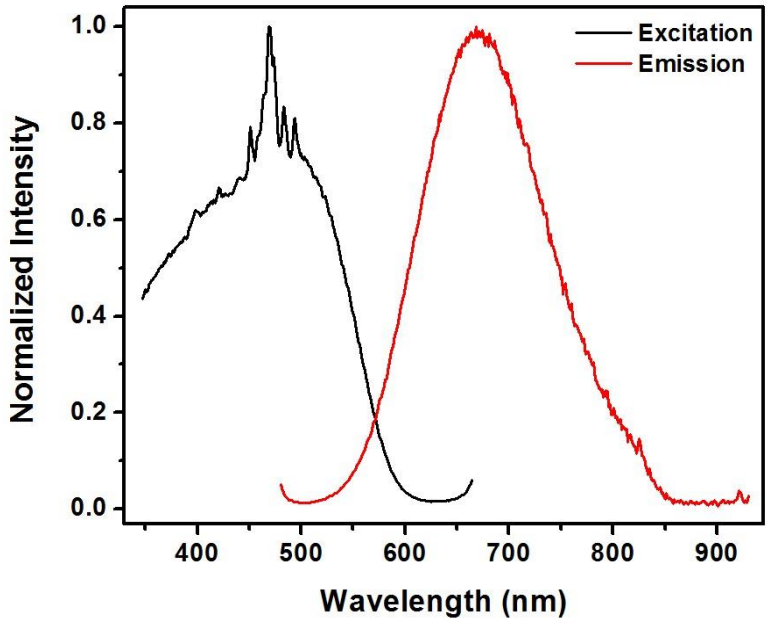

Figure 54. Solid-state excitation and emission profile of **11e** at room temperature.

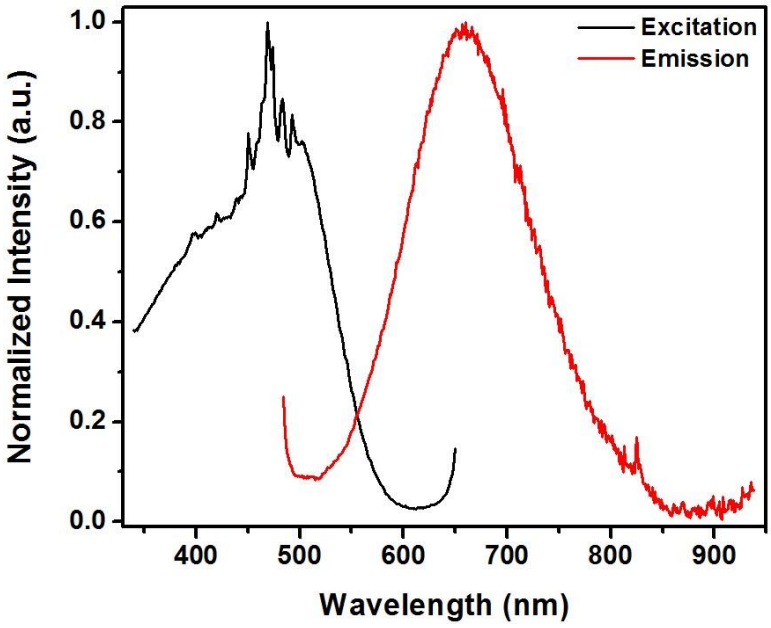

Figure 55. Solid-state excitation and emission profile of **11f** at room temperature.

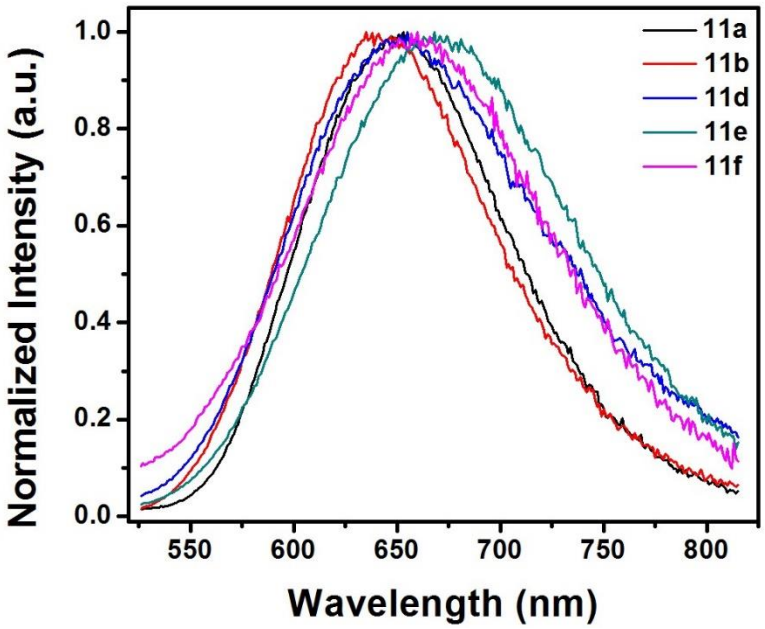

Figure 56. Overlay of the solid-state emission profile for **11a**, **11b**, and **11d-11f**.

Electroluminescence and LEEC Data for 11b

Electroluminescence (EL) spectra were recorded for light emitting electrochemical cell (LEEC) devices from pristine films and films augmented with 0.3%/wt $LiPF_6$ (Figure 57) by Slinker and co-workers at The University of Texas at Dallas. The $LiPF_6$ ionic additive has been shown to improve device metrics through improved ion mobility and enhancing double layer formation at the cathode.[95,98,99,101] The pristine device shows a broad peak consistent with a ^{3}MMLCT transition with a maximum at 695 nm. This is redshifted by 50 nm with respect to the solid-state film. Alternatively, the ionic additive device also exhibits a broad-spectrum indicative of a ^{3}MMLCT transition, but with a peak at 665 nm, considerably closer to the PL max.

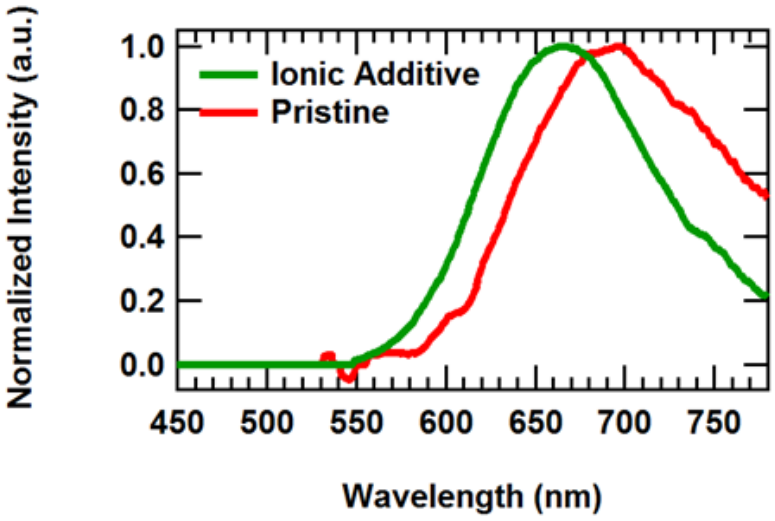

Figure 57. Electroluminescence spectra of **11b** LEEC devices with (Ionic Additive) and without (Pristine) 0.3% $LiPF_6$.

Electroluminescence in LEECs occurs within a thin region of the film between the electrodes as dictated by the relative injection efficiencies and mobilities of electrons and

holes.[92,94,104,113] The large spectral shift of the pristine device likely indicates that the EL emission zone is offset from the center and occurring in regions of high ionic space charge content where the electric field is high, such that the spectral shift is a Stark shift. Adding the ionic additive likely moves the location of the emission zone closer to the center of the device by balancing carrier injection to bring about emission more closely matching the thin film photoluminescence. This postulate can be further explored through study of the relative luminance and efficiency of the devices.

The luminance versus time graph of **11b** LEECs running at constant current is shown in Figure 58. The pristine device shows a slow onset of emission that maximizes after ~2 hr near 10 cd/m^2, then slowly decays with a half-life of approximately 13 hr. The maximum external quantum efficiency is less than 0.05% photons/electron for this device, a low value anticipated from the irreversibility of oxidation. Nonetheless, salt addition improves the performance. The maximum luminescence of the ionic additive device is enhanced twofold relative to the pristine device to 20 cd/m^2. The $LiPF_6$ ionic additive raises the maximum quantum efficiency to 0.22%. The onset of emission is seen almost immediately, and the luminance maximum is achieved in 30 s. This suggests that the ionic additive helps to balance carrier concentrations. This observation could also reconcile the EL spectra of Figure 57, as postulated above. The higher maximum efficiency and luminance of the ionic additive device is consistent with more balanced carrier injection. This ionic additive device, in turn, is more likely to produce an emission zone in the bulk and an emission spectrum more in line with that predicted from photoluminescence, as observed in Figure 58. Overall, this demonstrates that Pt dimers such as **11b** can produce appreciable electroluminescence as LEEC devices.

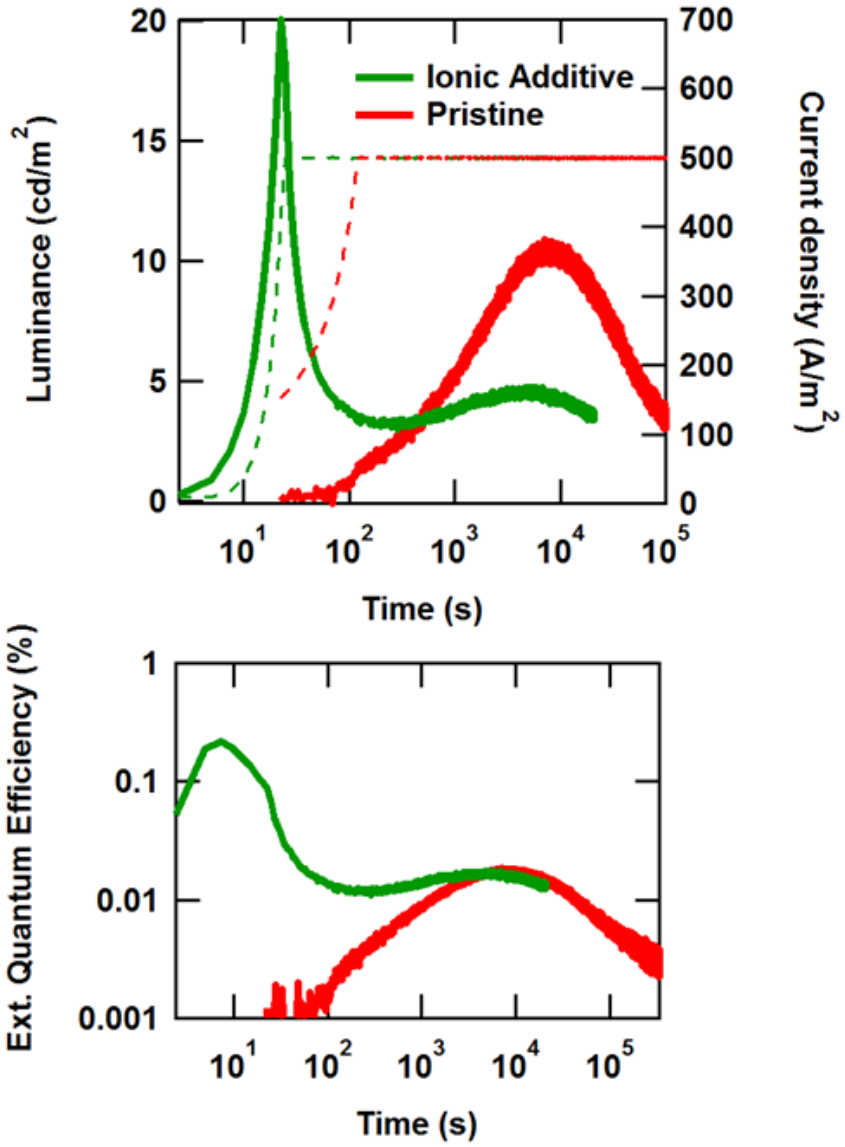

Figure 58. (Upper) Luminance (solid lines) and current density (dashed lines) vs. time plot of **11b** LEEC devices with (Ionic Additive) and without (Pristine) 0.3% $LiPF_6$ at 1.5 mA constant current (500 A/m^2 current density).

Interestingly, this ionic additive device exhibits a transient maximum that is followed by a second, more gradual increase to a maximum of 5 cd/m^2. The transient 20

cd/m^2 maximum occurs precisely at the transition from bias-limited to current-limited driving (Figure 58). That is, in the early stages of operation, the 10V bias compliance is reached as the devices are highly resistive. As ionic redistribution occurs, the device resistance is lowered as efficient charge injection is established. The rapid rise of the luminance is aided by the high potential across the device. When the current limit is reached, the bias must be lowered to maintain constant cur-rent. For an injection limited contact, decreasing the bias can exponentially lower the injected current, and so this lowered bias can decrease current balance, lowering luminance and efficiency until a new steady state is established. Interestingly, a second luminance peak emerges and decays on the same timescale of the pristine device, which likewise occurs under steady state conditions. This effect is not unique to these materials, as we have observed similar dynamics with some LEECs from mononuclear iridium complexes, particularly when large voltages are invoked for extended times. Dynamics are also likely impacted by the susceptibility of these materials to oxidative damage, as suggested by electrochemistry. Nonetheless, electroluminescence emerges, suggesting further improvements in stability could yield practical electro-luminescent materials.

Among small molecule LEECs,[40,97,102,105,106] other groups have followed the effects of binuclear complexes in LEECs. Leprêtre *et al.* investigated a binuclear ruthenium complex with the addition of lithium salts and crown ether solid electrolytes.[100] In this system, no luminance was observed with the pristine device, nor with lower amounts of the ether/salt mixture. Above a threshold of electrolyte/salt addition, the device operated at 0.02% external quantum efficiency. Wang *et al.* used a binuclear ruthenium complex to achieve near IR emission at 790 nm, but with efficiency estimated at 0.0005%.[103] Likewise, Wang *et al.* demonstrated bias-dependent emission from a copper complex, emitting 590 nm centered emission under forward bias and 618 nm emission under reverse bias.[93]

Absolute luminance and efficiency values were not reported. Costa *et al.* reported LEEC performance from a series of dumbbell-shaped dinuclear iridium complexes. Luminance was low (<10 cd/m^2), and a maximum quantum efficiency of 0.16% was observed from the series.[96] Thus, the performance of this dinuclear LEEC based on **11b** (maximum 20 cd/m^2, 0.22% external quantum efficiency) is noteworthy among this series.

CONCLUSIONS

In summary, square-planar Pt(II) complexes are very diverse in their applications ranging from chemosensors to materials in optoelectronic devices, and the unsaturated dz^2 orbital allows for the synthesis of red emitters via synthetically bringing two Pt(II) centers within close contact of each other. This synthetic modification allows for controlled access of the ^{3}MMLCT transition of these materials. A series of targeted pyrazolate-bridged dinuclear Pt(II) complexes were successfully synthesized with varying degrees of steric bulk imposed by the substitution of the 3- and 5-positions of the bridging pyrazolate ligands. The complexes were fully characterized and the electrochemical and photophysical properties were studied. There was a noticeable increase in the absorption spectra of the ^{3}MMLCT with increasing steric bulk imposed by the bridging-pyrazolate ligands. These complexes were highly luminescent in solution due to the synthetically accessed ^{3}MMLCT, with **11b** having the highest solution quantum yield of 86%. There was a noticeable bathochromic shift of the ^{3}MMLCT in the solution emission spectra when progressing from the most electron withdrawing bridging-pyrazolate ligand to the most electron donating bridging-pyrazolate ligand. Furthermore, there was a noticeable increase in the intensity of the ^{3}MMLCT in the steady-state frozen in 2-MeTHF glass at 77 K. However, there were no noticeable trends in the solid-state photophysics. Finally, in collaboration with Dr. Slinker at UT-Dallas, **11b** was used as the emitter in a light-emitting

electrochemical cell. The device made with **11b** and used $LiPF_6$ as an ionic additive exhibited a maximum luminescence of 20 cd/m^2 and an external quantum efficiency of 0.22%, making the performance of the device noteworthy among other dinuclear based LEEC devices.

Chapter 4: Crystallographic Study of Various Organic Molecules and Transition Metal Complexes

INTRODUCTION

Single crystal x-ray crystallography is a technique which can provide valuable chemical information on materials in the solid-state such as structure elucidation, bond distances and angles, intermolecular interactions such as hydrogen bonding, pi-stacking, and elemental identification. However, the sample must be crystalline where long-range, three-dimensional internal order is present.

This long-range, three-dimensional order is related within crystals by symmetry, which determines the space group of the crystals. Crystallographic symmetry consists of point symmetry elements such as identity, mirror planes, proper and improper rotation axes, and inversion centers. Allowed combinations of these symmetry elements are considered point groups. In total, there are 32 possible crystallographic point groups that can fill space. In addition to these point symmetry elements are translational symmetry. Translational symmetry consists of unit cell translations, centering translations, screw axes, and glide planes. When the 32 possible crystallographic point groups are combined with unit cell and centering translations, 73 symmorphic space groups are derived. A symmorphic space group is, apart from lattice translations, when all generating symmetry operations leave one common point fixed.[114] An additional 157 space groups can be derived by replacing rotation axes with screw axis and mirror planes with glide planes. This, in total, allows for 230 possible space groups in which all crystal systems fit.[115]

The fundamental building block for a crystalline solid is the unit cell, which is characterized by key dimensions (a, b, and c cell axes as well as the α, β, and γ angles between the cell axes), the symmetry present within the unit cell, and the atoms/molecules that are present. The unit cell is comprised of the asymmetric units of the crystal and is

related to all other unit cells within the crystal only through translation. The asymmetric unit is the fundamental building block of the unit cell, and contains the formula unit which is the component that is solved for and refined in the structural model generated to match the experimentally determined diffraction data.[115]

The symmetry within a crystal, as well as the location and atom identity of the asymmetric unit can be determined via diffraction experiments. In the diffraction experiment, an incident x-ray beam is directed at the crystalline solid, upon which electrons within the atoms scatter the x-ray radiation. Present within crystals are Miller indices or planes, and the vector normal to these planes generates points in reciprocal space, which in turn comprises the reciprocal lattice. The reciprocal lattice determines the location of the diffracted beams. Therefore, by investigation of the diffracted beams from the diffraction experiment, information is provided about the unit cell of the crystal. Furthermore, the diffracted beams also provide positional and intensity data that is used to develop the crystallographic model used for structure determination. Using a suitable detector, the location and intensities of the diffracted beams can be measured. The location of the beams provides information about the symmetry present within the crystal while the intensity of the beams provides information about the grouping of the atoms being repeated. By changing the angle at which the incident x-ray beam interacts with the crystal (or more accurately by rotating the crystal to achieve the same effect), a three-dimensional model of the asymmetric unit of the sample can be determined.[116]

EXPERIMENTAL

Crystal Structure Determination

Crystallographic data for compounds **12-17** and complexes **18-38** are given in Table S7-S34. Single crystals of **12** and **37** were grown via vapor diffusion of Et_2O into

separate solutions of **12** and **37** in MeCN. Single crystals of **14** were grown via slow evaporation of a 30% CH_2Cl_2/70% hexane solution (v/v) of **14**. Single crystals of **15** were grown from slow layer diffusion of hexane into a solution of **15** in CH_2Cl_2. Single crystals of **16** were grown via slow evaporation of an acetone solution of **16**. Single crystals of **17** were grown via slow evaporation of a saturated solution of **17** in CH_2Cl_2. Single crystals of **18-27** and **37** were grown via slow vapor diffusion of Et_2O into separate solutions of **18-27** and **37** in CH_2Cl_2. Single crystals of **28** were grown via slow evaporation of a EtOH/H_2O solution of **28**. Single crystals of **29a** and **29b** were grown via slow evaporation of **29a** and **29b** in phenylimidizole. Single crystals of **30** were grown via slow diffusion of pentane layered of a solution of **30** in CH_2Cl_2. Single crystals of **31** were grown via slow vapor diffusion of cyclohexane into a solution of **31** in 1,2-dichloroethane. Single crystals of **32** were grown via slow evaporation of **32** dissolved in MeCN. Single crystals of **33-35** were grown from slow vapor diffusion of pentane into separate solutions of **33-35** dissolved in CH_2Cl_2/1,2-dichloroethane (1:1 v/v). Single crystals of **38** were grown via slow diffusion of a solution of **38** dissolved in acetone layered with pentane. Crystals were covered in a Paratone/chloroform mixture and mounted on a nylon thread loop for the diffraction experiments.

Data were collected for **12**, **16**, **19**, **20**, **24-26**, **28**, **30**, **31**, **34**, and **37** at 100 K on an Agilent Technologies SuperNova Dual Source diffractometer equipped with an AtlasS2 CCD detector using a μ-focus Cu Kα radiation source (λ = 1.5418 Å) and an Oxford 700 Cryostream system. Data collection, unit cell refinement, and data reduction of **12**, **16**, **19**, **20**, **24-26**, **28**, **30**, **31**, **34**, and **37** were performed using Agilent Technologies CrysAlisPro software. Data was collected for **13**, **18**, **21**, **23**, **27**, and **32** at 120 K and **38** at 133 K on a Bruker-Nonius Kappa diffractometer equipped with a Bruker Apex II CCD detector using a μ-focus Mo Kα radiation source (λ = 0.7107 Å) and an Oxford 600 series Cryostream

system. Data collection, unit cell refinement, and data reduction of **13**, **18**, **21**, **23**, **27**, **32** and **38** were performed using Bruker's Apex II software. Data were collected for **14**, **22**, **33**, and **36** at 100 K on a Rigaku AFC-12 diffractometer equipped with a Saturn 724+ CCD detector using a μ-focus Mo Kα radiation source (λ = 0.7107 Å) and a Rigaku XStream low-temperature system. Data collection, unit cell refinement, and data reduction of **14**, **22**, **33**, and **36** were performed using Rigaku's CrystalClear software. Data was collected for **15** and **37** at 100 K on a Rigaku SCX-Mini diffractometer equipped with a Mercury 2+ CCD detector using a μ-focus Mo Kα radiation source (λ = 0.7107 Å) and a Rigaku XStream low-temperature system. Data collection, unit cell refinement, and data reduction of **15** and **37** were performed using Rigaku's CrystalClear software. Data was collected for **17**, **29a** and **29b** at 120 K on a Kappa APEX duo equipped with a Bruker Apex II CCD detector using a μ-focus Mo Kα radiation source (λ = 0.7107 Å). Data collection, unit cell refinement, and data reduction of **17**, **29a** and **29b** were performed using Bruker's Apex III software.

The structures of **12-38** were solved by direct methods using the SIR2014 program and refined by full-matrix least-squares on F^2 with anisotropic displacement parameters for all non-H atoms using SHELXL-2014. The structural analyses were performed using the PLATON98 and WinGX programs. The hydrogen atoms were placed in fixed, calculated positions with isotropic displacement parameters set to 1.2 x U_{eq} with respect to the attached atom. Crystallographic images were created using the Cambridge Crystallographic Data Centre's Mercury software and rendered using POV-ray. All bond angles, torsion angles, and intermolecular interactions were calculated using the Cambridge Crystallographic Data Centre's Mercury software. The intermolecular interactions are calculated by the Mercury software by looking for atoms within close contact of each other based on their Van der Waal's radii plus 0.15 Å.

RESULTS AND DISCUSSION

Molecular and Single Crystal Structures of Organic Molecules 12-17

Crystallography of LEEC Ionic Additives

Table 6. Molecular formula and crystallographic importance of **12**.

Compound	Molecular Formula	Synthesized By	Crystallographic Importance
12	$[C_{25}H_{19}N_2][BF_4]$	Matthew Moore	F-H, F-N interactions

The molecular structure and crystal packing of **12** are shown below in Figure 59. The molecular structure of **12** shows each phenyl group having an average torsion angle of 117.8 ± 11.6 degrees away from the plane of the 1H-benzo[d]imidazole moiety. The crystal structure of **12** is in the monoclinic space group P2/c with Z = 4. The packing of **12** shows six BF_4^- counter anions, four of which are cut in half by the unit cell axis, making for a total of four BF_4^- counter anions. There are short contacts between the fluorine atoms on the BF_4^- counter ions, and the hydrogen atoms on the phenyl rings and the nitrogen atoms of **12**. The crystal structure of **12** does not show any π-π interactions between any of the aromatic moieties, presumably due to the BF_4^- counter anions sitting in-between different the molecules of **12**.

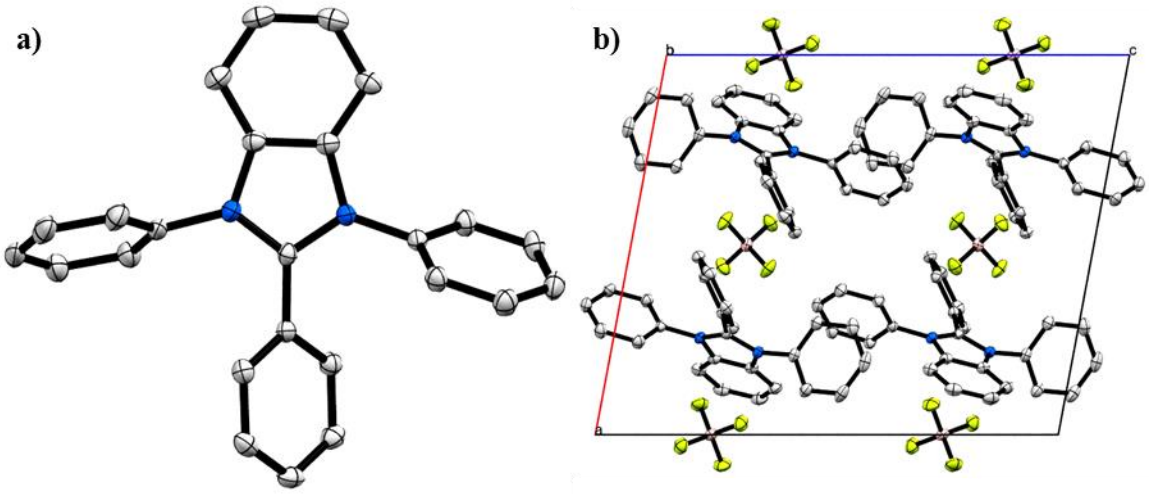

Figure 59. a) Molecular structure of **12** (50% thermal ellipsoid probability). BF_4^- counter ions removed for clarity. b) Crystal packing of **12** (50% thermal ellipsoid probability) looking down the b-axis.

Table 7. Molecular formula and crystallographic importance of **13**.

Compound	Molecular Formula	Synthesized By	Crystallographic Importance
13	$[C_{25}H_{19}N_2][BF_4]$	Matthew Moore	F-H, F-N interactions

The molecular structure and single crystal packing of **13** are shown below in Figure 60. The molecular structure of **13** shows each phenyl group having an average torsion angle of 121.1 ± 14.9 degrees away from the plane of the 1H-benzo[d]imidazole moiety, which is similar to the structure of **12**. The crystal structure of **13** is in the monoclinic space group $P2_1/c$ with Z = 4. Like the crystal structure of **12**, there are short contacts between the fluorine atoms on the BF_4^- counter ions and the nitrogen atoms on the 1H-benzo[d]imidazole moiety, which causes column type packing in the structure where each

molecule of **13** is rotated by 180 degrees (Figure 60). The crystal structure of **13** does not show any π-π interactions between any of the aromatic moieties, presumably due to the BF_4^- counter anions sitting in-between different the molecules of **13**.

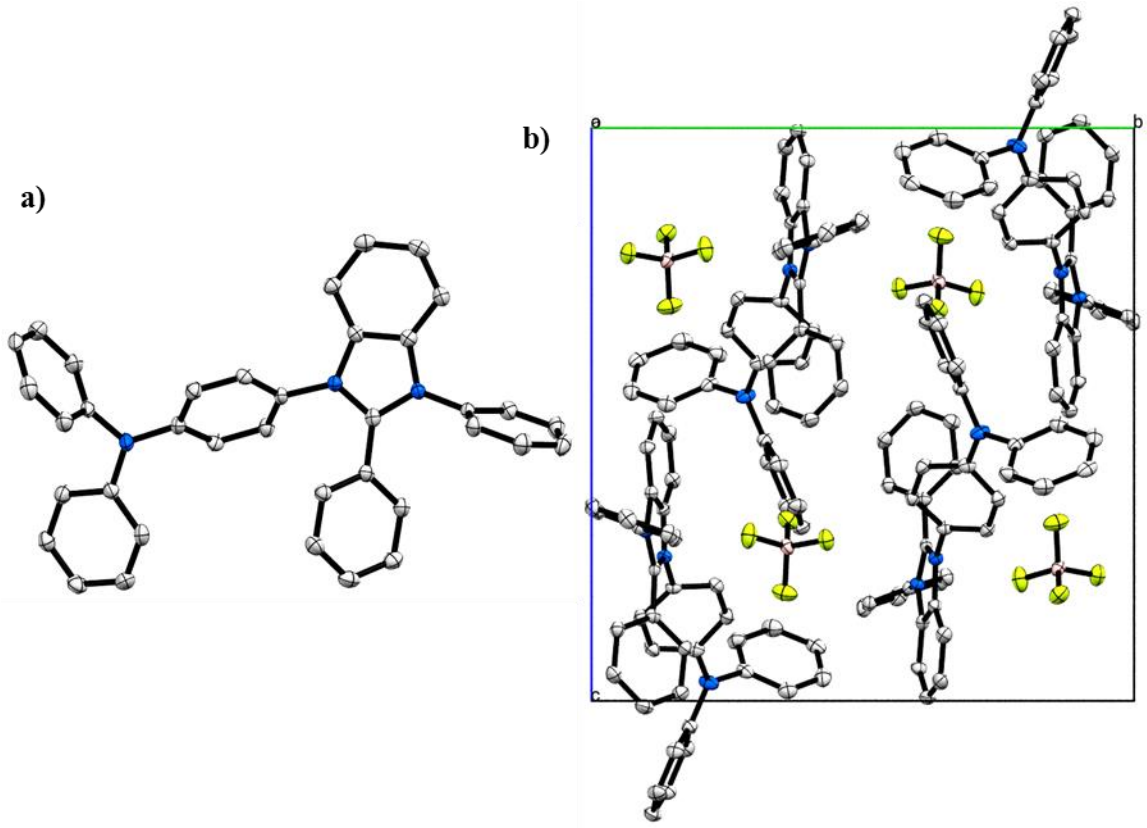

Figure 60. a) Molecular structure of **13** (50% thermal ellipsoid probability). BF_4^- counter ions removed for clarity. b) Crystal packing of **13** (50% thermal ellipsoid probability) looking down the a-axis.

Crystallography of Novel Bisphosphine Ligand

Table 8. Molecular formula and crystallographic importance of **14**.

Compound	Molecular Formula	Synthesized By	Crystallographic Importance
14	$C_{34}H_{28}P_2S_2$	Kory Mueller	F-S interactions

The molecular structure and single crystal packing of **14** are shown below in Figure 61. The molecular structure of **14** shows a torsion angle of 132.1 degrees between the two thiophene moieties. This is likely due to the steric bulk imposed by the diphenylphosphine groups bound to the 4-position of each thiophene. The crystal structure of **14** is in the triclinic space group P-1 with Z = 2. The crystal structure of **14** shows short contacts between the hydrogens on the diphenylphosine moieties of one molecule of **14** and the sulfur atoms on the bithiophene core of another molecule of **14**. The crystal structure of **14** does not show any π-π interactions between any of the aromatic moieties, but there are short contacts between the hydrogens on the diphenylphosphine groups of adjacent molecules of **14**.

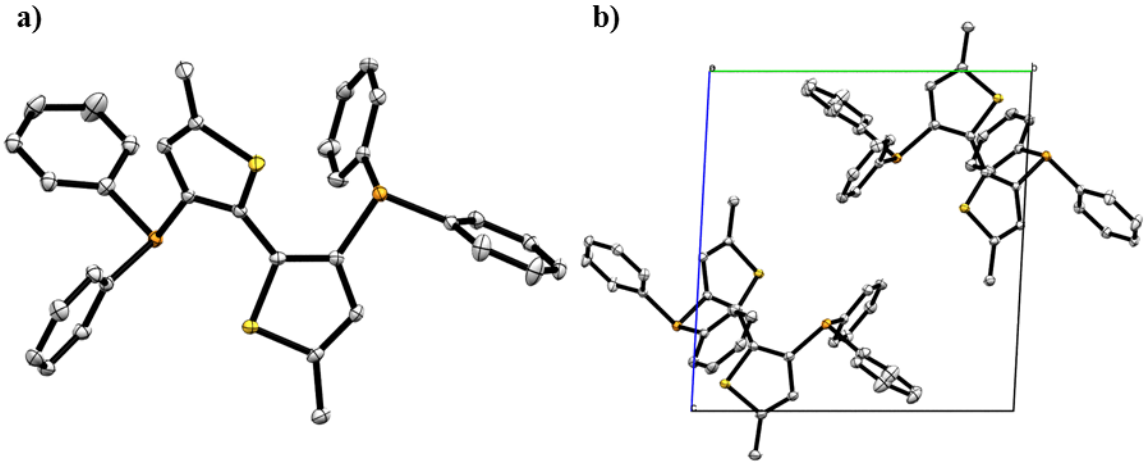

Figure 61. a) Molecular structure of **14** (50% thermal ellipsoid probability). b) Crystal packing of **14** (50% thermal ellipsoid probability) looking down the a-axis.

Crystallography of Lanthanide Chelating Ligands

Table 9. Molecular formula and crystallographic importance of **15**.

Compound	Molecular Formula	Synthesized By	Crystallographic Importance
15	$C_{25}H_{19}N_7O_6S_2$	Dan Strohecker	Intermolecular hydrogen bonding C-O, π-π interactions

The molecular structure and single crystal packing of **15** are shown below in Figure 62. The pyrazole moieties of the 2,6-bis(5-pyrazolyl)pyridine show an average torsion angle of 6.2 ± 2.0 degrees away from the pyridine moiety which is expected due to the favorable conjugation between the three groups. The amide 3,4-ethylenedioxythiophene

groups show an average torsion angle of 176.2 ± 1.5 degrees away from the 2,6-bis(5-pyrazolyl)pyridine core of the molecule. There is intermolecular hydrogen bonding between the oxygen atoms and the hydrogen atoms of the amide groups which keeps the molecule essentially flat. The crystal structure of **15** is in the triclinic space group P-1 with Z = 2. The solid-state packing of **15** is dominated by π-π interactions of 3.4 Å between the 2,6-bis(5-pyrazolyl)pyridine core of adjacent molecules (Figure 63). The crystal structure of **15** also shows short contacts between the carbon atoms of the ethyl moiety on the 3,4-ethylenedioxythiophene groups and the oxygen atom of the amide moiety on adjacent molecules of **15**.

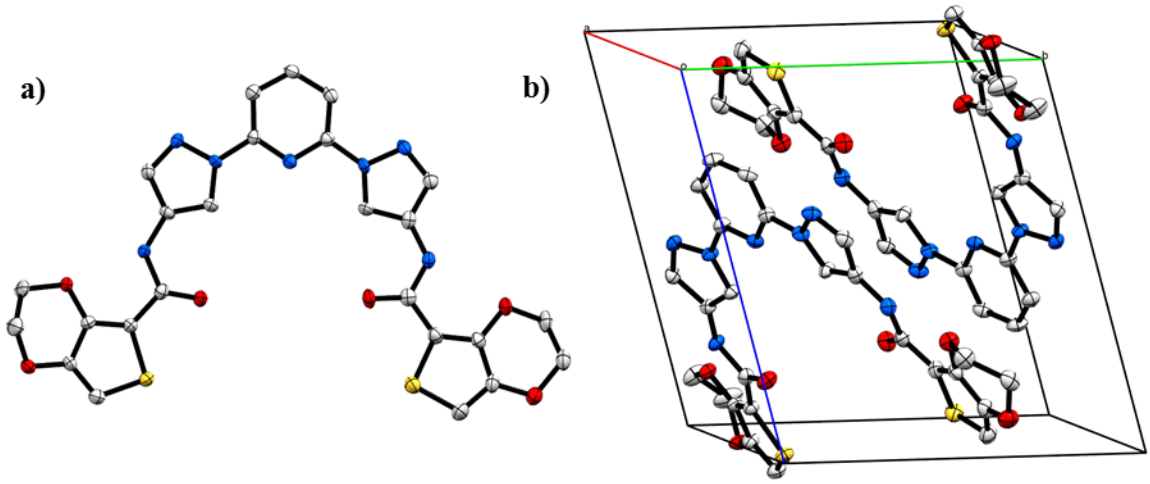

Figure 62. a) Molecular structure of **15** (50% thermal ellipsoid probability). b) Crystal packing of **15** (50% thermal ellipsoid probability).

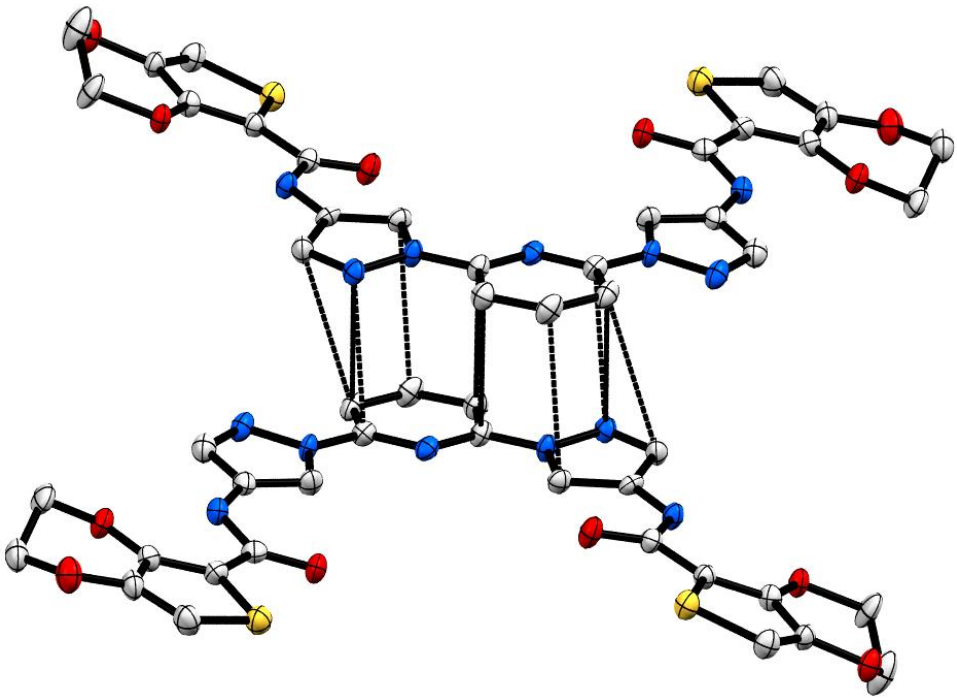

Figure 63. Pi-stacking between two 2,6-bis(5-pyrazolyl)pyridine moieties of **15**.

Table 10. Molecular formula and crystallographic importance of **16**.

Compound	Molecular Formula	Synthesized By	Crystallographic Importance
16	$C_{27}H_{23}N_7O_6S_2$	Dan Strohecker	O-H, O-C interactions

The molecular structure and single crystal packing of **16** are shown below in Figure 64. The molecular structure of **16** shows one of the methylamide moieties twisted away from the main plane of the 2,6-bis(5-pyrazolyl)pyridine moiety with a torsion angle of 58.0 degrees. The 3,4-ethylenedioxythiophene group bound to the twisted methylamide moiety is twisted even further with a torsion angle of 49.3 degrees. The methylamide moiety on

bound to the other side of the 2,6-bis(5-pyrazolyl)pyridine core shows only a slight torsion angle of 2.9 degrees away from the 2,6-bis(5-pyrazolyl)pyridine core. The 3,4-ethylenedioxythiophene group bound to this methylamide shows a torsion angle of 55.7 degrees. Overall, in comparison to the structure of **15**, **16** is much more twisted. This is likely due to the methyl group on the methylamide moieties breaking the favorable hydrogen bonds between the oxygen atoms on the 3,4-ethylenedioxythiophene groups and the amide moieties. The crystal structure of **16** is in the monoclinic space group $P2_1/n$ with Z = 4. There are short contacts between the 3,4-ethylenedioxythiophene groups of adjacent molecules of **16** as well as between the 3,4-ethylenedioxythiophene groups of one molecule and the 2,6-bis(5-pyrazolyl)pyridine core of an adjacent molecule.

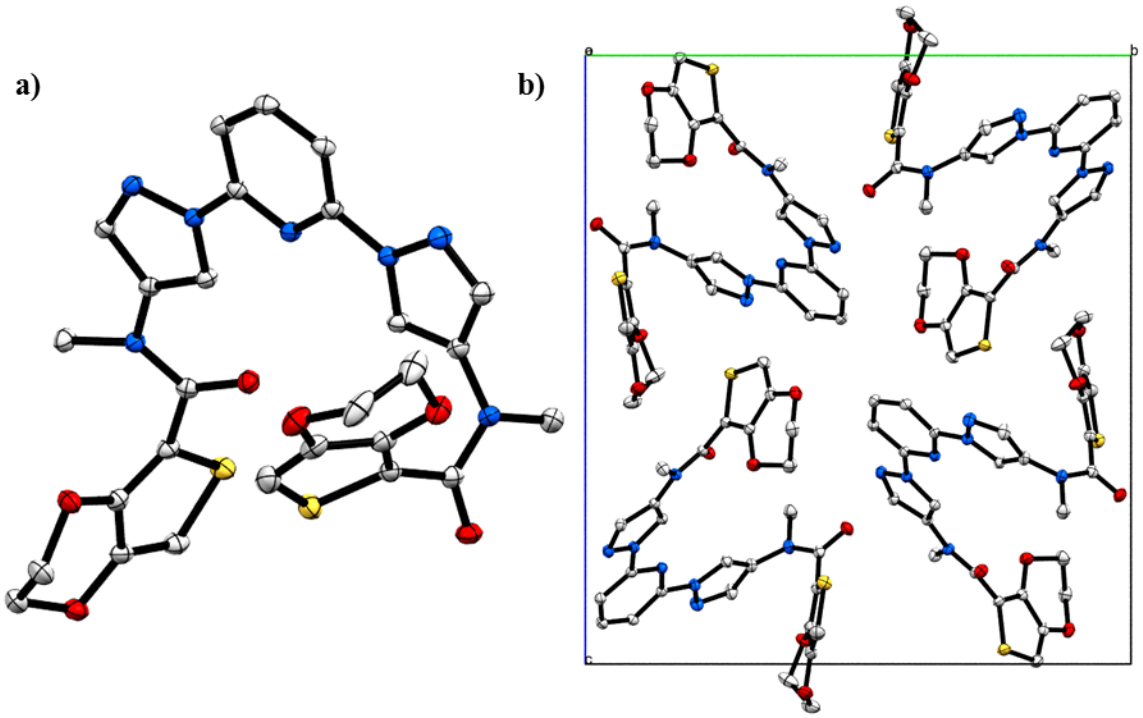

Figure 64. a) Molecular structure of **16** (50% thermal ellipsoid probability). b) Crystal packing of **16** (50% thermal ellipsoid probability) looking down the a-axis.

Crystallography of 4,6-diiodoresorcinol

Table 11. Molecular formula and crystallographic importance of **17**.

Compound	**Molecular Formula**	**Synthesized By**	**Crystallographic Importance**
17	$C_6H_4I_2O_2$	Leander Cinninger	Hydrogen bonding π-π, I-I, I-π, I-H interactions

The molecular structure and single crystal packing of **17** are shown below in Figure 65. The crystal structure of **17** is in the monoclinic space group $P2_1/n$ with Z = 8. The unit cell of **17** is essentially plate like in appearance, with unit cell lengths of a = 15.29 Å, b = 4.56 Å, and c = 23.86 Å. The crystal structure of **17** is dominated by hydrogen bonding, π-π interactions of 3.5 Å, short iodine-iodine contacts of 3.9 Å, iodine-π interaction of 3.9 Å, and iodine-hydrogen interactions of 3.1 Å (Figure 66 and Figure 67).

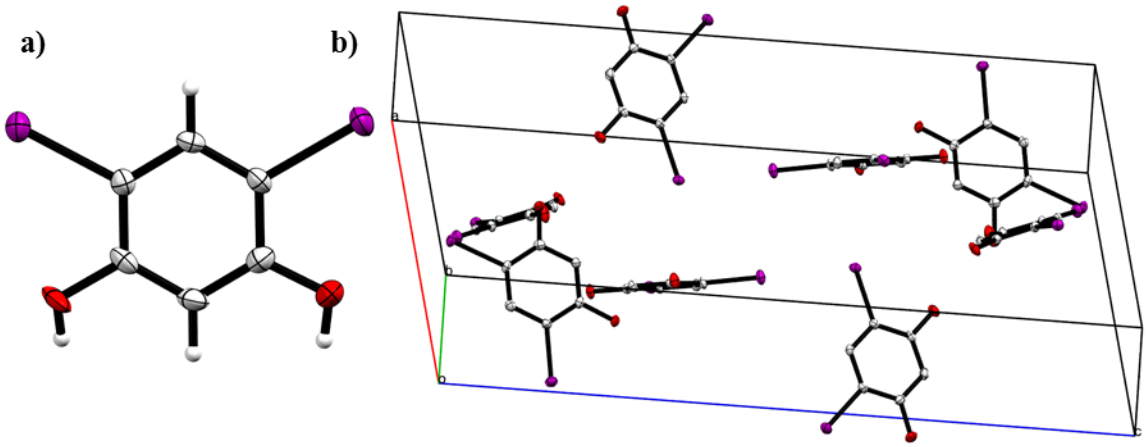

Figure 65. a) Molecular structure of **17** (50% thermal ellipsoid probability). b) Crystal packing of **17** (50% thermal ellipsoid probability).

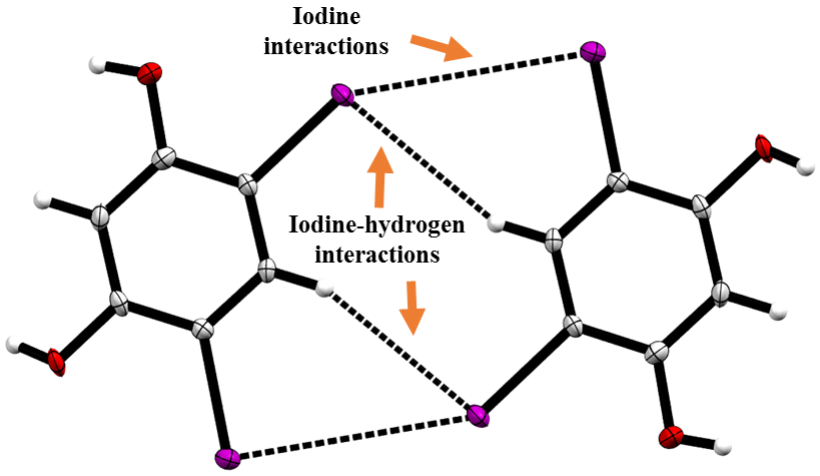

Figure 66. Crystal packing of **17** showing iodine-iodine interactions and iodine-hydrogen interactions.

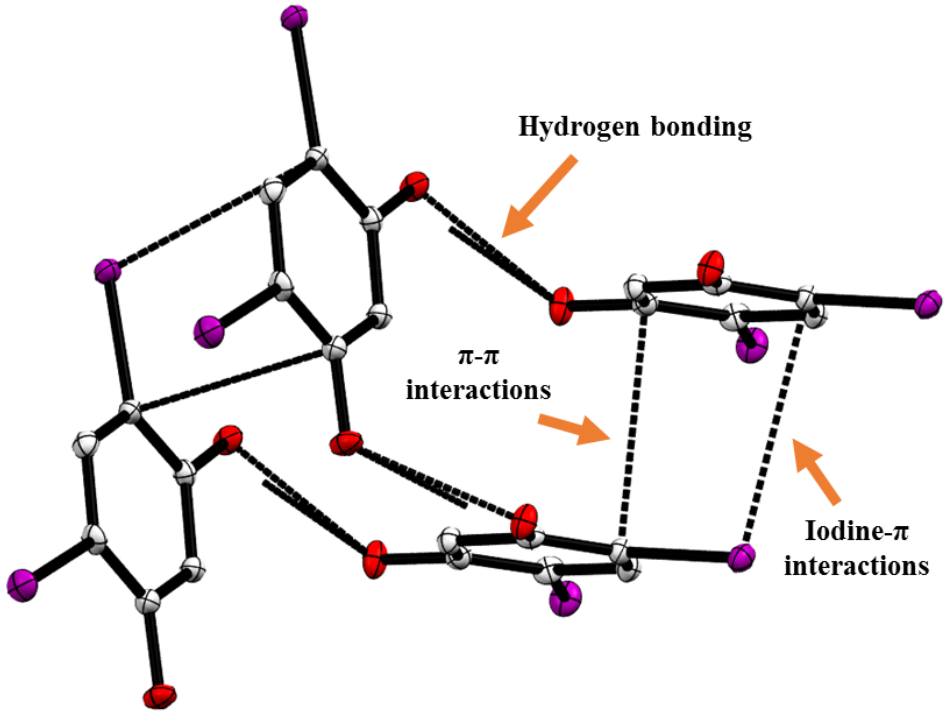

Figure 67. Crystal packing of **17** showing hydrogen bonding, π-π interactions, and iodine-π interactions.

Molecular and Single Crystal Structures of Transition Metal Complexes 18-38

Crystallography of Ag(I) Complex

Table 12. Molecular formula and crystallographic importance of **18**.

Compound	Molecular Formula	Synthesized By	Crystallographic Importance
18	$C_{48}H_{54}AgO_4N_6$	Rob Fimognari	F-H, π-π interactions

The molecular structure and single crystal packing of **18** are shown below in Figure 68 and Figure 69. The molecular structure of **18** shows the Ag(I) atom bound to two N-heterocyclic carbenes in a linear fashion. The phenyl rings of the phenylimidizole core display a torsion angle of 45.4 degrees away from the imidazole moiety. The norbornene moieties are bent back toward the maleimide groups by 114.1 degrees. The crystal structure of **18** is in the monoclinic space group C2/c with Z = 8. The crystal displays a base-centered Bravais lattice with the Ag atoms sit at the lattice points. There is also an additional Ag atom located at the center of the unit cell. There are fluorine-hydrogen interactions between the fluorine atoms of the PF_6^- counter anion and the hydrogens on the phenylimidizole core as well as between the fluorine atoms on the PF_6^- counter anion and the hydrogen atoms on the norbornene moieties. The PF_6^- counter anions sits in pockets between multiple molecules of **18**, where there are favorable fluorine-hydrogen interactions (Figure 69). There are also π-π interactions of 3.3 Å between the phenyl groups of the phenylimidizole cores of adjacent molecules of **18**.

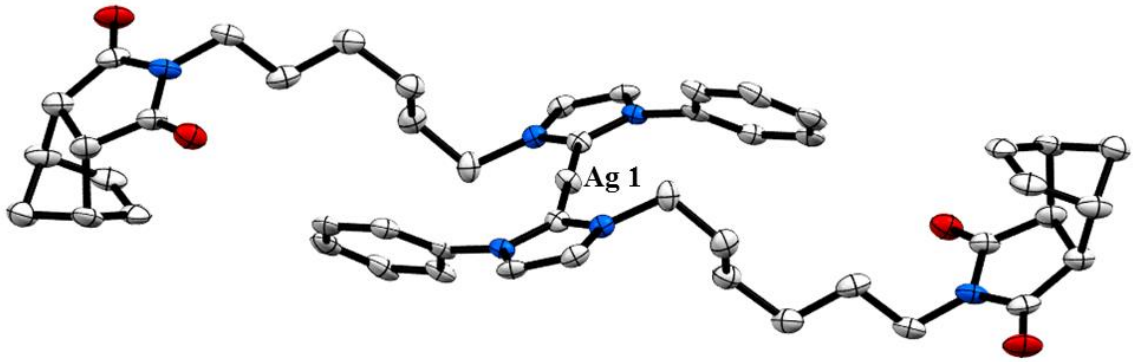

Figure 68. Molecular structure of **18** (thermal ellipsoid probability 50 %).

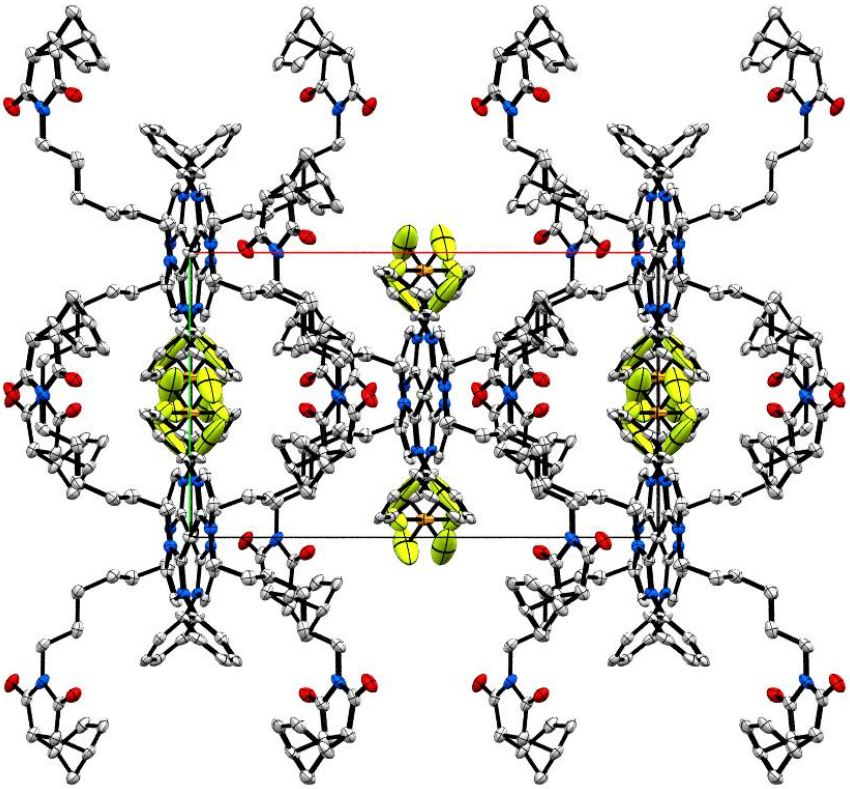

Figure 69. Crystal packing of **18** (thermal ellipsoid probability 50%) looking down the c-axis.

Crystallography of Cu(I) and Cu(II) Complexes

Table 13. Molecular formula and crystallographic importance of **19**.

Compound	Molecular Formula	Synthesized By	Crystallographic Importance
19	$[C_{39}H_{34}N_3P_2Cu][PF_6]$	Kory Mueller	F-H interactions

The molecular structure and single crystal packing of **19** are shown below in Figure 70. The molecular structure of **19** shows the Cu(I) atom bound in a tetrahedral geometry with the 1,2-bis(diphenylphosphino)benzene ligand having a bite-angle of 91.7 degrees and the 2-(3-methyl-1H-pyrazol-1-yl)pyridine ligand having a bite angle of 90.3 degrees. The phenyl groups of the 1,2-bis(diphenylphosphino)benzene ligand show an average torsion angle of 49.4 ± 28.4 degrees away from the benzene backbone. The crystal structure of **19** is in the monoclinic space group $P2_1/c$ with Z = 4. The crystal structure of **19** is dominated by fluorine-hydrogen interactions between the PF_6^- counter anions and the hydrogen atoms on the 1,2-bis(diphenylphosphino)benzene ligand and the methylpyrazolpyridine ligand (Figure 71).

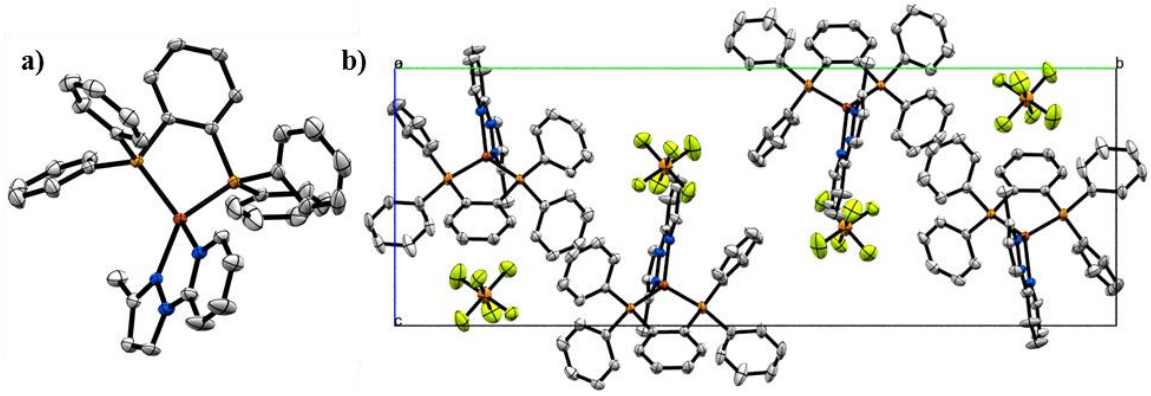

Figure 70. a) Molecular structure of **19** (50% thermal ellipsoid probability). PF_6^- counter anion removed for clarity. b) Crystal packing of **19** (50% thermal ellipsoid probability) looking down the a-axis.

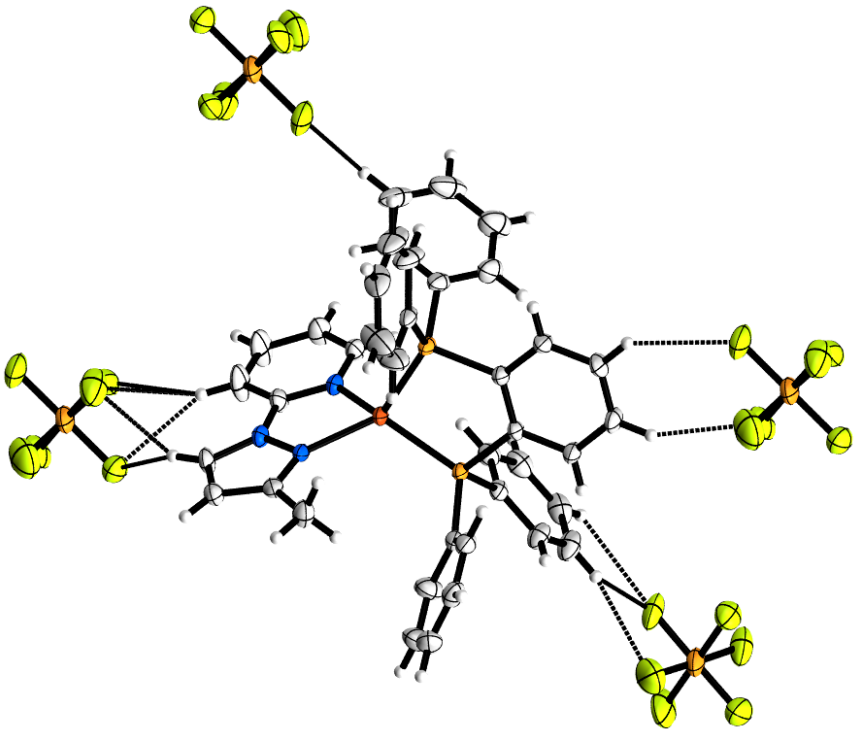

Figure 71. Fluorine-hydrogen interactions in **19** between the PF_6^- counter anions and the bis(diphenylphosphino)benzene ligand and the methylpyrazolpyridine ligand.

Table 14. Molecular formula and crystallographic importance of **20**.

Compound	Molecular Formula	Synthesized By	Crystallographic Importance
20	$[C_{38}H_{31}N_3P_2Cu][PF_6]$	Kory Mueller	π-π, F-H interactions

The molecular structure and single crystal packing of **20** are shown below in Figure 72. The molecular structure of **20** shows the Cu(I) atom bound in a tetrahedral geometry with the 1,2-bis(diphenylphosphino)benzene ligand having a bite angle of 89.0 degrees and

the 2-(1H-pyrazol-1-yl)pyridine ligand having a bite angle of 80.1 degrees. If considering the binding of the 1,2-bis(diphenylphosphino)benzene ligand with the Cu(I) atom to form a 5-membered ring consisting of Cu^P^C^C^P, this ring shows a distorted binding geometry with the Cu(I) center displaying a torsion angle of 24.8 degrees out of the plane of the P^C^C^P, which differs from the binding geometry of the Cu^P^C^C^P ring in **19** which is essentially flat (Figure 73). The crystal structure of **20** is in the monoclinic space group I2/a with Z = 8. The crystal structure is dominated by offset π-π interactions of ~3.5 Å, t-shaped π-π interactions of ~3.7 Å, and fluorine-hydrogen interactions of ~3.0 Å. The offset π-π interactions occur between phenyl rings on the 1,2-bis(diphenylphosphino)benzene ligands of adjacent molecules of **20**. The t-shaped π-π interactions occur between the phenyl rings of two different bis(diphenylphosphino)benzene ligands, as well as between the bis(diphenylphosphino)benzene ligand of one molecule of **20** and the phenylpyrazole of another molecule of **20**. The fluorine-hydrogen interactions occur between various different hydrogens on the molecules of **20** that surround the PF_6^- counter anions.

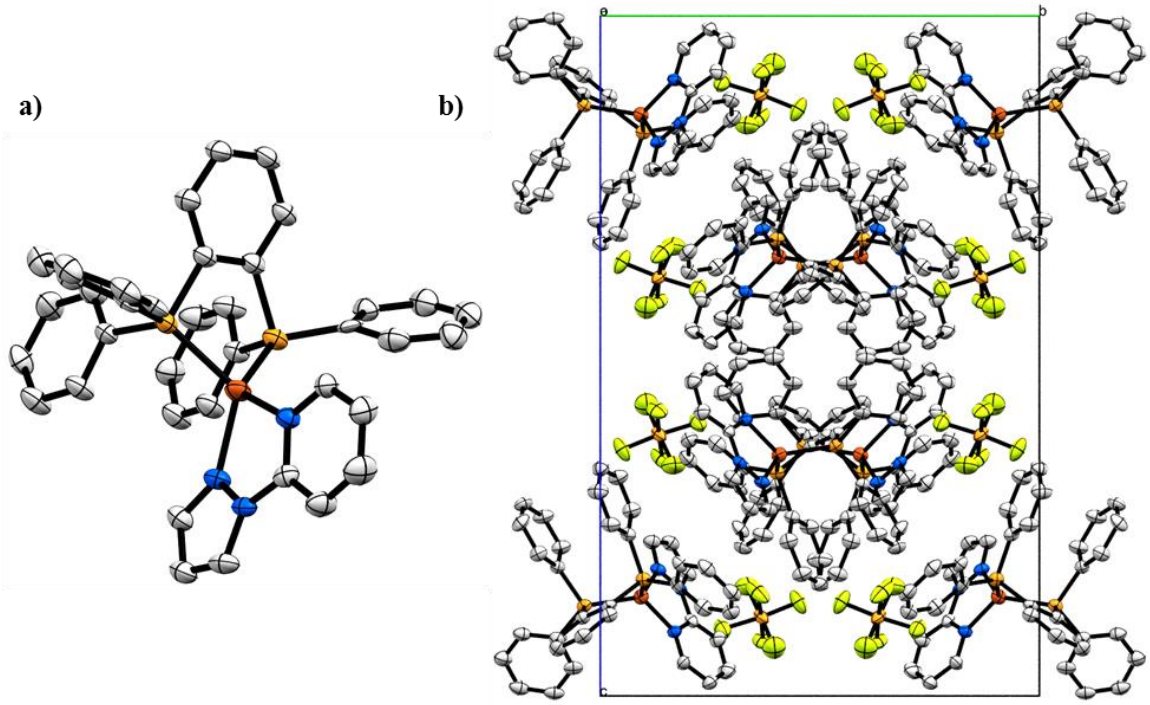

Figure 72. a) Molecular structure of **20** (50% thermal ellipsoid probability). PF_6^- counter anion removed for clarity. b) Crystal packing of **20** (50% thermal ellipsoid probability) looking down the a-axis.

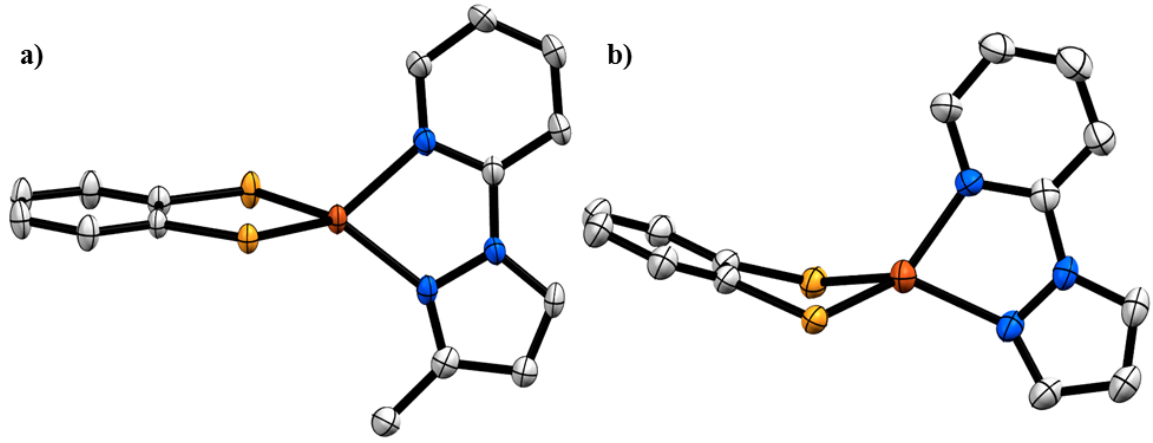

Figure 73. Binding distortion of the 1,2-bis(diphenylphosphino)benzene ligand in a) **19** and b) **20**. Phenyl rings on the 1,2-bis(diphenylphosphino)benzene ligands were removed for clarity.

Table 15. Molecular formula and crystallographic importance of **21**.

Compound	Molecular Formula	Synthesized By	Crystallographic Importance
21	$[C_{43}H_{34}F_3N_3P_2S_2][PF_6]$	Kory Mueller	F-F, F-H, F-S, S-H interactions

The molecular structure and single crystal packing of **21** are shown below in Figure 74. The molecular structure of **21** shows the Cu(I) center bound in a distorted tetrahedral coordination geometry. The (5,5'-dimethyl-[2,2'-bithiophene]-3,3'-diyl)bis(diphenylphosphane) ligand shows a bite angle of 108.4 degrees and the 2-(3-(trifluoromethyl)-1H-pyrazol-1-yl)pyridine ligand shows a bite angle of 78.1 degrees. The larger bite angle of the (5,5'-dimethyl-[2,2'-bithiophene]-3,3'-diyl)bis(diphenylphosphane) ligand, when compared to the bite angle of the 1,2-bis(diphenylphosphino)benzene ligands in **19** and **20** is not surprising due to the 2,2'-bithiophene moiety spacing the phosphines farther apart. The added flexibility of the (5,5'-dimethyl-[2,2'-bithiophene]-3,3'-diyl)bis(diphenylphosphane) ligand also causes the 2,2'-bithiophene moiety to be bent away from the Cu(I) center toward the trifluoromethyl group on the 2-(3-(trifluoromethyl)-1H-pyrazol-1-yl)pyridine ligand. However, there is no intermolecular fluorine interactions between the trifluoromethyl group and the (5,5'-dimethyl-[2,2'-bithiophene]-3,3'-diyl)bis(diphenylphosphane) ligand. The crystal structure of **21** is in the monoclinic space group $P2_1/c$ with Z = 4. The crystal structure also shows acetone solvent molecules within the solid-state packing. The crystal structure of **21** shows fluorine-fluorine interactions of ~3.0 Å, fluorine-hydrogen interactions of ~2.8 Å, fluorine-sulfur interactions of 3.3 Å, and sulfur-hydrogen interactions of ~2.9 Å. The fluorine-fluorine interactions are between the

PF_6^- counter anion and the trifluoromethyl groups on **21**. The fluorine-hydrogen interactions occur between the PF_6^- counter anion and the hydrogens on adjacent molecules of **21**. The fluorine-sulfur interactions occur between the sulfur atoms on the 2,2'-bithiophene moiety of **21** and the PF_6^- counter anions. The sulfur-hydrogen interactions occur between the sulfur atoms on the 2,2'-bithiophene moiety of **21** and the methyl group of the 2-(3-(trifluoromethyl)-1H-pyrazol-1-yl)pyridine ligand of an adjacent molecule of **21** as well as with the hydrogen atoms of the phenyl groups on the (5,5'-dimethyl-[2,2'-bithiophene]-3,3'-diyl)bis(diphenylphosphane) ligands of adjacent molecules of **21**. The acetone solvent molecules sits stacked in the space between the 2-(3-(trifluoromethyl)-1H-pyrazol-1-yl)pyridine ligand of two molecules of **21** which are turned back-to-back, if one considers the 2-(3-(trifluoromethyl)-1H-pyrazol-1-yl)pyridine ligand to be the back of **21** (Figure 75).

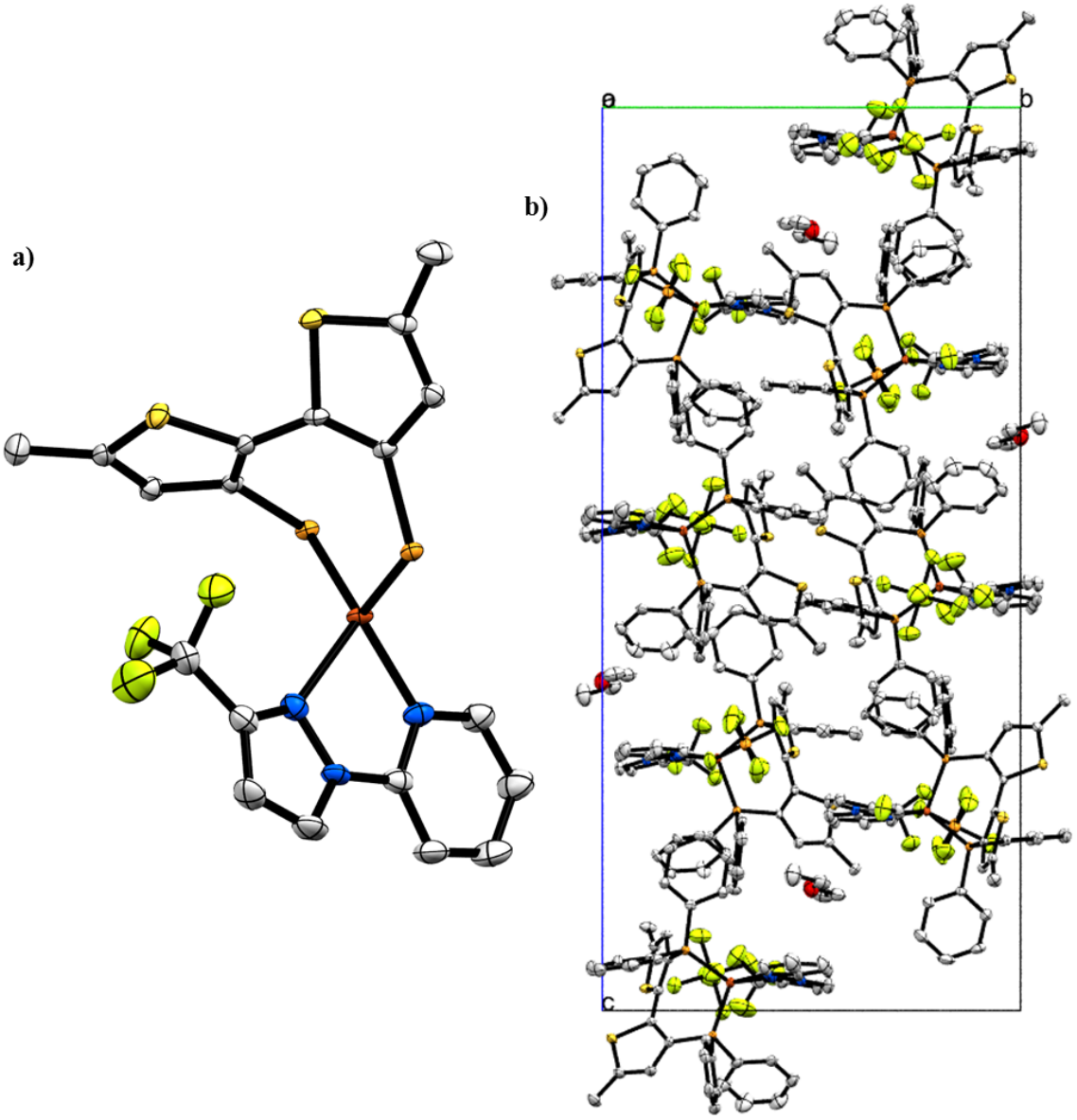

Figure 74. a) Molecular structure of **21** (50% thermal ellipsoid probability). Phenyl rings on the (5,5'-dimethyl-[2,2'-bithiophene]-3,3'-diyl)bis(diphenylphosphane) ligand were removed for clarity. b) Crystal packing of **21** (50% thermal ellipsoid probability) looking down the a-axis.

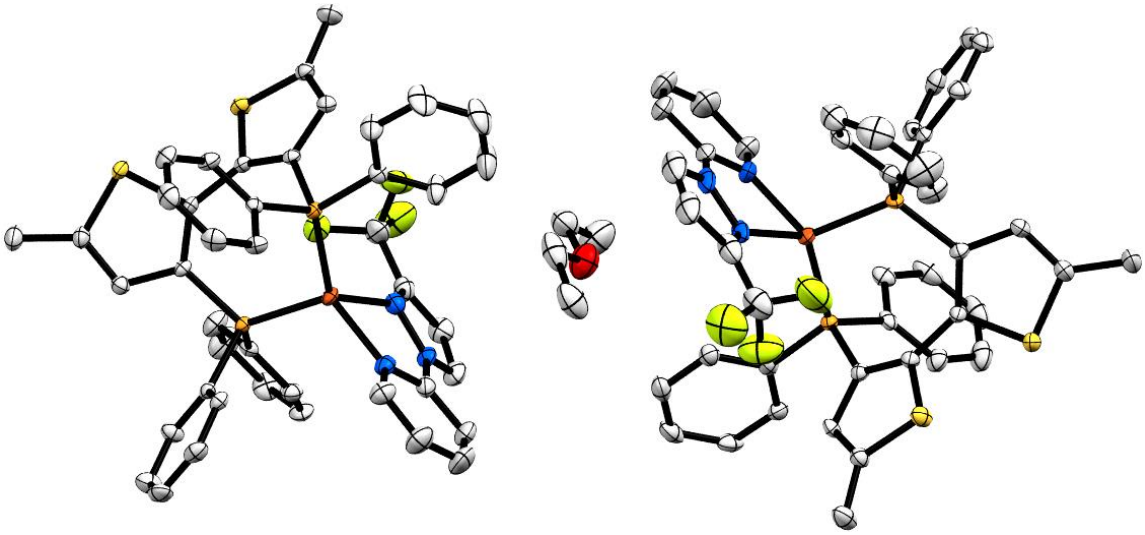

Figure 75. Picture showing the location of the acetone solvent molecule in the crystal structure of **21**.

Table 16. Molecular formula and crystallographic importance of **22**.

Compound	Molecular Formula	Synthesized By	Crystallographic Importance
22	$[C_{82}H_{68}Cu_2N_2P_4S_4]2[PF_6]$	Kory Mueller	F-S, F-H, S-C, O-H, π-π interactions

The molecular structure and single crystal packing of **22** are shown below in Figure 76 and Figure 77. The molecular structure of **22** shows an asymmetric dinuclear Cu(I) complex with one Cu(I) center bound to a (5,5'-dimethyl-[2,2'-bithiophene]-3,3'-diyl)bis(diphenylphosphane) ligand and the other Cu(I) center bound to a 2,9-dimethyl-1,10-phenanthroline ligand. The Cu(I) centers are bridged by another (5,5'-dimethyl-[2,2'-bithiophene]-3,3'-diyl)bis(diphenylphosphane) ligand. Each Cu(I) center is in a distorted trigonal pyramidal coordination geometry. The coordination geometry of Cu 1 is likely due

to the steric bulk imposed by three phenyl rings, two of which are on the bidentate (5,5'-dimethyl-[2,2'-bithiophene]-3,3'-diyl)bis(diphenylphosphane) ligand and the other on the bridging (5,5'-dimethyl-[2,2'-bithiophene]-3,3'-diyl)bis(diphenylphosphane) ligand (Figure 78). The coordination geometry of Cu 2 is likely due to the location of the acetone solvent molecule, which sits between the 2,9-dimethyl-1,10-phenanthroline ligand and the diphenylphosphine moiety bound to Cu 2 (Figure 78). The bite angle of the bidentate (5,5'-dimethyl-[2,2'-bithiophene]-3,3'-diyl)bis(diphenylphosphane) ligand is 105.0 degrees. The bite angle of the bridging (5,5'-dimethyl-[2,2'-bithiophene]-3,3'-diyl)bis(diphenylphosphane) ligand on Cu 1 is 91.1 degrees and on Cu 2 is 99.6 degrees. The bite angle of the 2,9-dimethyl-1,10-phenanthroline ligand is 91.6 degrees.

The crystal structure of **22** is in the monoclinic space group $P2_1/n$ with Z = 4 which shows fluorine-sulfur interactions, fluorine-hydrogen interactions, sulfur-carbon interactions, oxygen-hydrogen interactions, and t-shaped π-π interactions. The fluorine-sulfur interactions occur between the free sulfur on the bridging (5,5'-dimethyl-[2,2'-bithiophene]-3,3'-diyl)bis(diphenylphosphane) ligand but do not occur between the free sulfurs on the (5,5'-dimethyl-[2,2'-bithiophene]-3,3'-diyl)bis(diphenylphosphane) ligand bound to Cu 1. The fluorine-hydrogen interactions occur between hydrogen atoms on the molecules of **22** surrounding the PF_6^- counter anions. The sulfur-carbon interactions occur between one of the free sulfurs on the (5,5'-dimethyl-[2,2'-bithiophene]-3,3'-diyl)bis(diphenylphosphane) ligand bound to Cu 1 and a carbon atom on the 2,9-dimethyl-1,10-phenanthroline ligand of an adjacent molecule of **22**. The oxygen-hydrogen interactions occur between the oxygen on the acetone solvent molecule and a hydrogen on a phenyl ring of the of the bridging (5,5'-dimethyl-[2,2'-bithiophene]-3,3'-diyl)bis(diphenylphosphane) ligand of one molecule of **22** as well as a hydrogen atom on the methyl group of the 2,9-dimethyl-1,10-phenanthroline ligand on another molecule of

22. The t-shaped π-π interactions occur between a phenyl ring on the (5,5'-dimethyl-[2,2'-bithiophene]-3,3'-diyl)bis(diphenylphosphane) ligand bound to Cu 1 and the phenyl ring on the bridging (5,5'-dimethyl-[2,2'-bithiophene]-3,3'-diyl)bis(diphenylphosphane) ligand of another atom.

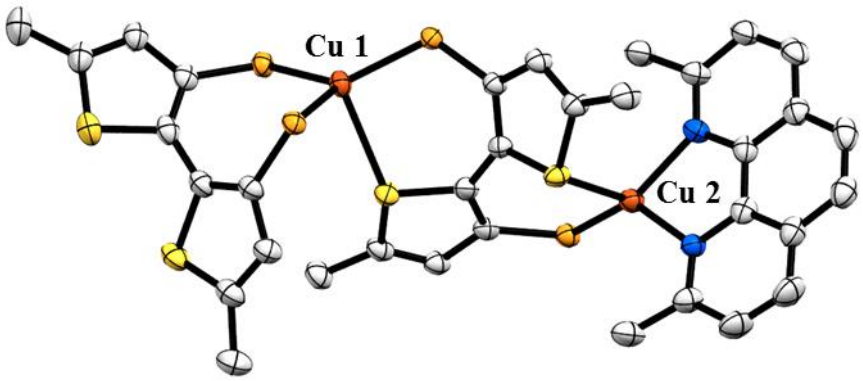

Figure 76. Molecular structure of **22** (50% thermal ellipsoid probability). The phenyl rings on the (5,5'-dimethyl-[2,2'-bithiophene]-3,3'-diyl)bis(diphenylphosphane) ligands have been removed for clarity.

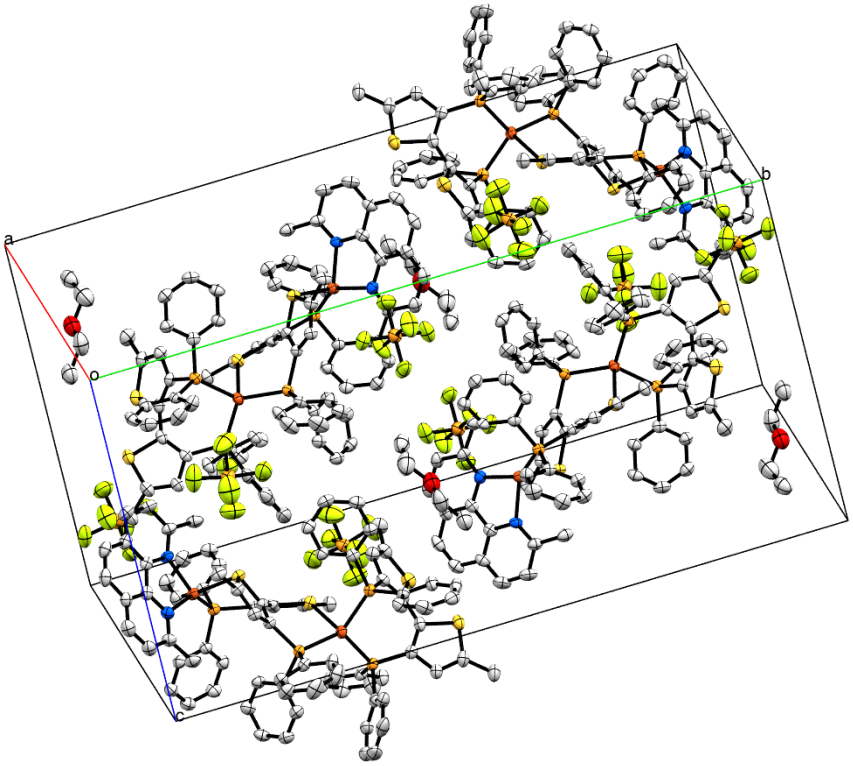

Figure 77. Solid-state packing and unit cell of the crystal structure of **22**.

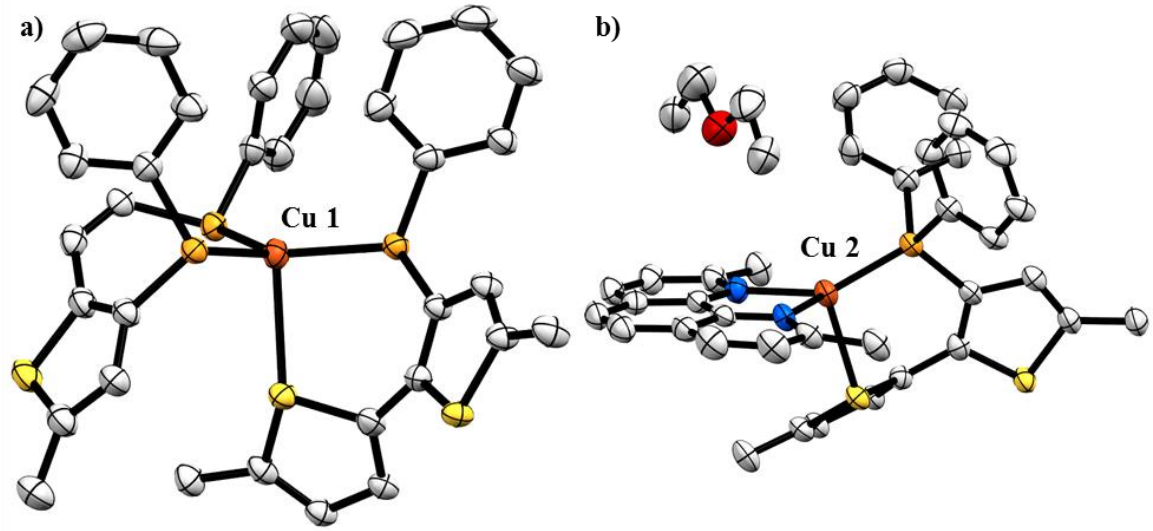

Figure 78. Coordination geometry of a) Cu 1 showing the steric bulk imposed by the three phenyl rings and b) Cu 2 showing steric bulk imposed by the acetone solvent molecule. Some atoms have been removed for clarity.

Table 17. Molecular formula and crystallographic importance of **23**.

Compound	Molecular Formula	Synthesized By	Crystallographic Importance
23	$[C_{42}H_{35}CuN_3P_2S_2][PF_6]$	Kory Mueller	F-S, F-H, S-H, π-π interactions

The molecular structure and single crystal packing of **23** are shown below in Figure 79. The molecular structure of **23** shows the Cu(I) center bound in a distorted tetrahedral coordination geometry. The (5,5'-dimethyl-[2,2'-bithiophene]-3,3'-diyl)bis(diphenylphosphane) ligand has a bite angle of 107.1 degrees and the 2-(1H-pyrazol-1-yl)pyridine ligand shows a bite angle of 81.4 degrees. The 2,2'-bithiophene moiety is bent away from the Cu(I) center, similar to the structure of **21**. The crystal

structure of **23** is in the triclinic space group P-1 with Z = 2 and shows fluorine-sulfur interactions, fluorine-hydrogen interactions, sulfur-hydrogen interactions, and offset π-π interactions. The fluorine-sulfur interactions are between the PF_6^- counter anions and one of the sulfur atoms on the 2,2'-bithiophene moiety on a nearby molecule of **23**. Due to the fluorine-sulfur interactions only occurring between one of the sulfur atoms on the (5,5'-dimethyl-[2,2'-bithiophene]-3,3'-diyl)bis(diphenylphosphane) ligand and the PF_6^- counter anion, this is likely the cause of the 2,2'-bithiophene moiety being bent away from the Cu(I) center. The fluorine-hydrogen interactions are between the hydrogen atoms on the molecules of **23** that surround the PF_6^- counter anions. The sulfur-hydrogen interactions are between the sulfur atoms on the 2,2'-bithiophene moiety of one molecule of **23** and the phenyl rings on the (5,5'-dimethyl-[2,2'-bithiophene]-3,3'-diyl)bis(diphenylphosphane) ligand of another nearby molecule of **23** while the offset π-π interactions occur between the phenyl rings on the (5,5'-dimethyl-[2,2'-bithiophene]-3,3'-diyl)bis(diphenylphosphane) ligands of two different molecules of **23**.

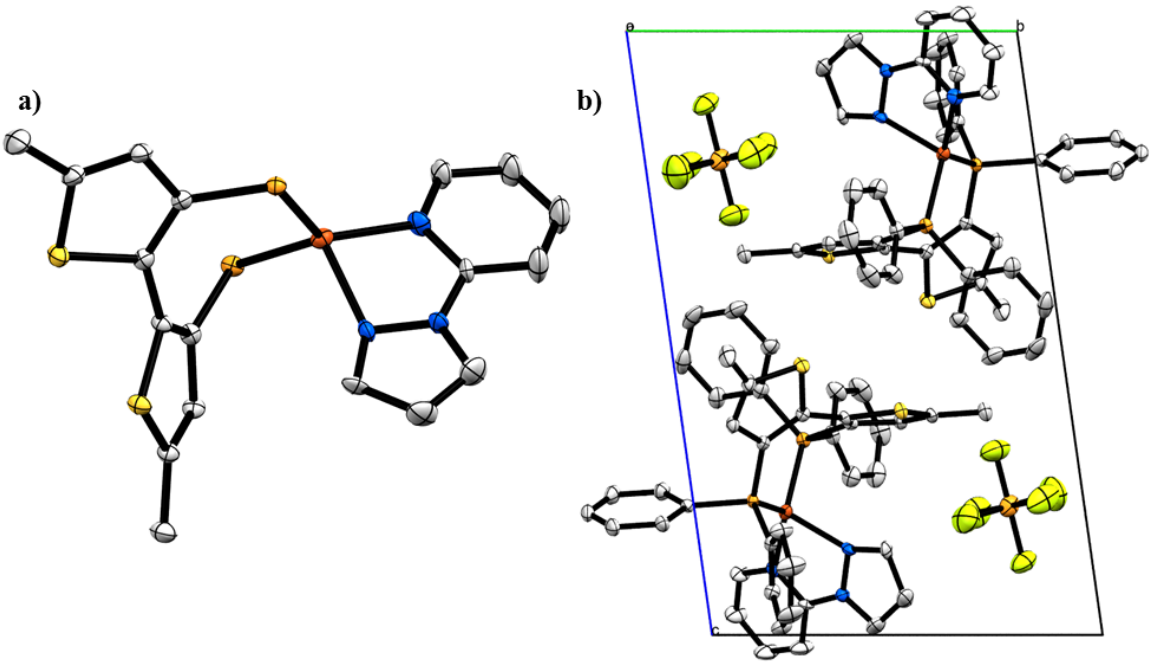

Figure 79. a) Molecular structure of **23** (50% thermal ellipsoid probability). Phenyl rings on the (5,5'-dimethyl-[2,2'-bithiophene]-3,3'-diyl)bis(diphenylphosphane) ligand were removed for clarity. b) Crystal packing of **23** (50% thermal ellipsoid probability) looking down the a-axis.

Table 18. Molecular formula and crystallographic importance of **24**.

Compound	Molecular Formula	Synthesized By	Crystallographic Importance
24	$[C_{37}H_{28}CuF_3N_3P_2S][PF_6]$	Kory Mueller	F-F, F-H, N-H, S-C interactions

The molecular structure and single crystal packing of **24** are shown below in Figure 80. The molecular structure of **24** shows a Cu(I) center bound in a slightly distorted tetrahedral coordination geometry. The 3,4-bis(diphenylphosphino)thiophene ligand of **24**

shows a bite angle of 93.8 degrees and the 2-(3-(trifluoromethyl)-1H-pyrazol-1-yl)pyridine ligand shows a bite angle of 80.0 degrees. The crystal structure of **24** is in the monoclinic space group C2/c with Z = 8 and shows fluorine-fluorine interactions, fluorine-hydrogen interactions, nitrogen-hydrogen interactions and sulfur-carbon interactions. The fluorine-fluorine interactions occur between two trifluoromethyl groups on adjacent molecules of **24**. There are also fluorine-fluorine interactions between the trifluoromethyl groups of **24** and the PF_6^- counter anion. The fluorine-hydrogen interactions occur between the fluorine atoms on the PF_6^- counter anions and the hydrogens on close-by molecules of **24**. The nitrogen-hydrogen interactions occur between pairs of **24**, where the nitrogen atoms of the pyrazole moiety on **24** interact with the hydrogen atoms on one of the phenyl rings on an adjacent molecule of **24**. This interaction occurs between both molecules, as shown in Figure 81. The sulfur-carbon interactions occur between the sulfur atom of **24** and a carbon on the 2-(3-(trifluoromethyl)-1H-pyrazol-1-yl)pyridine ligand of an adjacent molecule of **24**.

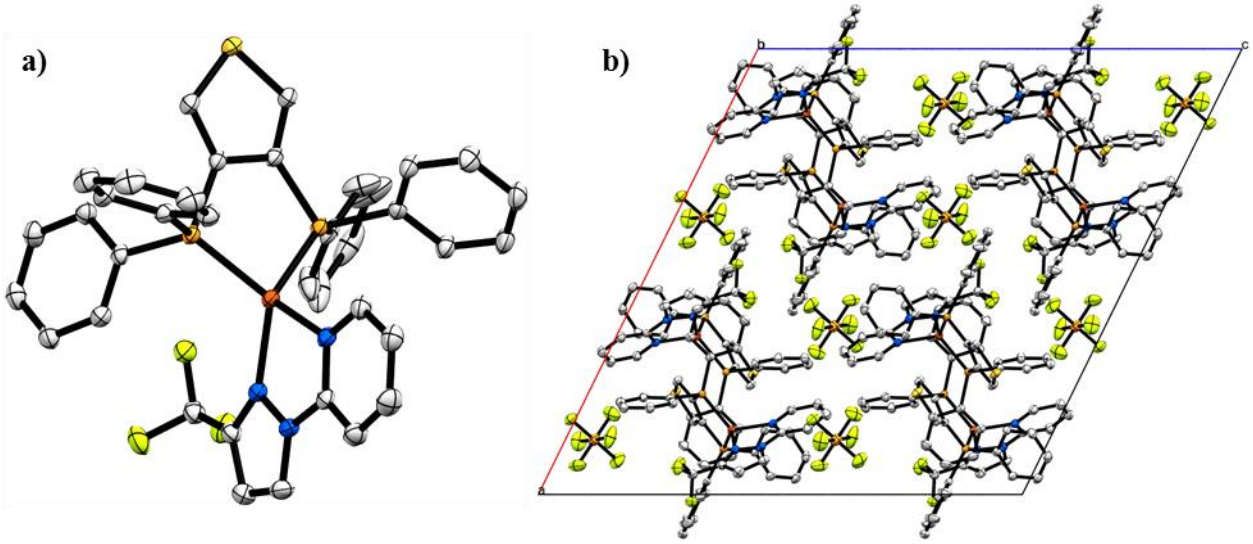

Figure 80. a) Molecular structure of **24** (50% thermal ellipsoid probability) and b) Crystal packing of **24** (50% thermal ellipsoid probability) looking down the b-axis.

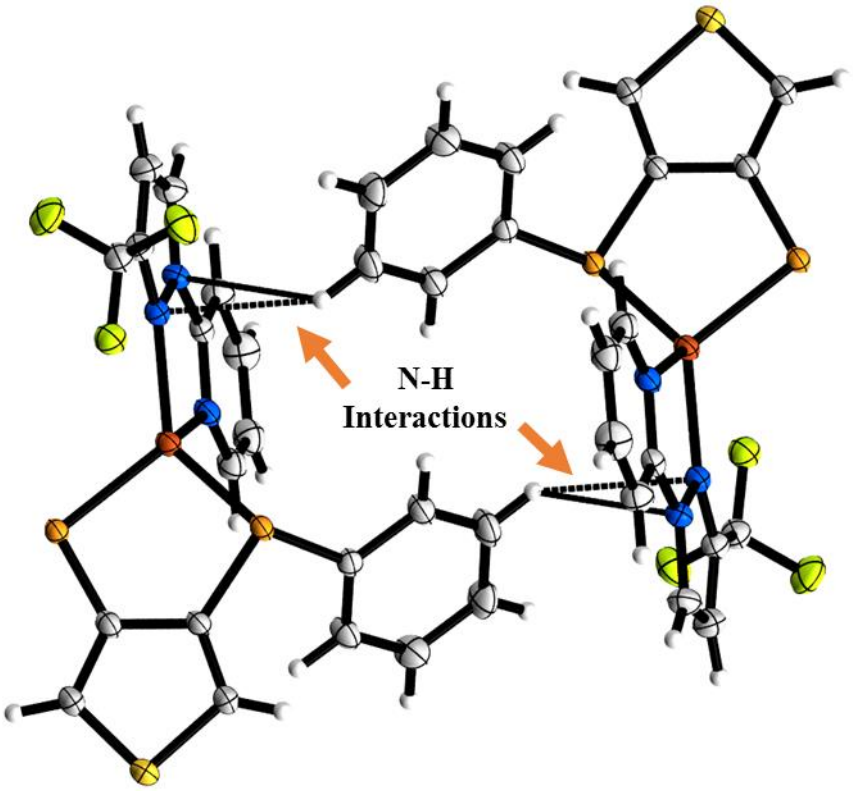

Figure 81. Nitrogen-hydrogen interactions between two molecules of **24**. Non-participating phenyl rings on the 3,4-bis(diphenylphosphino)thiophene ligands were removed for clarity.

Table 19. Molecular formula and crystallographic importance of **25**.

Compound	Molecular Formula	Synthesized By	Crystallographic Importance
25	$[C_{37}H_{31}CuN_3P_2S][PF_6]$	Kory Mueller	F-H, S-C, π-π interactions

The molecular and single crystal structure of **25** are shown below in Figure 82. The molecular structure of **25** shows a Cu(I) center bound in a slightly distorted tetrahedral

coordination geometry. The 3,4-bis(diphenylphosphino)thiophene ligand of **25** shows a bite angle of 93.4 degrees while the 2-(3-methyl-1H-pyrazol-1-yl)pyridine ligand shows a bite angle of 79.6 degrees. The crystal structure of **25** is in the monoclinic space group C2/c with Z = 8 and has fluorine-hydrogen interactions, sulfur-carbon interactions, and t-shaped π-π interactions. The fluorine-hydrogen interactions occur between the fluorine atoms on the PF_6^- counter anions and the hydrogen atoms of the surrounding molecules of **25**. The sulfur-carbon and sulfur-nitrogen interactions occur between the sulfur atom of the thiophene moiety of one molecule of **25** and the carbon atoms and nitrogen atoms of the 2-(3-methyl-1H-pyrazol-1-yl)pyridine ligand of another molecule of **25**. The t-shaped π-π interactions occur between the phenyl rings on two separate molecules of **25**.

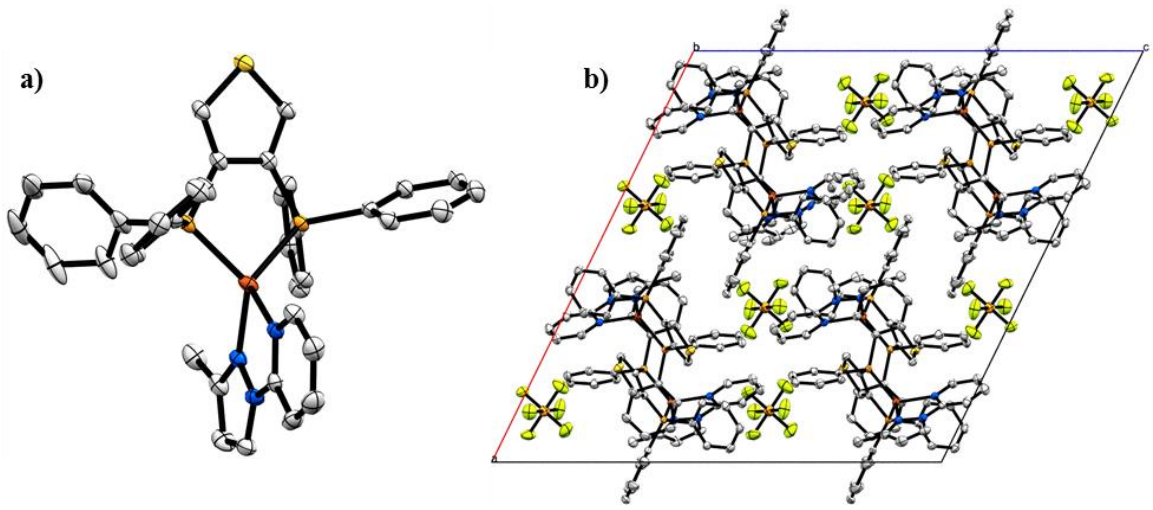

Figure 82. a) Molecular structure of **25** (50% thermal ellipsoid probability) and b) Crystal packing of **25** (50% thermal ellipsoid probability) looking down the b-axis.

Table 20. Molecular formula and crystallographic importance of **26**.

Compound	Molecular Formula	Synthesized By	Crystallographic Importance
26	$[C_{36}H_{32}CuN_3P_2S][PF_6]$	Kory Mueller	F-H, S-N, S-C, π-π interactions

The molecular structure and single crystal packing of **26** are shown below in Figure 83. The molecular structure of **26** shows the Cu(I) center bound in a tetrahedral coordination geometry. The 3,4-bis(diphenylphosphino)thiophene ligand has a bite angle of 93.6 degrees and the 2-(1H-pyrazol-1-yl)pyridine ligand has a bite angle of 85.9 degrees. The crystal structure of **26** is in the monoclinic space group C2/c with Z = 8 and has fluorine-hydrogen interactions, sulfur-nitrogen interactions, sulfur-carbon interactions and π-π interactions. The fluorine-hydrogen interactions occur between the fluorine atoms of the PF_6^- counter anions and the hydrogen atoms on adjacent molecules of **26**. The sulfur-nitrogen and sulfur-carbon interactions occur between the between the 2-(1H-pyrazol-1-yl)pyridine ligand of one molecule of **26** and the 3,4-bis(diphenylphosphino)thiophene ligand of another molecule of **26**. There are also sulfur-carbon interactions between sulfur atom on the 3,4-bis(diphenylphosphino)thiophene ligand of one molecule of **26** and the phenyl rings on the 3,4-bis(diphenylphosphino)thiophene ligand of another molecule of **26**. The π-π interactions occur between the phenyl rings on the 3,4-bis(diphenylphosphino)thiophene ligands of two different molecules of **26**.

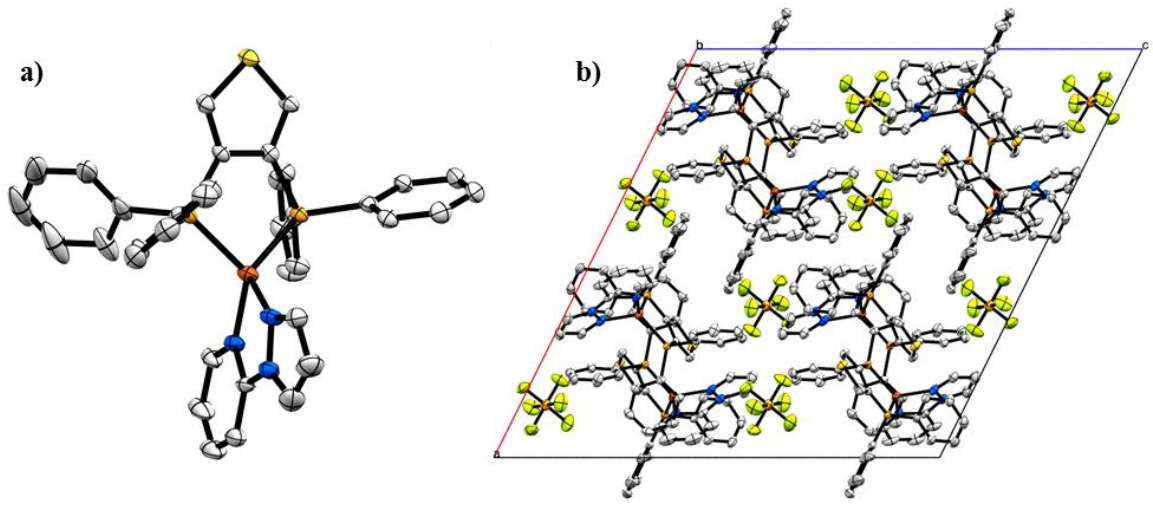

Figure 83. a) Molecular structure of **26** (50% thermal ellipsoid probability) and b) Crystal packing of **26** (50% thermal ellipsoid probability) looking down the b-axis.

Table 21. Molecular formula and crystallographic importance of **27**.

Compound	Molecular Formula	Synthesized By	Crystallographic Importance
27	$[C_{43}H_{37}CuN_3P_2S][PF_6]$	Kory Mueller	F-H, N-H, π-π interactions

The molecular structure and single crystal packing of **27** are shown below in Figure 84. The molecular structure of **27** shows the Cu(I) center bound in a distorted tetrahedral geometry with the (5,5'-dimethyl-[2,2'-bithiophene]-3,3'-diyl)bis(diphenylphosphane) ligand having a bite angle of 106.6 degrees and the 2-(3-methyl-1H-pyrazol-1-yl)pyridine ligand having a bite angle of 80.0 degrees. The distorted tetrahedral coordination geometry around the Cu(I) center is likely due to the large bite angle of the (5,5'-dimethyl-[2,2'-bithiophene]-3,3'-diyl)bis(diphenylphosphane) ligand. The crystal structure of **27** is in the

monoclinic space group $P2_1/c$ with Z = 4 and displays fluorine-hydrogen interactions, nitrogen-hydrogen interactions, and offset π-π interactions. The fluorine-hydrogen interactions occur between the PF_6^- counter anions and the hydrogen atoms of molecules of **27** that surround the PF_6^- anion. The nitrogen-hydrogen interactions occur between the 2-(3-methyl-1H-pyrazol-1-yl)pyridine ligands and hydrogen atoms on the acetone solvent molecules. The acetone molecules sit sandwiched between the 2-(3-methyl-1H-pyrazol-1-yl)pyridine ligands of two separate molecules of **27** (Figure 85). The offset π-π interactions occur between the phenyl rings of the (5,5'-dimethyl-[2,2'-bithiophene]-3,3'-diyl)bis(diphenylphosphane) ligands of two separate molecules of **27**.

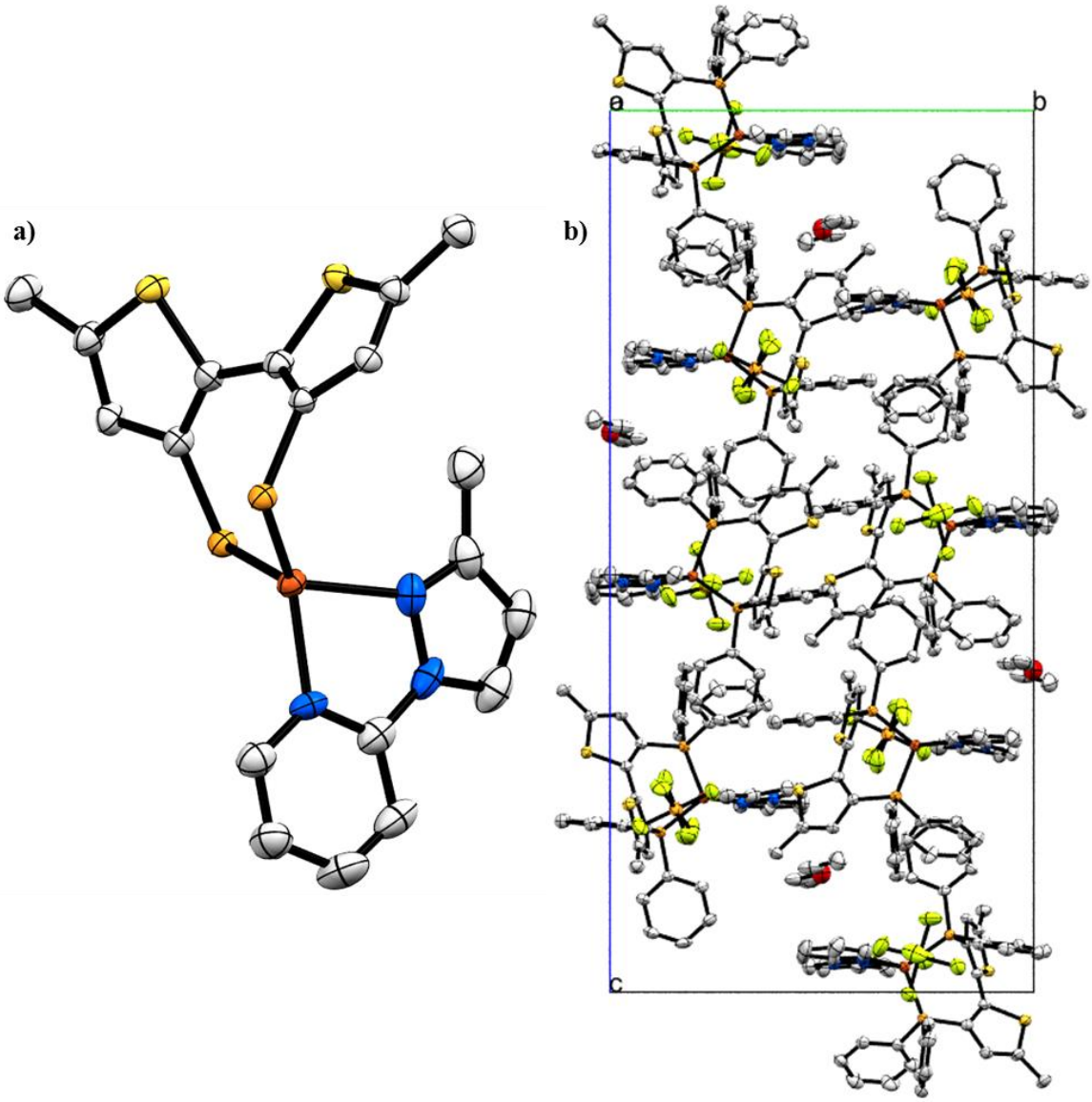

Figure 84. a) Molecular structure of **27** (50% thermal ellipsoid probability). The phenyl rings on the (5,5'-dimethyl-[2,2'-bithiophene]-3,3'-diyl)bis(diphenylphosphane) ligand have been removed for clarity. b) Crystal packing of **27** (50% thermal ellipsoid probability) looking down the a-axis.

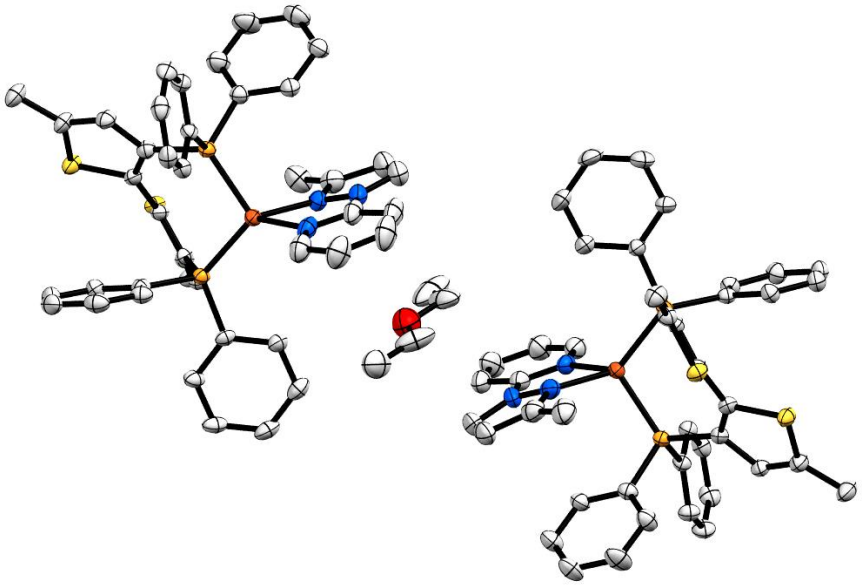

Figure 85. Acetone solvent molecule sandwiched between two different molecules of **27**.

Table 22. Molecular formula and crystallographic importance of **28**.

Compound	Molecular Formula	Synthesized By	Crystallographic Importance
28	$C_{44}H_{48}CuN_6O_{10}$	Rob Fimognari	Hydrogen bonding O-H interactions

The molecular structure and single crystal packing of **28** are shown below in Figure 86. The molecular structure of **28** shows a Cu(II) center bound in a distorted octahedral coordination geometry. The distortion is due to the binding of the two 3-((5-(1,3-dioxo-1,3,4,7-tetrahydro-2H-4,7-methanoisoindol-2-yl)pentyl)carbamoyl)benzoate pincer ligands. The crystal structure of **28** is in the monoclinic space group $P2_1/n$ with Z = 4 and shows hydrogen bonding between the 3-((5-(1,3-dioxo-1,3,4,7-tetrahydro-2H-4,7-

methanoisoindol-2-yl)pentyl)carbamoyl)benzoate ligands and the water solvent molecules. The crystal structure of **28** also shows oxygen-hydrogen interactions between the 3-((5-(1,3-dioxo-1,3,4,7-tetrahydro-2H-4,7-methanoisoindol-2-yl)pentyl)carbamoyl)benzoate ligand one molecule of **28** and the hydrogen atoms bound to carbon atoms on the 3-((5-(1,3-dioxo-1,3,4,7-tetrahydro-2H-4,7-methanoisoindol-2-yl)pentyl)carbamoyl)benzoate ligand of another molecule of **28**. There are also oxygen-hydrogen atoms that occur between the water solvent molecules and the hydrogen atoms bound to carbon atoms on the 3-((5-(1,3-dioxo-1,3,4,7-tetrahydro-2H-4,7-methanoisoindol-2-yl)pentyl)carbamoyl)benzoate ligands on surrounding molecules of **28**.

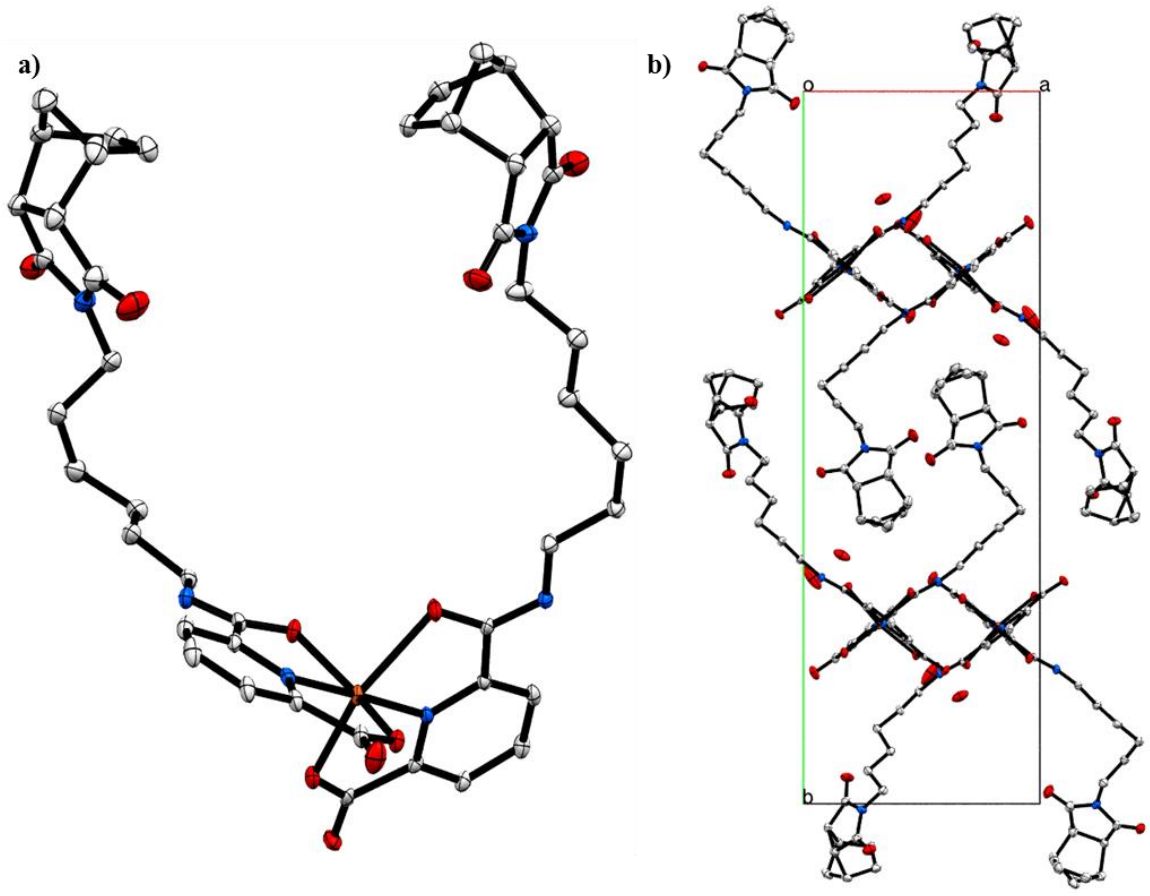

Figure 86. a) Molecular structure of **28** (50% thermal ellipsoid probability) and b) Crystal packing of **28** (50% thermal ellipsoid probability) looking down the c-axis. The floating oxygen atoms are solvent water molecules.

Polymorphism of Cu(II) Phenylimidizole Complex

Table 23. Molecular formula and crystallographic importance of **29a** and **29b**.

Compound	Molecular Formula	Synthesized By	Crystallographic Importance
29a and **29b**	$[C_{37}H_{28}CuF_3N_3P_2S][PF_6]$	Rob Fimognari	Polymorphs

The molecular structures of **29a** and **29b** are of the same tetraphenylimidizole copper(II) iodide complex (Figure 87). The Cu(II) center is bound in a slightly distorted trigonal pyramidal coordination geometry. The molecular structure shows an I^Cu^N average angle of 96.8 ± 1.8 degrees. The slight distortion is likely due to the iodide counter anion being located 3.6 Å directly below the Cu(II) center opposite of the bound iodide ligand.

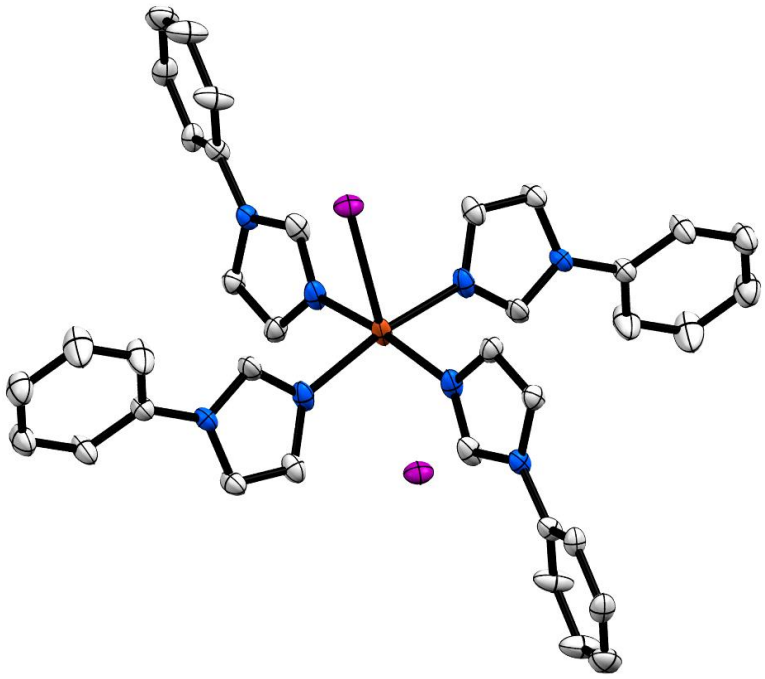

Figure 87. Molecular structure of **29a** and **29b** (50% thermal ellipsoid probability).

The crystal structure of **29a** is in the triclinic space group P-1 with Z = 1 and the crystal structure of **29b** is in the monoclinic space group $P2_1/c$ with Z = 4. The unit cell dimensions for both crystals are given below in Table 24. The crystal structures of both **29a** and **29b** are co-crystalized with non-binding phenylimidizole molecules and both crystal structure display iodide-hydrogen interactions, offset π-π interactions, and t-shaped π-π interactions. However, in the crystal structure of **29a**, the unbound phenylimidizole is badly disordered due to the middle of the phenylimidizole molecule sitting on a special position in the crystal structure, as well as disorder due to a slight side to side rotation of the phenylimidizole molecule. The iodide-hydrogen interactions occur between both the bound and unbound iodide molecules and the hydrogens one the bound and unbound phenylimidizole moieties. The offset π-π interactions occur between an unbound

phenylimidizole molecule and a bound phenylimidizole. The t-shaped π-π interactions occur between a phenylimidizole bound to the Cu(II) center and an unbound phenylimidizole as well as between two bound phenylimidizole ligands. The different crystal structures occur due to how the π-π interactions occur repeatedly throughout the crystal structure. In the crystal structure of **29a**, there are continuous rows of offset π-π interactions (Figure 88). In the crystal structure of **29b**, there are pockets of offset π-π interactions that consist of unbound phenylimidizole, bound phenylimidizole, bound phenylimidizole, unbound phenylimidizole. These pockets are then "capped" by t-shaped π-π interactions with both bound and unbound phenylimidizole moieties (Figure 89).

Table 24. Unit cell dimensions of **29a** and **29b**.

Crystal	a (Å)	b (Å)	c (Å)	α (deg)	β (deg)	γ (deg)	Volume ($Å^3$)
29a	8.69	9.71	13.85	69.76	76.04	76.01	1048
29b	11.58	17.15	12.63	90.00	95.53	90.00	2498

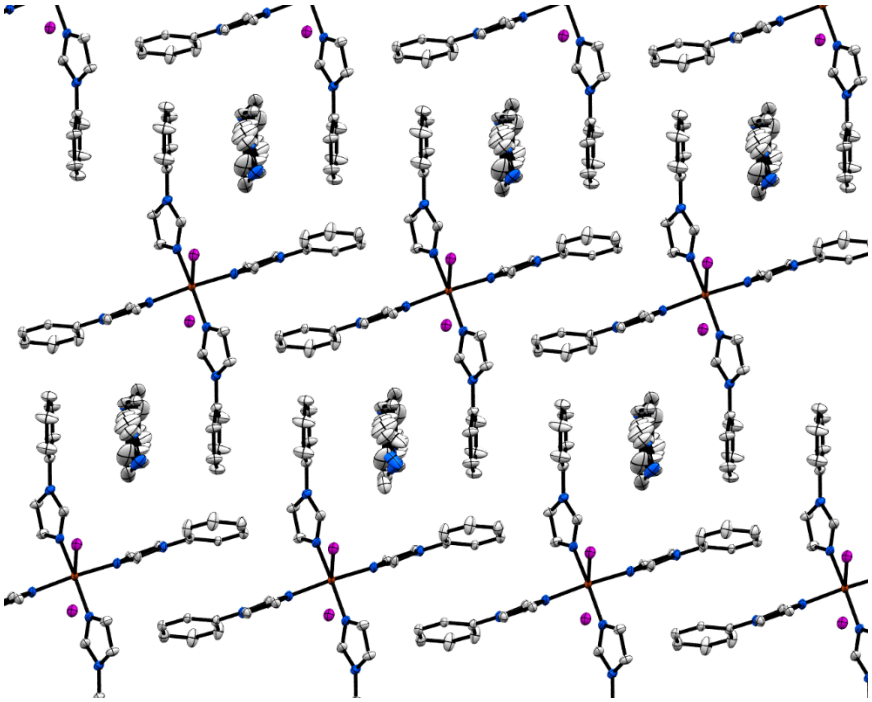

Figure 88. Crystal packing of **29a** showing the continuous rows of offset π-π interactions.

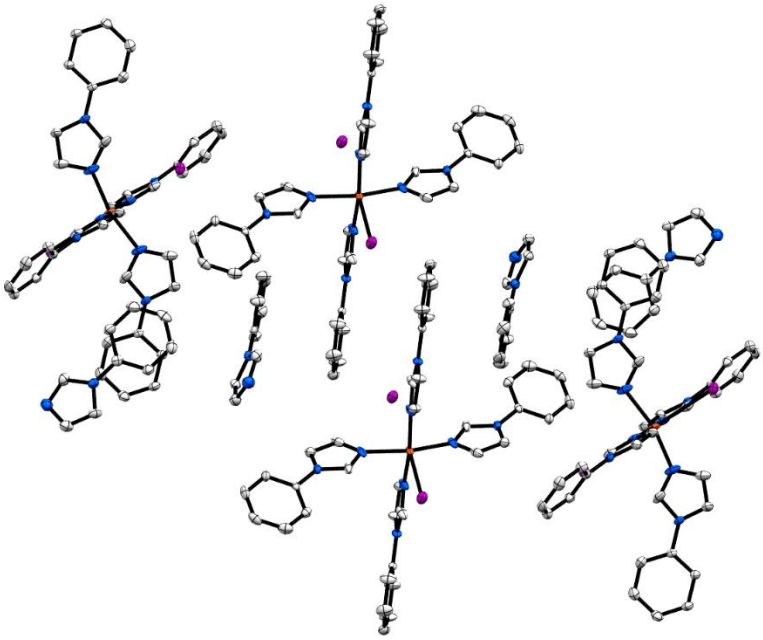

Figure 89. Crystal packing of **29b** showing the "capped" pockets of offset π-π interactions.

Crystallography of Ir(III) Complexes

Table 25. Molecular formula and crystallographic importance of **30**.

Compound	Molecular Formula	Synthesized By	Crystallographic Importance
30	$[C_{58}H_{46}IrN_6][PF_6]$	Matthew Moore	F-H, F-C, F-Cl, Cl-H, Cl-C, π-π interactions

The molecular structure and single crystal packing of **30** are shown below in Figure 90. The molecular structure of **30** shows the Ir(III) center bound in a slightly distorted octahedral coordination geometry by two 4-mesityl-2-phenylpyridine ligands and one dipyridophenazine ligand. The bite angle of the 4-mesityl-2-phenylpyridine ligands is 91.0 ± 0.1 degrees and the bite angle of the dipyridophenazine ligand is 77.0 degrees. The mesityl moieties on the 4-mesityl-2-phenylpyridine ligands show a torsion angle of 80.0 ± 1.8 degrees away from the plane of the phenylpyridine core. The crystal structure of **30** is in the triclinic space group P-1 with Z = 2. The crystal structure of **30** also has CH_2Cl_2 solvent molecules and PF_6^- counter anions. There are fluorine-hydrogen interactions, fluorine-carbon interactions, fluorine-chlorine interactions, chlorine-hydrogen interactions, chlorine-carbon interactions, and offset π-π interactions present. The fluorine-hydrogen interactions occur between the PF_6^- counter anions and hydrogens on the surrounding molecules of **30** as well as with the hydrogens on the CH_2Cl_2 solvent molecules. The fluorine-carbon interactions occur between the PF_6^- counter anions and carbon atoms on the dipyridophenazine ligands. The fluorine-chlorine interactions occur between the PF_6^- counter anions and the CH_2Cl_2 solvent molecules. The chlorine-hydrogen

interactions occur between the CH_2Cl_2 molecules and the hydrogens on the surrounding molecules of **30** as well as with the hydrogen atoms on other CH_2Cl_2 molecules. The chlorine-carbon interactions occur between the CH_2Cl_2 molecules and some of the carbons on the dipyridophenazine ligands. The offset π-π interactions occur between the dipyridophenazine ligands of two adjacent molecules of **30**.

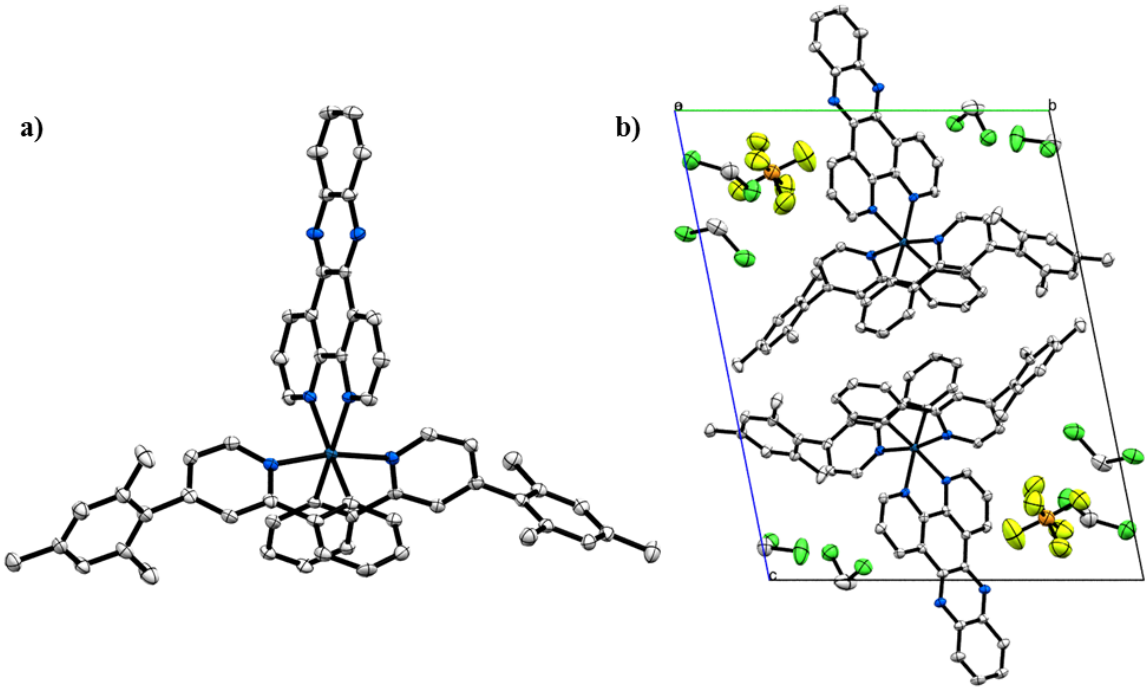

Figure 90. a) Molecular structure of **30** (50% thermal ellipsoid probability) and b) Crystal packing of **30** (50% thermal ellipsoid probability) looking down the a-axis.

Table 26. Molecular formula and crystallographic importance of **31**.

Compound	Molecular Formula	Synthesized By	Crystallographic Importance
31	$[C_{40}H_{26}IrN_6][PF_6]$	Matthew Moore	F-H, F-C, F-N. F-Cl, Cl-H, π-π interactions

The molecular structure and single crystal packing of **31** are shown below in Figures 91. The molecular structure of **31** shows the Ir(III) metal center bound in a slightly distorted octahedral geometry by two phenylpyridine ligands and one dipyridophenazine ligand. The two phenylpyridine ligands show a bite angle of 81.0 ± 0.5 degrees and the dipyridophenazine ligand shows a bite angle of 77.5 degrees. The crystal structure of **31** is in the triclinic space group P-1 with Z = 2 and also has PF_6^- counter anions and dichloroethane solvent molecules. The crystal structure of **31** shows fluorine-hydrogen interactions, fluorine-carbon interactions, fluorine-nitrogen interactions, fluorine-chlorine interactions, chlorine-hydrogen interactions, offset π-π interactions, and t-shaped π-π interactions. The fluorine-hydrogen interactions occur between the PF_6^- counter anions and the close by hydrogens on the molecules of **31** as well as with the hydrogens on surrounding dichloroethane solvent molecules. The fluorine-carbon and fluorine-nitrogen interactions occur between the PF_6^- counter anions and the dipyridophenazine ligands of **31** (Figure 92). The fluorine-chlorine interactions occur between the PF_6^- counter anions and the surrounding dichloroethane molecules. The chlorine-hydrogen interactions occur between the dichloroethane solvent molecules and the nearby hydrogen atoms on the surrounding dipyridophenazine ligands of **31**. The offset π-π interactions occur between the dipyridophenazine ligands of two molecules of **31** (Figure 92). There are also offset π-π

interactions between the phenylpyridine ligands of two molecules of **31**. The t-shaped π-π interactions occur between the phenylpyridine ligands of **31** and the dipyridophenazine of another molecule of **31** as well as with the phenylpyridine ligands of an adjacent molecule of **31**.

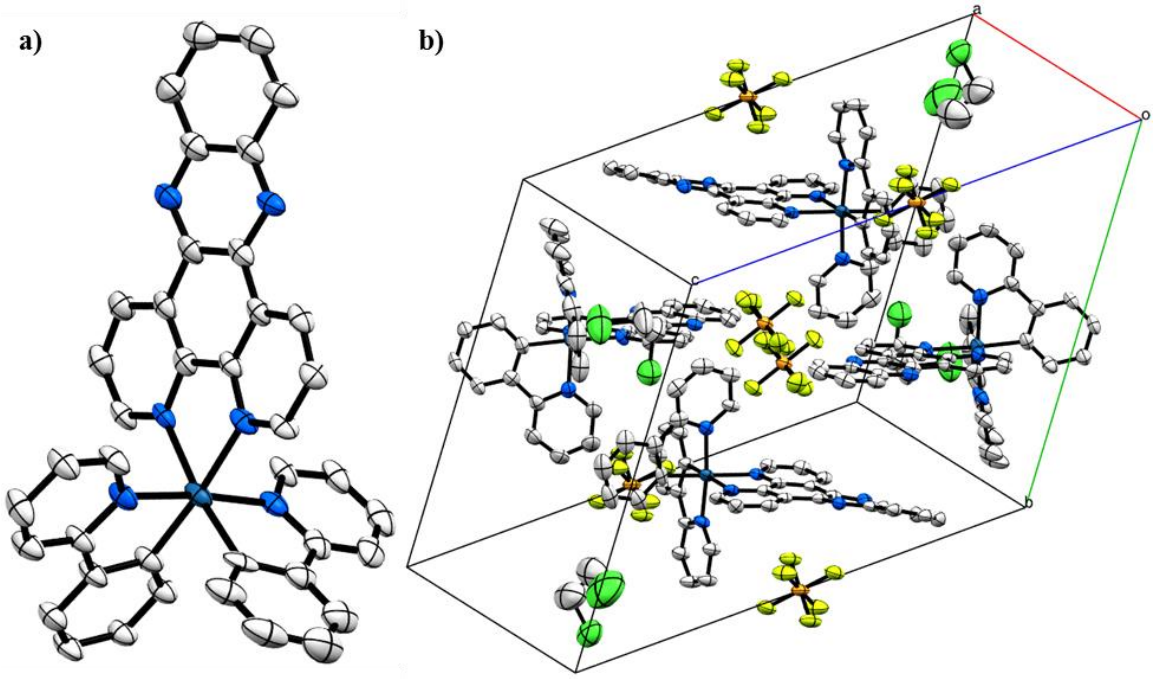

Figure 91. a) Molecular structure of **31** (50% thermal ellipsoid probability) and b) crystal packing of **31** (50% thermal ellipsoid probability).

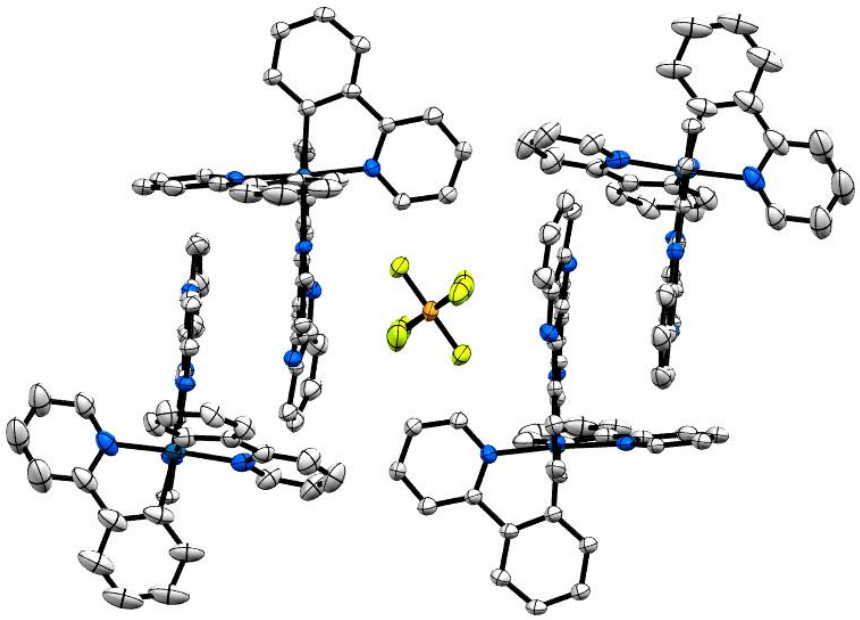

Figure 92. Interactions between the PF_6^- counter anion and the dipyridophenazine ligands of **31** as well as π-π interactions between the dipyridophenazine ligands of **31**.

Table 27. Molecular formula and crystallographic importance of **32**.

Compound	Molecular Formula	Synthesized By	Crystallographic Importance
32	$[C_{38}H_{42}IrN_6][PF_6]$	Matthew Moore	F-C, F-H, N-H interactions

The molecular structure and single crystal packing of **32** are shown below in Figure 93. The molecular structure of **32** shows the Ir(III) metal center bound in a slightly distorted octahedral coordination geometry by two 1-methyl-3-phenyl-2,3-dihydro-1H-imidazole ligands and one 4,4'-di-tert-butyl-2,2'-bipyridine ligand. The 1-methyl-3-phenyl-2,3-dihydro-1H-imidazole ligands shows a bite angle of 78.8 ± 0.1 degrees and the 4,4'-di-tert-

butyl-2,2'-bipyridine ligand shows a bite angle of 76.8 degrees. The crystal structure of **32** is in the monoclinic space group $P2_1/c$ with Z = 4. There are also PF_6^- counter anions and CH_3CN solvent molecules present in the crystal structure. Analysis of the crystal structure of **32** shows fluorine-carbon interactions, fluorine-hydrogen interactions, and nitrogen-hydrogen interactions. The fluorine-carbon interactions occur between the PF_6^- counter anions and the 4,4'-di-tert-butyl-2,2'-bipyridine ligands on nearby molecules of **32**. The fluorine-hydrogen interactions occur between the PF_6^- counter anions and the hydrogen atoms on surrounding molecules of **32**. The nitrogen-hydrogen interactions occur between the CH_3CN solvent molecules and the surrounding molecules of **32**.

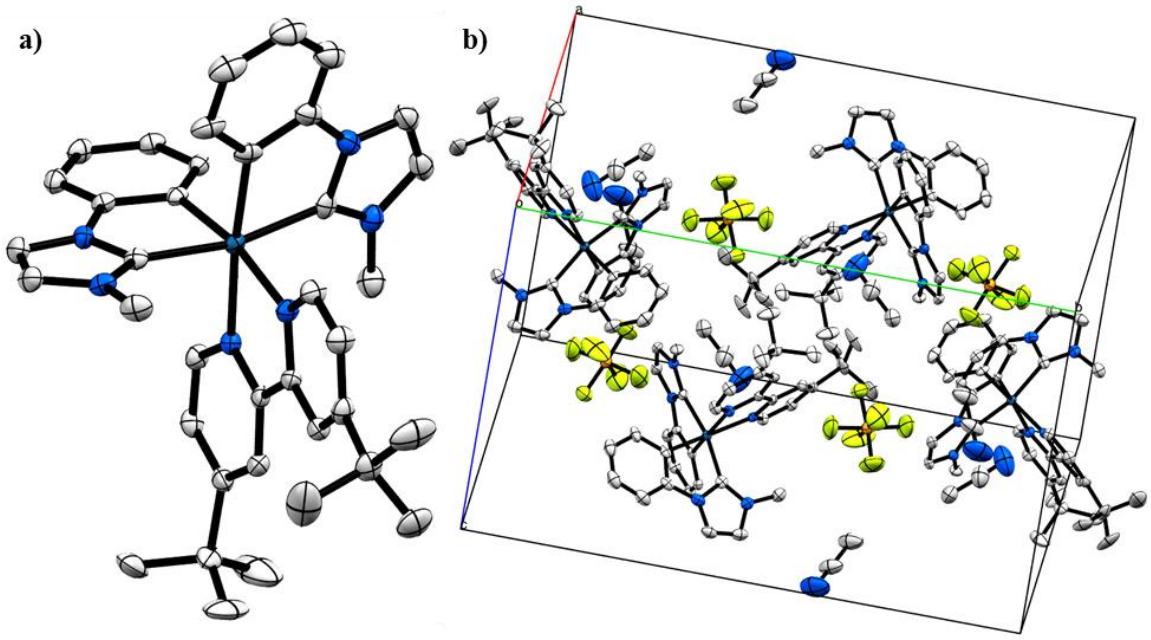

Figure 93. a) Molecular structure of **32** (50% thermal ellipsoid probability) and b) crystal packing of **32** (50% thermal ellipsoid probability).

Table 28. Molecular formula and crystallographic importance of **33**.

Compound	Molecular Formula	Synthesized By	Crystallographic Importance
33	$[C_{68}H_{64}IrN_4][PF_6]$	Matthew Moore	F-H, Cl-H, Cl-C, π-π interactions

The molecular structure and single crystal packing of **33** are shown below in Figure 94. The molecular structure of **33** shows the Ir(III) metal center bound in a slightly disordered octahedral coordination geometry by two 4-mesityl-2-phenylpyridine ligands and one 4,4'-dimesityl-2,2'-bipyridine ligand. The 4-mesityl-2-phenylpyridine ligands display a bite angle of 80.6 ± 0.4 degrees and the 4,4'-dimesityl-2,2'-bipyridine shows a bite angle of 76.2 degrees. The mesityl groups on the 4-mesityl-2-phenylpyridine ligands show a torsion angle of 64.9 ± 2.6 degrees away from the phenylpyridine core while the mesityl groups on the 4,4'-dimesityl-2,2'-bipyridine ligand shows a torsion angle of 88.5 ± 0.1 degrees away from the bipyridine core. The crystal structure of **33** is in the monoclinic space group $P2_1/c$ with Z = 5. There are also BF_4^- counter anions and CH_2Cl_2 solvent molecules present in the crystal structure which shows fluorine-hydrogen interactions, chlorine-hydrogen interactions, chlorine-carbon interactions, and t-shaped π-π interactions. The fluorine-hydrogen interactions occur between the BF_4^- counter anions and hydrogen atoms on the 4-mesityl-2-phenylpyridine ligands of surrounding molecules of **33** as well as with the hydrogen atoms on the surrounding CH_2Cl_2 solvent molecules. The chlorine-hydrogen and chlorine-carbon interactions occur between the CH_2Cl_2 solvent molecules and nearby molecules of **33**. The t-shaped π-π interactions occur between the mestityl groups of the 4-mesityl-2-phenylpyridine ligands of one molecule of **33** and the pyridine moieties of the 4,4'-dimesityl-2,2'-bipyridine ligands of another molecule of **33**.

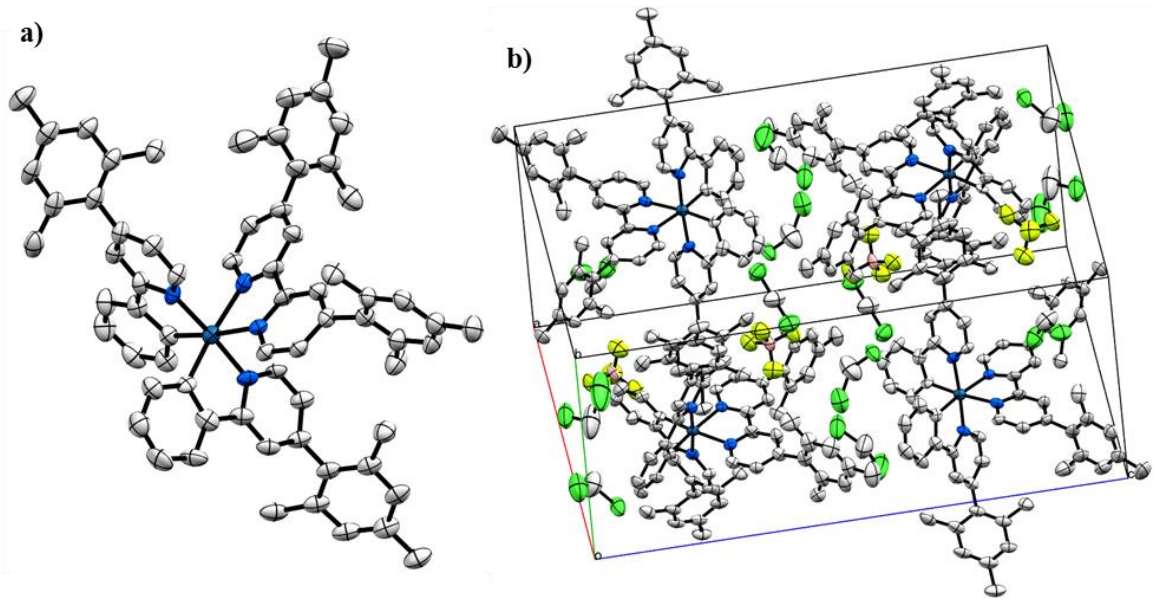

Figure 94. a) Molecular structure of **33** (50% thermal ellipsoid probability) and b) crystal packing of **33** (50% thermal ellipsoid probability).

Table 29. Molecular formula and crystallographic importance of **34**.

Compound	Molecular Formula	Synthesized By	Crystallographic Importance
34	$C_{80}H_{72}Cl_2Ir_2N_4$	Matthew Moore	Cl-H, π-π interactions

The molecular structure and single crystal packing of **34** are shown below in Figure 95. The molecular structure of **34** is a dinuclear Ir(III) complex with each Ir(III) metal center bound by two 4-mesityl-2-phenylpyridine ligands and the two Ir(III) centers bridged by two chloride ligands. Each Ir(III) metal center is in a slightly distorted octahedral coordination geometry with the 4-mesityl-2-phenylpyridine ligands showing a bite angle

of 80.8 ± 0.1 degrees. The Cl^Ir^Cl angle is 82.7 degrees. The mesityl groups on the 4-mesityl-2-phenylpyridine ligands show a torsion angle of 75.1 ± 10.1 degrees. The crystal structure of **34** is in the triclinic space group P-1 with Z = 3. The crystal structure also has residual CH_2Cl_2 and 1,2-dichloroethane solvent molecules. There are chlorine-hydrogen interactions and offset π-π interactions. The chlorine-hydrogen interactions occur between the residual CH_2Cl_2 and 1,2-dichloroethane solvent molecules and the hydrogen atoms on surrounding molecules of **34** as well as with the hydrogen atoms of other nearby CH_2Cl_2 and 1,2-dichloroethane molecules. The offset π-π interactions occur between the mesityl groups of the 4-mesityl-2-phenylpyridine ligands of one molecule of **34** and the phenyl moieties of the 4-mesityl-2-phenylpyridine ligands of another molecule of **34**.

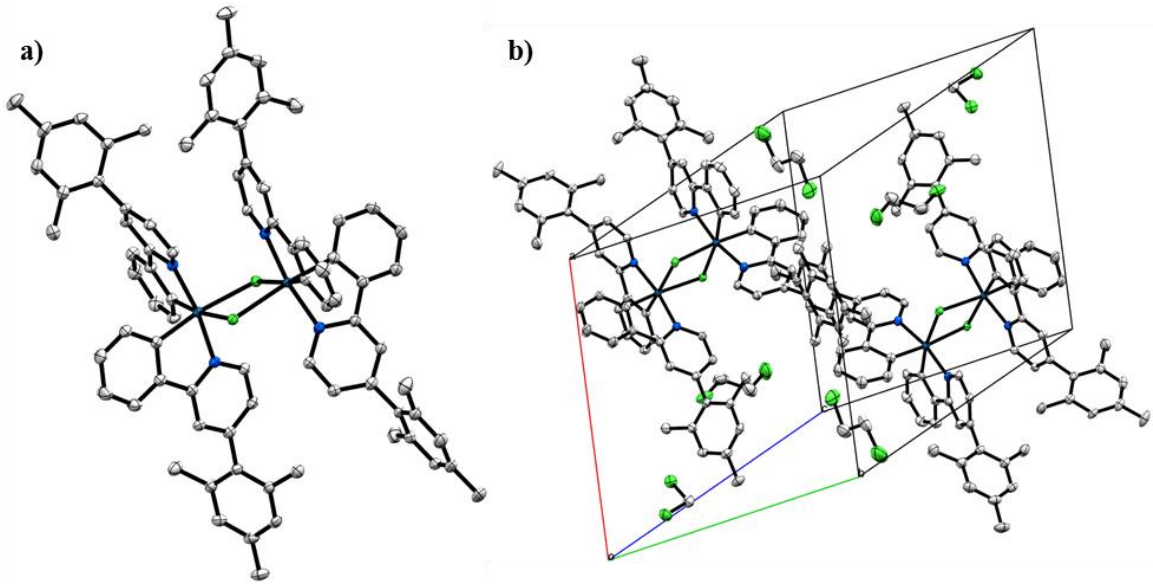

Figure 95. a) Molecular structure of **34** (50% thermal ellipsoid probability) and b) crystal packing of **34** (50% thermal ellipsoid probability).

Table 30. Molecular formula and crystallographic importance of **35**.

Compound	Molecular Formula	Synthesized By	Crystallographic Importance
35	$[C_{50}H_{44}IrN_4][PF_6]$	Matthew Moore	F-H, F-C, F-N, π-π interactions

The molecular structure and single crystal packing of **35** are shown below in Figure 96. The molecular structure of **35** shows the Ir(III) metal center bound in a slightly distorted octahedral coordination geometry by two 4-mesityl-2-phenylpyridine ligands and one 2,2'-bipyridine ligand. The 4-mesityl-2-phenylpyridine ligands show a bite angle of 80.4 degrees and the 2,2'-bipyridine ligand shows a bite angle of 76.0 degrees. The mesityl groups on the 4-mesityl-2-phenylpyridine ligands show a torsion angle of 63.8 ± 0.7 degrees away from the plane of the phenylpyridine core. The crystal structure of **35** is in the orthorhombic space group Pbca with Z = 8. The crystal structure also has PF_6^- counter anions present. The crystal structure of **35** displays fluorine-hydrogen interactions, fluorine-carbon interactions, fluorine-nitrogen interactions, t-shaped π-π interactions, and offset π-π interactions. The fluorine-hydrogen, fluorine-carbon, and fluorine-nitrogen interactions occur between the PF_6^- counter anions and the surrounding molecules of **35**. The t-shaped π-π interactions occur between the phenyl moieties of the 4-mesityl-2-phenylpyridine ligands on two adjacent molecules of **35** and the offset π-π interactions occur between the 2,2'-bipyridine ligands on two adjacent molecules of **35**.

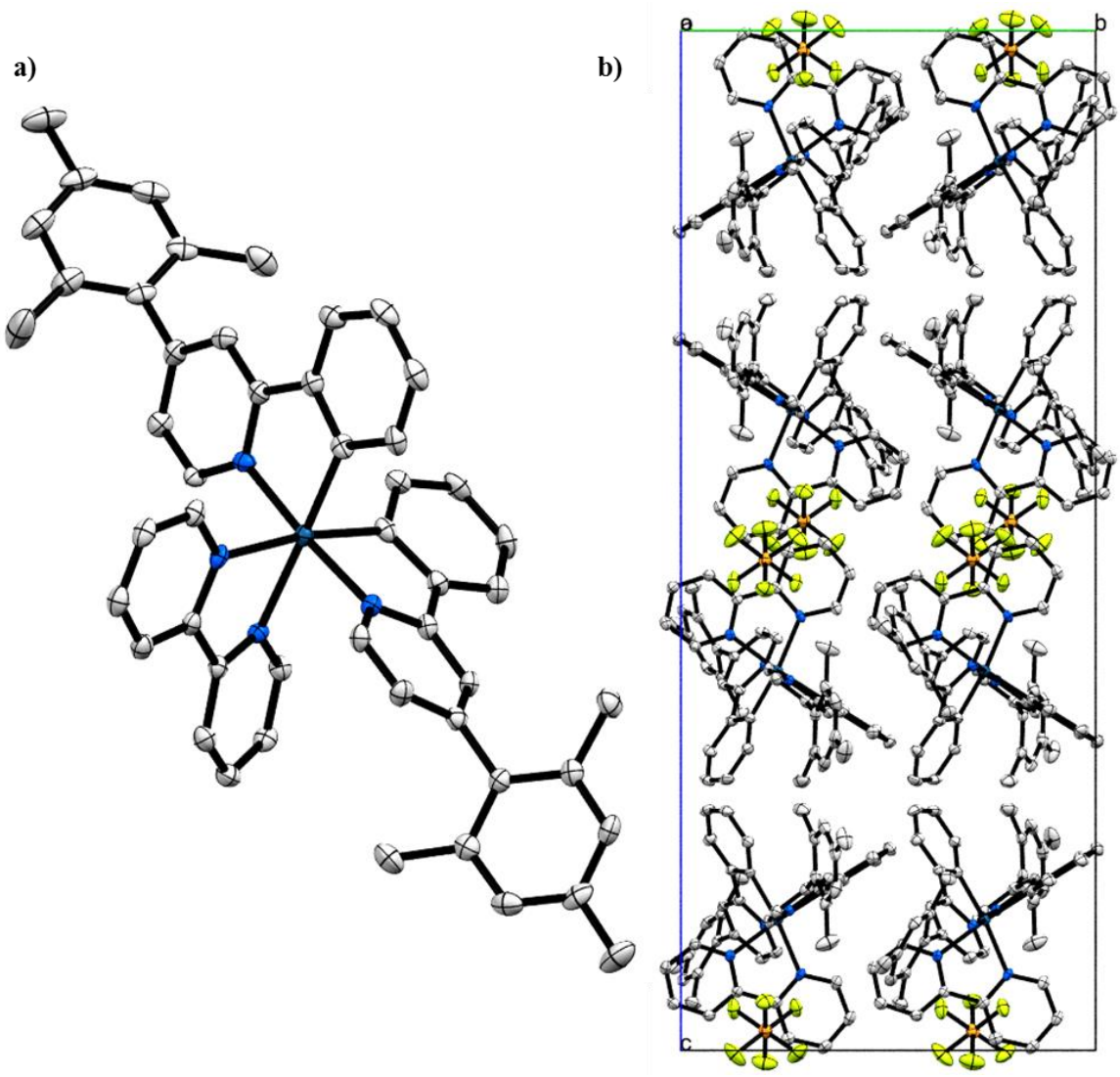

Figure 96. a) Molecular structure of **35** (50% thermal ellipsoid probability) and b) crystal packing of **35** (50% thermal ellipsoid probability) looking down the a-axis.

Crystallography of Pt(II) Complex

Table 31. Molecular formula and crystallographic importance of **36**.

Compound	Molecular Formula	Synthesized By	Crystallographic Importance
36	$[C_{28}H_{24}N_5PtS_2][PF_6]$	Matthew Moore	F-H, F-C, F-S, S-C, S-H, π-π interactions

The molecular structure and single crystal packing of **36** are shown below in Figure 97. The molecular structure of **36** shows a Pt(II) metal center bound in a slightly distorted square planar coordination geometry by a bidentate 2-phenylpyridine ligand and a bidentate 1,3-bis(3-(thiophen-2-yl)-2,3-dihydro-1H-imidazol-1-yl)propane ligand as well as a PF_6^- counter anion. The 2-phenylpyridine ligand shows a bite angle of 80.2 degrees and the 1,3-bis(3-(thiophen-2-yl)-2,3-dihydro-1H-imidazol-1-yl)propane ligand shows a bite angle of 89.0 degrees. The carbene moieties of the 1,3-bis(3-(thiophen-2-yl)-2,3-dihydro-1H-imidazol-1-yl)propane ligand show a torsion angle of 80.9 ± 2.5 degree away from the square planar plane formed by the 2-phenylpyridine ligand bound to the Pt(II) center. This torsion is due to the ethyl linker between the two carbene moieties.

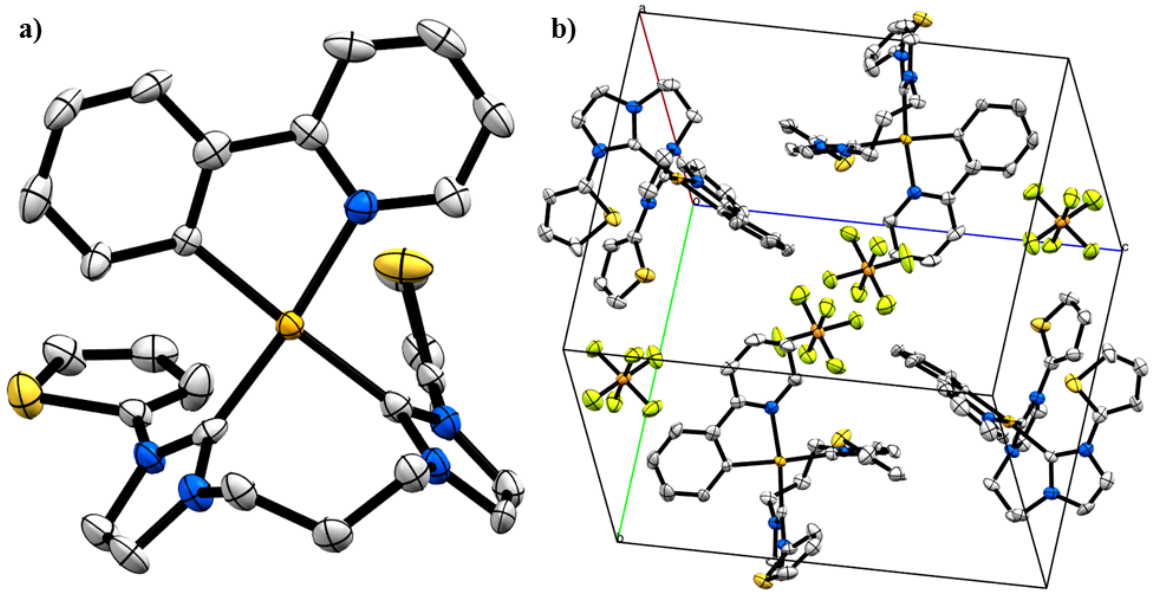

Figure 97. a) Molecular structure of **36** (50% thermal ellipsoid probability) and b) crystal packing of **36** (50% thermal ellipsoid probability).

The crystal structure of **36** is in the monoclinic space group $P2_1/c$ with Z = 4. There are fluorine-hydrogen interactions, fluorine-carbon interactions, fluorine-sulfur interactions, sulfur-carbon interactions, sulfur-hydrogen interactions, and offset π-π interactions present in the crystal structure of **36**. The fluorine-hydrogen and fluorine-carbon interactions occur between the PF_6^- counter anions and the surrounding molecules of **36**. The fluorine-sulfur interactions occur between the PF_6^- counter anions and the thiophene moieties of the 1,3-bis(3-(thiophen-2-yl)-2,3-dihydro-1H-imidazol-1-yl)propane ligand on **36**. The sulfur-carbon and sulfur-hydrogen interactions occur between the 1,3-bis(3-(thiophen-2-yl)-2,3-dihydro-1H-imidazol-1-yl)propane ligands of two molecules of **36** (Figure 98). The offset π-π interactions occur between the 1-(thiophen-2-yl)-2,3-dihydro-1H-imidazole moiety of one molecule of **36** and the 2-phenylpyridine moiety of another molecule of **36** (Figure 99).

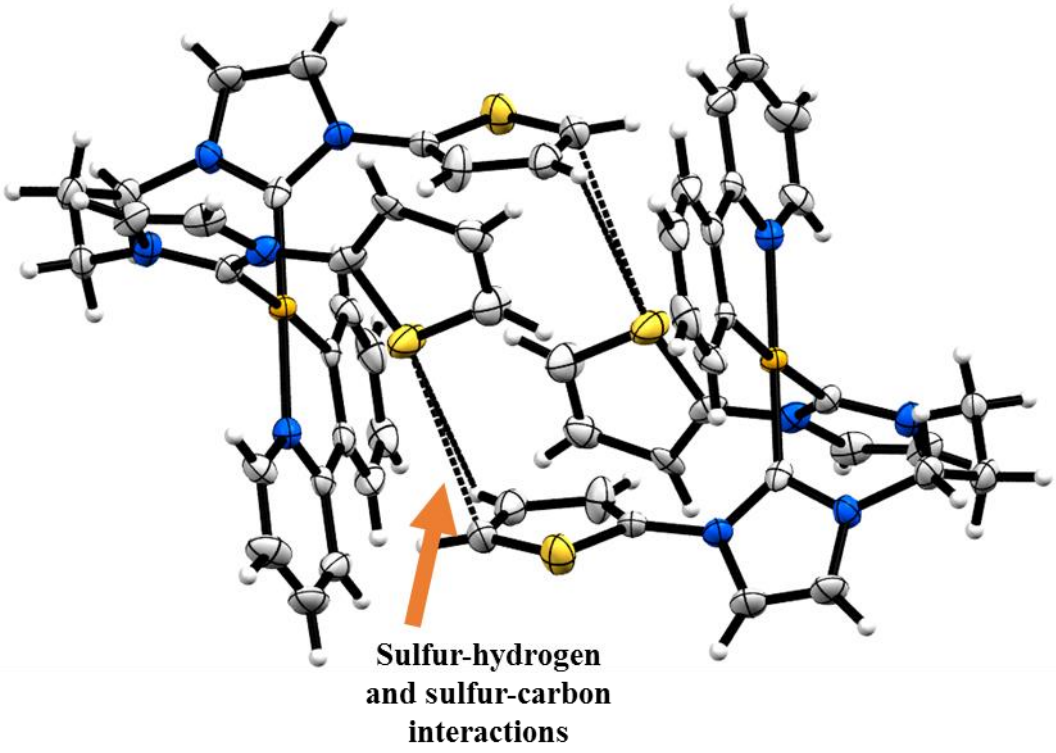

Figure 98. Sulfur-hydrogen and sulfur-carbon interactions between two molecules of **36**.

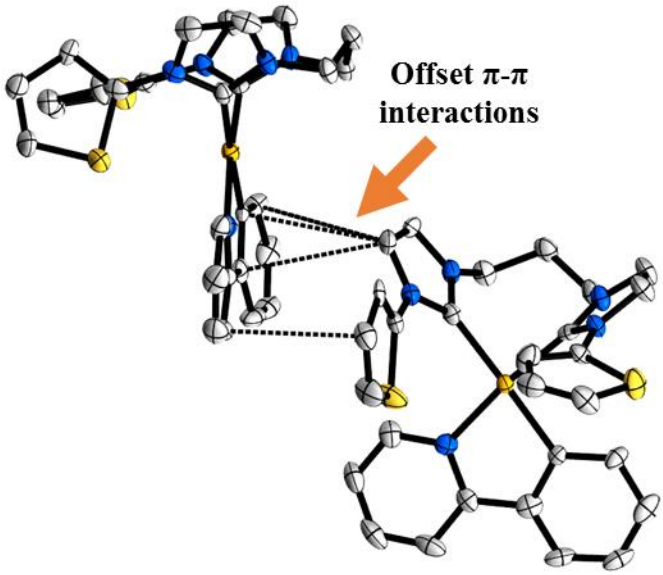

Figure 99. Offset π-π interactions between two molecules of **36**.

Crystallography of Rh(I) Complexes

Table 32. Molecular formula and crystallographic importance of **37**.

Compound	Molecular Formula	Synthesized By	Crystallographic Importance
37	$[C_{92}H_{74}N_4P_4Rh_2]2[BF_4]$	Kory Mueller	F-H, F-C, π-π interactions

The molecular structure and single crystal packing of **37** are shown below in Figure 100 and Figure 101. The molecular structure of **37** is a dinuclear Rh(I) complex with the Rh(I) metal centers bridged by a 9,10-diisocyanoanthracene ligand. Each Rh(I) metal center is bound in a square planar coordination geometry by the bridging 9,10-diisocyanoanthracene ligand, two triphenylphosphine ligands which are trans to each other, and a CH_3CN ligand which is trans to the bridging 9,10-diisocyanoanthracene ligand.

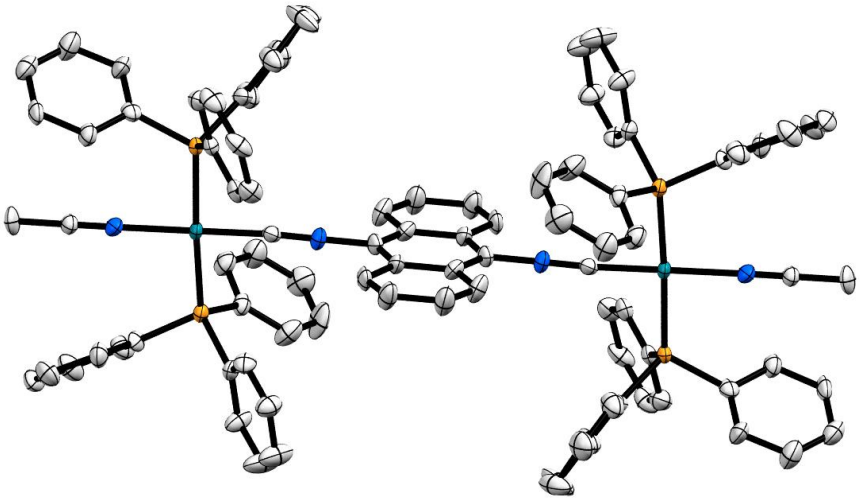

Figure 100. Molecular structure of **37** (50% thermal ellipsoid probability).

The crystal structure of **37** is in the monoclinic space group $P2_1/c$ with Z = 4. The crystal structure of **37** also has BF_4^- counter anions present. However, due to limitation in the Mercury software used to generate the molecular and crystal structures images, only one BF_4^- anion per molecule of **37** is shown. The crystal structure of **37** shows fluorine-hydrogen interactions, fluorine-carbon interactions, and t-shaped π-π interactions. The fluorine-hydrogen interactions occur between the BF_4^- counter anions and the hydrogen atoms on the surrounding molecules of **37** while the fluorine-carbon interactions occur specifically between the BF_4^- counter anions and the sp carbon on the CH_3CN ligands. The t-shaped π-π interactions occur between the phenyl rings of the triphenylphosphine ligands on adjacent molecules of **37**.

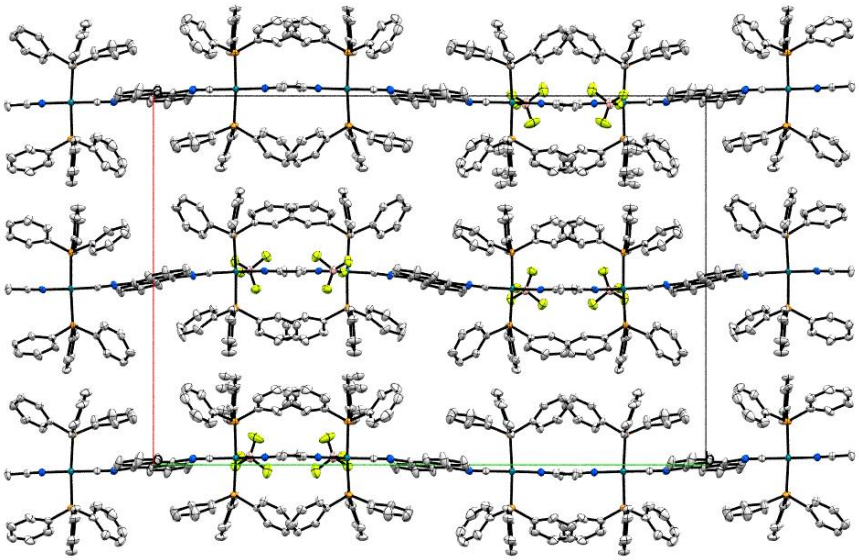

Figure 101. Crystal packing of **37** (50% thermal ellipsoid probability) looking down the c-axis.

Table 33. Molecular formula and crystallographic importance of **38**.

Compound	Molecular Formula	Synthesized By	Crystallographic Importance
38	$[C_{33}H_{53}NP_2Rh][BF_4]$	Kory Mueller	Agostic Rh-H bond F-H, π-π interactions

The molecular structure and single crystal packing of **38** are shown below in Figure 102. The molecular structure of **38** shows the Rh(I) center bound in a square planar coordination geometry by the pincer ligand, 1,3-bis((di-tert-butylphosphino)methyl)benzene, and a 2-isocyano-1,3-dimethylbenzene ligand. The Rh(I) center is bound to the 2-position of the 1,3-bis((di-tert-butylphosphino)methyl)benzene ligand; the benzene core of this ligand shows a 137.8 degree bond angle which is due to the agostic interaction with the hydrogen atom still bound to the benzene core at the two position (Figure 103).

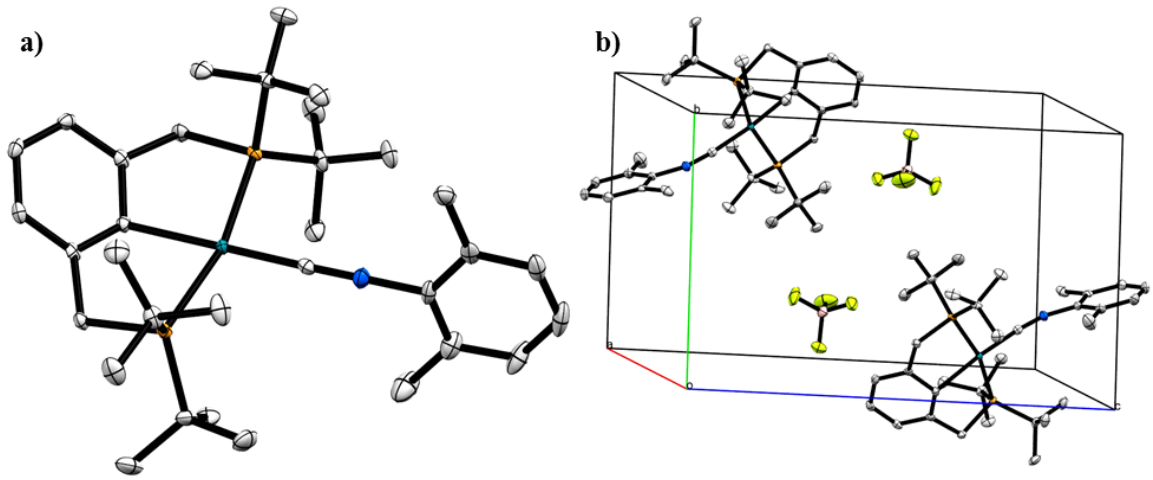

Figure 102. a) Molecular structure of **38** (50% thermal ellipsoid probability) and b) crystal packing of **38** (50% thermal ellipsoid probability).

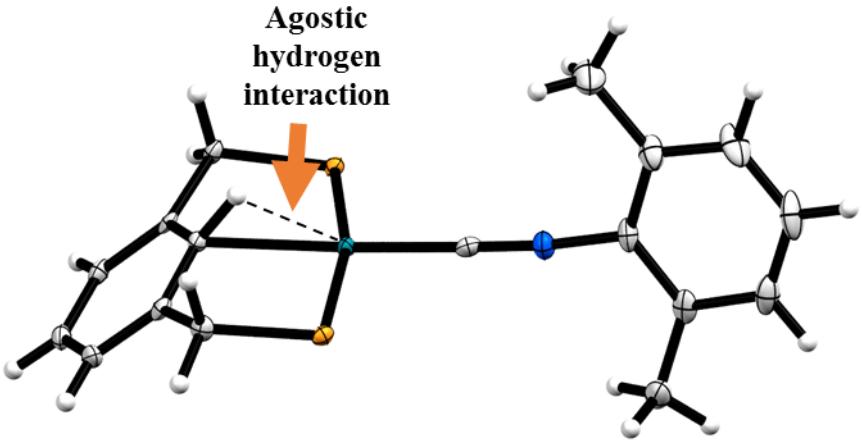

Figure 103. Molecular structure of **38** showing the agostic interaction with the hydrogen atom on the benzene core of the 1,3-bis((di-tert-butylphosphino)methyl)benzene ligand. The *t*-Bu groups on the phosphines were removed for clarity.

The crystal structure of **38** is in the triclinic space group P-1 with Z = 2. The crystal structure is also composed of BF_4^- counter anions which contribute to the fluorine-hydrogen interactions between fluorine atoms on the BF_4^- anions and the hydrogen atoms on the surrounding molecules of **38**. There are also offset π-π interactions, which occur between the 1,3-bis((di-tert-butylphosphino)methyl)benzene ligands of two adjacent molecules of **38** (Figure 104). There are also offset π-π interactions between the 2-isocyano-1,3-dimethylbenzene ligands of two adjacent molecules of **38** (Figure 104).

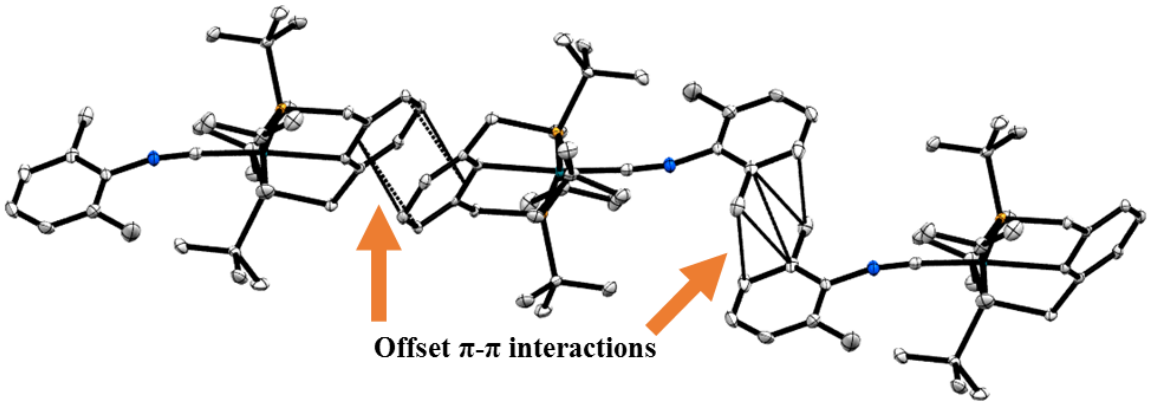

Figure 104. Offset π-π interactions between adjacent molecules of **38**.

Conclusion

In summary, we report the crystallographic analysis of various organic molecules and organometallic complexes. All crystal structures reported have R_1 values less than 0.10 and wR_2 values less than 0.25. Each crystal structure shows different types of interactions, ranging from intramolecular hydrogen bonding in the case of **15** to intermolecular halogen interactions between the counter anions/ residual solvent molecules and the organometallic complex in the case of **33**. These interactions have been shown to be key parts of how these molecules crystalize, especially in the case of the polymorphs **29a** and **29b**.

Crystal Tables

Table S1. Crystal data and structure refinement for **8**.

Identification code	shelx	
Empirical formula	C84 H130 Cl2 Ir2 O14 P4 S4	
Formula weight	2071.29	
Temperature	100(2) K	
Wavelength	1.54184 Å	
Crystal system	Monoclinic	
Space group	P 21/n	
Unit cell dimensions	a = 15.32950(10) Å	α = 90°.
	b = 37.6632(4) Å	β = 102.8940(10)°.
	c = 16.15180(10) Å	γ = 90°.
Volume	9090.22(13) $Å^3$	
Z	4	
Density (calculated)	1.513 Mg/m^3	
Absorption coefficient	8.122 mm^{-1}	
F(000)	4232	
Crystal size	0.2137 x 0.0615 x 0.0462 mm^3	
Theta range for data collection	3.042 to 66.597°.	
Index ranges	-18<=h<=18, -44<=k<=32, -19<=l<=19	
Reflections collected	82319	
Independent reflections	16070 [R(int) = 0.0351]	
Completeness to theta = 66.597°	100.0 %	
Absorption correction	Gaussian	
Max. and min. transmission	0.641 and 0.159	
Refinement method	Full-matrix least-squares on F^2	
Data / restraints / parameters	16070 / 1253 / 1301	
Goodness-of-fit on F^2	1.088	
Final R indices [I>2sigma(I)]	R1 = 0.0366, wR2 = 0.0840	
R indices (all data)	R1 = 0.0466, wR2 = 0.0874	
Extinction coefficient	n/a	
Largest diff. peak and hole	1.347 and -1.305 $e.Å^{-3}$	

Table S2. Crystal data and structure refinement for **11a**.

Identification code	shelx	
Empirical formula	C38 H25 Cl2 F12 N6 P Pt2	
Formula weight	1285.67	
Temperature	100(2) K	
Wavelength	1.54184 Å	
Crystal system	Monoclinic	
Space group	P 21/c	
Unit cell dimensions	a = 14.5924(2) Å	α = 90°.
	b = 20.5047(3) Å	β = 93.6220(10)°.
	c = 26.1065(3) Å	γ = 90°.
Volume	7795.80(18) $Å^3$	
Z	8	
Density (calculated)	2.191 Mg/m^3	
Absorption coefficient	15.763 mm^{-1}	
F(000)	4864	
Crystal size	0.1361 x 0.0319 x 0.0266 mm^3	
Theta range for data collection	2.742 to 75.733°.	
Index ranges	-17<=h<=17, -25<=k<=23, -18<=l<=32	
Reflections collected	31052	
Independent reflections	15668 [R(int) = 0.0340]	
Completeness to theta = 67.684°	99.5 %	
Absorption correction	Semi-empirical from equivalents	
Max. and min. transmission	1.00000 and 0.75482	
Refinement method	Full-matrix least-squares on F^2	
Data / restraints / parameters	15668 / 498 / 1210	
Goodness-of-fit on F^2	1.025	
Final R indices [I>2sigma(I)]	R1 = 0.0376, wR2 = 0.0901	
R indices (all data)	R1 = 0.0468, wR2 = 0.0951	
Extinction coefficient	n/a	
Largest diff. peak and hole	2.355 and -2.265 $e.Å^{-3}$	

Table S3. Crystal data and structure refinement for **11b**.

Identification code	shelx	
Empirical formula	C47 H33 F6 N6 P Pt2	
Formula weight	1216.94	
Temperature	100(2) K	
Wavelength	1.54184 Å	
Crystal system	Triclinic	
Space group	P -1	
Unit cell dimensions	a = 11.6122(3) Å	α = 78.630(2)°.
	b = 12.8540(3) Å	β = 89.257(2)°.
	c = 13.6623(4) Å	γ = 86.769(2)°.
Volume	1996.08(9) $Å^3$	
Z	2	
Density (calculated)	2.025 Mg/m^3	
Absorption coefficient	13.923 mm^{-1}	
F(000)	1164	
Crystal size	0.2277 x 0.2048 x 0.1294 mm^3	
Theta range for data collection	3.300 to 66.601°.	
Index ranges	-13<=h<=11, -15<=k<=14, -16<=l<=16	
Reflections collected	20885	
Independent reflections	7046 [R(int) = 0.0224]	
Completeness to theta = 66.601°	100.0 %	
Absorption correction	Semi-empirical from equivalents	
Max. and min. transmission	1.00000 and 0.63284	
Refinement method	Full-matrix least-squares on F^2	
Data / restraints / parameters	7046 / 429 / 615	
Goodness-of-fit on F^2	1.220	
Final R indices [I>2sigma(I)]	R1 = 0.0220, wR2 = 0.0552	
R indices (all data)	R1 = 0.0224, wR2 = 0.0554	
Extinction coefficient	0.000383(18)	
Largest diff. peak and hole	0.857 and -1.400 $e.Å^{-3}$	

Table S4. Crystal data and structure refinement for **11c**.

Identification code	shelx	
Empirical formula	C35 H25 F6 N6 P Pt2	
Formula weight	1064.74	
Temperature	100(2) K	
Wavelength	0.71075 Å	
Crystal system	Monoclinic	
Space group	C 2/c	
Unit cell dimensions	a = 15.315(5) Å	α = 90°.
	b = 13.743(4) Å	β = 103.365(5)°.
	c = 15.512(5) Å	γ = 90°.
Volume	3176.3(17) $Å^3$	
Z	4	
Density (calculated)	2.227 Mg/m^3	
Absorption coefficient	8.923 mm^{-1}	
F(000)	2008	
Crystal size	0.353 x 0.168 x 0.130 mm^3	
Theta range for data collection	2.016 to 25.028°.	
Index ranges	-18<=h<=18, -16<=k<=16, -16<=l<=18	
Reflections collected	14163	
Independent reflections	2749 [R(int) = 0.0694]	
Completeness to theta = 25.028°	97.4 %	
Refinement method	Full-matrix least-squares on F^2	
Data / restraints / parameters	2749 / 0 / 229	
Goodness-of-fit on F^2	1.122	
Final R indices [I>2sigma(I)]	R1 = 0.0379, wR2 = 0.1078	
R indices (all data)	R1 = 0.0381, wR2 = 0.1081	
Extinction coefficient	0.00024(7)	
Largest diff. peak and hole	2.213 and -2.071 $e.Å^{-3}$	

Table S5. Crystal data and structure refinement for **11e**.

Identification code	shelx	
Empirical formula	C41 H37 F6 N6 P Pt2	
Formula weight	1148.90	
Temperature	100(2) K	
Wavelength	0.71075 Å	
Crystal system	Orthorhombic	
Space group	P c c n	
Unit cell dimensions	a = 13.648(4) Å	α = 90°.
	b = 14.272(4) Å	β = 90°.
	c = 20.120(6) Å	γ = 90°.
Volume	3919(2) $Å^3$	
Z	4	
Density (calculated)	1.947 Mg/m^3	
Absorption coefficient	7.239 mm^{-1}	
F(000)	2200	
Crystal size	0.1600 x 0.1060 x 0.0920 mm^3	
Theta range for data collection	2.300 to 25.019°.	
Index ranges	-16<=h<=16, -16<=k<=12, -23<=l<=23	
Reflections collected	34621	
Independent reflections	3461 [R(int) = 0.0743]	
Completeness to theta = 25.019°	99.9 %	
Absorption correction	Semi-empirical from equivalents	
Max. and min. transmission	1.0000 and 0.8070	
Refinement method	Full-matrix least-squares on F^2	
Data / restraints / parameters	3461 / 0 / 255	
Goodness-of-fit on F^2	1.220	
Final R indices [I>2sigma(I)]	R1 = 0.0343, wR2 = 0.0734	
R indices (all data)	R1 = 0.0355, wR2 = 0.0740	
Extinction coefficient	n/a	
Largest diff. peak and hole	1.352 and -0.687 $e.Å^{-3}$	

Table S6. Crystal data and structure refinement for **11f**.

Identification code	shelx	
Empirical formula	C43 H41 F6 N6 P Pt2	
Formula weight	1176.97	
Temperature	100(2) K	
Wavelength	0.71073 Å	
Crystal system	Monoclinic	
Space group	P 21/n	
Unit cell dimensions	a = 9.2810(10) Å	α = 90°.
	b = 24.008(4) Å	β = 90.555(2)°.
	c = 17.949(3) Å	γ = 90°.
Volume	3999.2(10) $Å^3$	
Z	4	
Density (calculated)	1.955 Mg/m^3	
Absorption coefficient	7.097 mm^{-1}	
F(000)	2264	
Crystal size	0.2960 x 0.0940 x 0.0640 mm^3	
Theta range for data collection	1.417 to 25.027°.	
Index ranges	-11<=h<=11, -28<=k<=28, -17<=l<=21	
Reflections collected	51772	
Independent reflections	7050 [R(int) = 0.0719]	
Completeness to theta = 25.027°	99.9 %	
Absorption correction	Semi-empirical from equivalents	
Max. and min. transmission	1.0000 and 0.5973	
Refinement method	Full-matrix least-squares on F^2	
Data / restraints / parameters	7050 / 0 / 530	
Goodness-of-fit on F^2	1.141	
Final R indices [I>2sigma(I)]	R1 = 0.0337, wR2 = 0.0646	
R indices (all data)	R1 = 0.0352, wR2 = 0.0654	
Extinction coefficient	0.00007(2)	
Largest diff. peak and hole	0.927 and -0.939 $e.Å^{-3}$	

Table S7. Crystal data and structure refinement for **12**.

Identification code	shelx	
Empirical formula	C25 H19 B F4 N2	
Formula weight	434.23	
Temperature	100.01(10) K	
Wavelength	1.54184 Å	
Crystal system	Monoclinic	
Space group	P 2/c	
Unit cell dimensions	a = 13.6184(2) Å	α = 90°.
	b = 9.82670(10) Å	β = 100.6750(10)°.
	c = 16.3739(2) Å	γ = 90°.
Volume	2153.30(5) Å^3	
Z	4	
Density (calculated)	1.339 Mg/m^3	
Absorption coefficient	0.862 mm^{-1}	
F(000)	896	
Crystal size	0.2739 x 0.2265 x 0.1104 mm^3	
Theta range for data collection	3.302 to 73.411°.	
Index ranges	-16<=h<=16, -12<=k<=11, -20<=l<=20	
Reflections collected	21089	
Independent reflections	4287 [R(int) = 0.0295]	
Completeness to theta = 67.684°	100.0 %	
Absorption correction	Semi-empirical from equivalents	
Max. and min. transmission	1.00000 and 0.92132	
Refinement method	Full-matrix least-squares on F^2	
Data / restraints / parameters	4287 / 0 / 290	
Goodness-of-fit on F^2	1.038	
Final R indices [I>2sigma(I)]	R1 = 0.0337, wR2 = 0.0803	
R indices (all data)	R1 = 0.0368, wR2 = 0.0827	
Extinction coefficient	n/a	
Largest diff. peak and hole	0.198 and -0.245 e.Å^{-3}	

Table S8. Crystal data and structure refinement for **13**.

Identification code	shelx	
Empirical formula	C37 H28 B F4 N3	
Formula weight	601.43	
Temperature	100(2) K	
Wavelength	0.71073 Å	
Crystal system	Monoclinic	
Space group	P 21/c	
Unit cell dimensions	a = 10.8113(3) Å	α = 90°.
	b = 15.9249(4) Å	β = 92.075(2)°.
	c = 16.8175(6) Å	γ = 90°.
Volume	2893.55(15) $Å^3$	
Z	4	
Density (calculated)	1.381 Mg/m^3	
Absorption coefficient	0.099 mm^{-1}	
F(000)	1248	
Crystal size	0.508 x 0.282 x 0.236 mm^3	
Theta range for data collection	1.762 to 27.483°.	
Index ranges	-13<=h<=14, -20<=k<=20, -19<=l<=21	
Reflections collected	17834	
Independent reflections	6562 [R(int) = 0.0458]	
Completeness to theta = 25.242°	99.9 %	
Absorption correction	Numerical	
Refinement method	Full-matrix least-squares on F^2	
Data / restraints / parameters	6562 / 0 / 406	
Goodness-of-fit on F^2	1.007	
Final R indices [I>2sigma(I)]	R1 = 0.0464, wR2 = 0.1031	
R indices (all data)	R1 = 0.0935, wR2 = 0.1226	
Extinction coefficient	n/a	
Largest diff. peak and hole	0.304 and -0.260 $e.Å^{-3}$	

Table S9. Crystal data and structure refinement for **14**.

Identification code	shelx	
Empirical formula	C34 H28 P2 S2	
Formula weight	562.62	
Temperature	100 K	
Wavelength	0.71073 Å	
Crystal system	Triclinic	
Space group	P -1	
Unit cell dimensions	a = 9.745(3) Å	α = 93.048(8)°.
	b = 11.785(4) Å	β = 92.530(8)°.
	c = 12.394(4) Å	γ = 90.761(9)°.
Volume	1419.8(8) $Å^3$	
Z	2	
Density (calculated)	1.316 Mg/m^3	
Absorption coefficient	0.323 mm^{-1}	
F(000)	588	
Crystal size	0.2000 x 0.1400 x 0.0500 mm^3	
Theta range for data collection	3.096 to 27.483°.	
Index ranges	-12<=h<=12, -15<=k<=15, -16<=l<=16	
Reflections collected	15105	
Independent reflections	6468 [R(int) = 0.0408]	
Completeness to theta = 25.242°	99.8 %	
Absorption correction	Semi-empirical from equivalents	
Max. and min. transmission	1.0000 and 0.8098	
Refinement method	Full-matrix least-squares on F^2	
Data / restraints / parameters	6468 / 180 / 352	
Goodness-of-fit on F^2	1.029	
Final R indices [I>2sigma(I)]	R1 = 0.0450, wR2 = 0.0947	
R indices (all data)	R1 = 0.0609, wR2 = 0.1014	
Extinction coefficient	n/a	
Largest diff. peak and hole	0.555 and -0.265 $e.Å^{-3}$	

Table S10. Crystal data and structure refinement for **15**.

Identification code	shelx	
Empirical formula	C25 H19 N7 O6 S2	
Formula weight	577.59	
Temperature	100(2) K	
Wavelength	0.71075 Å	
Crystal system	Triclinic	
Space group	P -1	
Unit cell dimensions	a = 8.799(4) Å	α = 72.358(12)°.
	b = 11.773(4) Å	β = 87.606(14)°.
	c = 12.579(5) Å	γ = 85.694(18)°.
Volume	1238.1(9) Å^3	
Z	2	
Density (calculated)	1.549 Mg/m^3	
Absorption coefficient	0.274 mm^{-1}	
F(000)	596	
Crystal size	0.1560 x 0.0410 x 0.0350 mm^3	
Theta range for data collection	1.699 to 25.022°.	
Index ranges	-10<=h<=10, -14<=k<=13, -14<=l<=14	
Reflections collected	16517	
Independent reflections	4370 [R(int) = 0.0842]	
Completeness to theta = 25.022°	100.0 %	
Absorption correction	Semi-empirical from equivalents	
Max. and min. transmission	1.0000 and 0.7723	
Refinement method	Full-matrix least-squares on F^2	
Data / restraints / parameters	4370 / 0 / 369	
Goodness-of-fit on F^2	1.225	
Final R indices [I>2sigma(I)]	R1 = 0.0855, wR2 = 0.1456	
R indices (all data)	R1 = 0.1050, wR2 = 0.1540	
Extinction coefficient	n/a	
Largest diff. peak and hole	0.669 and -0.342 e.Å^{-3}	

Table S11. Crystal data and structure refinement for **16**.

Identification code	shelx	
Empirical formula	C27 H23 N7 O6 S2	
Formula weight	605.64	
Temperature	100 K	
Wavelength	1.54184 Å	
Crystal system	Monoclinic	
Space group	P 21/n	
Unit cell dimensions	a = 7.0155(4) Å	α = 90°.
	b = 18.3245(9) Å	β = 90.333(3)°.
	c = 20.4611(12) Å	γ = 90°.
Volume	2630.3(3) Å^3	
Z	4	
Density (calculated)	1.529 Mg/m^3	
Absorption coefficient	2.345 mm^{-1}	
F(000)	1256	
Crystal size	0.220 x 0.106 x 0.027 mm^3	
Theta range for data collection	3.238 to 75.932°.	
Index ranges	-7<=h<=8, -21<=k<=22, -22<=l<=25	
Reflections collected	14439	
Independent reflections	5279 [R(int) = 0.0249]	
Completeness to theta = 67.684°	99.1 %	
Absorption correction	Gaussian	
Max. and min. transmission	0.940 and 0.755	
Refinement method	Full-matrix least-squares on F^2	
Data / restraints / parameters	5279 / 0 / 381	
Goodness-of-fit on F^2	1.035	
Final R indices [I>2sigma(I)]	R1 = 0.0323, wR2 = 0.0803	
R indices (all data)	R1 = 0.0366, wR2 = 0.0830	
Extinction coefficient	n/a	
Largest diff. peak and hole	0.359 and -0.329 e.Å^{-3}	

Table S12. Crystal data and structure refinement for **17**.

Identification code	shelx	
Empirical formula	C6 H4 I2 O2	
Formula weight	361.89	
Temperature	120(2) K	
Wavelength	0.71073 Å	
Crystal system	Monoclinic	
Space group	P 21/n	
Unit cell dimensions	a = 15.290(3) Å	α = 90°.
	b = 4.5580(8) Å	β = 99.099(3)°.
	c = 23.861(4) Å	γ = 90°.
Volume	1642.0(5) Å^3	
Z	8	
Density (calculated)	2.928 Mg/m^3	
Absorption coefficient	7.599 mm^{-1}	
F(000)	1296	
Crystal size	0.176 x 0.145 x 0.075 mm^3	
Theta range for data collection	1.482 to 28.281°.	
Index ranges	-20<=h<=20, -6<=k<=6, -31<=l<=31	
Reflections collected	45297	
Independent reflections	4063 [R(int) = 0.0274]	
Completeness to theta = 25.242°	100.0 %	
Absorption correction	Numerical Mu From Formula	
Max. and min. transmission	1.000 and 0.492	
Refinement method	Full-matrix least-squares on F^2	
Data / restraints / parameters	4063 / 0 / 185	
Goodness-of-fit on F^2	1.270	
Final R indices [I>2sigma(I)]	R1 = 0.0176, wR2 = 0.0366	
R indices (all data)	R1 = 0.0186, wR2 = 0.0369	
Extinction coefficient	n/a	
Largest diff. peak and hole	0.767 and -0.572 e.Å^{-3}	

Table S13. Crystal data and structure refinement for **18**.

Identification code	shelx	
Empirical formula	C48 H54 Ag F6 N6 O4 P	
Formula weight	1031.81	
Temperature	100(2) K	
Wavelength	0.71073 Å	
Crystal system	Monoclinic	
Space group	C 2/c	
Unit cell dimensions	a = 18.6622(16) Å	α = 90°.
	b = 11.3451(9) Å	β = 91.035(6)°.
	c = 21.1959(14) Å	γ = 90°.
Volume	4487.0(6) $Å^3$	
Z	8	
Density (calculated)	1.527 Mg/m^3	
Absorption coefficient	0.563 mm^{-1}	
F(000)	2128	
Crystal size	0.486 x 0.385 x 0.282 mm^3	
Theta range for data collection	1.922 to 25.026°.	
Index ranges	-21<=h<=22, -13<=k<=13, -25<=l<=25	
Reflections collected	18532	
Independent reflections	3949 [R(int) = 0.0628]	
Completeness to theta = 25.026°	99.9 %	
Absorption correction	Numerical	
Refinement method	Full-matrix least-squares on F^2	
Data / restraints / parameters	3949 / 18 / 300	
Goodness-of-fit on F^2	1.041	
Final R indices [I>2sigma(I)]	R1 = 0.0552, wR2 = 0.1352	
R indices (all data)	R1 = 0.0777, wR2 = 0.1486	
Extinction coefficient	n/a	
Largest diff. peak and hole	1.591 and -1.449 $e.Å^{-3}$	

Table S14. Crystal data and structure refinement for **19**.

Identification code	shelx	
Empirical formula	C39 H33 Cu F6 N3 P3	
Formula weight	814.13	
Temperature	100 K	
Wavelength	1.54184 Å	
Crystal system	Monoclinic	
Space group	P 21/c	
Unit cell dimensions	a = 10.55110(10) Å	α = 90°.
	b = 31.9752(2) Å	β = 103.8890(10)°.
	c = 11.72890(10) Å	γ = 90°.
Volume	3841.33(6) Å^3	
Z	4	
Density (calculated)	1.408 Mg/m^3	
Absorption coefficient	2.514 mm^{-1}	
F(000)	1664	
Crystal size	0.3878 x 0.2208 x 0.1515 mm^3	
Theta range for data collection	2.764 to 76.160°.	
Index ranges	-12<=h<=13, -24<=k<=40, -13<=l<=14	
Reflections collected	32059	
Independent reflections	7981 [R(int) = 0.0244]	
Completeness to theta = 67.684°	100.0 %	
Absorption correction	Gaussian	
Max. and min. transmission	0.892 and 0.779	
Refinement method	Full-matrix least-squares on F^2	
Data / restraints / parameters	7981 / 211 / 566	
Goodness-of-fit on F^2	0.976	
Final R indices [I>2sigma(I)]	R1 = 0.0594, wR2 = 0.1580	
R indices (all data)	R1 = 0.0602, wR2 = 0.1585	
Extinction coefficient	n/a	
Largest diff. peak and hole	0.732 and -0.787 e.Å^{-3}	

Table S15. Crystal data and structure refinement for **20**.

Identification code	shelx	
Empirical formula	C38 H31 Cu F6 N3 P3	
Formula weight	800.11	
Temperature	100(2) K	
Wavelength	1.54184 Å	
Crystal system	Monoclinic	
Space group	I 2/a	
Unit cell dimensions	a = 17.2946(2) Å	α = 90°.
	b = 17.0163(2) Å	β = 92.9970(10)°.
	c = 26.3595(3) Å	γ = 90°.
Volume	7746.73(16) $Å^3$	
Z	8	
Density (calculated)	1.372 Mg/m^3	
Absorption coefficient	2.484 mm^{-1}	
F(000)	3264	
Crystal size	0.2420 x 0.0710 x 0.0585 mm^3	
Theta range for data collection	3.092 to 76.083°.	
Index ranges	-21<=h<=21, -21<=k<=21, -33<=l<=32	
Reflections collected	41242	
Independent reflections	8032 [R(int) = 0.0263]	
Completeness to theta = 67.684°	100.0 %	
Absorption correction	Gaussian	
Max. and min. transmission	0.899 and 0.687	
Refinement method	Full-matrix least-squares on F^2	
Data / restraints / parameters	8032 / 844 / 838	
Goodness-of-fit on F^2	1.205	
Final R indices [I>2sigma(I)]	R1 = 0.0536, wR2 = 0.1148	
R indices (all data)	R1 = 0.0566, wR2 = 0.1163	
Extinction coefficient	n/a	
Largest diff. peak and hole	0.460 and -0.428 $e.Å^{-3}$	

Table S16. Crystal data and structure refinement for **21**.

Identification code	shelx	
Empirical formula	C90 H78 Cu2 F18 N6 O P6 S4	
Formula weight	2042.72	
Temperature	100(2) K	
Wavelength	0.71073 Å	
Crystal system	Monoclinic	
Space group	P 21/c	
Unit cell dimensions	a = 14.7518(6) Å	α = 90°.
	b = 16.6999(6) Å	β = 94.492(2)°.
	c = 36.1854(14) Å	γ = 90°.
Volume	8887.0(6) $Å^3$	
Z	4	
Density (calculated)	1.527 Mg/m^3	
Absorption coefficient	0.770 mm^{-1}	
F(000)	4168	
Crystal size	0.280 x 0.260 x 0.190 mm^3	
Theta range for data collection	1.129 to 27.764°.	
Index ranges	-18<=h<=18, -21<=k<=20, -42<=l<=45	
Reflections collected	105009	
Independent reflections	17874 [R(int) = 0.0517]	
Completeness to theta = 25.242°	99.0 %	
Absorption correction	Semi-empirical from equivalents	
Max. and min. transmission	1.0000 and 0.8769	
Refinement method	Full-matrix least-squares on F^2	
Data / restraints / parameters	17874 / 2251 / 1270	
Goodness-of-fit on F^2	1.056	
Final R indices [I>2sigma(I)]	R1 = 0.0506, wR2 = 0.1078	
R indices (all data)	R1 = 0.0721, wR2 = 0.1168	
Extinction coefficient	n/a	
Largest diff. peak and hole	0.859 and -0.796 $e.Å^{-3}$	

Table S17. Crystal data and structure refinement for **22**.

Identification code	shelx	
Empirical formula	C90 H78 Cu2 F18 N6 O P6 S4	
Formula weight	2042.72	
Temperature	100(2) K	
Wavelength	0.71073 Å	
Crystal system	Monoclinic	
Space group	P 21/c	
Unit cell dimensions	a = 14.7518(6) Å	α = 90°.
	b = 16.6999(6) Å	β = 94.492(2)°.
	c = 36.1854(14) Å	γ = 90°.
Volume	8887.0(6) Å^3	
Z	4	
Density (calculated)	1.527 Mg/m^3	
Absorption coefficient	0.770 mm^{-1}	
F(000)	4168	
Crystal size	0.280 x 0.260 x 0.190 mm^3	
Theta range for data collection	1.129 to 27.764°.	
Index ranges	-18<=h<=18, -21<=k<=20, -42<=l<=45	
Reflections collected	105009	
Independent reflections	17874 [R(int) = 0.0517]	
Completeness to theta = 25.242°	99.0 %	
Absorption correction	Semi-empirical from equivalents	
Max. and min. transmission	1.0000 and 0.8769	
Refinement method	Full-matrix least-squares on F^2	
Data / restraints / parameters	17874 / 2251 / 1270	
Goodness-of-fit on F^2	1.056	
Final R indices [I>2sigma(I)]	R1 = 0.0506, wR2 = 0.1078	
R indices (all data)	R1 = 0.0721, wR2 = 0.1168	
Extinction coefficient	n/a	
Largest diff. peak and hole	0.859 and -0.796 e.Å^{-3}	

Table S18. Crystal data and structure refinement for **23**.

Identification code	shelx	
Empirical formula	C42 H35 Cu F6 N3 P3 S2	
Formula weight	916.30	
Temperature	120 K	
Wavelength	0.71073 Å	
Crystal system	Triclinic	
Space group	P -1	
Unit cell dimensions	a = 11.2880(10) Å	α = 79.062(2)°.
	b = 11.4770(10) Å	β = 79.312(2)°.
	c = 17.2810(10) Å	γ = 71.593(2)°.
Volume	2066.6(3) $Å^3$	
Z	2	
Density (calculated)	1.472 Mg/m^3	
Absorption coefficient	0.808 mm^{-1}	
F(000)	936	
Crystal size	0.472 x 0.377 x 0.193 mm^3	
Theta range for data collection	2.808 to 32.644°.	
Index ranges	-15<=h<=16, -17<=k<=16, -24<=l<=24	
Reflections collected	74184	
Independent reflections	13248 [R(int) = 0.0441]	
Completeness to theta = 25.242°	99.8 %	
Absorption correction	Semi-empirical from equivalents	
Refinement method	Full-matrix least-squares on F^2	
Data / restraints / parameters	13248 / 304 / 610	
Goodness-of-fit on F^2	1.051	
Final R indices [I>2sigma(I)]	R1 = 0.0382, wR2 = 0.0875	
R indices (all data)	R1 = 0.0549, wR2 = 0.0924	
Extinction coefficient	n/a	
Largest diff. peak and hole	0.654 and -0.493 $e.Å^{-3}$	

Table S19. Crystal data and structure refinement for **24**.

Identification code	shelx	
Empirical formula	C37 H28 Cu F9 N3 P3 S	
Formula weight	874.13	
Temperature	100(2) K	
Wavelength	1.54184 Å	
Crystal system	Monoclinic	
Space group	C 2/c	
Unit cell dimensions	a = 23.9215(7) Å	α = 90°.
	b = 14.5435(3) Å	β = 116.307(3)°.
	c = 23.3587(6) Å	γ = 90°.
Volume	7284.9(4) Å^3	
Z	8	
Density (calculated)	1.594 Mg/m^3	
Absorption coefficient	3.341 mm^{-1}	
F(000)	3536	
Crystal size	0.3721 x 0.1418 x 0.0287 mm^3	
Theta range for data collection	3.672 to 75.569°.	
Index ranges	-29<=h<=29, -18<=k<=18, -29<=l<=29	
Reflections collected	56482	
Independent reflections	7388 [R(int) = 0.0488]	
Completeness to theta = 67.684°	100.0 %	
Absorption correction	Semi-empirical from equivalents	
Max. and min. transmission	1.00000 and 0.54138	
Refinement method	Full-matrix least-squares on F^2	
Data / restraints / parameters	7388 / 265 / 611	
Goodness-of-fit on F^2	1.092	
Final R indices [I>2sigma(I)]	R1 = 0.0426, wR2 = 0.1049	
R indices (all data)	R1 = 0.0440, wR2 = 0.1063	
Extinction coefficient	n/a	
Largest diff. peak and hole	0.793 and -0.593 e.Å^{-3}	

Table S20. Crystal data and structure refinement for **25**.

Identification code	shelx	
Empirical formula	C37 H31 Cu F6 N3 P3 S	
Formula weight	820.16	
Temperature	100(2) K	
Wavelength	1.54184 Å	
Crystal system	Monoclinic	
Space group	C 2/c	
Unit cell dimensions	a = 23.6775(5) Å	α = 90°.
	b = 14.5990(2) Å	β = 116.184(3)°.
	c = 23.2669(5) Å	γ = 90°.
Volume	7217.3(3) $Å^3$	
Z	8	
Density (calculated)	1.510 Mg/m^3	
Absorption coefficient	3.207 mm^{-1}	
F(000)	3344	
Crystal size	0.3992 x 0.1699 x 0.1147 mm^3	
Theta range for data collection	3.673 to 71.511°.	
Index ranges	-29<=h<=28, -17<=k<=17, -28<=l<=20	
Reflections collected	20159	
Independent reflections	6928 [R(int) = 0.0199]	
Completeness to theta = 67.684°	100.0 %	
Absorption correction	Semi-empirical from equivalents	
Max. and min. transmission	1.00000 and 0.60799	
Refinement method	Full-matrix least-squares on F^2	
Data / restraints / parameters	6928 / 121 / 571	
Goodness-of-fit on F^2	1.005	
Final R indices [I>2sigma(I)]	R1 = 0.0308, wR2 = 0.0793	
R indices (all data)	R1 = 0.0323, wR2 = 0.0805	
Extinction coefficient	n/a	
Largest diff. peak and hole	0.679 and -0.378 $e.Å^{-3}$	

Table S21. Crystal data and structure refinement for **26**.

Identification code	shelx	
Empirical formula	C36 H29 Cu F6 N3 P3 S	
Formula weight	806.13	
Temperature	100(2) K	
Wavelength	1.54184 Å	
Crystal system	Monoclinic	
Space group	C 2/c	
Unit cell dimensions	a = 23.8839(9) Å	α = 90°.
	b = 14.4655(4) Å	β = 116.445(5)°.
	c = 23.3730(9) Å	γ = 90°.
Volume	7230.2(5) $Å^3$	
Z	8	
Density (calculated)	1.481 Mg/m^3	
Absorption coefficient	3.191 mm^{-1}	
F(000)	3280	
Crystal size	0.3122 x 0.1784 x 0.1313 mm^3	
Theta range for data collection	3.689 to 72.395°.	
Index ranges	-29<=h<=29, -17<=k<=17, -28<=l<=28	
Reflections collected	32399	
Independent reflections	6995 [R(int) = 0.0327]	
Completeness to theta = 67.684°	100.0 %	
Absorption correction	Gaussian	
Max. and min. transmission	0.963 and 0.918	
Refinement method	Full-matrix least-squares on F^2	
Data / restraints / parameters	6995 / 432 / 609	
Goodness-of-fit on F^2	1.060	
Final R indices [I>2sigma(I)]	R1 = 0.0358, wR2 = 0.0898	
R indices (all data)	R1 = 0.0367, wR2 = 0.0904	
Extinction coefficient	n/a	
Largest diff. peak and hole	0.566 and -0.407 $e.Å^{-3}$	

Table S22. Crystal data and structure refinement for **27**.

Identification code	shelx	
Empirical formula	C90 H84 Cu2 F12 N6 O P6 S4	
Formula weight	1934.77	
Temperature	100(2) K	
Wavelength	0.71073 Å	
Crystal system	Monoclinic	
Space group	P 21/c	
Unit cell dimensions	a = 14.693(8) Å	α = 90°.
	b = 16.896(9) Å	β = 93.869(8)°.
	c = 35.21(2) Å	γ = 90°.
Volume	8720(8) $Å^3$	
Z	4	
Density (calculated)	1.474 Mg/m^3	
Absorption coefficient	0.771 mm^{-1}	
F(000)	3976	
Crystal size	0.2000 x 0.2000 x 0.2000 mm^3	
Theta range for data collection	1.159 to 31.733°.	
Index ranges	-21<=h<=21, -24<=k<=24, -48<=l<=50	
Reflections collected	155122	
Independent reflections	26616 [R(int) = 0.0865]	
Completeness to theta = 25.242°	99.5 %	
Absorption correction	Semi-empirical from equivalents	
Max. and min. transmission	1.0000 and 0.7648	
Refinement method	Full-matrix least-squares on F^2	
Data / restraints / parameters	26616 / 620 / 1226	
Goodness-of-fit on F^2	1.190	
Final R indices [I>2sigma(I)]	R1 = 0.0883, wR2 = 0.1948	
R indices (all data)	R1 = 0.1121, wR2 = 0.2102	
Extinction coefficient	n/a	
Largest diff. peak and hole	1.294 and -1.049 $e.Å^{-3}$	

Table S23. Crystal data and structure refinement for **28**.

Identification code	shelx	
Empirical formula	C44 H52 Cu N6 O12	
Formula weight	920.45	
Temperature	100(2) K	
Wavelength	1.54184 Å	
Crystal system	Monoclinic	
Space group	P 21/n	
Unit cell dimensions	a = 11.3467(4) Å	α = 90°.
	b = 32.3727(12) Å	β = 108.319(4)°.
	c = 13.0107(4) Å	γ = 90°.
Volume	4536.9(3) Å^3	
Z	4	
Density (calculated)	1.348 Mg/m^3	
Absorption coefficient	1.247 mm^{-1}	
F(000)	1932	
Crystal size	0.4422 x 0.0824 x 0.0333 mm^3	
Theta range for data collection	2.730 to 66.597°.	
Index ranges	-13<=h<=13, -25<=k<=38, -15<=l<=14	
Reflections collected	16212	
Independent reflections	7966 [R(int) = 0.0538]	
Completeness to theta = 66.597°	99.2 %	
Absorption correction	Semi-empirical from equivalents	
Max. and min. transmission	1.00000 and 0.77692	
Refinement method	Full-matrix least-squares on F^2	
Data / restraints / parameters	7966 / 7 / 587	
Goodness-of-fit on F^2	1.010	
Final R indices [I>2sigma(I)]	R1 = 0.0491, wR2 = 0.1025	
R indices (all data)	R1 = 0.0792, wR2 = 0.1165	
Extinction coefficient	n/a	
Largest diff. peak and hole	0.314 and -0.571 e.Å^{-3}	

Table S24. Crystal data and structure refinement for **29a**.

Identification code	shelx	
Empirical formula	C54 H48 Cu I2 N12	
Formula weight	1182.39	
Temperature	120(2) K	
Wavelength	0.71073 Å	
Crystal system	Triclinic	
Space group	P -1	
Unit cell dimensions	a = 8.6919(2) Å	α = 69.7580(10)°.
	b = 9.7073(2) Å	β = 76.0400(10)°.
	c = 13.8462(3) Å	γ = 76.0070(10)°.
Volume	1047.54(4) $Å^3$	
Z	1	
Density (calculated)	1.644 Mg/m^3	
Absorption coefficient	2.041 mm^{-1}	
F(000)	514	
Crystal size	0.319 x 0.176 x 0.078 mm^3	
Theta range for data collection	1.592 to 36.349°.	
Index ranges	-14<=h<=14, -16<=k<=16, -23<=l<=23	
Reflections collected	77622	
Independent reflections	10125 [R(int) = 0.0226]	
Completeness to theta = 25.242°	100.0 %	
Absorption correction	Numerical Mu From Formula	
Max. and min. transmission	1.0000 and 0.8459	
Refinement method	Full-matrix least-squares on F^2	
Data / restraints / parameters	10125 / 332 / 362	
Goodness-of-fit on F^2	1.064	
Final R indices [I>2sigma(I)]	R1 = 0.0212, wR2 = 0.0572	
R indices (all data)	R1 = 0.0240, wR2 = 0.0589	
Extinction coefficient	n/a	
Largest diff. peak and hole	1.199 and -0.749 $e.Å^{-3}$	

Table S25. Crystal data and structure refinement for **29b**.

Identification code	shelx	
Empirical formula	C54 H48 Cu I2 N12	
Formula weight	1182.39	
Temperature	120(2) K	
Wavelength	0.71073 Å	
Crystal system	Monoclinic	
Space group	P 21/c	
Unit cell dimensions	a = 11.5813(13) Å	α = 90°.
	b = 17.1507(19) Å	β = 95.533(2)°.
	c = 12.6335(14) Å	γ = 90°.
Volume	2497.7(5) Å^3	
Z	4	
Density (calculated)	1.572 Mg/m^3	
Absorption coefficient	1.724 mm^{-1}	
F(000)	1182	
Crystal size	0.128 x 0.093 x 0.093 mm^3	
Theta range for data collection	1.767 to 27.485°.	
Index ranges	-15<=h<=15, -22<=k<=22, -16<=l<=16	
Reflections collected	70085	
Independent reflections	5737 [R(int) = 0.0403]	
Completeness to theta = 25.242°	100.0 %	
Absorption correction	Numerical Mu From Formula	
Max. and min. transmission	1.0000 and 0.8850	
Refinement method	Full-matrix least-squares on F^2	
Data / restraints / parameters	5737 / 0 / 316	
Goodness-of-fit on F^2	1.279	
Final R indices [I>2sigma(I)]	R1 = 0.0431, wR2 = 0.1000	
R indices (all data)	R1 = 0.0479, wR2 = 0.1018	
Extinction coefficient	n/a	
Largest diff. peak and hole	0.676 and -1.153 e.Å^{-3}	

Table S26. Crystal data and structure refinement for **30**.

Identification code	shelx	
Empirical formula	C62 H54 Cl8 F6 Ir N6 P	
Formula weight	1503.88	
Temperature	100(2) K	
Wavelength	1.54184 Å	
Crystal system	Triclinic	
Space group	P -1	
Unit cell dimensions	a = 10.0319(2) Å	α = 78.5440(10)°.
	b = 15.6278(2) Å	β = 84.8400(10)°.
	c = 20.0644(3) Å	γ = 89.0110(10)°.
Volume	3070.46(9) $Å^3$	
Z	2	
Density (calculated)	1.627 Mg/m^3	
Absorption coefficient	8.196 mm^{-1}	
F(000)	1500	
Crystal size	0.2418 x 0.1959 x 0.1587 mm^3	
Theta range for data collection	2.885 to 66.600°.	
Index ranges	-11<=h<=11, -18<=k<=18, -23<=l<=23	
Reflections collected	69002	
Independent reflections	10811 [R(int) = 0.0406]	
Completeness to theta = 66.601°	99.8 %	
Absorption correction	Gaussian	
Max. and min. transmission	0.758 and 0.647	
Refinement method	Full-matrix least-squares on F^2	
Data / restraints / parameters	10811 / 213 / 819	
Goodness-of-fit on F^2	1.195	
Final R indices [I>2sigma(I)]	R1 = 0.0497, wR2 = 0.1324	
R indices (all data)	R1 = 0.0508, wR2 = 0.1331	
Extinction coefficient	n/a	
Largest diff. peak and hole	1.405 and -1.363 $e.Å^{-3}$	

Table S27. Crystal data and structure refinement for **31**.

Identification code	shelx	
Empirical formula	C168 H120 Cl8 F18 Ir4 N24 P3	
Formula weight	3962.27	
Temperature	100(2) K	
Wavelength	1.54184 Å	
Crystal system	Triclinic	
Space group	P -1	
Unit cell dimensions	a = 13.1324(4) Å	α = 62.476(4)°.
	b = 19.1510(8) Å	β = 72.684(3)°.
	c = 19.6621(8) Å	γ = 74.904(3)°.
Volume	4142.2(3) Å^3	
Z	2	
Density (calculated)	1.588 Mg/m^3	
Absorption coefficient	8.195 mm^{-1}	
F(000)	1947	
Crystal size	0.1700 x 0.1041 x 0.0474 mm^3	
Theta range for data collection	2.590 to 73.544°.	
Index ranges	-16<=h<=16, -23<=k<=22, -24<=l<=21	
Reflections collected	47011	
Independent reflections	16232 [R(int) = 0.0615]	
Completeness to theta = 67.684°	99.8 %	
Absorption correction	Gaussian	
Max. and min. transmission	0.929 and 0.813	
Refinement method	Full-matrix least-squares on F^2	
Data / restraints / parameters	16232 / 241 / 1015	
Goodness-of-fit on F^2	1.039	
Final R indices [I>2sigma(I)]	R1 = 0.0580, wR2 = 0.1502	
R indices (all data)	R1 = 0.0822, wR2 = 0.1680	
Extinction coefficient	n/a	
Largest diff. peak and hole	2.795 and -1.936 e.Å^{-3}	

Table S28. Crystal data and structure refinement for **32**.

Identification code	shelx	
Empirical formula	C42 H48 F6 Ir N8 P	
Formula weight	1002.05	
Temperature	120 K	
Wavelength	0.71073 Å	
Crystal system	Monoclinic	
Space group	P 21/c	
Unit cell dimensions	a = 15.0310(10) Å	α = 90°.
	b = 22.847(2) Å	β = 111.216(4)°.
	c = 13.3080(10) Å	γ = 90°.
Volume	4260.4(6) $Å^3$	
Z	4	
Density (calculated)	1.562 Mg/m^3	
Absorption coefficient	3.238 mm^{-1}	
F(000)	2008	
Crystal size	0.407 x 0.297 x 0.171 mm^3	
Theta range for data collection	2.300 to 25.027°.	
Index ranges	-17<=h<=17, -27<=k<=27, -15<=l<=15	
Reflections collected	122329	
Independent reflections	7497 [R(int) = 0.0611]	
Completeness to theta = 25.027°	99.7 %	
Absorption correction	Semi-empirical from equivalents	
Max. and min. transmission	1.000 and 0.693	
Refinement method	Full-matrix least-squares on F^2	
Data / restraints / parameters	7497 / 396 / 677	
Goodness-of-fit on F^2	1.041	
Final R indices [I>2sigma(I)]	R1 = 0.0212, wR2 = 0.0501	
R indices (all data)	R1 = 0.0268, wR2 = 0.0527	
Extinction coefficient	n/a	
Largest diff. peak and hole	0.795 and -0.391 $e.Å^{-3}$	

Table S29. Crystal data and structure refinement for **33**.

Identification code	shelx	
Empirical formula	C71 H70 B Cl6 F4 Ir N4	
Formula weight	1471.04	
Temperature	100(2) K	
Wavelength	1.54184 Å	
Crystal system	Monoclinic	
Space group	P 21/c	
Unit cell dimensions	a = 18.4758(4) Å	α = 90°.
	b = 13.2942(3) Å	β = 91.276(2)°.
	c = 27.1536(6) Å	γ = 90°.
Volume	6667.8(3) Å^3	
Z	5	
Density (calculated)	1.465 Mg/m^3	
Absorption coefficient	6.539 mm^{-1}	
F(000)	2976	
Crystal size	0.1213 x 0.0866 x 0.0701 mm^3	
Theta range for data collection	2.392 to 66.601°.	
Index ranges	-21<=h<=19, -15<=k<=15, -26<=l<=32	
Reflections collected	36710	
Independent reflections	11778 [R(int) = 0.0564]	
Completeness to theta = 66.601°	100.0 %	
Absorption correction	Gaussian	
Max. and min. transmission	0.952 and 0.919	
Refinement method	Full-matrix least-squares on F^2	
Data / restraints / parameters	11778 / 386 / 917	
Goodness-of-fit on F^2	1.224	
Final R indices [I>2sigma(I)]	R1 = 0.0898, wR2 = 0.2117	
R indices (all data)	R1 = 0.0965, wR2 = 0.2159	
Extinction coefficient	n/a	
Largest diff. peak and hole	2.628 and -1.932 e.Å^{-3}	

Table S30. Crystal data and structure refinement for **34**.

Identification code	shelx	
Empirical formula	C85 H82 Cl8 Ir2 N4	
Formula weight	1827.59	
Temperature	100 K	
Wavelength	1.54184 Å	
Crystal system	Triclinic	
Space group	P -1	
Unit cell dimensions	a = 15.06350(10) Å	α = 81.2230(10)°.
	b = 15.1212(2) Å	β = 82.7260(10)°.
	c = 18.5667(2) Å	γ = 73.5110(10)°.
Volume	3992.16(8) $Å^3$	
Z	3	
Density (calculated)	1.520 Mg/m^3	
Absorption coefficient	9.173 mm^{-1}	
F(000)	1820	
Crystal size	0.2685 x 0.1859 x 0.1057 mm^3	
Theta range for data collection	2.417 to 66.600°.	
Index ranges	-17<=h<=17, -17<=k<=17, -22<=l<=22	
Reflections collected	118818	
Independent reflections	14106 [R(int) = 0.0373]	
Completeness to theta = 66.600°	100.0 %	
Absorption correction	Gaussian	
Max. and min. transmission	0.844 and 0.669	
Refinement method	Full-matrix least-squares on F^2	
Data / restraints / parameters	14106 / 240 / 960	
Goodness-of-fit on F^2	1.030	
Final R indices [I>2sigma(I)]	R1 = 0.0220, wR2 = 0.0545	
R indices (all data)	R1 = 0.0233, wR2 = 0.0556	
Extinction coefficient	n/a	
Largest diff. peak and hole	0.959 and -0.868 $e.Å^{-3}$	

Table S31. Crystal data and structure refinement for **35**.

Identification code	shelx	
Empirical formula	C50 H44 F6 Ir N4 P	
Formula weight	1038.06	
Temperature	100 K	
Wavelength	1.54184 Å	
Crystal system	Orthorhombic	
Space group	P b c a	
Unit cell dimensions	a = 15.5085(2) Å	α = 90°.
	b = 15.0445(3) Å	β = 90°.
	c = 36.8769(4) Å	γ = 90°.
Volume	8604.0(2) Å^3	
Z	8	
Density (calculated)	1.603 Mg/m^3	
Absorption coefficient	6.925 mm^{-1}	
F(000)	4144	
Crystal size	0.148 x 0.057 x 0.043 mm^3	
Theta range for data collection	2.396 to 66.599°.	
Index ranges	-18<=h<=18, -15<=k<=17, -43<=l<=43	
Reflections collected	47802	
Independent reflections	7573 [R(int) = 0.0310]	
Completeness to theta = 66.599°	99.7 %	
Absorption correction	Gaussian	
Max. and min. transmission	0.905 and 0.764	
Refinement method	Full-matrix least-squares on F^2	
Data / restraints / parameters	7573 / 0 / 565	
Goodness-of-fit on F^2	1.212	
Final R indices [I>2sigma(I)]	R1 = 0.0310, wR2 = 0.0600	
R indices (all data)	R1 = 0.0360, wR2 = 0.0616	
Extinction coefficient	n/a	
Largest diff. peak and hole	0.793 and -1.128 e.Å^{-3}	

Table S32. Crystal data and structure refinement for **36**.

Identification code	shelx	
Empirical formula	C28 H24 F6 N5 P Pt S2	
Formula weight	834.70	
Temperature	100(2) K	
Wavelength	0.71073 Å	
Crystal system	Monoclinic	
Space group	P 21/c	
Unit cell dimensions	a = 11.770(4) Å	α = 90°.
	b = 15.330(4) Å	β = 95.658(5)°.
	c = 15.992(5) Å	γ = 90°.
Volume	2871.4(15) $Å^3$	
Z	4	
Density (calculated)	1.931 Mg/m^3	
Absorption coefficient	5.157 mm^{-1}	
F(000)	1624	
Crystal size	0.123 x 0.070 x 0.050 mm^3	
Theta range for data collection	2.188 to 25.027°.	
Index ranges	-14<=h<=14, -14<=k<=18, -18<=l<=19	
Reflections collected	18895	
Independent reflections	5057 [R(int) = 0.0580]	
Completeness to theta = 25.027°	100.0 %	
Absorption correction	Semi-empirical from equivalents	
Max. and min. transmission	1.0000 and 0.7862	
Refinement method	Full-matrix least-squares on F^2	
Data / restraints / parameters	5057 / 126 / 452	
Goodness-of-fit on F^2	1.154	
Final R indices [I>2sigma(I)]	R1 = 0.0447, wR2 = 0.0924	
R indices (all data)	R1 = 0.0481, wR2 = 0.0942	
Extinction coefficient	n/a	
Largest diff. peak and hole	1.284 and -1.365 $e.Å^{-3}$	

Table S33. Crystal data and structure refinement for **37**.

Identification code	shelx	
Empirical formula	C92 H74 B2 F8 N4 P4 Rh2	
Formula weight	1738.87	
Temperature	100 K	
Wavelength	0.71073 Å	
Crystal system	Monoclinic	
Space group	P 21/c	
Unit cell dimensions	a = 23.497(13) Å	α = 90°.
	b = 35.31(5) Å	β = 90°.
	c = 10.557(9) Å	γ = 90°.
Volume	8760(15) Å^3	
Z	4	
Density (calculated)	1.319 Mg/m^3	
Absorption coefficient	0.513 mm^{-1}	
F(000)	3544	
Crystal size	0.3700 x 0.1190 x 0.0660 mm^3	
Theta range for data collection	1.443 to 25.025°.	
Index ranges	-27<=h<=27, -42<=k<=42, -12<=l<=12	
Reflections collected	69099	
Independent reflections	15413 [R(int) = 0.0628]	
Completeness to theta = 25.025°	99.8 %	
Absorption correction	Semi-empirical from equivalents	
Max. and min. transmission	1.0000 and 0.7528	
Refinement method	Full-matrix least-squares on F^2	
Data / restraints / parameters	15413 / 282 / 1067	
Goodness-of-fit on F^2	1.063	
Final R indices [I>2sigma(I)]	R1 = 0.0577, wR2 = 0.1312	
R indices (all data)	R1 = 0.0699, wR2 = 0.1411	
Extinction coefficient	n/a	
Largest diff. peak and hole	0.918 and -0.969 e.Å^{-3}	

Table S34. Crystal data and structure refinement for **38**.

Identification code	shelx	
Empirical formula	C33 H53 B F4 N P2 Rh	
Formula weight	715.42	
Temperature	133(2) K	
Wavelength	0.71073 Å	
Crystal system	Triclinic	
Space group	P -1	
Unit cell dimensions	a = 8.7780(10) Å	α = 96.628(2)°.
	b = 11.3910(10) Å	β = 94.877(2)°.
	c = 17.4560(10) Å	γ = 98.610(2)°.
Volume	1704.9(3) $Å^3$	
Z	2	
Density (calculated)	1.394 Mg/m^3	
Absorption coefficient	0.640 mm^{-1}	
F(000)	748	
Crystal size	0.432 x 0.226 x 0.124 mm^3	
Theta range for data collection	2.359 to 25.000°.	
Index ranges	-9<=h<=10, -13<=k<=13, -20<=l<=20	
Reflections collected	31074	
Independent reflections	5991 [R(int) = 0.0307]	
Completeness to theta = 25.242°	96.9 %	
Absorption correction	Semi-empirical from equivalents	
Max. and min. transmission	1.000 and 0.907	
Refinement method	Full-matrix least-squares on F^2	
Data / restraints / parameters	5991 / 0 / 397	
Goodness-of-fit on F^2	1.048	
Final R indices [I>2sigma(I)]	R1 = 0.0204, wR2 = 0.0493	
R indices (all data)	R1 = 0.0235, wR2 = 0.0521	
Extinction coefficient	n/a	
Largest diff. peak and hole	0.595 and -0.424 $e.Å^{-3}$	

References

1. Karl, T. R.; Trenberth, K. E. **2016**, *302* (5651), 1719–1723.

2. Treut, L.; Somerville, R.; Cubasch, U.; Ding, Y.; Mauritzen, C.; Mokssit, a; Peterson, T.; Prather, M.; Qin, D.; Manning, M.; Chen, Z.; Marquis, M.; Averyt, K. B.; Tignor, M. *Earth* **2007**, *Chapter 1* (October), 93–127.

3. Blasing, T. J. Recent Greenhouse Gas Concentrations http://cdiac.ornl.gov/pns/current_ghg.html (accessed Apr 14, 2017).

4. Climate Change 2007: Synthesis Report https://www.ipcc.ch/publications_and_data/ar4/syr/en/spms2.html (accessed Apr 14, 2017).

5. Lowe, D. C.; Zealand, N. *Change* **2007**, *30* (22), 129–234.

6. IPCC WG1 - The physical science basis. *Fifth Assess. Rep.* **2013**, No. January 2014, 1–177.

7. Stocker, T. F.; Dahe, Q.; Plattner, G.-K.; Alexander, L. V.; Allen, S. K.; Bindoff, N. L.; Bréon, F.-M.; Church, J. A.; Cubash, U.; Emori, S.; Forster, P.; Friedlingstein, P.; Talley, L. D.; Vaughan, D. G.; Xie, S.-P. *Clim. Chang. 2013 Phys. Sci. Basis. Contrib. Work. Gr. I to Fifth Assess. Rep. Intergov. Panel Clim. Chang.* **2013**, 33–115.

8. Press, R. J.; Santhanam, K. S. V.; Miri, M. J.; Bailey, A. V.; Takacs, G. A. *Introduciton to Hydrogen Technology*; John Wiley & Sons, Inc.: Hoboken, New Jersey, 2009.

9. Collodi, G. *Chem. Eng. Trans.* **2010**, *19* (37), 1–6.

10. How Coal Gasification Power Plants Work https://energy.gov/fe/how-coal-gasification-power-plants-work (accessed Apr 15, 2017).

11. Carmo, M.; Fritz, D. L.; Mergel, J.; Stolten, D. *Int. J. Hydrogen Energy* **2013**, *38* (12), 4901–4934.

12. Schlapbach, L.; Schlapbach, L.; Züttel, A. *Nature* **2001**, *414* (May 2016), 353–358.

13. Britt, D. *Chem. Soc. Rev.* **2009**, *38* (5), 1294–1314.

14. Wang, X. Sen; Ma, S.; Forster, P. M.; Yuan, D.; Eckert, J.; López, J. J.; Murphy, B. J.; Parise, J. B.; Zhou, H. C. *Angew. Chemie - Int. Ed.* **2008**, *47* (38), 7263–7266.

15. Dincă, M.; Dailly, A.; Long, J. R. *Chem. - A Eur. J.* **2008**, *14* (33), 10280–10285.

16. Cheon, Y. E.; Suh, M. P. *Angew. Chemie - Int. Ed.* **2009**, *48* (16), 2899–2903.

17. Lee, Y. G.; Moon, H. R.; Cheon, Y. E.; Suh, M. P. *Angew. Chemie - Int. Ed.* **2008**, *47* (40), 7741–7745.

18. Kaye, S. S.; Dailly, A.; Yaghi, O. M.; Long, J. R. *J. Am. Chem. Soc.* **2007**, *129* (46), 14176–14177.

19. Li, Y.; Yang, R. T. *Langmuir* **2007**, *23* (26), 12937–12944.

20. Latroche, M.; Surble, S.; Serre, C.; Mellot-Draznieks, C.; Llewellyn, P. L.; Lee, J. H.; Chang, J. S.; Sung, H. J.; Ferey, G. *Angew. Chemie - Int. Ed.* **2006**, *45* (48), 8227–8231.

21. Preuster, P.; Papp, C.; Wasserscheid, P. *Acc. Chem. Res.* **2017**, *50* (1), 74–85.

22. Schildhauer, T.; Newson, E.; Muller, S. *J. Catal.* **2001**, *198*, 355–358.

23. Yolcular, S.; Olgun, Ö. *Catal. Today* **2008**, *138* (3–4), 198–202.

24. Bruckner, N.; Obesser, K.; Bosmann, A.; Teichmann, D.; Arlt, W.; Dungs, J.; Wasserscheid, P. *ChemSusChem* **2014**, *7*, 229–235.

25. Stark, K.; Keil, P.; Schung, S.; Muller, K.; Wasserscheid, P.; Arlt, W. *J. Chem. Eng. Data* **2016**, *4* (61), 1441–1448.

26. Dean, D.; Davis, B.; Jessop, P. J. *New J. Chem.* **2011**, *35*, 417–422.

27. Yamaguchi, R.; Ikeda, C.; Takahashi, Y.; Fujita, K. I. *J. Am. Chem. Soc.* **2009**, *131* (24), 8410–8412.

28. Lighting Efficiency https://www.c2es.org/technology/factsheet/LightingEfficiency (accessed Apr 15, 2017).

29. Global Greenhouse Gas Emissions Data https://www.epa.gov/ghgemissions/global-greenhouse-gas-emissions-data (accessed Apr 15, 2017).

30. Armaroli, N.; Balzani, V. *Energy Environ. Sci.* **2011**, *4* (9), 3193–3222.

31. LED Light Bulbs: Comparison Charts http://eartheasy.com/live_led_bulbs_comparison.html (accessed Apr 22, 2017).

32. Krames, M. R.; Shchekin, O. B.; Mueller-Mach, R.; Mueller, G. O.; Zhou, L.; Harbers, G.; Craford, M. G. *IEEE/OSA J. Disp. Technol.* **2007**, *3* (2), 160–175.

33. Morkoc, H.; Mohammad, S. N. *Science (80-.).* **1995**, *267* (5194), 51–55.

34. The Light-Emitting Diode http://www.electronics-tutorials.ws/diode/diode_8.html (accessed Apr 22, 2017).

35. Geffroy, B.; le Roy, P.; Prat, C. *Polym. Int.* **2006**, *55* (6), 572–582.

36. Helfrich, W.; Schneider, W. G. *Phys. Rev. Lett.* **1965**, *14*, 229–231.

37. Tang, C. W.; Van Slyke, S. A. *Appl. Phys. Lett.* **1987**, *51* (12), 913–915.

38. Gong, S.; Yang, C.; Qin, J. *Chem. Soc. Rev.* **2012**, *41* (14), 4797–4807.

39. Liu, M. S.; Niu, Y.; Luo, J.; Chen, B.; Kim, T.; Bardecker, J.; Jen, A. K. -Y. *J. Macromol. Sci. Part C Polym. Rev.* **2006**, *46* (1), 7–26.

40. Meier, S. B.; Tordera, D.; Pertegás, A.; Roldán-Carmona, C.; Ortí, E.; Bolink, H. J. *Mater. Today* **2014**, *17* (5), 217–223.

41. Wu, C. C.; Wu, C. I.; Sturm, J. C.; Kahn, A. *Appl. Phys. Lett.* **1997**, *70* (11), 1348–1350.

42. Kim, J. S.; Cacialli, F.; Cola, A.; Gigli, G.; Cingolani, R. *Appl. Phys. Lett.* **1999**, *75* (1), 19–21.

43. Baldo, M. A.; O'Brien, D. F.; You, Y.; Shoustikov, A.; Sibley, S.; Thompson, M. E.; Forrest, S. R. *Nature* **1998**, *395*, 151–154.

44. Adachi, C.; Baldo, M. A.; Thompson, M. E.; Forrest, S. R. *J. Appl. Phys.* **2001**, *10*, 5048–5051.

45. O'Brien, D. F.; Baldo, M. a.; Thompson, M. E.; Forrest, S. R. *Appl. Phys. Lett.* **1999**, *74* (3), 442.

46. Peng, B.; Chen, J. *Energy Environ. Sci.* **2008**, 479–483.

47. Ramachandran, P. V.; Gagare, P. D. *Inorg. Chem.* **2007**, *46* (19), 7810–7817.

48. Bluhm, M. E. .; Bradley, M. G. .; Butterick III, R. .; Kusari, U. .; Sneddon, L. G. . *ACS Natl. Meet. B. Abstr.* **2006**, *232*, 7748–7749.

49. Wideman, T.; Sneddon, L. G.; T.Widman; L.G.Sheddon. *Inorg. Chem.* **1995**, *34* (4), 1002–1003.

50. Gutowska, A.; Li, L.; Shin, Y.; Wang, C. M.; Li, X. S.; Linehan, J. C.; Smith, R. S.; Kay, B. D.; Schmid, B.; Shaw, W.; Gutowski, M.; Autrey, T. *Angew. Chemie - Int. Ed.* **2005**, *44* (23), 3578–3582.

51. Nelson, D. J.; Truscott, B. J.; Egbert, J. D.; Nolan, S. P. *Organometallics* **2013**, *32* (13), 3769–3772.

52. San Nacianceno, V.; Azpeitia, S.; Ibarlucea, L.; Mendicute-Fierro, C.; Rodriguez-Dieguez, A.; Seco, J. M.; San Sebastian, E.; Garralda, M. A. *Dalt. Trans.* **2015**, *44*, 13141–13155.

53. Lapin, N. V.; D'yankova, N. Y. *Inorg. Mater.* **2013**, *49*, 975–979.

54. Jiang, H. L.; Xu, Q. *Catal. Today* **2011**, *170*, 56–63.

55. Yan, J. M.; Zhang, X. B.; Akita, T.; Haruta, M.; Xu, Q. *J. Am. Chem. Soc.* **2010**, *132*, 5326–5327.

56. Jiang, H. L.; Umegaki, T.; Akita, T.; Zhang, X. B.; Haruta, M.; Xu, Q. *Chem. - A Eur. J.* **2010**, *16*, 3132–3137.

57. Zhang, X.; Kam, L.; Trerise, R.; Williams, T. J. *Acc. Chem. Res.* **2017**, *50*, 86–95.

58. Vance, J. R.; Robertson, A. P. M.; Lee, K.; Manners, I. *Chem. - A Eur. J.* **2011**, *17* (15), 4099–4103.

59. Baker, R. T.; Gordon, J. C.; Hamilton, C. W.; Henson, N. J.; Lin, P. H.; Maguire, S.; Murugesu, M.; Scott, B. L.; Smythe, N. C. *J. Am. Chem. Soc.* **2012**, *134* (12), 5598–5609.

60. Bhattacharya, P.; Krause, J. A.; Guan, H. *J. Am. Chem. Soc.* **2014**, *136* (31), 11153–11161.

61. Buss, J. A.; Edouard, G. A.; Cheng, C.; Shi, J.; Agapie, T. *J. Am. Chem. Soc.* **2014**, *136*, 11272–11275.

62. Denney, M. C.; Pons, V.; Hebden, T. J.; Heinekey, D. M.; Goldberg, K. I. *J. Am. Chem. Soc.* **2006**, *128* (37), 12048–12049.

63. Dietrich, B. L.; Goldberg, K. I.; Heinekey, D. M.; Autrey, T.; Linehan, J. C. *Inorg. Chem.* **2008**, *47* (19), 8583–8585.

64. Jaska, C. A.; Temple, K.; Lough, A. J.; Manners, I. *J. Am. Chem. Soc.* **2003**, *125* (31), 9424–9434.

65. Jaska, C. A.; Manners, I. *J. Am. Chem. Soc.* **2004**, *126* (5), 1334–1335.

66. Shrestha, R. P.; Diyabalanage, H. V. K.; Semelsberger, T. A.; Ott, K. C.; Burrell, A. K. *Int. J. Hydrogen Energy* **2009**, *34* (6), 2616–2621.

67. Douglas, T. M.; Chaplin, A. B.; Weller, A. S. *J. Am. Chem. Soc.* **2008**, *130* (44), 14432–14433.

68. Alcaraz, G.; Sabo-Etienne, S. *Angew. Chemie - Int. Ed.* **2010**, *49* (40), 7170–7179.

69. Keaton, R. J.; Blacquiere, J. M.; Baker, R. T. *J. Am. Chem. Soc.* **2007**, *129* (7), 1844–1845.

70. Kim, S. K.; Han, W. S.; Kim, T. J.; Kim, T. Y.; Nam, S. W.; Mitoraj, M.; Piekoś, L.; Michalak, A.; Hwang, S. J.; Kang, S. O. *J. Am. Chem. Soc.* **2010**, *132* (29), 9954–9955.

71. Kim, S. K.; Hong, S. A.; Son, H. J.; Han, W. S.; Michalak, A.; Hwang, S. J.; Kang, S. O. *Dalton Trans.* **2015**, *44* (16), 7373–7381.

72. Blaquiere, N.; Diallo-Garcia, S.; Gorelsky, S. I.; Black, D. A.; Fagnou, K. *J. Am. Chem. Soc.* **2008**, *130* (43), 14034–14035.

73. Käss, M.; Friedrich, A.; Drees, M.; Schneider, S. *Angew. Chem. Int. Ed. Engl.* **2009**, *48* (5), 905–907.

74. Rossin, A.; Rossi, A.; Peruzzini, M.; Zanobini, F. *Chempluschem* **2014**, *79* (9), 1316–1325.

75. Boulho, C.; Djukic, J.-P. *Dalton Trans.* **2010**, *39* (38), 8893–8905.

76. Staubitz, A.; Sloan, M. E.; Robertson, A. P. M.; Friedrich, A.; Schneider, S.; Gates, P. J.; Manners, I.; Schmedt auf der Guenne, J. *J. Am. Chem. Soc.* **2010**, *132*, 13332–13345.

77. Goettker-Schnetmann, I.; Brookhart, M. *J. Am. Chem. Soc.* **2004**, *126* (30), 9330–9338.

78. White, P.; Brookhart, M.; Goettker-Schnetmann, I. *J. Am. Chem. Soc.* **2004**, *126* (6), 1804–1811.

79. Song, C.; Swager, T. M. *Macromolecules* **2005**, *38* (11), 4569–4576.

80. Thomsen, I.; Torssell, K. B. G. *Acta Chem. Scand.* **1991**, *45*, 539–542.

81. Liang, Z.; Ma, S.; Yu, J.; Xu, R. *Tetrahedron* **2007**, *63* (4), 977–985.

82. Boddeker, K. W.; Shore, S. G.; Bunting, R. K. *J. Am. Chem. Soc.* **1966**, *88*, 4396–4401.

83. White, P. S.; Brookhart, M.; Gottker-Schnetmann, I. *Organometallics* **2004**, *23* (8), 1766–1776.

84. Williams, J. A. G. *Top. Curr. Chem.* **2007**, *281* (July 12, 2007), 205–268.

85. Rice, S. F.; Gray, H. B. *J. Am. Chem. Soc* **1983**, *105*, 4571–4575.

86. Lai, S.-W.; Chan, M. C.-W.; Cheung, T.-C.; Peng, S.-M.; Che, C.-M. *Inorg. Chem.* **1999**, *38*, 4046–4055.

87. Lu, W.; Chan, M. C. W.; Zhu, N.; Che, C. M.; Li, C.; Hui, Z. *J. Am. Chem. Soc.* **2004**, *126* (24), 7639–7651.

88. Ma, B.; Li, J.; Djurovich, P. I.; Yousufuddin, M.; Bau, R.; Thompson, M. E. *J. Am. Chem. Soc.* **2005**, *127* (1), 28–29.

89. Ding, J.; Pan, D.; Tung, C. H.; Wu, L. Z. *Inorg. Chem.* **2008**, *47* (12), 5099–5106.

90. Chakraborty, A.; Deaton, J. C.; Haefele, A.; Castellano, F. N. *Organometallics* **2013**, *32* (14), 3819–3829.

91. Han, M.; Tian, Y.; Yuan, Z.; Zhu, L.; Ma, B. *Angew. Chemie Int. Ed.* **2014**, *53*, 10908–10912.

92. Van Reenen, S.; Matyba, P.; Dzwilewski, A.; Janssen, R. A. J.; Edman, L.; Kemerink, M. *J. Am. Chem. Soc.* **2010**, *132* (39), 13776–13781.

93. Wang, Y. M.; Teng, F.; Hou, Y. B.; Xu, Z.; Wang, Y. S.; Fu, W. F. *Appl. Phys. Lett.* **2005**, *87* (23), 1–3.

94. Slinker, J. D.; DeFranco, J. a; Jaquith, M. J.; Silveira, W. R.; Zhong, Y.; Moran-Mirabal, J. M.; Craighead, H. G.; Abruña, H. D.; Marohn, J. a; Malliaras, G. G. *Nat. Mater.* **2007**, *6* (11), 894–899.

95. Bastatas, L. D.; Lin, K. Y.; Moore, M. D.; Suhr, K. J.; Bowler, M. H.; Shen, Y.; Holliday, B. J.; Slinker, J. D. *Langmuir* **2016**, *32* (37), 9468–9474.

96. Costa, R. D.; Fernández, G.; Sánchez, L.; Martín, N.; Ortí, E.; Bolink, H. J. *Chem. - A Eur. J.* **2010**, *16* (32), 9855–9863.

97. Slinker, J. D.; Rivnay, J.; Moskowitz, J. S.; Parker, J. B.; Bernhard, S.; Abruna, H. D.; Malliaras, G. G. *J. Mater. Chem.* **2007**, *17* (29), 2976.

98. Shen, Y.; Kuddes, D. D.; Naquin, C. A.; Hesterberg, T. W.; Kusmierz, C.; Holliday, B. J.; Slinker, J. D.; Shen, Y.; Kuddes, D. D.; Naquin, C. A.; Hesterberg, T. W.; Kusmierz, C.; Holliday, B. J.; Slinker, J. D. **2013**, *203305*.

99. Lin, K. Y.; Bastatas, L. D.; Suhr, K. J.; Moore, M. D.; Holliday, B. J.; Minary-Jolandan, M.; Slinker, J. D. *ACS Appl. Mater. Interfaces* **2016**, *8* (26), 16776–16782.

100. Leprêtre, J.-C.; Deronzier, A.; Stéphan, O. *Synth. Met.* **2002**, *131* (1–3), 175–183.

101. Bandiello, E.; Sessolo, M.; Bolink, H. J. *J. Mater. Chem. C* **2016**, *4* (46), 10781–10785.

102. Costa, R. D.; Orti, E.; Bolink, H. J.; Monti, F.; Accorsi, G.; Armaroli, N. *Angew. Chemie - Int. Ed.* **2012**, *51* (33), 8178–8211.

103. Wang, S.; Li, X.; Xun, S.; Wan, X.; Wang, Z. Y. *Macromolecules* **2006**, *39* (22), 7502–7507.

104. Gao, J.; Dane, J. *Appl. Phys. Lett.* **2003**, *83* (15), 3027–3029.

105. Costa, R. D.; Ortí, E.; Bolink, H. J. *Pure Appl. Chem.* **2011**, *83* (12), 2115–2128.

106. Hu, T.; He, L.; Duan, L.; Qiu, Y. *J. Mater. Chem.* **2012**, *22* (10), 4206–4215.

107. Rudmann, H.; Shimada, S.; Rubner, M. F. *J. Am. Chem. Soc.* **2002**, *124*, 4918–4921.

108. Aebischer, A.; Gumy, F.; Bünzli, J.-C. G. *Phys. Chem. Chem. Phys.* **2009**, *11* (9), 1346–1353.

109. Fernandez-Castano, C.; Foces-Foces, C.; Jagerovic, N.; Elguero, J. *J. Mol. Struct.* **1995**, *355*, 265–271.

110. Katagiri, S.; Sakamoto, R.; Maeda, H.; Nishimori, Y.; Kurita, T.; Nishihara, H. *Chemistry* **2013**, *19* (16), 5088–5096.

111. Cárdenas, D. J.; Echavarren, A. M. *Organometallics* **1999**, *18* (17), 3337–3341.

112. Wang, Z.; Turner, E.; Mahoney, V.; Madakuni, S.; Groy, T.; Li, J. *Inorg. Chem.* **2010**, *49* (11), 11276–11286.

113. deMello, J. C. *Phys. Rev. B* **2002**, *66* (23), 235210.

114. Symmorphic Space Group http://reference.iucr.org/dictionary/Symmorphic_space_groups (accessed Apr 23, 2017).

115. Giacovazzo, C. In *Fundamentals of Crystallography*; Oxford University Press: Oxford, New York, 2011; pp 1–65.

116. Giacovazzo, C. In *Fundamentals of Crystallography*; Oxford University Press: Oxford, New York, 2011; pp 157–234.